Chemistry & Magnetism

of Single Molecule Magnet

Monolayers on Gold Surfaces

Francesco Pineider

Università degli Studi di Firenze

Dipartimento di Chimica

Scuola di Dottorato in Scienze

Dottorato di Ricerca in Scienze Chimiche

XXI Ciclo

CHIM/03 - Chimica Generale ed Inorganica

Chemistry and Magnetism of Single Molecule Magnet Monolayers on Gold Surfaces

PhD. Thesis by

Francesco Pineider

Tutor	*Coordinator*
Prof. Roberta Sessoli	Prof. Gianni Cardini

Contents

List of Figures

List of Tables

List of acronyms and abbreviations

AEY   Auger Electron Yield
AF   Antiferromagnetic
AFM   Atomic Force Microscopy
BE   Binding Energy
BM   Bending Magnet
DCM   Dichloromethane
DFT   Density Functional Theory
dpm   *dipivaloylmethane*
EM   Electromagnetic
EPR   Electron Paramagnetic Resonance
ESN–STM   Electron Spin Noise–Scanning Tunneling Microscopy
FFT   Fast Fourier Transform
FM   Ferromagnetic
FWMH   Full Width at Half–Maximum
ID   Insertion Device
J–T   Jahn–Teller
MCD   Magnetic Circular Dichroism
MFM   Magnetic Force Microscopy
ML   Monolayer
MOKE   Magneto–Optical Kerr Effect
PDMS   *poly(dimethylsiloxane)*
PEM   Piezo-Electric Modulator
PEY   Partial Electron Yield
PMMA   *poly(methylmetacrylate)*
PS   *poly(styrene)*
QCM   Quartz Crystal Microbalance
SERS   Surface–Enhanced Raman Spectroscopy
SH   Spin Hamiltonian
SMM   Single Molecule Magnet
SPHM   Scanning Hall Probe Microscopy
SP–STM   Spin Polarized–Scanning Tunneling Microscopy
SQUID   Superconducting Quantum–Interference Device
STM   Scanning Tunneling Microscopy
TBT   Très Bas Temperature
TEY   Total Electron Yield
THF   Tetrahydrofuran
ToF–SIMS   Time of Flight–Secondary Ion Mass Spectrometry
UHV   Ultra High Vacuum
VSM   Vibrating Sample Magnetometer
VTI   Variable Temperature Insert
XAS   X-ray Absorption Spectroscopy
XPS   X-ray Photoelectron Spectroscopy
XMCD   X-ray Magnetic Circular Dichroism
XMLD   X-ray Magnetic Linear Dichroism
XNCD   X-ray Natural Circular Dichroism
XNLD   X-ray Natural Linear Dichroism
ZFS   Zero–Field Splitting

Introduction

At the beginning of the year 2009, when this thesis work has been completed, the discovery of Single Molecule Magnet behavior is little more than 15 years old. During these three lustres, the field has had the time to evolve to a mature research area, thanks to the joint effort of various and different scientific communities both in Europe, that can still be considered somewhat the stronghold of Molecular Magnetism, in the Americas and the Far East. The finding that Single Molecule Magnets (SMMs) could keep magnetic memory by exhibiting slow relaxation of magnetization at low temperature[1] just like very small and perfectly monodisperse magnetic nanoparticles, immediately sounded very appealing. In fact, from the technological point of view, SMMs are true functional nano–objects with sizes typically ranging from 2 to 4 nanometers, that could in principle store information *at least* in a binary from (magnetization up/down). However, if the promises held by SMMs in applicative fields were high, even more was to be expected from the point of view of fundamental research in magnetism: just a few years after the first observation of the opening of magnetic hysteresis in fact, the first experimental evidence of Quantum Tunneling of Magnetization was reported,[2] showing the coexistence of classical and quantum phenomena in this class of molecules.

The evolution from that point moved in various directions: from purely theoretical studies to fully understand the physics underlying SMM behavior,[3,4] to synthetic effort aimed at obtaining molecules able to freeze magnetization at higher temperature,[5] and the study of their properties in non–crystalline environments.

One of the most active research fields in recent yeas has been that of covalently binding these magnets to surfaces,[6] taking advantage of their molecular nature for proper functionalization. The scientific community then faced the challenge of addressing such very diluted systems in order to know if the magnets were actually there, and in what shape. After about ten years from the first report of SMM behavior then, what has been studied through the joint knowledge of inorganic chemistry, magnetism and calculus became the field of materials science and nanotechnology as well. The impulse toward this type of research came from two directions: on one side fixed, potentially addressable magnetic objects on a flat surface promptly reminds the magnetic memory of a hard drive, while from the fundamental point of view it is not straightforward to

assume that SMMs will not be altered by the interaction with a surface. Technology and fundamental science go alongside once again.

The main aim of this thesis work was to obtain a proof of concept that SMMs and surfaces were not incompatible: as it s quite clear, while on the long run the study points to application, it is in fact fundamental research. The time line in Figure 1 shows the evolution of this research field in relation to the first, *ante litteram* preparation of a single molecule magnet, and the first discoveries in the field.
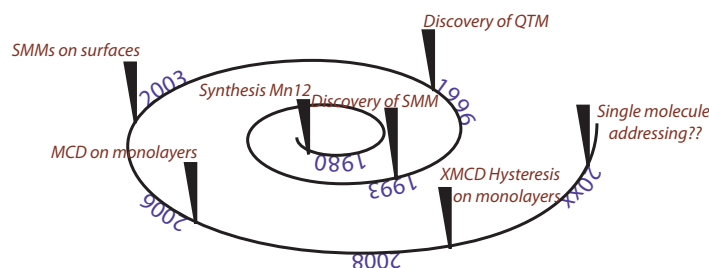
Figure 1: Time line of the progress in surface anchoring of SMMs

The contribution of this thesis dates to a time when the study on the formation of monolayers of Mn12 derivatives on gold was already established, and the first steps toward grafting of Fe4 on the same surface were taken. In parallel, the first bits of magnetic information at the monolayer level were being retrieved from XMCD.

This thesis is structured as follows: **Chapter 1** gives a basic description of the theory underlying SMM behavior, then I describe very briefly the structure and magnetic properties of the compounds that have been used more extensively throughout this work. **Chapter 2** starts with the explanation of the basic features that make a SMM a good grafting unit in general, and for gold surface in particular. In the rest of the chapter there is some in–depth information on my work with monolayers of Mn12 on gold obtained from self–assembly from solution; in particular the influence that the solvent has on the morphology of monolayer is described, along with the spontaneous arising of lateral order in some areas of the adsorbate, and some other features. The data presented in this chapter is almost completely coming from Scanning Tunneling Microscopy (STM) and X-ray Photoelectron Spectroscopy.

Chapter 3 describes the study of another very promising SMM, Fe4, that has been recently modified to be grafted to gold:[7] while the approach is similar to the one used for Mn12, it is more systematic, and contains information on monolayers of two different Fe4 derivatives, deposited from four types of solvent and with three techniques, adding Time of Flight Secondary Ions Mass Spectrometry (ToF–SIMS) to the techniques mentioned above. These first results

on Fe4 monolayers on gold are very encouraging and coherently suggest that this SMM is quite compatible with the surface, at least from a chemical point of view.

In the second part of this thesis I move to the magnetic characterization of the monolayers studied in Chapters 2 and 3. Both techniques we used are based on the interaction of polarized light with the spins of the sample: in **Chapter 4** some theory of Magnetic Circular Dichroism in the valence band (MCD) is given, in order to introduce the experiments carried out on bulk and monolayer samples of Mn12 and Fe4. For bulk experiments, dispersion of the magnetic molecules in transparent polymeric matrices was optimized, while in the case of monolayers we have tried to enhance the signal by preparing plasmonic gold substrates.

Finally, in **Chapter 5** I describe the key experiments that allowed us to finally have a clear picture of the situation of the gold surface: thanks to very high sensitivity, element selectivity of the X–ray Magnetic Circular Dichroism the and exceedingly low temperature of the ^{3}He–^{4}He dilution cryostat, we were able to ascertain that Mn12 is doubly incompatible with the surface environment, both for chemical and structural weaknesses. This somewhat shocking conclusion was well balanced by the observation of open XCMD hysteresis loops in monolayers of the other, more robust SMM studied, Fe4. This finding gave us the long–awaited proof of concept that single molecule magnets can indeed maintain their magnetic properties when bound to a metallic surface.

Chapter 1

Single Molecule Magnets

1.1 The cycles of magnetism

Molecular magnetism has covered in time a sort of cyclic pathway. In the day x-ray diffractometers were not available the magnetism of simple paramagnetic metal complexes was investigated to gather information on the coordination polyhedron around the metal center.[8,9] The investigation of pairs and oligomers of transition metal ions was the focus of the research in the early eighties and allowed to establish useful correlations between the molecular structure and the efficiency in transmitting the exchange interaction between the paramagnetic centers.[10] With this information in hand, chemists got able to construct extended structures that could order magnetically close to room temperature.[11–13] The main advantage of this molecular approach to ordered magnetic materials resides in the possibility to combine different properties brought in by the different building-blocks forming the molecular materials. A very recent example consists in the coexistence of magnetic order and optical chirality to yield a strong magneto-chiral effect.[14]

The nineties were characterized by an intense research on a new class of molecular materials, also known as Single Molecule Magnets (SMMs).[15–17] These are in general polynuclear coordination complexes comprising paramagnetic metal ions efficiently connected by the ligand atoms but shielded one from the other by the organic part of the ligands. They can be figured as tiny pieces of metal oxides or hydroxides whose growth to form extended lattices has been blocked by capping organic molecules. The most interesting aspect is that a few of these molecular clusters, those featuring a combination of a large spin and an easy axis magnetic anisotropy, are characterized by a dramatic slowing down of the fluctuations of the magnetization at low temperature, and in some cases a magnetic hysteresis is observed.[13] Contrarily to what occurs in more conventional materials, this type of hysteresis has a pure molecular origin and does not require long range order. The great potentiality of Single Molecule Magnets to store information in their magnetic memory immediately appeared clear, even

if the temperatures at which the hysteresis is observed remains, despite the synthetic effort, in the liquid helium region, thus prohibitive for technological applications. This however has not diminished the interest in these materials as model systems to investigate magnetism at the nanoscale, in particular the coexistence of quantum phenomena with the classical hysteretical behavior.[18]
A key issue that has been addressed in recent years is the possibility to address the magnetism of a single object, indeed a mandatory step to fully exploit the molecular nature of SMMs. The circular pathway is therefore closing on the isolated magnetic objects; this time however, the environment is not anymore that of the crystal lattice but the nanostructure built around the magnetic molecule. This gives the possibility to combine the rich quantum-dynamics of SMMs with transport properties, in the the emerging field known as molecular spintronics.[19] The first step in this direction has been the organization of isolated SMMs on conducting and semi conducting surfaces, an approach that has the double advantage of allowing single molecule addressing, thanks to the very high lateral resolution of scanning probes techniques, as well as to probe the conductance of the molecule.
As the field of molecular magnetism merged with surface science, researchers involved in the field are beginning to face a new challenge: the surface is not innocent with respect to the electronic and magnetic structures of the grafted molecules, and the tiny amount of material that is deposited in a monolayer makes their characterization very demanding. Synchrotron based techniques have revealed as the ideal tools to investigate SMMs deposited on surfaces and have recently lead to important results (See Chapter 5).
We will then briefly describe preparation and magnetic behavior of the SMM used in this thesis work.

1.2   Molecular magnetism in a nutshell

In the following sections, we shall give an overview of the general concepts underlying the most important properties of single molecule magnets, in particular slow relaxation and quantum tunneling of the magnetization.

1.2.1   Building up a large spin

If we exclude the fascinating case of mononuclear lanthanide complexes of high symmetry, for instance the double decker compounds with phthalocyanine[20] or ions embedded in polyoxometallates,[21] all other molecules presenting slow relaxation of the magnetization are constituted by polynuclear complexes of paramagnetic metal ions.
In the case of metal ions with a quenched orbital contribution the leading term in the effective Spin Hamiltonian (SH) is isotropic exchange:

$$\mathcal{H}_{ex} = \sum_{i>j} J_{ij} \boldsymbol{S}_i \cdot \boldsymbol{S}_j \qquad (1.1)$$

where i and j run over all sites of the cluster. Usually only interactions between nearest neighbor magnetic sites are considered, even if sizeable next nearest neighbor interactions are sometimes encountered. The resulting spin states are derived by following the procedure of coupling of angular momenta and are characterized by a total spin state S_T which in general varies between 0 and 1/2, depending on the total number of unpaired electrons.[22,23] The energy of the different S_T states can be calculated analytically in some high symmetry cases, in particular when a central spin exhibits the same exchange interaction with all the neighboring ones. This is also known as the Kambe approach[24] and spin systems comprising up to 13 coupled spins have been handled in this way.[25] A spin system that can be handled with this approach is the tetrameric unit is sketched in Figure 1.1:
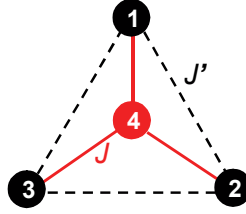
Figure 1.1: Coupling scheme in a star-like tetramer.

This spin topology is encountered in a large family of tetranuclear iron(III) clusters[26,27] also known as iron stars,[28] some of which have been extensively studied in this thesis work.
The SH that describes the exchange interactions in this system is

$$\mathcal{H}_{ex} = J[\boldsymbol{S}_1 \cdot \boldsymbol{S}_4 + \boldsymbol{S}_2 \cdot \boldsymbol{S}_4 + \boldsymbol{S}_3 \cdot \boldsymbol{S}_4] + J'[\boldsymbol{S}_1 \cdot \boldsymbol{S}_2 + \boldsymbol{S}_2 \cdot \boldsymbol{S}_3 + \boldsymbol{S}_1 \cdot \boldsymbol{S}_3]. \quad (1.2)$$

Every spin state arising from the coupling of the four spins is defined by three quantum numbers $|S_a, S_{ext}, S_T\rangle$, where $S_a = S_1 + S_2$, $S_{ext} = S_a + S_3$, and $S_T = S_4 + S_{ext}$. There are many spin states that have the same S_T but the other quantum numbers different. In the case of high symmetry, however, the total energy depends only on two of them, S_T and S_{ext}, according to:

$$E(S_T, S_{exp}) = \frac{J}{2}[S_T(S_T + 1) - S_{ext}(S_{ext} + 1) - S_4(S_4 + 1)] +$$

$$\frac{J'}{2}[S_{ext}(S_{ext} + 1) - S_1(S_1 + 1) - S_3(S_3 + 1) - S_2(S_2 + 1) - S_1(S_1 + 1)]$$

$$(1.3)$$

Considering that all terms involving pure spins act only as an offset on the energy, (1.3) can be simplified as:

$$E(S_T, S_{exp}) = \frac{J}{2}[S_T(S_T + 1) - S_{ext}(S_{ext} + 1)] + \frac{J'}{2}[S_{ext}(S_{ext} + 1)], \quad (1.4)$$

which means that in order to consider the correct degeneracy, one must simply count all possible states arising from the coupling of four spins. In general, however, the diagonalization of big matrices is required and, as soon as the number of magnetic centers increases, the calculation of the energy of all resulting spin states becomes very demanding. Different approaches have been developed[29,30] and the most used one for moderate cluster sizes is based on the irreducible tensor operators.[31]

The presence of intra–cluster exchange interactions able to stabilize a large spin of the ground state is a necessary condition, although not sufficient, to observe slow relaxation of the magnetization. At present a good control of the spin of the ground state has been achieved thanks to many studies on magneto-structural correlations. The basic ones are also known as Goodenough and Kanamori rules[32–35] and refer to the overlap of the wavefunction describing the unpaired electrons of the two interacting fragments. It must be stressed that in coordination compounds the exchange interaction is most frequently mediated by the coordinating atoms of the bridging ligands, giving rise to the so called *super–exchange*, and only rarely by direct overlap of the metal *d*-orbitals. It is therefore more correct to refer to a molecular orbital of the metal fragment carrying the unpaired electron, which has a small but significant spin density on the bridging atom. The Goodenough and Kanamori rules can be stated as follows:

- An antiferromagnetic interaction is expected if an overlap of the magnetic orbitals occurs.

- A ferromagnetic interaction is expected if the magnetic orbitals of the two interacting fragments are orthogonal.

- If a magnetic orbital shows a significant overlap with a fully occupied or with an empty orbital of the second fragment the exchange interaction is ferromagnetic.

From these simple rules it is clear that antiferromagnetism in polynuclear compounds is expected to be much more common and that strict orthogonality of the orbitals is achieved only in highly symmetric molecules. Antiferromagnetic coupling is the most commonly encountered case in SMMs, including the archetypal Mn12 clusters,[36] where the $S_T = 10$ ground state results from exchange interactions that are antiferromagnetic and align the external spin $S = 2$ of Mn^{3+} anti-parallel to the $S = 3/2$ spins of the internal Mn^{4+} ions, as shown in Figure 1.2.[15,16,29,30] In analogy to the uncompensated magnetism of different sublattices discovered by Neél, these type of spin clusters are often called ferrimagnetic, with the necessary clarification that these are zero-dimensional
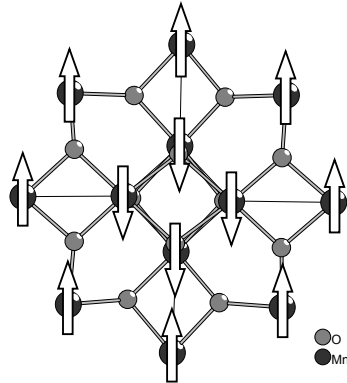
Figure 1.2: Core structure and coupling scheme in a Mn12 cluster.

objects where the correlation is limited to a finite number of spins and does not diverge as in traditional magnets.

A significant number of spin clusters showing ferromagnetic interactions are however present in the literature and ferromagnetism is encountered in the case of the molecular system exhibiting the largest spin ground state, $S_T = 87/2$,[37] and in the hexanuclear manganese cluster, that holds record for the lowest reported temperature at which the magnetization freezes.[5] The spin structure of the SMM is strongly correlated to the dynamics of the magnetization and can be considered as a sort of fingerprint of the SMM.

1.2.2 Magnetic anisotropy in SMMs

The second key ingredient in SMM is magnetic anisotropy. In traditional magnets, three factors give equally important contributions to the anisotropy, namely surface, strain, and magnetocrystalline contributions; in SMMs instead, the only significant one is magnetocrystalline and is brought in by a combination of spin–orbit coupling with the low symmetry environment around the metal centers constituting the SMM. Dipolar contributions are in most cases negligible. A quantitative treatment of the magnetic anisotropy is based on the effective spin–hamiltonian approach where only the spin variables appear, while the orbital contributions are introduced through parameters.[38] The magnetic anisotropy is treated with a multipolar expansion, which should be extended to the $2S$ order, where S is the spin of the system. Very often SMM have a low symmetry and thus the lower terms of the expansion dominate. For a system with no symmetry at all the multipolar expansion up to the second order gives:

$$\mathcal{H}_{an} = \boldsymbol{S} \cdot \boldsymbol{D} \cdot \boldsymbol{S} = D \left[S_z^2 - \frac{1}{3} S(S+1) \right] + E(S_x^2 - S_y^2), \qquad (1.5)$$

where $D = D_{zz} - 1/2D_{xx} - 1/2D_{yy}$ represents the axial anisotropy, and $E = 1/2(D_{xx} - D_{yy})$ the transverse (or rhombic) one. The value of E is intrinsically limited to $1/3D$ since higher values correspond to a change in the axis of the leading anisotropy. The transverse term can be more conveniently rewritten in terms of ladder operators as $1/2E(S_+^2 + S_-^2)$.

The effect of the magnetic anisotropy on the $2S + 1$ levels is that of splitting their energy also in the absence of an external field; such effect is thus also named Zero Field Splitting (ZFS), especially among spectroscopists. The term $1/3S(S + 1)$ introduces only an offset of all levels to maintain the center of weight of the energy spectrum and is often dropped if only relative energies inside the S multiplet are concerned.

The effect of a negative value of D is that the system is magnetized much more easily when the field is applied along the main, i.e. z, axis. In SMMs the anisotropy energy is associated to the energy gap in zero field between the states characterized by the largest and smallest $|m|$, where m is the eigenvalue of S_z.[17] In the case of pure axial anisotropy, $E = 0$, the gap corresponds to $|D|S^2$ and $|D|(S^2 - 1/4)$ for integer and half-integer spins, respectively. A system showing easy axis magnetic anisotropy ($D < 0$) has the ground doublet characterized by $m = \pm S$, which correspond to two potential wells separated by an energy barrier, U_{eff}, as reported in Figure 1.3a.
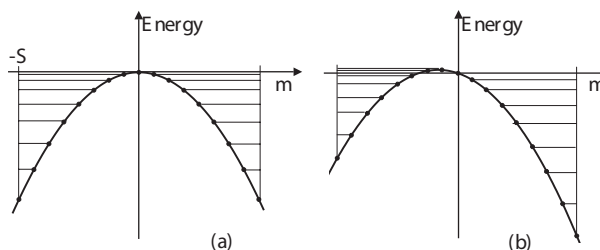
Figure 1.3: (a) Zero field splitting of the 2S+1 levels in a system with negative D value. (b) Energy level splitting in non zero applied field.

The value of D is quite easy to access experimentally for single paramagnetic centers by means of electron paramagnetic resonance (EPR) spectroscopy,[39–42] inelastic neutron scattering experiments,[43] or magnetometry, especially if performed on a single crystal specimen. The magnetic anisotropy can also be estimated theoretically, with a great variety of approaches, ranging from simple perturbation theory, starting from a spectroscopical estimation of the energy separation of the partially filled d orbitals,[44,45] to a ligand field treatment based on the Angular Overlap Model.[46] More recently *ab–initio* calculations, either based on Density Functional Theory[4] or on post Hartree-Fock approaches[47] have also shown a good predictive capability.

The situation is more complicate in the case of a polynuclear metal system, which is the typical case for SMMs. In general working with first row transi-

tion metal ions the magnetic anisotropy is weaker than intramolecular exchange interactions, so the resulting states are well described by the quantum number corresponding to the total spin state, as derived from (1.1) and the magnetic anisotropy is introduced as a perturbation. The magnetic anisotropy of a certain total spin S_T can be related to the single ion contributions, or to the anisotropic part of the interaction (of either dipolar or exchange nature) by using projection techniques:[23]

$$\boldsymbol{D}_{S_T} = \sum_i d_i \boldsymbol{D}_i + \sum_{i>j} d_{ij} \boldsymbol{D}_{ij} \qquad (1.6)$$

where i and j refer to the magnetic centers inside the SMM. The values of the projection coefficients d_i and d_{ij} depend on how the individual spins project on the total spin state under consideration, D_i are the single ion contributions and D_{ij} the anisotropy brought in by two–spin interactions. The values of d coefficients can be calculated by means of a recursive algorithm, and very small values are are typically found. This indicates that it is not straight forward to combine a large spin with a large magnetic anisotropy: although an increase in S would apparently lead to a quadratic effect on the height of the barrier, the reduced projection of the anisotropies of the single ion makes the barrier to scale linearly with S.
We will now introduce the so called *giant spin approximation*, which consists evaluating the dynamics of the magnetization behind the assumption that the whole molecule behaves like a unique large spin characterized by its axial and transverse anisotropies (derived according to (1.6)). This is justified by the fact that at low temperature only the ground spin state is populated.

1.2.3   Magnetization dynamics in SMMs

Thermally activated relaxation   Slow relaxation of the magnetization was first observed in Mn12 thanks to ac susceptibility experiments.[15] Decreasing further the temperature the relaxation becomes so slow that an opening of the hysteresis is observable.[1] This dramatic slowing down of the fluctuations has its origin in the double well potential reported in Figure 1.3, characteristic of a large spin with a negative D parameter.
The application of a magnetic field has the effect of populating the stabilized well. Once the field is removed equal population of the two wells, corresponding to zero magnetization, is only achieved by transferring part of the population on the other well. Transitions from one state to the other are promoted by deformations of the metal coordination environment. These deformations can affect the spin degrees of freedom thanks to spin orbit coupling but, at the first level of approximation, rotations and strains that modify the geometrical environment of the magnetic center, and thus its magnetic anisotropy, can only induce transitions between states differing in m_s by ± 1 and ± 2. To overcome the energy barrier a multiphonon mechanism is necessary. In analogy to a chemical reaction involving many elementary processes, the overall speed is

determined by the slowest step. In the case of SMM this is the one situated on top of the barrier, since at low temperature the highest states are less populated and also because of the quadratic energy spacing induced by eq. (1.5). The combination of these two factors yields an exponential dependence of the characteristic time, typical of thermally activated mechanism, following the Arrhenius law:

$$\tau = \tau_0 e^{\frac{U_{eff}}{k_B T}}.$$

(1.7)

For SMMs the pre–exponential factor τ_0, i.e. the inverse of the attempting frequency, is assumes much greater values than those observed for magnetic nanoparticles: for Mn12 found values were $U_{eff} = 62$ K, thus not far from $100|D| \simeq 70$ K, and $\tau_0 \simeq 10^{-7}$ s, that is 3-4 orders of magnitude greater than typical values of magnetic nanoparticles.

The question that immediately arises is why SMM behavior was not observed before, for instance in smaller clusters or even mononuclear complexes. The answer can be found in the quantum mechanics of angular momenta: in the case of pure axial symmetry the eigensatates of eq. (1.5) are pure m_s states and transitions between the two ground states with $m_S = \pm S$ can only occur through the multi-Orbach process schematized in Figure 1.3.[48] However, this is an ideal picture, while in a real systems many mechanisms are able to admix states on opposite sides of the barrier. A transverse anisotropy due to symmetry reduction, or a transverse field, either externally applied or of internal origin (dipolar of hyperfine), introduce in (1.5) in S_x and S_y terms that admix the states, and the eigenstates are described as a linear combination of the pure m_s states:

$$|\Psi_i\rangle = \sum_{m=-S}^{S} \varphi_i(m) |m\rangle .$$

(1.8)

In general, if the transverse term is a small perturbation of the axial anisotropy one of the $|m\rangle$ states is the leading term for each $|\Psi\rangle$. This is particularly true for the states lowest in barrier, because the transverse terms in the SH only mix these states at a high order of perturbation, i.e. at order S^{th} if it is induced by a transverse anisotropy or at order $2S^{th}$ if a transverse field is concerned. In the case of a small spin instead, the $S = 2$ of a Mn^{3+} ion for instance, unavoidable transverse terms make the energy barrier become transparent and the low temperature divergence of the relaxation time responsible of the SMM behavior is not observed.

Quantum tunneling of magnetization   Most SMMs, including the Fe4 complex previously mentioned, do not follow a thermally activated relaxation process at very low temperature: in fact, when decreasing temperature the relaxation time levels off.[27,49,50] This suggests that under–barrier pathways

not involving phonons are active. We have seen previously that transverse term in the SH admix states on opposite sides of the barrier. In analogy to the quantum mechanics of a particle in a double well potential, it is clear that the larger is the delocalization of the wavefunction on the other side of the barrier, the higher is the probability that the particle is found on the opposite well. In the case of spins however, an additional factor enters in the scenario: the magnetic field. A field applied along the anisotropy axis, thus coupling with the S_z component of the spin, has the effect of shifting levels on opposite sides of the barrier toward opposite directions. Perturbation theory tells us that any admixing is more efficient the closer the energy of the unperturbed states.

The case of zero field, reported in Figure 1.3a, is a special case where all unperturbed levels are degenerate in pairs. This is therefore expected to be a favorite case for tunnel relaxation. However this energy matching is re–established for other characteristic values of the applied field (Figure 1.3b):

$$H_n = n\frac{|D|}{g\mu_B} \tag{1.9}$$

Figure 1.4 shows the Zeeman diagram for a spin S with uniaxial anisotropy when exposed to an axial field.
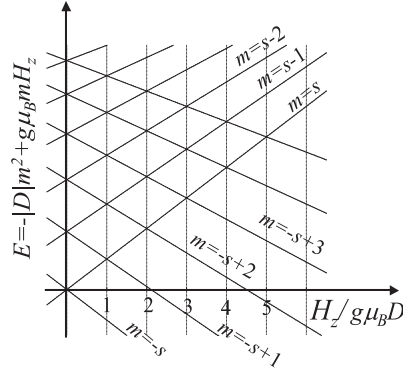
Figure 1.4: Diagram of Zeeman splitting for a spin S system and uniaxial anisotropy.

This phenomenon, known as resonant *quantum tunneling of the magnetization* (QTM), has been first observed in the ac magnetic susceptibility of Mn12 SMM[51] and then, more spectacularly, in the hysteresis curve,[2,52] which is characterized by steps at the resonant fields (see Figure 1.5).

It is interesting to notice that quantum effects are also observed in a regime where phonons play a role. In fact the admixing of levels is more efficient for states higher in the barrier (smaller $|m|$), making quantum tunneling among these thermally populated states competitive even at intermediate tempera-

tures. The mechanism is named thermally activated resonant quantum tunneling.[3]
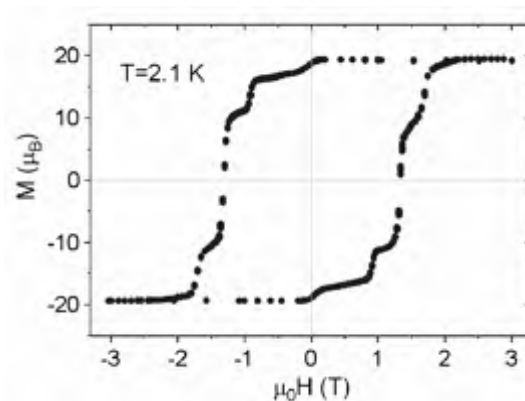
Figure 1.5: Stepped hysteresis loop of a Mn12Ac single crystal.

The vertical segments of the curve in Figure 1.5 are therefore accelerations of the relaxation times and can be theoretically reproduced with the approach developed before, by taking into account that the true eigenstates of the system are not pure $|m\rangle$ states but they are described by eq. (1.8).

The fascinating interplay of quantum and classical effects in the dynamics of the magnetization of molecular nanomagnets have attracted a large interests among physicists and chemists and the discovery of QTM was recently included in the 'Milestones of Spin' issue edited by Nature Physics[a].

1.3 The Mn12 family of SMMs

In 1980, Lis reported the synthesis, structure and basic magnetic properties of $[Mn_{12}O_{12}(O_2CCH_3)_{16}(H_2O)_4]\cdot 2CH_3CO_2H\cdot 4H_2O$, called Mn12 acetate.[36] The dodecanuclear cluster with the disc–shaped geometry, with a tetragonal lattice and a crystallographically imposed S_4 axis. Its structure is that of a mixed valence manganese oxide, with four Mn^{4+} ions and eight Mn^{3+} ions. A central Mn_4O_4 cubane unit contains the Mn^{4+} centers with three unpaired electrons $(S = 3/2)$ each; this structure is surrounded by a non–planar ring of the eight Mn^{3+} centers, each with four unpaired electrons $(S = 2)$. The metal ions are connected by oxide bridges, but the growth of the manganese oxide particles is broken by the presence of the sixteen acetate groups: four in axial positions bridging Mn^{3+} and Mn^{4+} ions, four in axial positions bridging Mn^{3+} ions and eight in equatorial positions bridging Mn^{3+} ions. These carboxylates and four

---

[a]DOI: 10.1038/nphys877, 2008

terminal water molecules complete the coordination spheres of each Mn center to give an octahedral coordination environment.

The valences of the metal ions can be clearly determined by the x-ray crystal structure. In fact Mn^{3+} ions in octahedral symmetry have a ground ^5E_g state,[53] which is prone to Jahn-Teller distortions; the external metal ions in Mn12Ac are all in tetragonally elongated environment, positively identifying them as Mn^{3+} ions; the J-T elongation axis of Mn^{3+} ions are all oriented roughly in the direction of the main crystallographic axis, which is also the easy axis. Mn^{4+} ions on the other hand do not show J-T elongation, all Mn–O distances being very similar.

Lis' comment on his basic magnetometric characterization of the complex was 'such a complicated dodecameric unit should have interesting magnetic properties'. He was quite right.

We shall not spend more time on the magnetic properties of the archetypal Mn12Ac spin cluster; these are very well known and described in a huge number of articles, reviews, books, PhD theses and popular magazines. We will instead stress that ligand exchange can be very easily achieved by means of wet chemistry processes, and a great number of carboxylates can be introduced around the inorganic core without altering its magnetic properties.[54]

1.3.1 Mn12BnSMe

This Mn12 derivative was designed, synthesized and characterized during this thesis work, so its description will serve as the basis for the more brief introduction to the other Mn12 complexes presented.

The choice of the ligand, αa-methylthio-4-toluic acid (HO$_2$CBnSMe), will be detailed in section 2.8, all we are interested in at this point is that it belongs to the series of sulphur–containing carboxylic acids that make Mn12 able to graft to gold surfaces.[6] This ligand was prepared by following a literature procedure[55] with a simple two–step synthesis, and inserted around the Mn12 core by the ligand exchange method, as depicted in Figure 2.1.

The new derivative, Mn12BnSMe, was first characterized from the structural point of view, both in crystalline samples and in solution.

X-ray diffraction. Single crystals suitable for x-ray diffraction were precipitated from dichloromethane solutions by slow diffusion of hexane (about 1:3 ratio of solvent/precipitating agent by volume in tightly capped vials. X-ray diffraction measurements were carried out on an Oxford Diffraction Xcalibur3 diffractometer equipped with a MoKα radiation source and CCD area detector. The data collection and data reduction were performed with the CRYSALIS CCD and CRYSALIS RED programs (Oxford Diffraction Ltd., Version 1.171.31.2), respectively. Absorption corrections were applied through the program ABSPACK. The structure was solved by direct methods using the package SIR-97[56] and subsequently refined on the F^2 values by full-matrix

least-squares methods by using the SHELXL-97 software package[b].

The unit cell was found to be triclinic of space group $P\bar{1}$ and containing two units of the complex related by a crystallographic center of inversion. The collected data confirmed the identity of the inorganic core, featuring four Mn^{4+} ions in the central cubane unit and eight Mn^{3+} ions in the surrounding ring; the complete substitution of the sixteen acetate ligands with the incoming carboxylates was also assessed. The structure is shown in Figure 1.6.
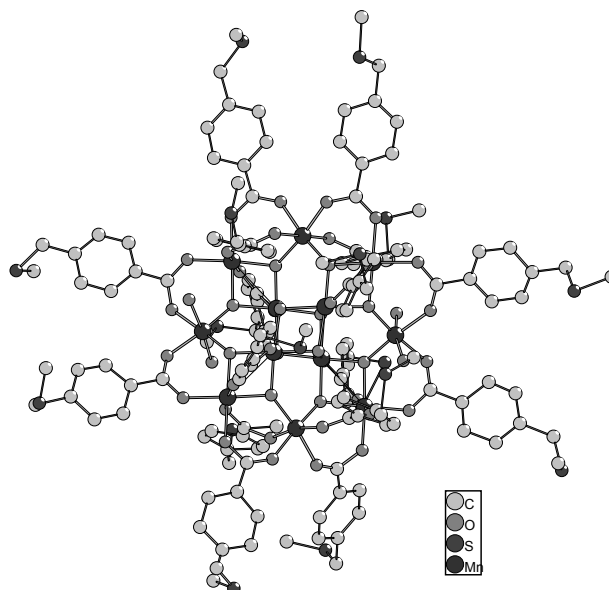
Figure 1.6: Structure of Mn12BnSMe from single crystal x-ray diffraction.

The main structural difference between the starting complex, Mn12 acetate (Mn12Ac) and this derivative is an exotic intercalation of the axial Mn^{4+}-Mn^{3+} bridging aromatic carboxylates with the water molecules that complete the octahedral coordinating sphere of Mn^{3+} ions: the four water molecules in fact are found in couples on the two axial coordinating positions of two opposite Mn^{3+} ions, instead of being situated on alternated axial positions of four Mn^{3+} ions. This structural feature reduces the symmetry of the complex from S_4 to *pseudo*–C_2. A different distribution of water molecules with respect to Mn12Ac or even cases of missing water molecules have been reported for several other derivatives of the Mn12 family.[17]

The Mn^{3+} ions feature a Jahn-Teller elongation in the direction of the main axis as expected except one of them, that does not exhibit any elongation, thus lowering the overall symmetry of the crystal. This has been ascribed to the

---

[b]G.M. Sheldrick SHELXL-97: Program for the Refinement of Crystal Structures from Diffraction Data; University of Göttingen, Göttingen, Germany, 1997.

presence of an isomer in which the Jahn-Teller distortion axis of the apparently non–elongated Mn ion is tilted by 90°, as it has already been reported in literature for other members of the Mn12 family,[57] and confirmed by the ac susceptibility measurements discussed further in this section.

^{1}H–NMR spectroscopy. This type of structural characterization was carried out in order to ascertain the stability of the cluster in solution. ^{1}H–NMR spectra were recorded using a Varian Gemini 300 spectrometer operating at a frequency of 300 MHz; measurements were carried out in CD_2Cl_2 and are shown in Figure 1.7.
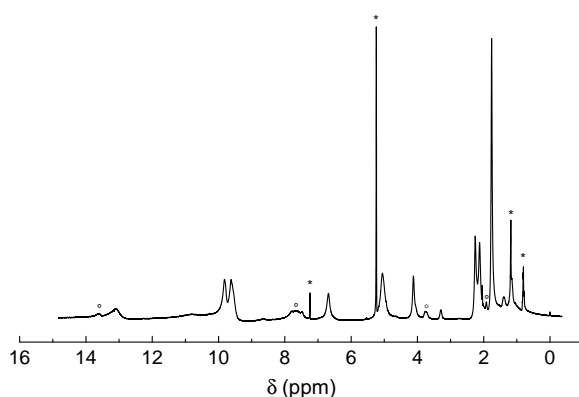
Figure 1.7: ^{1}H–NMR spectrum of Mn12BnSMe in CD_2Cl_2. Asterisks mark peaks relative to solvents and circles those of the free ligand.

In solution the Mn^{3+}-Mn^{3+} bridging axial ligands quickly exchange with the neighboring water molecules, so that the non–equivalence is partly removed, thus raising the symmetry of the complex to *pseudo*-S_4. The symmetry–equivalent ligands in this case are four groups of four, namely axial Mn^{4+}-Mn^{3+} bridging units, axial Mn^{3+}-Mn^{3+} bridging units and two sets of equatorial units (every second equatorial ligand is symmetry–equivalent). All the peaks in the spectrum can be reasonably assigned to these four classes of symmetry–equivalent ligands resonances, as summarized in Table 1.1. It must be pointed out that the two sets of equatorial ligands originate fully overlapping peaks, with the exception of a poorly resolved couple of methylene signals around 9.7 ppm, in turn partially overlapping with a peak attributed to the *meta* aromatic hydrogens of the axial Mn^{3+}-Mn^{4+} bridging ligands.

Magnetic measurements. The magnetic characterization of Mn12BnSMe was carried out on pressed pellets of microcrystalline samples. For static (hys-

δ (ppm)	Assignment
13.1	8H, m–CH (III-III)$_{ax}$
10.8	8H, o–CH (III-IV)$_{ax}$
9.8-9.6	16H, CH$_2$ (III-III)$_{eq}$
9.5	8H, m–CH (III-IV)$_{ax}$
7.6	8H, o–CH (III-III)$_{ax}$
6.7	8H, CH$_2$ (III-IV)$_{ax}$
5.1	16H, m–CH (III-III)$_{eq}$
4.1	8H, CH$_2$ (III-III)$_{ax}$
2.3-2.1	12H, CH$_3$ (III–III)$_{ax}$
	12H, CH$_3$ (III–IV)$_{ax}$
1.8	24H, CH$_3$ (III–III)$_{eq}$
2-0	16H, o–CH (III-III)$_{eq}$

Table 1.1: Assignment of the ^{1}H–NMR peaks for Mn12BnSMe.

teresis loop) and dynamic (ac) magnetic measurements we employed an Oxford Instruments VSM–12T equipped with a home–built ac coil apparatus; ZFC-FC measurements were carried out on a Cryogenic S600 SQUID magnetometer.

The hysteresis loop between ±120 kOe was recorded at 1.8 K and is shown in Figure 1.8a. The Mn12 family has a ground spin state of $S = 10$, so the value of the magnetization at saturation is 20 μ_B: as it can be seen in Figure 1.8a, saturation is not fully reached at 120 kOe but the magnetization definitely tends to the expected value. The compound shows hysteretic behavior, with a residual magnetization of about 5 μ_B and a coercive field of 4.8 kOe; these values are somewhat low when compared to those of other Mn12 derivatives.[17] Zero field cooled/field cooled measurements in a field of 50 Oe (Figure 1.8b showed a blocking temperature of 2.7 K.
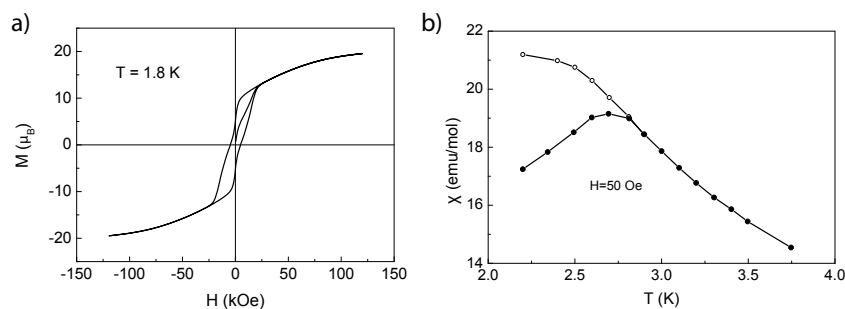
Figure 1.8: a) VSM hysteresis loop and b) zero–field cooled/field cooled susceptibility measurement of a polycrystalline sample of Mn12BnSMe. Field used was 50 Oe.

Ac susceptibility measurements (Figure 1.9) carried out in zero Oe static field and 3 Oe alternating field revealed the presence of two frequency–dependent peaks in the out of phase component χ'', that confirm the dynamic origin of the hysteretic behavior observed in the system. From the susceptibility data the relaxation times were determined by assuming that at the temperature corresponding to the maximum of χ'', the relaxation time equals the experimental measuring time, $\tau = (2\pi\nu)^{-1}$. The data could be nicely fitted to the Arrhenius law and the best fit parameters are $\tau_0 = 1.9 \times 10^{-9}$ s, $\Delta E/k_B = 64.0$ K and $\tau_0 = 2.3 \times 10^{-10}$ s, $\Delta E/k_B = 29.7$ K for the high and low temperature peaks, respectively (Figure 1.9c). While the parameters of the former are in good agreement with the typical values of the Mn12 family, the latter shows a behavior that has to be ascribed to the presence of a Mn12 isomer with a tilted JahnTeller elongation axis on a Mn^{3+} ion, as it has been evidenced by the crystallographic analysis. The relative abundance of this low energy barrier isomer is about 47%, based on χ'' peak integration; it is worth pointing out that at the temperature at which the hysteresis curve was acquired (1.8 K), this isomer has a relaxation time τ of about 3 ms, that is shorter than the time scale of the static experiment, so at this temperature it behaves as a paramagnet. Therefore the magnetization curve shown in Figure 1.8a is the sum of an irreversible component (slow-relaxing species) and of a reversible one (fast-relaxing species) and exhibits a lower remnant magnetization than expected.[57]

1.3.2   Mn12PhSMe

The cluster Mn12PhSMe, shown in Figure 2.4, page 30 is very similar to the one described in the previous section, and has been synthesized a few years before this thesis work started[54] and has been thoroughly described in its bulk properties. However, since during this work it has been extensively studied as a monolayer on gold, we will very briefly report some of its structural and magnetic properties.

X-ray diffraction.   The complex crystallizes in the space group $I\bar{4}$, with eight $CHCl_3$ crystallization molecules and two Mn12 molecules in the unit cell. The structure exhibits crystallographic S_4 symmetry. On the basis of Mn-O bond distances one can distinguish the Jahn-Teller distorted Mn^{3+} atoms. Also in this derivative J-T isomerism is observed.

^{1}H–NMR spectroscopy.   The spectrum in CD_2Cl_2 is very similar to that of Mn12PhSMe, and all of the peaks are found within a relatively narrow chemical shift window (from 14 to 0 ppm), as might be expected from a complex with all protons significantly removed from the paramagnetic center; all peaks were assigned to a subset of carboxylate ligands. We can then conclude the the complex is stable in solution.
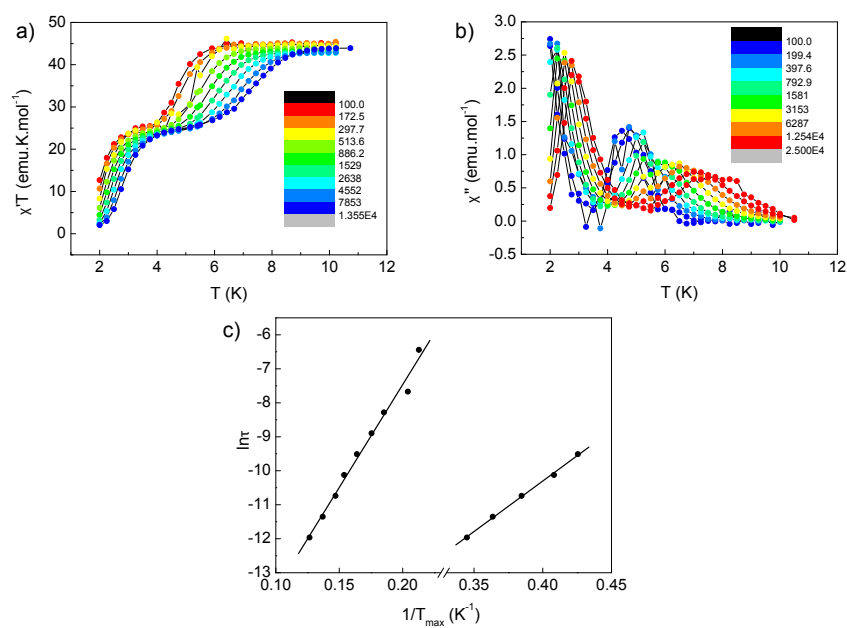
Figure 1.9: Ac susceptibility measurement of a polycrystalline sample of Mn12BnSMe. (a) In phase χ' component, (b) out of phase χ'' component, and (c) Arrhenius plot for the high and low temperature out of phase peaks.

Magnetic measurements. In addition to standard static magnetic measurements, among which M vs H curves show opening if the hysteresis, ac susceptibility experiments were carried out and identified two temperature–dependent peaks in the out of phase component. The dynamic parameters obtained from these data are: $\tau_0 = 1.42 \times 10^{-9}$ s and $\Delta E/k_B = 65.9$ K for the higher anisotropy J-T isomer and $\tau_0 = 0.7 \times 10^{-10}$ s and $\Delta E/k_B = 39.4$ K for the lower anisotropy isomer.

1.4   The Fe4 family of SMMs

Fe4 clusters are among the simplest inorganic systems showing SMM behavior.[26,58,59] The archetypal member of this class is the tetrairon(III) compound $[Fe_4(OMe)_6(dpm)_6]$ (Hdpm=dipivaloylmethane). The six μ–methoxide ligands bridge a central iron(III) ion to three peripheral iron centers arranged at the vertices of an isosceles triangle[26] with a crystallographic C_2 symmetry, and some disorder which yields three different isomers in the lattice. At low temperature, the cluster has a high-spin state ($S = 5$) and easy-axis magnetic anisotropy.

This complex can be converted into a new class of SMMs by exchanging the bridging methoxides with tripodal ligands R–$C(CH_2OH)_3$.[27] The reaction, similar to the ligand exchange in Mn12, proceeds smoothly in organic solvents and allows to modulate the molecular structure and magnetic parameters of the clusters: this site-specific ligand replacement provides a means to raise the symmetry of Fe4 clusters from C_2 to D_3, and the magnetic properties are in general enhanced and the anisotropy barrier is larger than that in the parent compound, reaching values up to 17 K. Such energy barrier is still very low compared to those typical of Mn12, and to directly observe the blocking of the magnetization it is necessary to reach sub–Kelvin temperatures.

The chelating effect of the triol ligands also make the complex much more stable than its precursor, thus allowing a much easier manipulation.

As we have done for Mn12, we will describe the details of magnetic properties directly for the Fe4 derivative that has been the most used in this thesis work, Fe4C9SAc.

1.4.1   Fe4C9SAc

This compound was prepared by introducing the appropriate triol ligand around the Fe4 core by ligand exchange.[7] Standard structural and magnetic characterization is reported in the following paragraphs.

X-ray diffraction. The cluster Fe4C9SAc crystallizes in space group $C2/c$, with half tetrametallic complex in the asymmetric unit and consequently four molecules per unit cell. In spite of the long, flexible alkyl chain the crystals are excellent x-ray diffractors. The thioacetyl-terminated alkyl chain is found

disordered over three positions with respective occupancies 0.36, 0.28 and 0.36. Noticeably, the distance between the two S atoms in each molecule is as large as 2.6–2.9 nm. The structure of the tetrairon central unit is planar and the distances between the central iron and the peripheral centers is the same for all three iron atoms. The structure is shown in Figure 3.1 on page 54.

^{1}H–NMR spectroscopy. The resonances in Fe4 clusters are very complicated and difficult to assign, unless one uses deuterium–containing derivatives and D-NMR, that allows full peak assignment.[50] Standard proton NMR however, can give very valuable information of the integrity of the cluster in solution: the complex is in fact rather unstable with respect to acidic protons, and the proton on $CHCl_3$ is acidic enough to make it gradually decompose to Fe_2 units. This can be easily monitored by the shift in the broad signal around 10.5 ppm in Figure 1.10, relative to *tert*–butyl hydrogen atoms of the dpm ligand: upon decomposition of the tetramer to dimers, this peak shifts to slightly higher ppm values, and a second broad resonance appears around 12.5 ppm. In CH_2Cl_2, which possesses less acidic protons, no time evolution of the spectrum is observed, and the compound is stable.
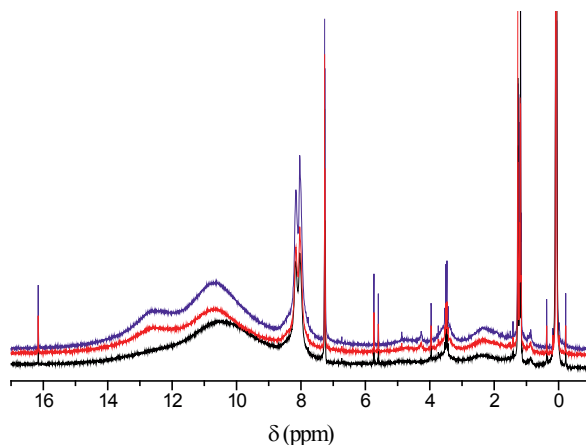
Figure 1.10: ^{1}H–NMR spectrum of Fe4C9SAc in $CDCl_3$. Time evolution from 0 hours (black) to 24 hours (red) and 65 hours (blue).

Magnetic measurements. The temperature behavior of χT in a 100 Oe applied field (Figure 1.11)is typical of antiferromagnetic coupling in a system whose spin topology does not allow full compensation of the magnetic moments. The value of χT is 12.24 emu.K.mol^{-1} at 270 K and decreases upon lowering the temperature, going through a minimum at $T = 100$ K ($\chi T = 10.51$ emu.K.mol^{-1}), and then increases to reach the value of 14.53 emu.K.mol^{-1} at 9.5 K. Below this temperature a small decrease of χT is observed: this is not

to be ascribed to saturation but might be originated either by inter–cluster antiferromagnetic interactions or by the presence of zero field splitting of the ground $S = 5$ spin multiplet.
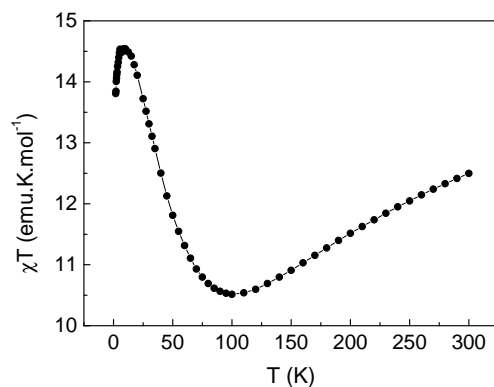
Figure 1.11: Temperature dependence of χT in Fe4C9SAc in an applied field of 1000 Oe.

Due to its very low blocking temperature, hysteresis loops on Fe4C9SAc were carried out on a μ–SQUID setup equipped with a dilution setup by Wolfgang Wernsdorfer at the Institut Neél in Grenoble; such curves show opening of butterfly–shaped hystereses; these variable temperature measurements are shown in the Chapter dedicated to XMCD studies, in Figure 5.26 on page 166. Fitting of the curves gave the axial anisotropy parameter $D = -0.412$ cm^{-1} for this compound.

Dynamic susceptibility measurements, carried out on zero Oe static and 5 Oe oscillating fields are shown in Figure 1.12. Just one peak in the out of phase component is visible at low temperature. Using the same procedure described for Mn12BnSMe we could extract the characteristic dynamic parameters from the positions of the peaks in χ'': these were found to be $\tau_0 = 1.49 \times 10^{-7}$ s and $\Delta E/k_B = 18.1$ K.

In the next two Chapters we will return to these Mn12 and Fe4 derivatives, and we shall focus on the correlations between the molecular structure of the ligands and their function for the purpose of surface grating of the magnetic complexes.
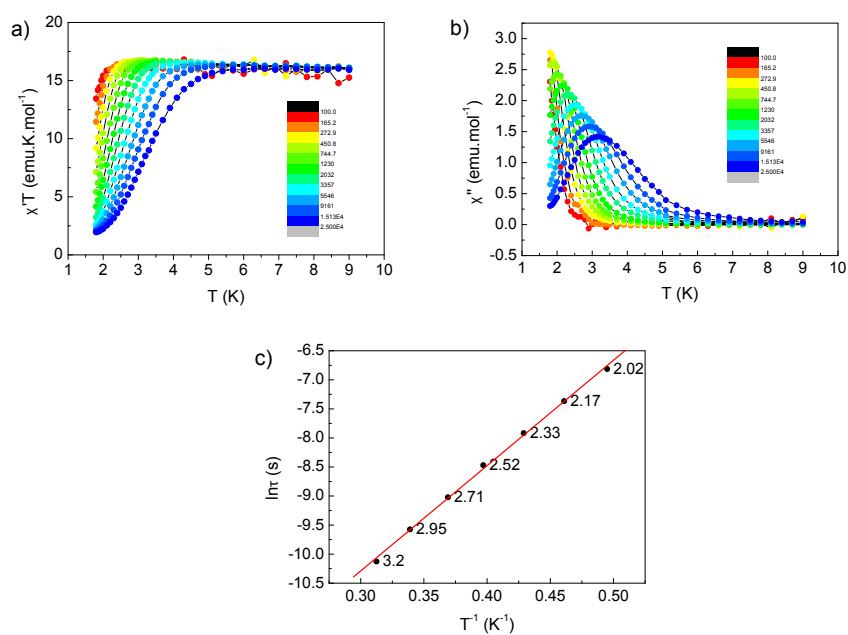
Figure 1.12: Ac susceptibility measurement of a polycrystalline sample of Fe4C9SAc. (a) In phase χ' component, (b) out of phase χ'' component, and (c) Arrhenius plot for the high and low temperature out of phase peaks.

Chapter 2

Monolayers of Mn12

2.1 The Art of casting single layers

The possibility of addressing a single layer and, finally single magnetic molecules is a very interesting and challenging goal. Needless to say, the shift from three-dimensional to two-dimensional systems carries difficulties besides advantages, as charmingly pointed out by W. Pauli[a], the first issue being the process itself of producing a layer of intact units on a flat surface. To this aim, a wealth of methods are reported in the literature, ranging from extremely neat ultrahigh vacuum environment deposition techniques to solution phase methods, that rely on various degrees of self-organization to obtain the final layer. Due to the bulky and delicate nature of transition metal clusters, deposition pathways involving evaporation in ultrahigh vacuum are quite challenging, and are at a very basic level for SMMs. On the other hand, the molecular nature of these nanomagnets makes them very suitable for functionalization and deposition onto surface from solution. The technique we used to deposit SMMs on metallic surfaces is very similar to the Self-Assembly of Monolayers technique.

The first reports on monolayers date back to 1946, when Ziesman[60] found that a surfactant adsorbed as a single layer on metallic surfaces; nevertheless, the real birth of the research field on Self-Assembled Monolayers (SAMs) was in 1983, when Nuzzo and Allara[61] discussed the tendency of aliphatic thiols to form ordered bidimensional structures of gold surfaces. The ease of preparation, involving minimal substrate pre-treatment, and no active participation of the operator during the process itself, opened the path to a great number of studies on SAM preparation and properties. A general definition of SAM is that of an ordered array of molecules bound by means of a specific interaction to a surface. Molecules that are able to organize on a surface are usually made up of a surface binding group and a tail, usually simple aliphatic chains of aromatic moieties; a second functional group can be present on the molecule to

---

[a]God created the solids, the devil their surfaces.

expand the features of the SAM. The forces involved in SAM formation are essentially two:[62] the headgroup–surface interaction, that drives the adsorption of the molecule to the surface, and the tail–tail interaction that, in thermodynamically controlled processes, leads to the formation of an organized network, that can be regarded as a bidimensional lattice; the functional groups can in turn give rise to a third type of interaction, like interchain H–bonding networks for SAMs of carboxylic acids.

2.2   Mn12 and monolayer–oriented design

The family of Mn12 single molecule magnets can be expanded at will by properly designing the carboxylate ligands that surround the inorganic core of the complex. The proper ligand is introduced by means of wet chemical synthesis, either by using the functionalized carboxylate as a starting material, or more conveniently by a ligand exchange reaction[63] starting from a simple Mn12 derivative, typically Mn12-acetate, Mn12-pivalate or Mn12-benzoate. The ligand exchange reaction, depicted in Figure 2.1 is governed mainly by the relative concentration of the incoming and leaving ligands and the acidity ratio of their carboxylic functions, as well the steric hindrance of the ligands. In addition to these factors, another specific effect can be exploited when working with Mn12-acetate as the starting material, is azeotropic distillation of the outgoing acetic acid in toluene. The possibility to perform such simple yet powerful chemistry on this class of magnetic compounds has fueled a wide range of functionalizations with various aims.[17] Focussing our interest on surface grafting-oriented modifications, it is interesting to point out how most of the chemically compatible functions have been introduced around Mn12 units in order to take advantage of the specific adsorption interactions on surface: among the ones that have been studied the most are the sulphur-gold interaction,[54,64,65] alchene-silicon,[6] silyl chloride-silicon and electrostatic interactions.[6] In order to give a more schematic and general point of view, we will break down the ligands' structure into three parts:[b]

1. **Complexing function**: This part is in contact with the inorganic core. For Mn12 complexes it is mostly (but not always[17]) a carboxylate.

2. **Spacer**: The backbone of the ligand. The main distinction is between aliphatic and aromatic moieties.

3. **Linker**: The active group that is responsible for the surface binding capabilities of the ligand.

In this thesis work the efforts have been focussed on grafting sulphur-functionalized Mn12 derivatives to Au(111) surfaces. The linker groups used were derivatives

---

[b]This formalism shall be used throughout the text and will be used to describe also ligands for Fe4 complexes.

of thiol functions and spacers were aromatic moieties, though some work has been carried out on Mn12 derivatives with aliphatic chains.
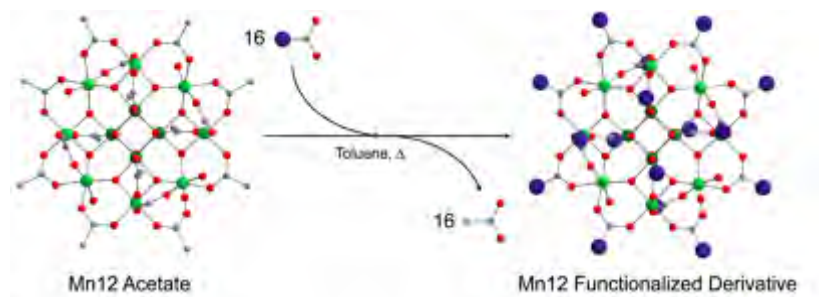
Figure 2.1: Schematics of the ligand exchange process.

The choice of using protected thiols as linker groups was driven by the well known redox instability of the Mn12 core with respect to free thiols;[64] instead asymmetric thioethers and thioacetyl groups were used. For what concerns spacers, aliphatic chains are more flexible and insulating with respect to aromatic rings. In Figure 2.2 the three ligands investigated in this work are reported, along with their short names. The functional ligands were introduced in the Mn12 core by the ligand exchange method described above and the Mn12 thus obtained were identified by the stenography Mn12(deprotonated ligand) meaning that the inorganic core is surrounded by sixteen such ligands and four molecules of water.
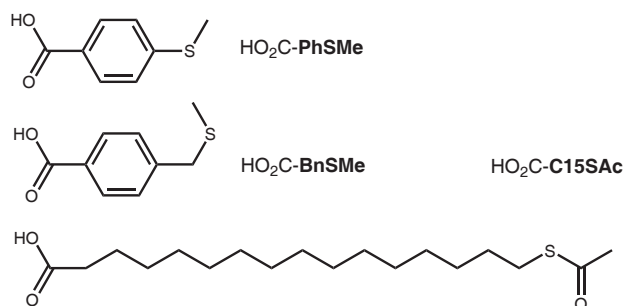
Figure 2.2: Mn12 ligands used in this thesis.

2.3 Methods

Gold substrates. The substrates used throughout out this work were evaporated gold films on various supports. The preferred substrate was a commercial

200 nm thick layer of gold on mica (Agilent Technologies). This type of substrates show rather disordered surfaces (an STM image of the 'as prepared' layers is shown in Figure 2.3a). In order to improve the quality of the surface, flame annealing process can be conveniently carried out both with hydrogen and butane flames; no significative difference was found between substrates prepared in the two flames. The flame annealing process consists in repeatedly heating to incandescence the substrate's surface with the flame for a short time (in the order of seconds); the gold surfaces thus obtained feature extended terraces of the Au(111) face. The outcome of such treatment in terms of morphology can be appreciated in Figure 2.3b. In addition to the morphological reconstruction, flame annealing also works excellently as a surface cleaning technique, as organic impurities adsorbed on the surface of gold are decomposed by the high temperature treatment, leaving a layer of gold atoms on the surface. No interaction of the gold atoms and the atmospheric oxygen is expected, nor usually observed, gold oxides being formed only under very harsh conditions.[62] Nevertheless, traces of gold oxides that might have formed can be dissolved by an ethanol wash.
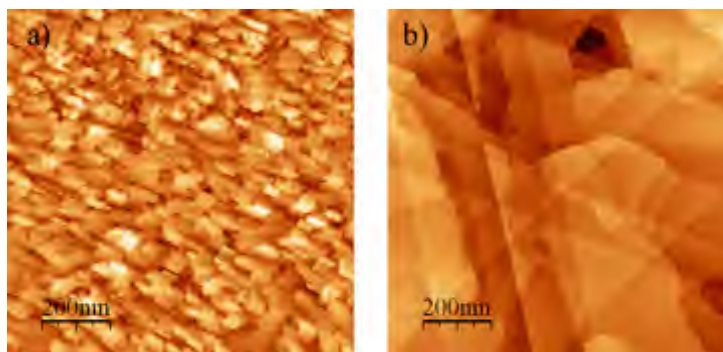
Figure 2.3: Flame annealing of evaporated gold layers. (a) STM topography image of the as evaporated layer and (b) STM topography image of a flame annealed surface. Atomically flat triangular terraces of the Au(111) face can be clearly seen.

STM measurements. In air STM characterization was performed on an NT-MDT Nova instrument working with a custom made low current head and using 90:10 Pt/Ir tips obtained by mechanical sharpening. Tunneling parameters are reported for each scan in the text. Sample preparation was carried out under the protective environment of a glove box, in order to prevent moisture to adsorb to the surface upon solvent evaporation when the gold surface was removed from the washing solvent.

XPS measurements.   XPS measurements were performed on a Perkin–Elmer Φ 5600ci spectrometer using a monochromatized (15 kV, 300 W) Al K$_\alpha$ radiation (1486.6 eV). The working pressure was lower than 10^{-9} mbar. Sample preparation was carried out in a portable glove bag under dry nitrogen environment; the samples were directly mounted on steel sample holders in the glove bag which was then directly connected to the fast entry system of the XPS vacuum chamber for sample mounting, in order to reduce sample atmospheric contamination. The sample analysis area was 800 μm in diameter. Survey scans were run in the 0-1300 eV range and acquired for at least 3 hours for monolayer samples. Detailed scans were recorded for the C$_{1s}$, O$_{1s}$, S$_{2p}$, Mn$_{2p}$ and Au$_{4f}$ signals; the signal was acquired for at least 10 hours (in total) for monolayer samples. The reported Binding Energies (BEs, standard deviation = 0.2 eV) were corrected for charging effects assigning to the adventitious C$_{1s}$ line a BE of 284.8 eV. The analysis involved Shirley-type background subtraction, and, whenever necessary, spectral deconvolution which was carried out by non-linear least-squares curve fitting, adopting a Gaussian-Lorentzian sum function. The atomic composition of the samples was calculated by peak integration, using sensitivity factors provided by the spectrometer manufacturer (Φ V5.4A software) and taking into account the geometric configuration of the apparatus.

2.4   Self-organization on surfaces

The self-organization process is under many points of view very similar to the SAM mechanism process that has been described for simple thiols: in fact, the adsorption of the molecule in solution to the surface is driven by the strong interaction of the sulphur atom with gold. Nevertheless, the second important interaction involved in the formation of SAMs, namely the van der Waals and/or stacking interactions between the tails of the molecules. In the case of Mn12 clusters instead, no distinction between head and tail can be made, as the functionalized complex behaves roughly like a 'sticky ball' on the gold surface, as sulphur atoms protrude virtually in every direction, as shown in Figure 2.4. This results in a loss of lateral ordering and no bidimensional lattice is formed by the adsorbate. Further in this chapter it will be shown that some kind of ordering can in effect be achieved for layers of Mn12 complexes, but the driving force is of a completely different nature.

The described method was first reported by our group[64] in 2003; in that paper the derivative grafted to the surface was Mn12C15SAc. The acetyl group used to protect the thiol function was removed *in situ* by the addition of small amounts of ammonia to the Mn12 solution. Further studies, performed during this thesis work demonstrated that not only the addition of ammonia in unnecessary in order to obtain a grafted layer, but seems even detrimental to the integrity of the adsorbed clusters.

Since then, other studies have been published by our[54] and others groups[66–68] have been working on the deposition of various types of Mn12 derivatives.
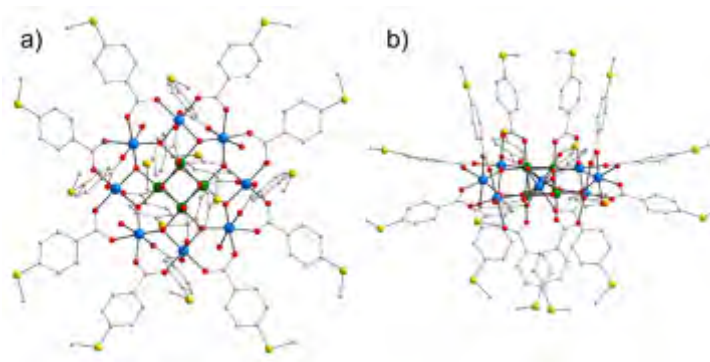
Figure 2.4: The cluster Mn12PhSMe. (a) View along the main symmetry axis and (b) orthogonal view.

Part of this thesis work has been dedicated to a more in depth study of Mn12 adsorbates; in particular the first systematic study has been carried out on the cluster Mn12PhSMe ($Mn_{12}O_{12}(O_2CC_6H_4CH_2SCH_3)_{16}(H_2O)_4$). This derivative, appeared for the first time in the publication by Zobbi *et al.*[54] and has been fully characterized both from the structural point of view (crystal structure is shown in Figure 2.4) and for what concerns magnetic properties; at variance with Mn12C15SAC, the protection of the thiol was achieved by adding a methyl group, thus obtaining a methyl thioether that allows an efficient grafting to gold. Various interesting points have been found and studied and shall be discussed in the following sections.

2.5   Solvent dependence of the adsorbates

In the literature several reports can be found on the dependence of the adsorbate qualities upon the solvent used to dissolve thiols.[69,70] With this concept in mind, we have tried the same kind of experiment on the Mn12PhSMe cluster with two different solvents: tetrahydrofuran (THF) and dichloromethane (DCM); monolayers prepared from THF and DCM solutions are refereed to as **exTHF** and **exDCM**, respectively.[65]

Mn12PhSMe-exTHF Monolayers

The deposition of the Mn12PhSMe **exTHF** layer was firstly carried out under the same conditions of the work by Zobbi *et al.* as a starting experiment: 30 min immersion in a 0.1 mM THF solution of Mn12PhSMe followed by a 10 min rinse in THF. STM topography scans revealed the presence of round objects of 3.3 ± 0.3 nm, in good agreement with the crystallographic dimensions of the complex (2.8×2.1 nm).[54] Consistently with what previously reported, the all inspected areas were found to be homogeneously covered by un-aggregated

molecules, with an average density of 0.2 units/nm^2. The tunneling conditions in STM experiments were varied between weak tip-sample interaction ($U = 0.9$ V, $I = 4$ pA) to strong interaction ($U = 0.2$ V, $I = 30$ pA) without any observable difference in the morphology of the scanned areas. A representative topography image of the adsorbate obtained is given in Figure 2.5.
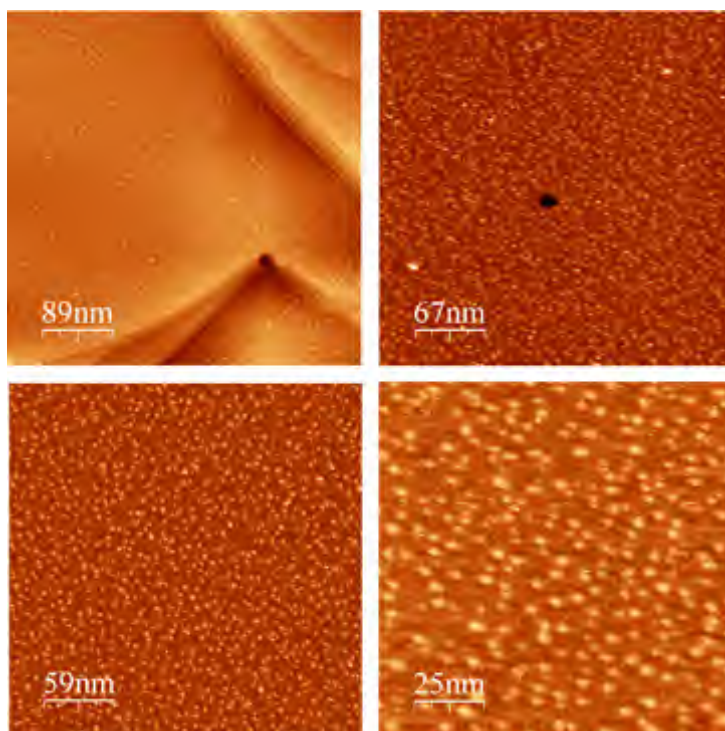
Figure 2.5: STM topography images (tunneling conditions: $U = 0.4$ V, $I = 10$ pA) of a typical **exTHF** adsorbate.

In addition to morphological inspection by means of STM, a rather in depth study on the chemical composition of the surface has been carried out by means of XPS. In the case of SMM monolayers on surface, standard photoelectron spectroscopy is quite pushed to the extreme as the number of clusters on the surface is very small; furthermore some elements, such as sulphur, are present in a very small atomic fraction with respect to the other elements in the complex (the detection of sulphur is further hampered by the low sensitivity factor of XPS for that element). Finally, the Mn$_{2p}$ peak partially overlaps with the Au$_{4p1/2}$ peak, and Mn$_{3p}$ with Au$_{5p3/2}$, gold bearing by far the most intense peaks of the XPS spectrum of these systems. These difficulties prevented previous studies to obtain profitable quantitative information on monolayers of Mn12 systems; our approach was that of a very careful sample preparation and

long acquisition times. This allowed us to obtain good spectra and coherent
quantitative information on the relative elemental abundance on the surface.
Survey scans were performed in order to ascertain the presence of the elements
forming the cluster; a scan is shown in Figure 2.6. Subsequently, detailed
scans were acquired on selected peaks of the elements Manganese (Mn_{2p}), Sul-
phur (S_{2p}), Carbon (C_{1s}) and Oxygen (O_{1s}) that are present in the cluster
Mn12PhSMe. The scans of their spectral areas are shown in Figure 2.7.

Relative integration values of the peaks were analyzed, in order to compare
them to the expected atomic ratios of the grafted complex. From the formula
of Mn12PhSMe, $Mn_{12}O_{12}(O_2CC_6H_4CH_2SCH_3)_{16}(H_2O)_4$ a brute formula of
$Mn_{12}C_{128}H_{120}O_{48}S_{16}$ is found; neglecting hydrogen atoms, which are not de-
tected by the XPS technique, the total number of atoms n_{tot} in the complex is
324. Percent atomic abundance p_i is then calculated from:

$$p_i = \frac{n_i}{n_{tot}} \times 100 \qquad (2.1)$$
$$i = Mn, C, O, S,$$

where n_i is the number or atoms of each element. Table 2.1 shows the found
and expected values for **Mn12PhSMe-exTHF**:

	Mn	S	C	O
BE (eV)	653.7	162.6	284.8	532.1
%Calculated	5.9	7.8	62.7	23.5
%Found	2.5	5.5	62.9	29.1

Table 2.1: Comparison of expected and found relative elemental abundance
in the **Mn12PhSMe-exTHF** monolayer.
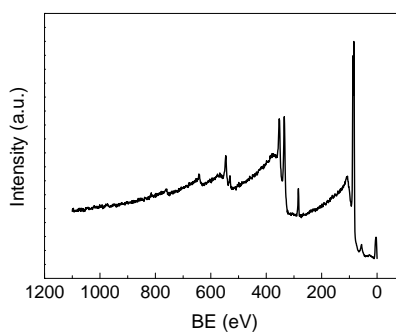
Figure 2.6: XPS survey spectrum of a **Mn12PhSMe-exTHF** adsorbate on
Au(111).
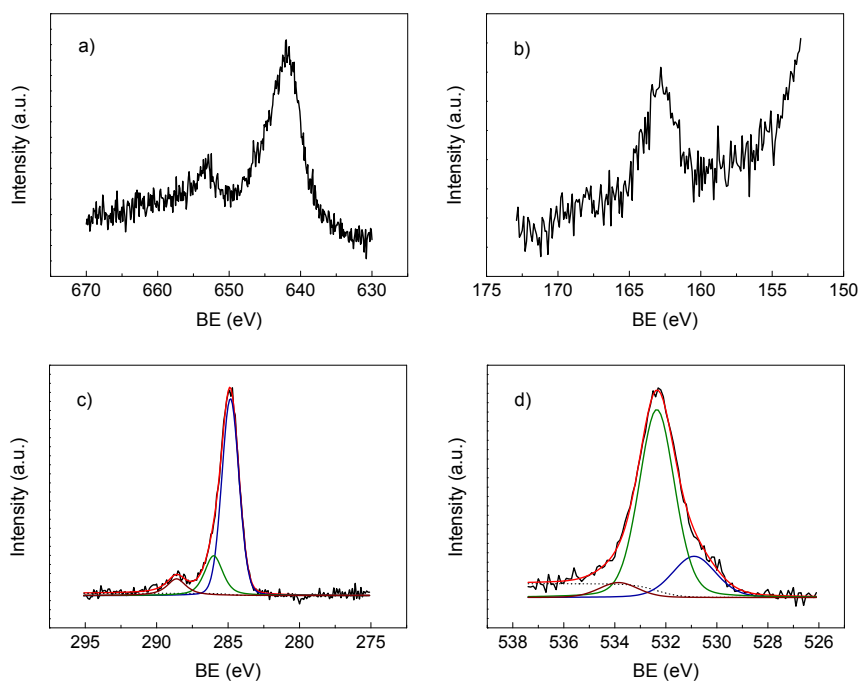
Figure 2.7: XPS spectra of a **Mn12PhSMe-exTHF** adsorbate on Au(111). (a) Mn_2p peak; (b) S2p peak; (c) C_1s experimental peak (black) with fitting (red) and with aromatic/adventitious (blue), sulfur-bound (green), and oxygen-bound carboxylic (brown) components and a Shirley-type background (dotted line); and (d) O_1s experimental peak (black) with fitting (red) and with carboxylic (green), μ-oxo (blue), and water (brown) components and a Shirley-type background (dotted line).

The XPS photopeaks also give additional information:

- **Mn$_{2p}$** (Figure 2.7a): The peak, split in the spin-orbit components $j = 1/2$ and $j = 3/2$, but the latter partially overlaps with the Au$_{4p1/2}$ component peak; as a consequence, only the Mn$_{2p1/2}$ peak at 654.3 eV is diagnostic of the presence of Mn on the surface.

- **S$_{2p}$**(Figure 2.7b): A single, weak peak centered at 163.4 eV can be seen; this BE is consistent with thioether sulphur atoms that do not interact with the surface, consistent with the fact that just a limited and variable/unknown number of the sixteen sulphur atoms bind to gold, depending on the possible absorption geometries (see Figure 2.8 and its caption for some hypotheses). On the other hand, the relatively high Full Width at Half Maximum (FWHM) of the peak is large enough to have a second, lower Binding Energy (BE) weak component, i.e. a signal of a more electron-rich sulphur species; no trustworthy deconvolution can be attempted though, due to the weakness of the signal. Finally, no sign of oxidized sulphur species can be found in these data as no component at higher BE is seen, in contrast with what has been previously reported for aromatic thiol sub-monolayers on gold.[71] In that case, SAMs exposed to air underwent oxidation of the sulphur atom to sulphone species due to fact that in incomplete layers sulphur can be reached by oxygen, in contrast to full monolayers where sulphur is protected by the tightly packed tails of the molecules. In our case oxidation was probably prevented by the protective nitrogen environment under which the monolayer was kept before the sample was introduced in the vacuum chamber.

- **C$_{1s}$** (Figure 2.7c): The strong signal of the C$_{1s}$ peak clearly shows the presence of various components, corresponding to different chemical environments. Spectral deconvolution was carried out and three components were found, centered at 248.8, 286.0 and 288.6 eV, respectively, with relative areas of 8.2 : 1.8 : 1. The preponderant lower BE component, shown in Figure 2.7c in blue is relative to electron-rich species, namely -CH$_n$- species of Mn12PhSMe's ligand shell and the hydrocarbon contamination layer. The shift of the two higher BE components nicely agree with the more electron depleted species: sulphur-bound carbon at 286.0 eV[72] (shown in green in Figure 2.7c) and carboxylic carbon at 288.6 eV (shown in red in Figure 2.7c). In addition, the experimental integral ratio of 1.8 : 1 is very close to expected ratio of 2 : 1. Lower BE peak exceeds the expected relative area of 5 : 1 with respect to carboxylic carbon; this is very probably due to the overlap of signals relative to the ligands with the adventitiuous carbon.

- **O$_{1s}$** (Figure 2.7d): Oxygen is present both in the carboxylate moieties of the ligands, in the Mn$_{12}$O$_{12}$ inorganic core and in the water molecules that complete the coordination of the complex, in the ratio of 8 : 3 : 1.

As expected, the relatively wide distribution of BEs can be reasonalby deconvoluted into three components centered at 530.9, 532.3 and 533.8 eV respectively, which were attributed to oxo-type (shown in blue in Figure 2.7d), carboxylic (shown in green in Figure 2.7d) and water[73] (shown in brown in Figure 2.7d) oxygen species. The found integral ratios were 11.4 : 3.0 : 1, oxo to water ratio being in excellent agreement with the expected values and carboxylic oxygen being in slight excess.
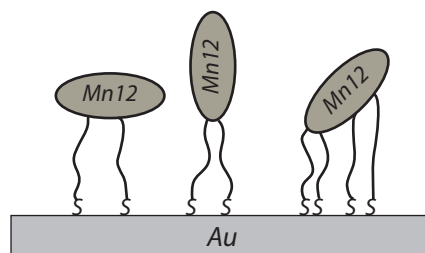
Figure 2.8: Possible adsorption geometries of Mn12 on surface. Anchoring through the axial ligands (left), the equatorial ligands (middle) or both (right).

Mn12PhSMe-exDCM Monolayers

Monolayers from dichloromethane solution were prepared using the same parameters of the **exTHF** systems: 30 minutes of incubation of the gold substrate in a 0.1 mM DCM solution of Mn12PhSMe and 10 minutes rinse in fresh DCM; also in this case the preparation was carried out in glove box. STM inspection of **exDCM** monolayers revealed a substantially different situation from **exTHF** ones; in fact, as can be seen in Figure 2.9, a full coverage of round features is observed in this case. The size of the objects can be estimated to be around 3 nm, coherently with the dimensions of objects found in **exTHF** samples. In this case however, tunneling conditions do influence imaging as, while mild tip-sample interaction scanning (i.e. high bias voltage and low tunneling current) yields imaging of the unaltered monolayer, if the tip is kept closer to the sample (low bias voltage and high tunneling current), mechanical interactions seems to displace the clusters; this finding, that shall be addressed in more details in paragraph 2.7, seems to indicate that Mn12 clusters grafted from DCM solution interact more weakly with the Au(111) surface.

XPS analysis revealed the presence of all elements contained in Mn12PhSMe, plus the dominant gold photopeaks, as can be seen from the survey scan in Figure 2.10. Considering the sensitivity to the first few nanometers of surface of the XPS technique, the fact that the substrate's signal is clearly visible indicates the presence of a very thin layer of adsorbed molecules. As expected for a full layer of molecules, signal intensity is stronger that that of **exTHF** samples and single element acquisition gave rather sharp peaks (shown in Figure
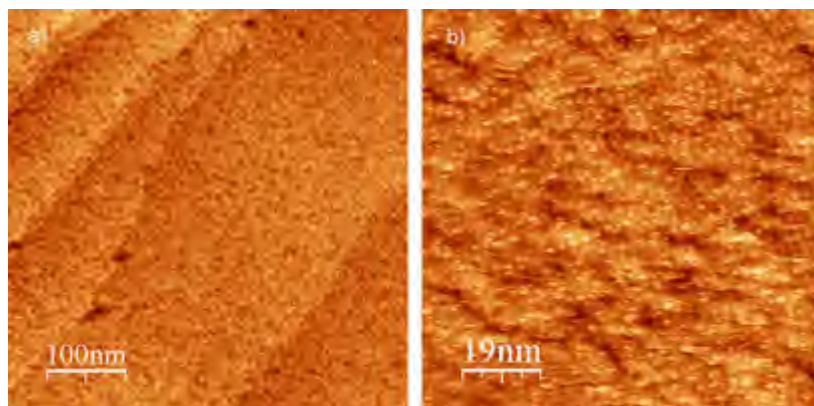
Figure 2.9: STM topography image (tunneling conditions: $U = 0.9$ V, $I = 4$ pA) of a typical **exDCM** adsorbate.

2.11); semi-quantitative information on the elemental relative abundance was extracted from the integrated values of the peak areas. The resulting values are compared to the expected ones in Table 2.2: in particular, found sulphur to manganese ratio is matching the expected value very well.

	Mn	S	C	O
BE (eV)	653.7	162.6	284.8	532.1
%Calculated	5.9	7.8	62.7	23.5
%Found	3.8	5.1	67.5	23.6

Table 2.2: Comparison of expected and found relative elemental abundance in the **Mn12PhSMe-exDCM** monolayer.

Detailed description of single element peaks' features are reported:

- **Mn$_{2p}$** (Figure 2.11a): As detailed for the **exTHF** system, only the Mn$_{2p1/2}$ peak can be considered independent from the signal of the Au$_{4p1/2}$ component. Nevertheless, in the case of **exDCM** systems the signal is stronger and the quantitative information gathered from these data is definitely more reliable than in the case of **exTHF** monolayers.

- **S$_{2p}$** (Figure 2.11b): In this case the sulphur peak, centered at 162.6 eV, exhibits a smaller peak width than **exTHF** S$_{2p}$ peak; in particular, no low BE component seems to be present, which is to be ascribed to sulphur strongly interacting with gold. Such weaker interaction would be consistent with the aforementioned observation that it is possible to displace Mn12 units with the STM tip.
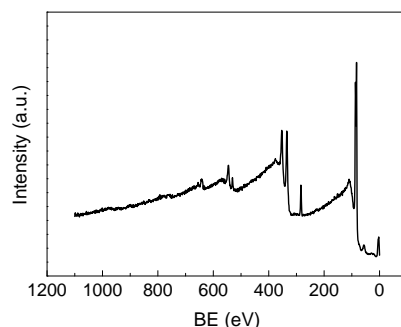
Figure 2.10: XPS survey spectrum of a **Mn12PhSMe-exDCM** adsorbate on Au(111).

- **C_{1s}** (Figure 2.11c): The C_{1s} peak was deconvoluted into three components centered at 284.8, 285.7 and 288.6 eV. The three deconvoluted peaks, integrating 5.9 : 2.0 : 1, were attributed to aromatic/adventitious carbon (Figure 2.11c in blue), sulfur-bound carbon (Figure 2.11c in green), and carboxylic carbon (Figure 2.11c in brown), respectively. It is worth noticing how good the agreement is with the expected 5 : 2 : 1 ratio, the slight excess of the main component being reasonably attributable to adsorbed hydrocarbon contamination; the fact that this compact layer exhibits lower values of adventitious carbon is in line with the observation that in **exTHF** layers part of the Au(111) face is directly exposed to the physisorption of hydrocarbons, which is well known to occur quite efficiently, while here the tight layer of Mn12 units is very probably a poorer substrate for hydrocarbon physisorption.

- **O_{1s}** (Figure 2.11d): The asymmetric oxygen peak was fitted with three components assigned to μ-oxo (530.7 eV, blue in Figure 2.11c), carboxylic (532.0 eV, green in Figure 2.11c), and water (533.3 eV, brown in Figure 2.11c) oxygen species.[73] Integral ratios of 2.9 : 8.1 : 1 were found to agree excellently with the expected values (3 : 8 : 1); the sharpness of the fitted peaks (≈ 1.6 eV) also suggests the presence of a uniform and chemically homogeneous layer adsorbed to the gold surface.

  Oxygen is present both in the carboxylate moieties of the ligands, in the $Mn_{12}O_{12}$ inorganic core and in the water molecules that complete the coordination of the complex, in the ratio of 8 : 3 : 1. As expected, the relatively wide distribution of BEs can be reasonalby deconvoluted into three components centered at 530.9, 532.3 and 533.8 eV respectively, which were attributed to oxo-type (shown in blue in Figure 2.7d), carboxylic (shown in green in Figure 2.7d) and water[73] (shown in brown in Figure 2.7d) oxygen species. The found integral ratios were 11.4 : 3.0 : 1,
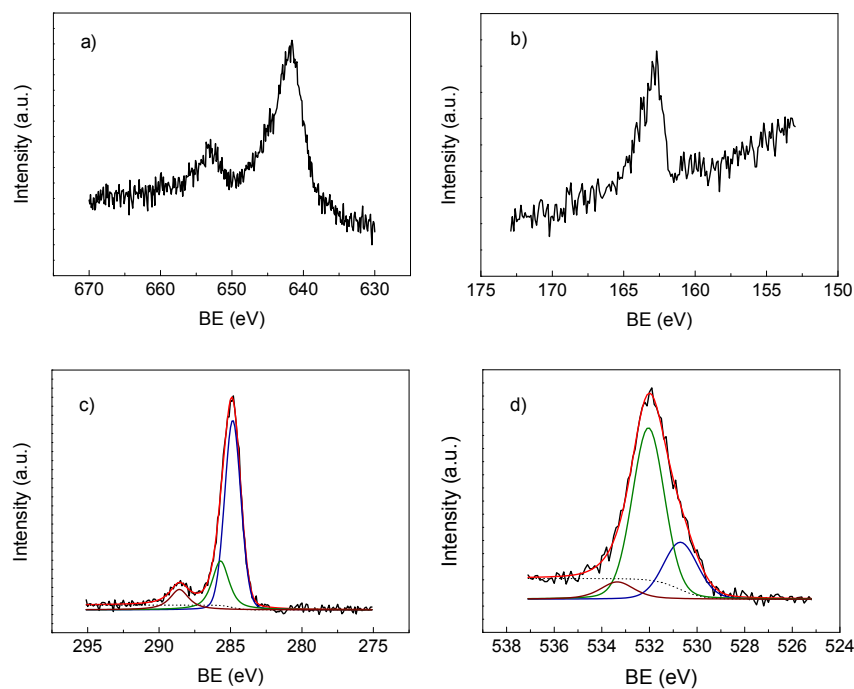
Figure 2.11: XPS spectra of a **Mn12PhSMe-exDCM** adsorbate on Au(111). (a) Mn$_{2p}$ peak; (b) S$_{2p}$ peak; (c) C$_{1s}$ experimental peak (black) with fitting (red) and with aromatic/adventitious (blue), sulfur-bound (green), and oxygen-bound carboxylic (brown) components and a Shirley-type background (dotted line); and (d) O$_{1s}$ experimental peak (black) with fitting (red) and with carboxylic (green), μ-oxo (blue), and water (brown) components and a Shirley-type background (dotted line).

oxo to water ratio being in excellent agreement with the expected values and carboxylic oxygen being in slight excess.

The effect of solvent on the adsorbate quality has been clearly shown to be important and reproducible; we then carried out a series of additional experiments in order to gain a better understanding of the mechanisms involved in the monolayer formation.

Effect of the washing solvent

The last operation that is carried out before sample inspection is the final wash in fresh solvent; this step is extremely important, as the excess unbound molecules are removed from the surface, thus leaving on the surface only those that form the monolayer. It is very reasonable to suppose that some parameters, for example the different solubility of the Mn12PhSMe cluster in the two solvents might influence the efficiency with which the fresh solvent can remove adsorbed molecules from the surface.
In order to address this point, we tried to change the solvent used to wash the samples after the self-organization step; more precisely, the the monolayer incubated in the DCM solution of Mn12PhSMe was washed in THF. The monolayer obtained in this way was inspected by means of STM, and no difference was found between this sample and standard **exDCM** systems, the result being a full layer of round objects. We then concluded that THF is not responsible for a partial desorption of adsorbed Mn12 units.
The same solvent inversion was tried for **exTHF** layers with DCM as the rinsing solvent; considering that **exDCM** layers seem to be made of Mn12 units that interact weakly with the surface (i.e. they can can be displaced by the STM tip), this test should be able to determine whether DCM acts as a poorly efficient washing solvent of aspecifically adsorbed molecules. The result however rules out also this hypothesis, as STM imaging of THF-incubated, DCM-washed samples gave identical results to **exTHF** systems.
From these two cross experiments it can be concluded that the solvent dependence is not determined by the washing step and no different capability of the two solvents to desorb Mn12 units from the surface was observed; the influence must then be considered to act on a different mechanism of monolayer formation.

Effect of the solvent on the substrate

A possible effect of the solvent is that of modifying the features of the Au(111) substrate in various ways, thus making it more or less prone to adsorption of Mn12 units. It has been observed that solvents like DCM can etch the surface of gold on the microscopic scale, with the result of making atomic step edges less regular. In addition to this, despite the rather harsh conditions to which the gold substrate undergoes during flame annealing, thus removing adsorbed

impurities, some contaminant is weakly adsorbed by the surface when in contact with atmosphere. A possible effect of the solvent could be that one of the two is capable of removing such impurities more efficiently than the other.

In order to address this point, a slight variation of the experiment was set up, that aims at decoupling to some extent the solvent-substrate interaction: the gold plate was first immersed for 30 minutes into a solvent, then the standard grafting procedure was carried out but from the other solvent, i.e. if the first immersion was carried out in fresh DCM, the subsequent grafting was carried out from a THF Mn12PhSMe solutions and washing was performed in THF. This procedure was carried out for both the possible combinations.

STM analysis found no detectable difference between these pre-incubated systems and standard **exTHF** and **exDCM** samples. In addition, the surfaces were inspected by means of STM also after pre-incubation and before the Mn12 adsorption step, in order to determine if etching or different phenomena might have changed the morphology of the surface, but also this case no significant different features were observed with respect to as-prepared Au(111) surfaces. This also shows that solvent-driven etching effects do not occur on this time scale.

Effect on incubation time

Being able to rule out both the responsibility of the washing step and the solvent-substrate interaction, we had to conclude that the solvent directly influences the adsorption step. Considering that the incubation time is kept fixed at 30 minutes for both THF and DCM solutions, different adsorption kinetics can be thought to be responsible for the different coverage of the surface by Mn12 units: according to this hypothesis, THF solutions would allow grafting more slowly than DCM solutions of Mn12PhSMe.

To verify such hypothesis, we carried out a series of experiments in which the only parameter to be varied was the incubation time; if such kinetics were responsible for the difference between **exTHF** and **exDCM** monolayers, longer incubation times for the former and shorter of the latter should give similar coverages.

For the **exTHF** system incubation times of 30 seconds and 2 hours were tried, in addition to the standard 30 minutes incubation: all samples were indistinguishable to STM inspection. This indicates that the adsorption from THF is very fast and does not evolve in time.

In a similar way, **exDCM** were prepared with incubation times of 30 seconds, 5 minutes and 15 minutes. All samples were inspected by STM, and their morphology resulted very similar to samples incubated for the standard time (30 minutes). However, some differences were found: as it is possible to see from STM imaging (in Figure 2.12 the 5 minute-incubated sample is shown), some areas are not fully covered by objects. The hypothesis that the removal could be caused by the STM tip during imaging is very unlikely, since the

tunneling conditions were the same weak ones used for all other **exDCM** samples; moreover, the uncovered areas are not situated in straight lines along the fast scanning direction, but seem to be randomly distributed along the surface. Covered areas, on the other hand, are completely similar to fully formed layers. These observations lead to the conclusion that the kinetics[c] of adsorption of Mn12PhSMe from DCM solutions is slower than from THF. In addition, these findings discredit the hypothesis that the differences between the two types of adsorbate are of kinetic nature: in fact, longer incubation time for **exTHF** systems and shorter time for **exDCM** do not yield layers with converging coverage properties, but seems to lead to totally different directions, the former system not evolving in time, the latter proceeding *via* a spot-like coverage.
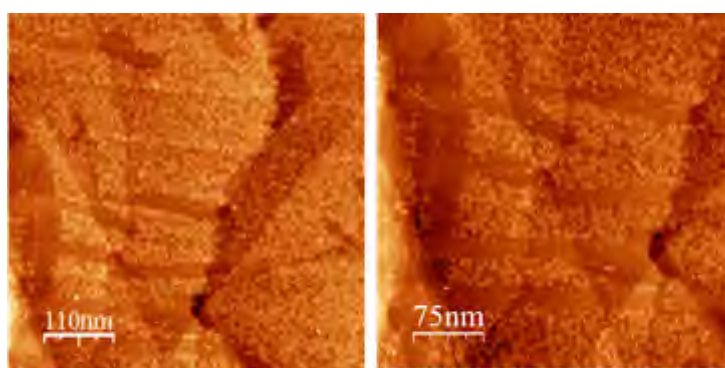
Figure 2.12: STM topography images (tunneling conditions: $U = 0.9$ V, $I = 4$ pA) of a typical **exDCM** adsorbate incubated for 15 minutes.

Summary

The work carried out on the study of solvent dependence of the Mn12PhSMe adsorbates gave findings that can be summarized as follows:

- The solvent used to dissolve the functionalized magnetic cluster influences dramatically the adsorbate features.

- Tetrahydrofuran gives submonolayers of isolated clusters, while dichloromethane yields full monolayers according to STM inspection.

- XPS analysis reveals the presence of manganese, sulphur, carbon and oxygen in reasonable ratios and the signal is stronger for **exDCM** samples.

- It seems that in **exTHF** systems clusters interact strongly with the Au(111) while in **exDCM** systems the interaction is weaker.

---

[c]More precisely, the time required to reach the final state, since for THF solutions the adsorption seems to spontaneously stop before full monolayer coverage.

- The solvent does not influence the adsorbate features in the washing step

- The different features of the adsorbate do not depend on solvent-substrate interactions.

- Adsorption seems to take place following different pathways for the two solvents, i.e. homogeneous coverage with isolated objects for THF and full coverage of discrete areas to complete coverage for DCM.

As can be easily appreciated, all experiments suggest that the solvent influences the adsorption step itself: all other possible influences have been reasonably ruled out. We can also postulate completely different adsorption mechanisms for the two solvents. No direct evidence of the reasons underlying such differences was found. The two solvents have very similar dielectric constants, so the bulk polarity can not be considered the cause of such differences; the only macroscopic difference between the two solvents is the much larger solubility of Mn12PhSMe in dichloromethane, probably for the softer character of this solvent. The different solubility of the SMM in the two solvents is likely to reflect in some complex manner on the adsorption mechanism of the cluster on the gold surface.

2.6 Spontaneous ordering of Mn12PhSMe on Au(111)

It was found that **Mn12PhSMe-exTHF** systems (Figure 2.5) occasionally show an ordered adsorption geometry over large areas (exceeding 1 μm^2).[65] STM topography images of such areas are shown Figure 2.13; as can be seen, the round objects tend to order in parallel lines each several hundreds of nanometers long, while no regularity in the object distribution within lines can be observed. This can be seen more precisely by applying 2D-FFT to an image taken on a smaller area, like the one shown in Figure 2.14: in this case, two couples of sharp peaks can be seen in the Fourier transform image on the axis going from upper left to lower right, corresponding to regular distances in the relative directions. This means that the linear molecular arrays, in this area clearly placed in two non-parallel sets of lines, are spaced by a regular distance; by measuring the peak-to origin distance in the FFT image one obtains the inverse of such distance, which was found to be around 8 nm.

As it has already been pointed out in Section 2.4, lateral ordering of Mn12 adsorbates is not to be considered likely on the basis of the forces involved in the formation of standard SAMs, since the globular structure of the complex does not offer any close interaction between its ligands. Moreover, STM topography images clearly indicate that the units are well separated one from the other, thus not interacting.

The line spacing of 8 nm instead, suggests that another type of effect might be
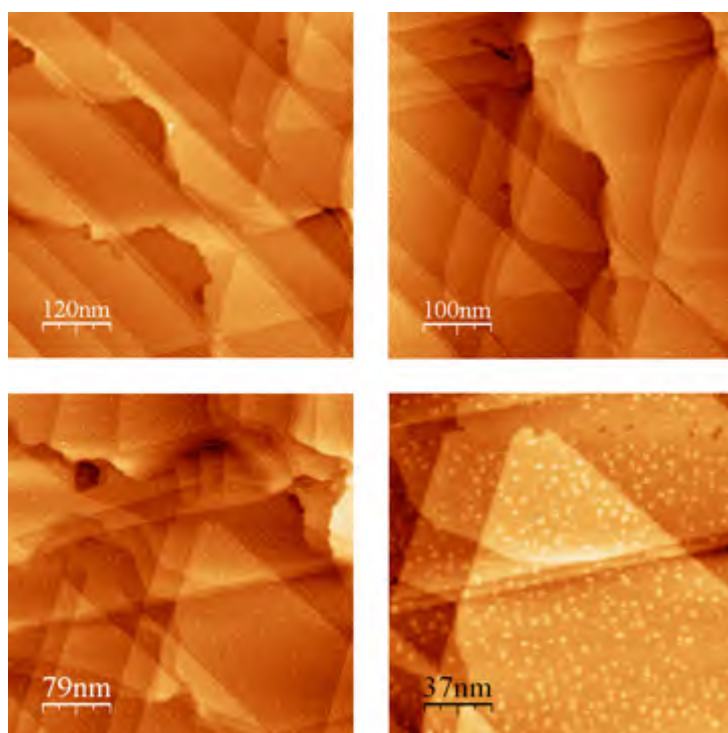
Figure 2.13: STM topography scans of ordered areas of **Mn12PhSMe-exTHF** ($U = 0.4$ V, $I = 10$ pA).
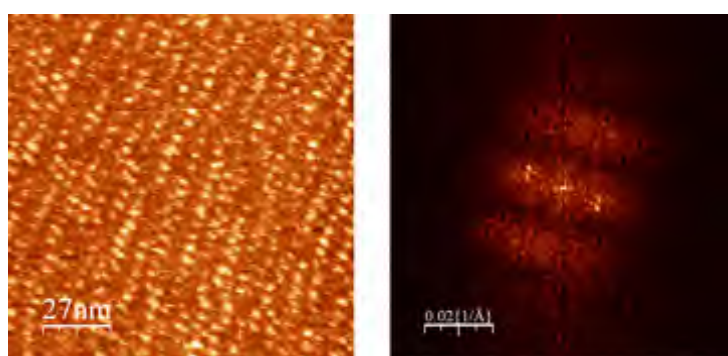
Figure 2.14: Close–up on an ordered area of **Mn12PhSMe-exTHF** (left, $U = 0.4$ V, $I = 10$ pA) and 2D-FFT of the same area (right).

the cause of the observed ordering. It is well known that the Au(111) can spontaneously undergo a reconstruction of the first atomic layers usually referred to as the 'herringbone' reconstruction,[74–76] shown in Figure 2.15; this structure is made up of alternating *fcc*-like and *hcp*-like domains that are separated by soliton walls. Gold atoms situated in such walls are slightly higher in topography than the others, resulting in a brighter contrast of the STM image. As can be seen in Figure 2.15, areas between boundaries present a bimodal width distribution; this is due to the fact that *fcc*-like domains are slightly more favorable in terms of energy with respect to *hcp*-like ones, so form larger domains. Surface energy is further lowered by a secondary *zig-zag* reconstruction of the soliton walls, that contain dislocations at the elbows.
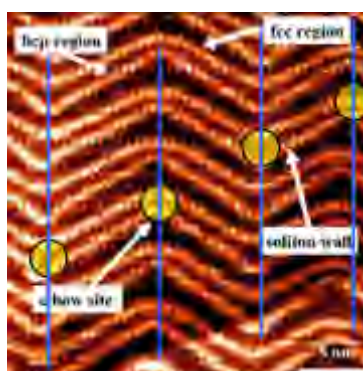
Figure 2.15: STM topography image of Au(111)'s herringbone reconstruction (Reproduced from Mina *et al.*[77]). Circles indicate the possible adsorption sites of Mn12 units.

Such herringbone elbow sites are well known to harbor clusters of evaporated atomic species in a low coverage regime,[78] thus acting as templates for the preparation of ordered sub-monolayers. However, it has been reported that upon formation of standard thiol SAMs;[79] nevertheless, some aromatic thiols are known to adsorb selectively at elbow sites in the sub-monolayer regime without disrupting the reconstruction,[80] on the contrary such adsorption process is thought to favor the formation of the herringbone reconstruction by the authors of that work.

In our case, the situation cannot be directly compared to that of standard SAMs, however the fact that not only vapor-phase deposited atomic species, but also sulphur atoms of aromatic thiols exhibit preferential adsorption from solution in the described sub-monolayer regime is a strong argument in favor of the hypothesis that a templating effect of the underlying herringbone reconstruction might be the driving force of the ordering observed for some areas of **exTHF**. In this case, the found spacing between parallel lines of clusters would correspond to the typical elbow-elbow distance inside the same type of domain. Of course, being able to simultaneously image Mn12 units and the

herringbone reconstruction would be a solid evidence to support such hypothesis, however, the roughness of the surface due to the adsorption of such bulky objects as Mn12PhSMe is in itself a sufficient reason to impair the observation of the very subtle topographic differences involved in Au(111) herringbone reconstruction, at least on the instrument we used and in our working conditions.

2.7 Nanopatterning of Mn12PhSMe monolayers

As it has been mentioned in section 2.4, in **Mn12PhSMe-exDCM** monolayers the Mn12 units exhibit a rather weak interaction with the gold surface, according to STM and XPS experiments.
We decided to study this interesting phenomenon more in detail, since it can be a useful tool to better understand the adsorption process and the gold cluster interaction. Moreover, the ability to locally remove adsorbed cluster from areas with a resolution of a few nanometers can be quite appealing for nanopatterning of functional monolayers. Surface patterning with Mn12 derivatives using *pseudo*–self–organization techniques such as micro–contact printing has been carried out previously by our group;[81] this technique consists in transferring the litographycally defined pattern of a PDMS stamp to a surface by soaking the stamp in a solution of surface-binding molecules (such as thiols on gold) and simply - yet carefully - putting the stamp in contact with the surface to be patterned. This technique yields extended patterns whose size and shape are defined by the features of the stamp, so no high lateral resolution can be reached.
A different approach to nanopatterning is the local one, in which the tip of a scanning probe microscope, typically STM or AFM, displaces the adsorbed molecules to create the desired pattern.[82] Typically, in such experiments STM is used to displace small molecules such as alkyl thiols by applying a voltage pulse under ultrahigh vacuum, in order to remove desorbed molecules; alternatively, the AFM tip in strong interaction mode can displace molecules; such experiments are carried out in liquid to prevent readsorption of the displaced species.
In our case, by simply scanning the surface with the STM with a smaller tip-sample distance than usual, more precisely using bias voltages around 0.2 V (instead in 0.9 V) and tunneling currents of about 20 pA (instead of 4 pA), the grafted Mn12PhSMe units can be desorbed from the gold surface,[65] as can be seen from Figure 2.16. The images were obtained by scanning in low interaction conditions after a smaller area scan was carried out in the strong interaction regime with no voltage pulses applied; in fact, this system behaves in a similar way to the AFM nanopatterning mentioned above.

This type of experiment is useful to determine that the observed full layer
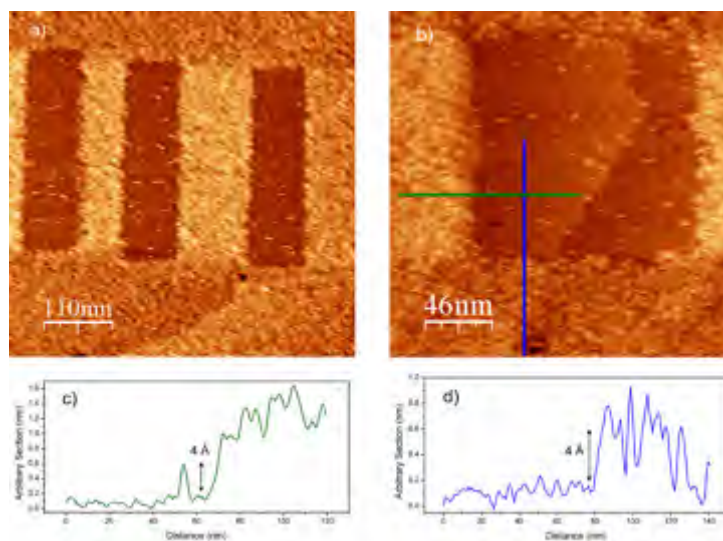
Figure 2.16: (a) and (b): STM topography images of the scratched areas in a **Mn12PhSMe-exDCM** adsorbate. (c) and (d): line scans along the fast and slow scanning directions, respectively.

is in effect a single layer: in fact, as it can be clearly seen from Figures 2.16a,b, scratched areas show a flat morphology, with distinct atomic step edges of gold; on the other hand, round objects can be clearly appreciated at the borders of the naked area.

Even if topographic information is a convolution of real height differences of the surface and the different work functions of the materials involved in the tunneling process, some interesting observations can be made on a basis of height differences in the scans. In fact, we can empirically attribute a numeric value to the 'effective height' of a Mn12PhSMe on a Au(111) surface by observing the topographic profile of an isolated cluster from an STM scan on a **exTHF** monolayer, one can evaluate the step between the covered and the scratched areas in Figure 2.16 in terms of number of Mn12 molecules; this is a reasonable assumption, because the height jump is between the adsorbed molecule and the naked gold surface; the height value found in this way is about 0.5 nm for a Mn12PhSme molecule. Line scans across the border of the scratched area in the **exDCM** sample, shown in Figure 2.16b, gives two height ranges: 0.4-0.6 nm along the slow scan direction (i.e. the perpendicular to the fast scan direction) and exceeding 0.8 nm along the slow scan direction; these are shown respectively in Figure 2.16c and 2.16d. The slow scan height profile clearly indicates that a one-molecule height jump is present at the border, thus confirming that the removed layer is single; on the other hand, the > 0.8 nm jump in the fast scan direction indicates the presence of a double layer of molecules.

During scratching, i.e. strong interaction scanning, the fast scan direction is the same as the one used for imaging; if we couple this observation to a question concerning the fate of the displaced molecules (no UHV or solvents are there to remove desorbed molecules), we may find here a reasonable answer: Mn12 units are probably moved to the sides of the scanned area.

In some points of the scratched area some round objects with the approximate size of 3 nm can be resolved; these features can be seen in Figure 2.16b and seem to be Mn12 units that were not removed by the STM tip. These cannot be removed even after repeated strong interaction scans: such feature is reminiscent of the behavior of **exTHF** adsorbates under strong interaction STM scanning, so one might speculate that some areas on the Au(111) surface are preferential adsorption sites for Mn12PhSMe, that interacts much more strongly than in other areas, irrespective to the solvent used to dissolve the magnet.

From an applicative point of view, using this STM technique can be interesting to create in no time local nanometer-sized architectures, a simple example of which is given in Figure 2.16. Due to the fact the patterning technique involves a STM tip, this could be particularly interesting for structuration of monolayers and contextual *in situ* characterization by means of advanced SPM techniques, such as scanning Hall probe microscopy[83] and magnetic force microscopy.[84]

2.8 Insertion of Mn12 in thiol SAMs

The direct grafting method is well established, and is considered a standard procedure for our purposes. However, some investigation was carried out also on variations of the grafting method with the aim of obtaining different types of adsorbate.

One route that we have been studying was that of inserting a Mn12 derivative, Mn12BnSMe (structure shown in Figure 1.6, page 16), into a preformed monolayer of simple aromatic thiols.[85] This approach, that has already been reported for the insertion of rather bulky molecules into thiol SAMs,[86] is supposed to yield completely isolated magnetic units inserted in a chemically controlled and inert surface. In addition to this, one obtains also a completely different environment for the SMMs, since no direct contact would occur between the inserted molecule and the metallic surface if not through the ligand of the molecule; the SMM would instead be completely surrounded by an apolar insulating array of organic moieties formed by the tails of the self-organized thiols. Another advantage of this approach is the fact that the monolayer-covered surface is more inert that the naked gold surface, and less prone to aspecific adsorption. The process of insertion into preformed monolayers is sketched in Figure 2.17.

The first step to insert Mn12 derivatives in a preformed monolayer is the choice of the thiols and the ligands that are to interact in the process. For this reason, we designed and prepared a new *ad hoc* thio-functionalized Mn12
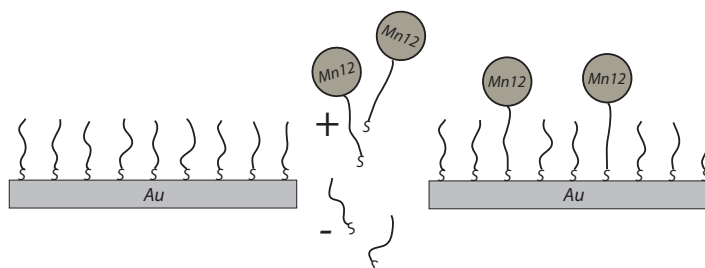
Figure 2.17: Scheme of the insertion process on Mn12 into a preformed thiol monolayer.

derivative that is suitable for this purpose. A we have already mentioned, the preparation of a new Mn12 complex boils down to the synthesis of the proper carboxylated ligand that is introduced by means of the ligand exchange process. The carboxylated ligand we chose was α-methylthio-4-toluic acid (HO_2C–BnSMe). This ligand is very similar to the one used in the one-step adsorption described in the previous sections (HO_2C–PhSMe); the only difference is the presence of a methylene unit situated between the aromatic ring and the sulphur atom; nevertheless this little difference is crucial for the orientation of these molecules as they adsorb to the Au(111) surface. In fact it has been shown[87] that the additional methylene unit favors the ordered packing of the monolayer by reducing the probability of the molecules to be parallel to the surface, as sketched in Figure 2.18. In such bidimensional lattices, the lateral interactions that are responsible for this order can be exploited to include functionalized Mn12 molecules.
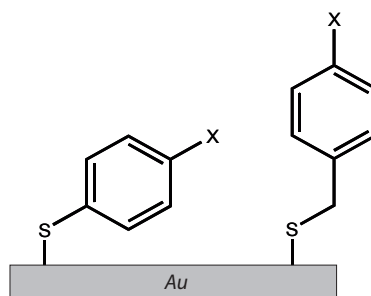
Figure 2.18: Schematic representation of the correlation between structure and adsorption geometry of aromatic thiols.

Insertions give better results when carried out using similar molecular structures for the starting adsorbate and the incoming units, so we have chosen

thiobenzyl derivatives for both the SAM and the ligand that drives the insertion of the Mn12 cluster in the monolayer. The new Mn12 derivative, $Mn_{12}O_{12}(O_2CBnSMe)_{16}(H_2O)_4$ (Mn12BnSMe) has been synthesized, fully characterized in its bulk phase (see section 1.3.1) and inserted in two kinds of monolayers: a benzyl disulfide (Bn2S2) SAM and a benzyl methyl sulfide (BnSMe) SAM. These two sulfur-based compounds have different assembling features on the gold surface, that are expected to affect the grafting of Mn12.

The preparation of the precursor substrates, i.e. the monolayers of Bn2S2 and BnSMe substrates was carried out using the standard self-organization approach:[88,89] the freshly annealed gold surface was dipped into a 1 mM ethanolic solution of the thio-derivative for 16 h, then thoroughly rinsed in fresh ethanol and dried under a nitrogen flow. The monolayers thus obtained were characterized in their morphology by means of STM microscopy. Both types of system showed the expected bidimensional lattice that could be easily resolved to the molecular level as can be seen in Figure 2.19. It is well known[90] that disulfides adsorb to Au(111) surfaces by the omolysis of the SS bond, while sulfides are thought to couple to the surface without any SC bond cleavage;[91] as we shall discuss further in the text, this point is of crucial importance for the final Mn12 insertion.
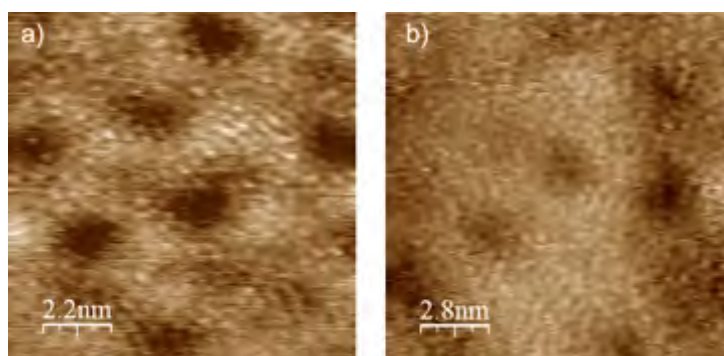
Figure 2.19: STM topography scans of a Bn2S2 (left) and (right) of a BnSMe monolayer ($U = 0.3$ V, $I = 15$ pA).

The insertion of the Mn12 derivative was performed by incubating the Bn2S2 preformed monolayer in a 0.1 mM THF solution of the cluster for times ranging from 30 min to three days. The systems were then inspected by means of STM; no detectable dependence of the number of inserted clusters into the monolayer on the incubation time was observed. Some representative examples of these systems are shown in Figure 2.20. As can be seen, the surface shows round features of about 3.3 nm, which is in good agreement with the dimensions of cluster Mn12BnSMe according to crystallographic data; the presence of the underlying SAM is confirmed by the presence of packing defects through-

out the underlying substrate. The degree of insertion seems rather low and mostly domain-like, with some areas featuring a relatively high concentration of clusters, in contrast with larger areas that seem completely un-affected by the insertion process. The origin of this behavior is likely to be found in the features of the substrate, most probably due to the presence of extended areas in the SAM where a less efficient packing of the Bn2S2 molecules allows an easier exchange of the surface-adsorbed species with the solution. A defect nucleation mechanism may be invoked as a model to explain the non-homogeneous grafting distribution of Mn12 molecules: the methyl group on the incoming ligand is likely to locally disrupt the bidimensional order of the benzyl thiolate units on the gold surface, thus promoting the entrance of other clusters in the vicinity of the first one.
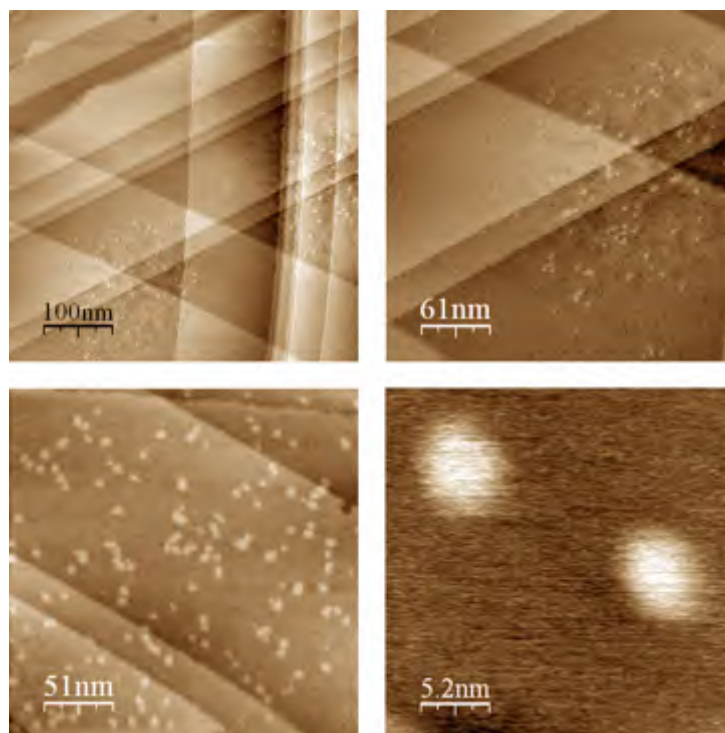
Figure 2.20: STM topography scans of Mn12BnSMe inserted into a Bn2S2 monolayer ($U = 0.3$ V, $I = 15$ pA).

In order to gain further insight in the insertion process, the insertion of Mn12BnSMe was carried out also in a BnSMe SAM; in this case the substrate is made up of molecules that have exactly the same structure of the incoming ligand present in Mn12BnSMe. The experimental procedure was the same

used for the insertion of the previous system. Figure 2.21 shows some typical
morphology images of such adsorbates acquired with STM.
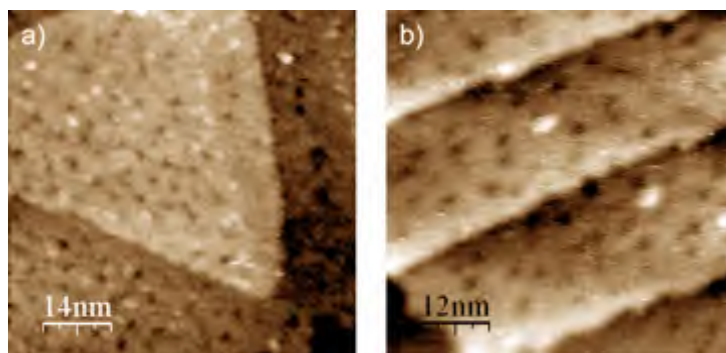
Figure 2.21: STM topography scans of Mn12BnSMe inserted into a BnSMe
monolayer ($U = 0.3$ V, $I = 15$ pA).

Also in this case different incubation times of the preformed monolayer in
the solution of Mn12BnSMe gave rise to no detectable differences in the degree
of insertion. On the other hand on these systems insertion seems to be less
dense than in those based on a Bn2S2 SAM: no domains of Mn12 are observed,
while the inserted clusters are more homogeneously dispersed throughout the
surface.

This observation is in agreement with our hypotheses, in fact when inserting the
Mn12BnSMe complex in a BnSMe monolayer, no disruption of the lateral or-
dering is to be expected: the incoming molecule and the adsorbate have exactly
the same structure and the driving forces that are involved in the formation of
the host monolayer are weaker than those of Bn2S2 systems. As a consequence,
Mn12 can be included in the bidimensional lattice without strongly affecting
its surroundings.

In conclusion, the new derivative Mn12BnSMe can be inserted in a SAM of
thiol-related molecules; a selected functional group and its structural similarity
those used for each of the two SAMs allows Mn12 to be locked in the pristine
monolayer. In particular, the structural affinity of the molecule forming the
SAM and that of the ligand of Mn12 resulted to be a key parameter to affect
the outcome of the insertion and quite probably the insertion mechanism itself.
The insertion process was carried out on Bn2S2 substrates and evidenced the
presence of domains in which the cluster was adsorbed as isolated units, prob-
ably due either to the presence of defects in the SAM or to a local generation
of defects upon the insertion of Mn12BnSMe units. Further tests on BnSMe
SAMs resulted in a lower degree of insertion of the complex and the absence
of domains; while the small number of inserted units was somewhat surpris-
ing, as the similarity of the lateral chain of adsorbed and incoming molecules

would suggest an easier exchange, it can corroborate the hypothesis of a defect-assisted insertion mechanism, since no defects are induced by Mn12BnSMe in a BnSMe SAM.

The advantages of this method of grafting Mn12 to surfaces are the greater control over the chemistry of the surface (an organic SAM is less prone to contaminations than a bare gold surface), and the possibility of obtaining very well defined systems of isolated clusters surrounded by an insulating environment. Further developments of this technique may be achieved in order to obtain a more extensive coverage of the inserted cluster by fine-tuning the interaction between adsorbed molecules and incoming Mn12-bound thiolated ligand; in any case this approach seems very promising for the study of the magnetic properties of single Mn12 units on surface by means of scanning probe magnetic techniques, such as magnetic force microscopy,[83] scanning hall probe microscopy[84] and spin polarized-STM.[92]

Chapter 3

Monolayers of Fe4

3.1 The iron option

The family of clusters introduced in section 1.4 and known as Fe4, is the second class of SMMs that has been successfully adapted to the grafting to surfaces. In a similar fashion to Mn12, in fact, Fe4 is extremely versatile from the chemical point of view, allowing the synthetic chemist to prepare a wide range of functionalized derivatives. In particular, the discovery by Cornia's group in cooperation with our group[27] that the six axial, μ-oxo bridging methoxide ligands could be replaced by two tripodal triols, was a major breakthrough in this regard. While the main focus of that work was the remarkable observation of an increase of the anisotropy in the tripodal-coordinated Fe4 derivatives with respect to the original compound, a very exciting effect was also a greatly increased stability of the complex, due to a more efficient ion coordination, and the possibility of performing a wide-ranging rational design of triol ligands. The appealing route to surface grafting of Fe4 was then opened, and both gold- and silicon-binding derivatives of Fe4 were synthesized by Cornia *et al.*;[7] the crystal structure of the gold-binding surface derivative reported in that work is shown in Figure 3.1.

Surface binding Fe4 complexes features a striking difference with the related Mn12 derivatives: in fact, only part of the ligands participate to the ligand exchange, the six *dpm* ligands remaining in their place and only the six methoxide groups being displaced by the two tripods. As seen for Mn12 functionalized derivatives, also for Fe4 specific semi-systematic stenography was created, as pointed out in Figure 3.2, where we show the structures of the ligands used in this thesis work to yield the gold-binding Fe4 derivatives. As can be seen, the stenography indicates the ligand's structure keeping the triol moiety implicit; the name of the related Fe4 will then be Fe4*ligand*, meaning that the Fe4 core is surrounded by six *dpm* molecules and two triols (after threefold deprotonation) identified by the stenography. In a similar way to Mn12 ligands, also these ligands can be broken down into the three functional units **complexing**
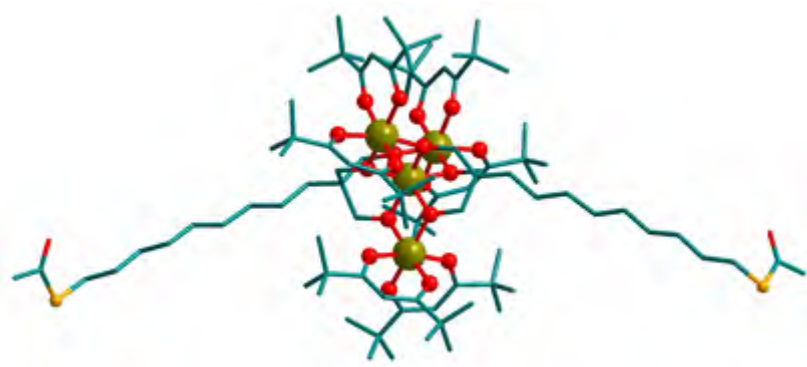
Figure 3.1: Crystal structure of the first sulphur-functionalized Fe4 derivative,
Fe4C9SAc.

unit, **spacer** and **linker**.
As mentioned above, this selective partial ligand substitution yields Fe4 units
that have just two functional units per molecule, in contrast to the sixteen func-
tions in Mn12, which also have a very defined spatial distribution, i.e. along the
easy axis of the magnet. This is a rather interesting feature, since such systems
could, at least in principle, adsorb on the gold surface in an anisotropic manner,
the most favorable case being the upright position, with the anisotropy axis
perpendicular to the surface: this clearly contrasts with what can be antici-
pated for Mn12 adsorbates, whose the sixteen functional ligands are distributed
pseudo-isotropically around the Mn12 inorganic core, thus allowing various of
orientations of the molecule on the surface.
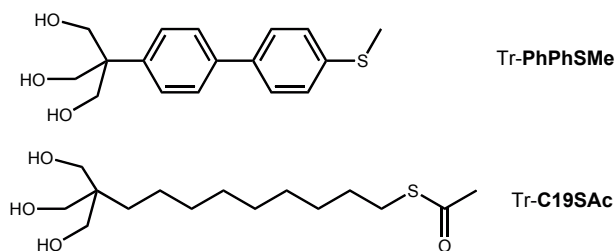
Figure 3.2: Fe4 ligands used in this thesis.

While previous studies on depositing Fe4 functionalized derivatives on sili-
con substrates have been carried out by Fragalá's group in collaboration with
Cornia's group,[93] when this thesis was written the process of grafting these
compounds to a conducting surface such as Au(111) surfaces has never been
carried out, to the best of our knowledge. During this thesis work then, the

first steps were taken to prepare single layers of Fe4 on gold, and to thoroughly characterize such systems.

Of the Fe4 derivatives obtained with the ligands shown in Figure 3.2 only two were used for an in-depth characterization of their adsorbates, namely Fe4C9SAc and Fe4PhPhSMe. The features of their ligands are quite different, since the former has a long alkyl chain as the spacer, which is extremely flexible, while the biphenyl moiety of the latter makes it much more rigid. In addition, ligand C9SAc has the sulphur atom protected as a thioacetyl function and in PhPhSMe sulphur is present as a methyl thioether. As we will see in the next few sections, some of the differences in the two adsorbates must be attributed to this two protecting methods, while in some other cases protection was quite surprisingly found to be non influent.

The monolayers were prepared using self-organization from solution, and were characterized with the same techniques used for Mn12, namely STM for morphological studies and XPS to probe their chemical composition. In addition to these techniques, ToF–SIMS mass spectrometry was used to spot Fe4 units on the surface; the ability of this technique to detect the mass peak on such bulky polynuclear coordination compounds was a good achievement, since all similar tests carried out on Mn12 adsorbates prior to this thesis work[64,81] could only ascertain the presence of fragments of the cluster. The lower molecular weight of Fe4 and the chelating effect of the tripods were favorable parameters.

Considering the effects that the different solvents were found to have on the features of the adsorbate of Mn12 derivatives, which were addressed in detail in section 2.5, a systematic solvent dependence study has been carried out also on Fe4 adsorbates, for which four solvents were used (dichloromethane, hexane, toluene and dioxane) and the resulting adsorbates were characterized by means of the techniques mentioned above (STM, XPS and ToF–SIMS); all this was done both for Fe4C9SAc and Fe4PhPhSMe derivatives.

This chapter contains a great quantity of information on two Fe4 derivatives. For each of these, a three-dimensional array of data has been gathered by inspecting monolayers yielded from different solvents by means of STM, XPS and ToF–SIMS techniques.

Since this amount of data can be rather confusing to the reader, I have placed several summary points in order to restore clarity in the exposition.

3.2   Methods

Monolayers were prepared with the same procedure that has been described for Mn12 adsorbates in section 2.4: after incubation of the gold surface in a solution of the magnetic complex, the gold plate was washed with fresh solvent (the same one used to dissolve the complex. Also in this case all procedures

were carried out under the dry nitrogen atmosphere of a glove box. XPS measurements were carried out in the same conditions as detailed for Mn12.

ToF–SIMS analysis was carried out with a TRIFT III time-of-flight secondary ion mass spectrometer (Physical Electronics, Chanhassen, MN) equipped with a Au^+ primary ion source. Positive and negative ions spectra were acquired with a pulsed, bunched 15 keV primary ion beam at 600 pA by rastering the ion beam over a 100×100 μm sample area. Also for these experiments a portable glove bag was used to prepare the samples and approach them to the fast entry system of the instrument, in order to minimize atmospheric contamination.

3.3   Fe4C9SAc

Complex Fe4C9SAc was prepared by means of ligand exchange technique for Fe4 from the starting Fe4, $(Fe4(dpm)_6(OMe)_6)$, using the especially designed tripodal ligand C9SAc. The synthesis of the ligand was performed by Cornia and our group.[7]

The monolayers of this derivative were prepared by incubating the gold surfaces for 20 hours (unless specified otherwise) in 0.3 mM solutions of the cluster in the four different solvents; similarly to what has been done for Mn12, the various adsorbates were labeled **Fe4C9SAc-exDCM**, **-exHex**, **-exTol** and **-exDiox**, accordingly to the solvent used to dissolve the complex (dichloromethane, hexane, toluene and dioxane respectively).

The system **Fe4C9SAc-exDCM** has been by far the most intensively studied Fe4 monolayer during this thesis work. In fact, in addition to the characterization that are reported in this section, other studies have been carried out both with magnetic circular dichroism and x-ray magnetic circular dichroism that will be discussed in sections 4.5 and 5.7, respectively.

The acetyl group protecting the sulphur atom was chosen after a similar derivatization of the Mn12 complex, reported in Cornia's work.[64] In that work, however, ammonia was used to deprotect the sulphur atom *in situ* upon adsorption on the gold surface. It was found later, though, that no ammonia is needed for the cluster to graft to the surface so this step, that can also be harmful to the integrity of the molecule, was removed and a direct adsorption was carried out.

3.3.1   STM Studies

At variance with Mn12 adsorbates, that could be inspected by means of scanning probe microscopy rather easily (see Figures and 2.5 2.9 for example) and good quality images could be routinely obtained, Fe4C9SAc monolayers proved to be much more challenging surfaces to image with STM. Nevertheless, repeated studies allowed us to find the right scanning conditions in order to obtain significative and reproducible imaging of the monolayers.

Fe4C9SAc-exDCM

A representative set of images of **exDCM** Fe4 monolayers is shown in Figure 3.3.

The topography images clearly show that the gold surface features a tight coverage throughout the surface, while high resolution imaging reveals that the layer is made up of round objects whose average diameter is 2.5 ± 0.1 nm (see statistics in figure 3); this dimension is in good agreement with the size that can be estimated from the crystal structure of the complex. The best scanning conditions were found in an average tunneling interaction regime, with bias voltages around 0.3-0.4 V and tunneling currents of the order of 10 pA; no significant dependence was found on the tunneling conditions for what concerns the ability of the tip to displace Fe4 units from the surface, while molecular resolution can be achieved only with interactions not stronger than those indicated above. This is probably due to the fact that the tip, while not being able to actually remove the molecules from the surface, scans through them, elastically displacing them with the result of noisy and unresolved imaging.
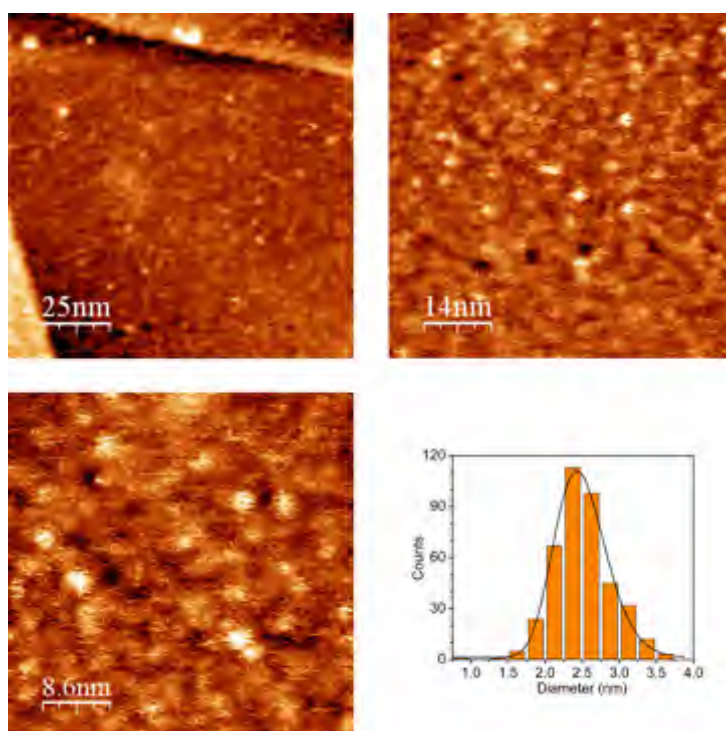
Figure 3.3: STM topography images (tunneling conditions: $U = 0.35$ V, $I = 9$ pA) of a typical **exDCM** adsorbate. Bottom right: statistic of the objects' diameter.

If we consider the structure of the complex, one can see that the alkyl chains are long enough to bind simultaneously to the gold surface, thus placing the molecular axis roughly parallel to it, giving rise to something similar to what is called a *lying down* phase in classical SAM terminology; in the opposite situation, Fe4 units can interact asymmetrically with the surface, i.e. with only one sulphur atom, and with a distribution of orientations that is centered around the surface normal, resembling the *standing up* phase of classic SAMs[a]. Considering the relatively low definition of the STM scans, it is difficult to determine whether the SMM units are adsorbed with one or two ligands interacting with the surface. Nevertheless, some observations seem to suggest a *standing up*-like adsorption mode: in the first place, the circular shape of the resolved objects hardly fits with the hypothesis of flat-lying clusters (length to width ratio for Fe4C9SAc is ~ 2 according to crystallographic measurements). In addition, the *lying down* phase, due to the anisotropic nature of the self-organizing objects, would hardly allow a tight coverage of the surface like the one observed in Figure 3.3.

The striking difference between the quality of STM images taken on Mn12 layers and those of Fe4 is probably due to the distribution of the surface-linking functions around the molecule. In fact, in Mn12 there is just one type of ligand (besides water molecules) that can be functionalized by introducing sulphur-functionalized ligands around the Mn12 core one produces a complex that has more than one active site interacting with the surface, thus after grafting it will loose some degrees of liberty (i.e. it will not be able to rotate). In the case of Fe4 derivatives instead, only two ligands are replaced upon functionalization of the cluster, the six equatorial *dpm* ligands remaining unaltered by the ligands exchange process. If we consider that functionalized Fe4 clusters graft to the surface using just one sulphur atom (and leaving the other one 'dangling in the air'), the molecules are free to rotate around their main axis of symmetry and, to some extent, tilt with respect to the surface. These conditions would cause a greater mobility of the molecule with respect to the STM tip, so imaging would be strongly impaired. According to this hypothesis, reducing the kinetic energy of the system would have a very strong effect on the mobility of the adsorbate, thus enabling easier imaging; unluckily no low temperature STM setup was available during this thesis work.

Fe4C9SAc-exHex

Fe4 clusters could be resolved with STM imaging on the surface of monolayers yielded from hexane solutions; samples were prepared using standard conditions in glove box. As we can see in Figure 3.4, most of the layer is hard to resolve, while isolated protruding units can be spotted rather easily.

---

[a]Once again, it must be remarked that similarities of these systems with proper thiol SAMs (ordered layers made of simple thiols) are limited to the sulphur-gold interaction that links the complex to the surface.
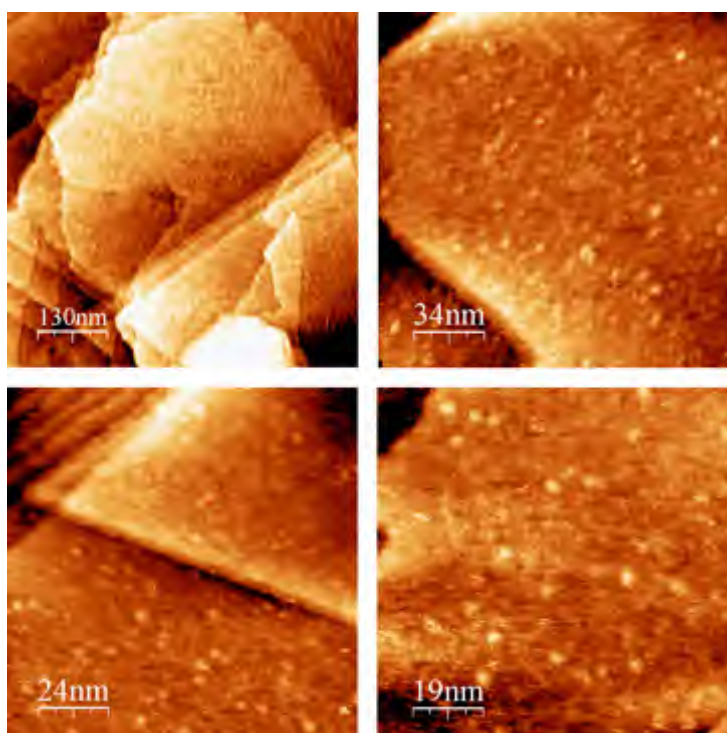
Figure 3.4: STM topography images (tunneling conditions: $U = 0.35$ V, $I = 9$ pA) of a typical **exHex** adsorbate.

Fe4C9SAc-exTol

STM imaging on monolayers obtained from toluene solutions gave the same, hard to resolve monolayer found for DCM solutions. No characteristic morphological feature was found.

Fe4C9SAc-exDiox

No images giving resolved objects resembling Fe4 units could be obtained on these type of monolayers. This is coherent with the XPS data collected on this system, presented in the next section, that show no sign of the complex on the surface.

Summary of STM measurements

STM imaging is definitely more difficult on Fe4C9SAc than on Mn12 derivatives, however a tightly packed layer can be resolved for **exDCM exHex** and **exTol** monolayers, all with similar features. No resolved images could be acquired for **exDiox** samples.

3.3.2   XPS Studies

XPS experiments were carried out in a similar way as those on Mn12 monolayers, described in sections 2.1 and 2.2. The experimental details can be found in section 2.3: Methods on page 27.

Bulk phase Fe4C9SAc

While reports of the XPS characterization of Mn12 in the bulk phase can be found in literature, no such characterization existed for Fe4 clusters. We then considered that the most appropriate starting point for an XPS study on Fe4 was a characterization of its bulk phase. We adopted two approaches for sample preparation: direct study of crystalline matter and study on drop cast complex from DCM solutions on gold substrates.
The first approach is the most straightforward: the big single crystals of Fe4C9SAc were mounted on the sample holder with no particular precaution; a survey scan (energy range 0-1300 eV) is shown in Figure 3.5a, while multiplex scans are reported in Figure 3.6.
Direct analysis of crystalline samples proved to be efficient for bulk analysis of the complex, nevertheless it has few drawbacks, namely the rather large amount of sample needed (though it can be recovered), the non-flat surface and in addition a stronger charging effect (about 3 eV, as estimated from the C1s peak shift).
Cast samples were prepared by dropping a few microliters of a solution of Fe4 on a standard gold substrate under nitrogen atmosphere and allowing solvent

to evaporate; the relatively thick layers (few hundreds of nanometers) that are obtained by this convenient procedure can be considered bulk samples. Figure 3.5b clearly shows that no strong signals from the underlying gold substrate are present in the survey scan. Again, detailed spectra of the areas of interest are compared with those of the crystalline sample in Figure 3.6. The use of drop cast layers for bulk reference measurements seemed to us more convenient than the use of single crystals for a number of reasons. In the first place, the measurement is more reproducible, since the geometry, even if far from being atomically flat, is much more controlled than in the case of random crystals; moreover the sample quantity that is used is negligible (solutions are the same used for monolayer self-organization, that is 0.3 mM solutions). Finally, charging effects due to loss of photoelectrons, although still present, are less intense than those observed for crystalline samples (around 2 eV against 3 eV, all spectra are shift–corrected).
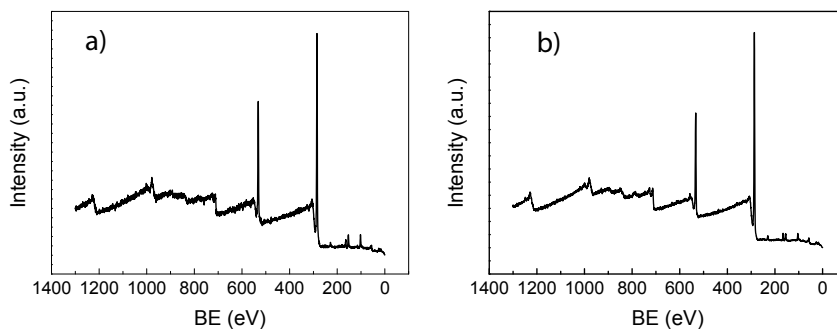
Figure 3.5: XPS survey spectrum of a) crystals and of b) a drop cast sample of Fe4C9SAc.

Quantitative information on the relative abundance of the four elements was recovered from the integrals of the peak areas; expected percent values for Fe4C9SAc for each atomic species were calculated using eq. (2.2), considering the brute formula $Fe_4C_{96}O_{20}S_2$ ($n_{tot} = 122$). Calculated and experimental values of atomic percentage for both crystalline and drop cast samples are reported in Table 3.2.
By looking at the survey scans of both systems (Figures 3.5a and b) though, one can easily spot the presence of an additional weak peak (around 102 eV, after correction for charging effects) due to silicon 2p transition. This impurity is not so surprising, since some steps of the chemical manipulation is carried out under nitrogen; this requires airtight junctions in the glassware, which is often achieved (as in this case) by using silicon grease; there is no chemical interference between silicon grease and the magnetic molecules used in this study. If
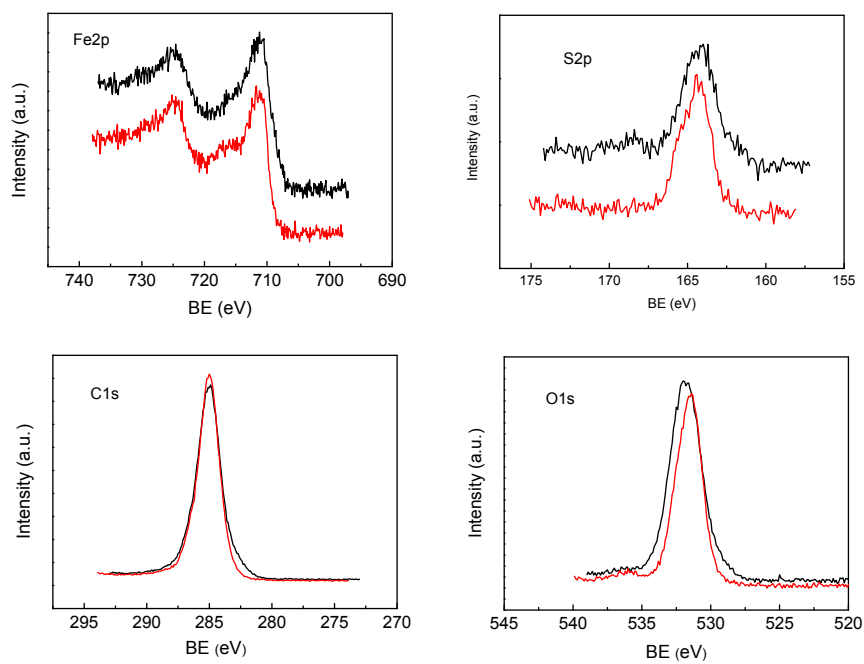
Figure 3.6: Detailed XPS spectra of Fe_{2p}, S_{2p}, C_{1s} and O_{1s} peaks carried out on Fe4C9SAc crystals (black lines) and on a drop cast sample (red lines).

one ponders its composition though, will remark that the grease is made up of is polydimethylsiloxane (PDMS, BEs between 101.4 and 102.5 eV) with small quantities of silicon dioxide[b] (typical BEs between 103.3 and 104.0 eV): these two compounds obviously alter the carbon and oxygen integral values in the semi-quantitative analysis of the samples. For this reason, Si_{2p} peak was added in the multiplex analysis of both samples in order to estimate the contribution of the grease contamination. The contribution of SiO_2 can reasonably be neglected, so all silicon is considered to originate from a PDMS contamination. PDMS is formed by chains of alternating silicon and oxygen atoms, with two methyl groups bound to each silicon atom; chains are long enough to neglect chain termination in atomic composition. From these considerations one finds an atomic ratio between silicon, carbon and oxygen of $1 : 2 : 1$; the contribution of PDMS to C_{1s} and O_{1s} peaks can then be evaluated by comparing the integral ratios between Si_{2p}, C_{1s} and O_{1s} in the acquired spectra and subtracting from the percentage value of carbon and oxygen the relative values thus calculated for silicon grease contribution. The corrected results are shown as well in Table 3.2.

Found values are in very good agreement with the calculated ones for both systems, while silicon grease corrected values seem to have better effect on crystalline samples.

Peak deconvolution was attempted for the C1s peak, and three components were found: a dominant one that can be ascribed to aliphatic/adventitiuous carbon, a second component at higher BE that is attributed to oxygen-bound carbon (no distinction could be made between alcoholate carbon from the triol ligands and the oxygen-bound carbon in *dpm* ligands) and a very weak component at even higher BE: this component can be coherently assigned to the electron-depleted thioacetyl carbon. Peak C_{1s}, along with the scheme of the assignments for each carbon atom of the ligands are shown in Figure 3.7.

Relative integral values of the three components were evaluated and are reported in Table 3.1 along with the BE value of each peak and its FWHM; integral values are also compared with the expected atomic percentages of each type of carbon. Low BE component results to be slightly higher than expected, coherently with the fact that adventitiuous carbon falls into this peak; curiously, the ratio between O-bound and thioacetyl carbon fits the expected value very closely (8.4 vs 8.9), despite the fact that the latter component is very weak, thus prone to significative errors in the integration. For the same reason, while this very nicely confirms the structure of the molecule, it should not be taken as a final proof of it.

Oxygen O_{1s} could not be resolved into the two components originating from the different ligands, since no meaningful peak shift is expected for the types of oxygen.

These measurements were considered as the standard for the comparison XPS data acquired on the monolayer systems described in the next few para-

---

[b]SiO_2 is added to promote cross linking between chains.
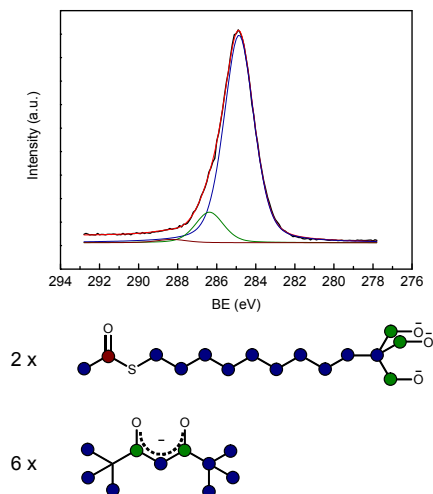
Figure 3.7: Peak deconvolution for C_{1s} of drop cast Fe4C9SAc and color-coded scheme of the types of carbon atoms.

BE (eV)	FWHM (eV)	%Calculated	%Found
284.8	1.8	79.2	86.9
286.4	1.7	18.7	11.7
288.3	1.8	2.1	1.4

Table 3.1: Component details and relative abundance for the deconvolution of the C_{1s} peak in a Fe4C9SAc drop cast sample.

graphs.

	Fe	S	C	O
%Calculated	3.3	1.6	78.7	16.4
%Crystals	2.6	1.3	77.2	18.9
%Corrected	3.1	1.6	79.0	16.3
BE (eV)	714.1	167.1	288.0	534.8
%Drop cast	2.8	1.6	79.5	16.1
%Corrected	3.1	1.7	80.6	14.6
BE (eV)	713.4	164.5	287.0	533.6

Table 3.2: Comparison of expected and found relative elemental abundance in the Fe4C9SAc crystalline and drop cast samples.

Fe4C9SAc-exDCM

Samples were prepared in the same conditions as those inspected by means of STM (i.e. 20 hour incubation in a 0.3 mM solution of the complex and wash in the same fresh solvent). Also for Fe4 systems, incubation and rinsing were carried out under nitrogen in a portable glove bag setup, in order to minimize atmospheric contamination. Scans were carried out using very long acquisition time, to improve the signal to noise ratio of the very weak signals.

A survey scan, taken in the energy range of 0-1300 eV is shown in Figure 3.8: signals from iron, sulphur, carbon and oxygen can be seen, as well as the strong peaks originating from gold photoelectrons, which give the strongest signals. The detailed scans of Iron (Fe_{2p}), Sulphur (S_{2p}), Carbon (C_{1s}) and Oxygen (O_{1s}) that are contained in the magnetic cluster are reported in Figure 3.9.

The spectral features are very similar to those of the bulk samples described in the previous paragraph, all photopeaks showing relatively low broadening and the expected BEs. Of course, gold peaks are the preponderant signals but in the case of Fe4 no overlap between these and the inspected peaks is present, at variance with the case of Mn photoelectrons (see section 2.5). No charging effects are seen for the signals, since neutrality of the single layer of molecules is easily restored through the conducting gold surface.

Peak integration yielded the relative abundance of the elements on the surface, which is reported in Table 3.3: the values are in rather good agreement with the calculated ones, in particular the very important iron to sulphur ratio, that is expected to be 2 (found: 2.05). This ratio is a good indicator that the cluster is still intact, since sulphur sits at the end of the long chained tripodal ligand, i.e. on the other side of the weak coordinative bond to iron atoms; partial or total disruption of the cluster would have yielded a monolayer of free tripodal ligands (the only units that are able to interact with gold), with subsequent lack of iron, that would have been carried away by the solvent

wash after incubation. On the other hand, carbon and oxygen integrals do not perfectly agree with the expected values, the former integrating slightly less then expected, and the latter being in slight excess: curiously enough, no excess of carbon was found, while in general it is rather easy to find it in slight excess, due to unavoidable atmospheric contamination. We tried to find a *rationale* for this (reproducible)[c] behavior, for example by modeling the loss of one or more equatorial, non surface-active ligands (*dpm*), and comparing the new calculated theoretical values with the found values, but this did not seem to match the experimental results. Since the hypothesis of covalent bond breaking seems a rather poor hypothesis and the found ratios are extremely systematic, we it is possible that the deviation from the theoretical values are to be attributed to calibration discrepancies of the experimental setup when working with this kind of monolayers.

A significative difference with Mn12 adsorbates can be spotted in the S_{2p} peak. In fact, the XPS S_{2p} signal in Mn12 monolayers cannot be used as a probe for electron density changes on the sulphur atom as a consequence of covalent interaction with gold, since only few sulphur atoms per cluster can bind to gold (see section 2.5), with the only effect of broadening the peak. In the case of Fe4 instead, an adsorbed cluster can have one or two gold-bound sulphur atoms, corresponding to 50 and 100% of the total number of sulphur atoms per cluster, so the peak shift can be used as a diagnostic tool for cluster-substrate interaction.

Indeed, the S_{2p} peak in the **exDCM** adsorbate shows a significant shift of around 2 eV with respect to the maximum in the peak of the bulk references (after correction for charging effects), along with some broadening, as can be seen in Figure 3.9. Even if the resolution is not sufficient to precisely determine by means of this observable whether Fe4 is bound to the gold surface with one or two ligands, the shift is strongly symptomatic of a covalent-like interaction.

In order to gain some insight on the timescale of the adsorption process, a monolayer incubated for 45 minutes was inspected by means of XPS spectroscopy as well. Semiquantitative analysis was carried out on this sample, and relative elemental abundance for this system was found to be very similar to the standard systems incubated for 20 hours (data shown in Table 3.3).

Peak deconvolution was carried out on the C_{1s} photopeak of both the 20 hours, using three components corresponding to the carbon types shown in Figure 3.10 together with the deconvoluted peak, in a similar way to what has been done on the reference drop cast sample. The parameters for each component are reported in Table 3.4 along with their relative abundance compared to the calculated one. Curiously, not only do the fitted curves show excellent agreement with the experimental data, but also integral ratios are very similar to the theoretical values. If we choose to trust this type of data processing, we can then conclude that the Fe4 complex binds to the surface without loosing

---

[c]Batch to batch reproducibility was carefully checked and the results are completely systematic. In addition, monolayers grafted from other solvents, as explained in the next paragraphs give similar spectroscopic data.
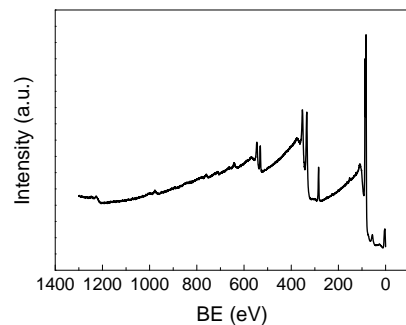
Figure 3.8: XPS survey spectrum of a **Fe4C9SAc-exDCM** adsorbate on Au(111).
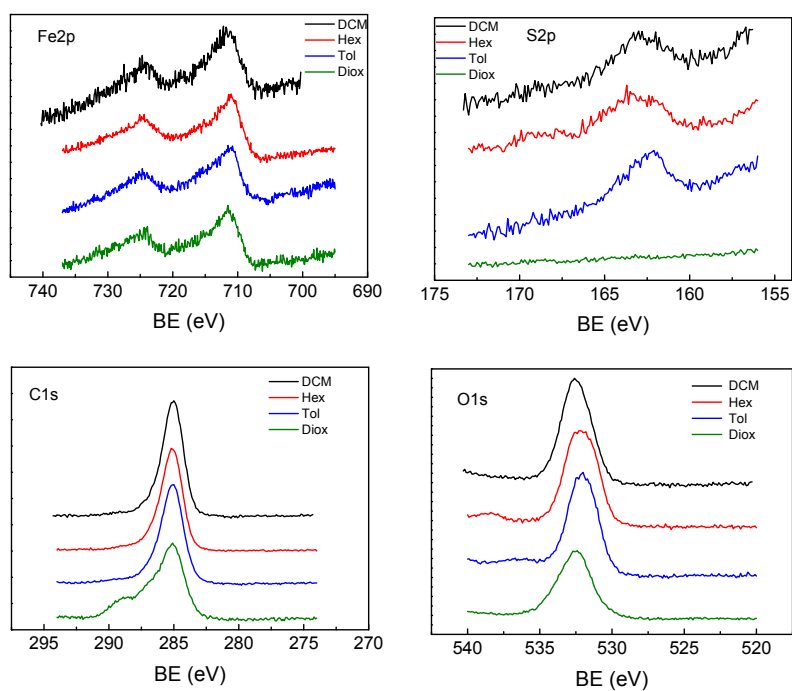
Figure 3.9: Detailed XPS spectra of Fe_{2p}, S_{2p}, C_{1s} and O_{1s} peaks carried out on Fe4C9SAc monolayers.

	Fe	S	C	O
%Calculated	3.3	1.6	78.7	16.4
%**exDCM** 20 h	3.7	2.0	71.5	22.8
BE (eV)	711.2	162.7	284.8	532.2
%**exDCM** 45'	3.7	1.8	71.9	22.6
BE (eV)	711.1	163.3	284.6	531.9

Table 3.3: Comparison of expected and found relative elemental abundance in **Fe4C9SAc-exDCM** monolayers on Au(111).

any on the two acetyl groups; in the case of double acetyl loss if fact, no component at high BE would be observed, and in the case of single acetyl loss, the integral ratio between the two higher BE components should be as high as 18 versus a found value of 7.9.
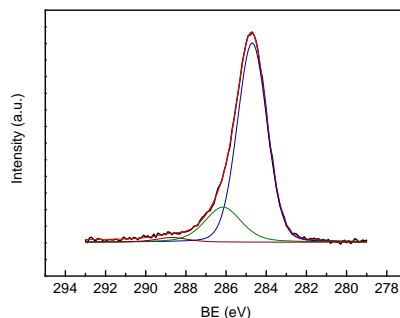
Figure 3.10: Peak deconvolution for C_{1s} of a **Fe4C9SAc-exDCM** monolayer. The color-coding scheme is given in Figure 3.7.

BE (eV)	FWHM (eV)	%Calculated	%Found
284.8	1.7	79.2	78.6
286.2	2.1	18.7	19.0
288.8	1.9	2.1	2.4

Table 3.4: Component details and relative abundance for the deconvolution of the C_{1s} peak in a **Fe4C9SAc-exDCM** monolayer incubated for 20 hours.

Fe4C9SAc-exHex

Monolayers prepared from hexane solutions of Fe4C9SAc for XPS analysis were prepared using the standard grafting conditions under the same inert

atmosphere of a portable glove bag, as detailed in the previous paragraph for **exDCM** samples. The acquisition of the survey and multiplex spectra were carried out using the same conditions used for bulk samples and monolayers from DCM. The survey spectrum is reported in Figure 3.11, while the individual element scans are shown in Figure 3.9.
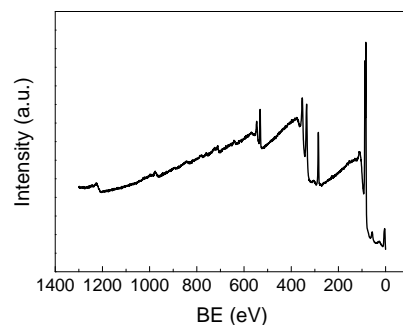
Figure 3.11: XPS survey spectrum of a **Fe4C9SAc-exHex** adsorbate on Au(111).

Interestingly, the shape and shift of the S_{2p} peak differ from those of the **exDCM** monolayer: in fact, while in that system the peak is centered at 162.5 eV, in this case the peak maximum is slightly shifted to higher binding energies, i.e. 163.7 eV; moreover, even if the signal is rather noisy, a minor component at the same BE as the **exDCM** system can be spotted, indicating that in the case of **exHex** samples sulphur atoms experience two slightly different environments.

Semi-quantitative analysis *via* peak integration gave coherent results with what was found for **exDCM** samples. The percent values are reported in Table 3.5; as one can see, the deviations from the calculated values that have been observed for **exDCM** samples are more pronounced in the case of **exHex** monolayers. In fact, despite the Fe/S ratio being very close to the expected value of 2, carbon was found in rather low amount, when compared to the theoretical value.

Fe4C9SAc-exTol

XPS analysis on monolayers prepared from toluene solutions gave well resolved peaks that confirm the presence of Fe4C9SAc on the gold surface. Survey scan is shown in Figure 3.12, and multiplex scans are shown in Figure 3.9. In this case, the S_{2p} peak is completely similar to that found for **exDCM** systems, both in BE and in peak broadening.

	Fe	S	C	O
%Calculated	3.3	1.6	78.7	16.4
%exHex	4.6	2.4	69.5	23.5
BE (eV)	710.9	163.5	285.1	532.1

Table 3.5: Comparison of expected and found relative elemental abundance in **Fe4C9SAc-exHex** monolayers on Au(111).

Relative elemental abundance is reported in Table 3.6; the values are in line with those found on the systems described above. In this case though, sulphur is in slight excess, while relative values for carbon and oxygen are closer to the expected ones than those of the other systems.
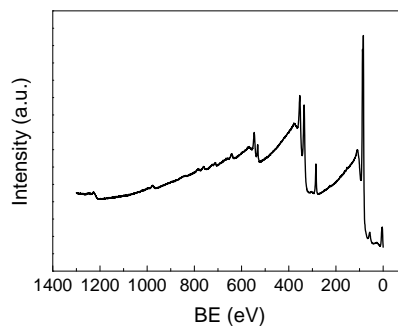
Figure 3.12: XPS survey spectrum of a **Fe4C9SAc-exTol** adsorbate on Au(111).

	Fe	S	C	O
%Calculated	3.3	1.6	78.7	16.4
%exTol	3.6	2.3	73.4	20.7
BE (eV)	711.4	162.4	285.1	531.9

Table 3.6: Comparison of expected and found relative elemental abundance in **Fe4C9SAc-exTol** monolayers on Au(111).

Fe4C9SAc-exDiox

Survey scans of this adsorbates prepared from this solvent showed no presence of sulphur, little amount of carbon and an anomalous amounts of iron and oxygen. Nevertheless, multiplex acquisition was carried out, in order to quantify the species and to ascertain the absence of detectable quantities of sulphur.

Survey scan is reported in Figures 3.13, while the detailed scans can be found
in Figure 3.9. This finding, which is coherent with STM imaging carried out
on these type of samples (see previous section), that was not able to resolve
any meaningful feature that could be considered as Fe4 clusters. As multiplex
clearly shows, no sulphur could be detected even after long acquisition time,
while carbon is very low with respect to iron and oxygen, which are unusually
strong. The conclusion that one must make from these experiments is that
the cluster decomposes on the surface upon adsorption from dioxane solution;
this is somewhat unexpected, since Fe4C9SAc is not unstable in this solvent.
In fact, while the Fe4C9SAc cluster is known to be prone to decomposition in
acidic solvents, such as chloroform, due to protonation of the basic ligands and
in basic conditions (using dimethylformamide as a solvent, for instance), under
which the acetyl group is removed from the sulphur atom, thus creating a thiol
group that reduces the iron(III) ions[d]. Dioxane on the other hand, has neither
acidic protons nor basic functions, so this behavior is somewhat puzzling.
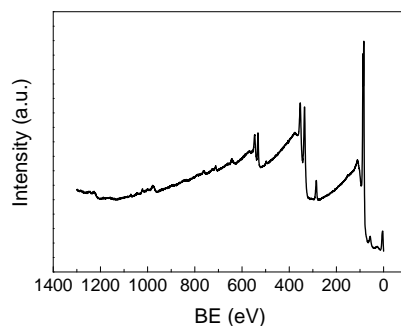
Figure 3.13: XPS survey spectrum of a **Fe4C9SAc-exDiox** adsorbate on
Au(111).

Summary of XPS measurements

Solvent dependance of the adsorbates of Fe4C9SAc on gold has been studied
with the following solvents: dichloromethane, hexane, toluene and dioxane. At
variance with what has been observed for Mn12PhSMe, spectroscopic measure-
ments allowed to find qualitative differences between the various adsorbates,
even if STM imaging showed no detectable difference in the morphology of the
samples; sulphur atoms in particular showed an interesting shift changes from
the bulk to **exHex** with a lowering of the BE and broadening of the peak (prob-
ably due to the presence of two different components) to the two very similar

---

[d]No such lability is observed on thioether-protected derivatives, such as Fe4PhPhSMe,
that is perfectly stable in dimethylformamide.

low BE-shifted peaks of the **exDCM** and **exTol** systems. The shift toward low energy can be interpreted in general as an increase of electron density on sulphur due to the covalent-like interaction with gold; the S_{2p} peak in **exHex** systems can be interpreted either as a somewhat weaker molecule-substrate interaction or as the coexistence of two different binding modes.

For what concerns quantitative information that could be gathered from the spectra, good iron/sulphur ratios are found for all samples (**exDCM** systems being in best agreement and **exTol** the most divergent), while a systematically decreased quantity of carbon was found, along with an excess of oxygen; this is more striking if one compares these data with those found for bulk drop cast films, that exhibit a nearly perfect agreement from the calculated values of atomic relative abundance. Nevertheless, considering that the probed sample is a single layer of complex molecules in which some elements are present in a quantity of few per cent, and that the signal are all coming out from a strong background due to the underlying gold, the quantitative data found for these monolayers is more than satisfactory.

A particular mention must be made around the **exDiox** system, that failed to give any sign of cluster integrity on the surface, while anomalous quantities of iron and oxygen were found.

3.3.3   ToF-SIMS Studies

Secondary ions mass spectrometry proved to be an extremely powerful tool for the inspection of monolayers of Fe4 on gold. In fact, the ionization mechanism used by this type of spectrometry is particularly suited for the desorption of non-fragmented bulky molecules that are kept together by coordination bonds. Moreover, the technique is completely surface sensitive, since only the first molecular layers of the sample are involved in the ionic bombardment and subsequent desorption.

Analysis of Fe4 clusters by this technique is previously unreported, so no reference data on bulk samples is available: for this reason, reference measurements were carried out on a bulk sample of Fe4C9SAc. Spectra were acquired both in the positive and negative ion modes.

Bulk phase Fe4C9SAc

Mass spectrometry on bulk material was carried out on drop cast samples. The DCM solution of Fe4C9SAc was deposited on a silicon wafer (under controlled atmosphere) to yield the drop cast sample.

Figure 3.14 show selected areas of the negative ions mass spectrum for the drop cast sample.

The molecular peak[e] for Fe4C9SAc is at 1928.90 m/z. As can be seen, the

---

[e]This value is related to the most abundant isotope and corresponds to the most intense
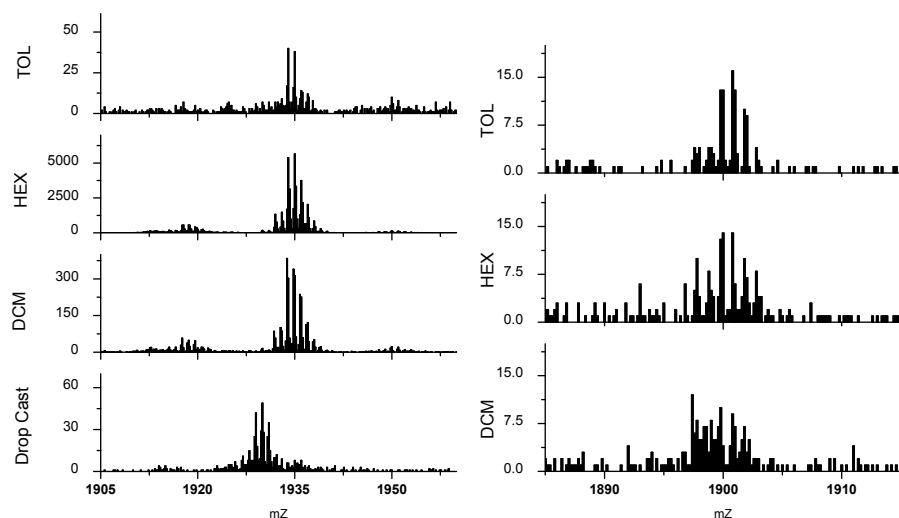
Figure 3.14: Negative (left) and positive (right) ions ToF–SIMS spectra of Fe4C9SAc.

molecular peak can be observed in effect in the negative mode spectrum of the drop cast sample. This finding is a very interesting one, since molecular peak detection was largely un-achievable for the type of SMM studied in the previous chapter, Mn12. This class of compounds in fact is much more fragile and heavy than Fe4 derivatives, so mass spectrometry measurements[81] never achieved detections of more than small fragments of the molecule. In the case of Fe4 instead, it is possible to directly assess the integrity of the molecule; we thus found in ToF–SIMS a very precious ally for monolayer characterization.

In addition to the molecular peak, other strong diagnostic signals in the positive ions mode were found; these correspond to molecular fragments where one or more of the components have detached (often plus an oxygen atom) and have been reported, along with their molecular structure, in Tables 3.7 and 3.8; in the tables the following formalism is introduced: M indicates the molecular peak, while L indicates the tripodal ligand (C9SAc). All peaks exhibit the expected isotopic distribution of the corresponding molecular peak.

It is worth mentioning that ToF–SIMS measurements were attempted also on a powder sample of the original Fe4 compound, the un-derivatized Fe4(dpm)$_6$(OMe)$_6$, that is the cluster in which no tripodal ligands have been inserted in the place of the six methoxides. In this case, despite the fact that the molecular weight is smaller than Fe4C9SAc, no molecular peak was detected; this is a nice indication of the greater lability of the un-derivatized clusters with respect to the tethered structure of the triolated derivatives.

---

signal in the isotopic distribution of the peak; the effective molecular weight averaged over isotopic abundance of Fe4C9SAc is 1929.86 m/z.

Peak (m/z)	Molecular formula	Fragment
1928.90	$Fe_4(C_{11}H_{19}O_2)_6(C_{15}H_{27}O_4S)_2$	$[M]^-$
1506.58	$Fe_3(C_{11}H_{19}O_2)_4(C_{15}H_{27}O_4S)_2$	$[M\text{-}Fe\text{-}2dpm]^-$
183.14	$C_{11}H_{19}O_2$	$[dpm]^-$

Table 3.7: Selected diagnostic peaks in the negative ions mode mass spectrum of Fe4C9SAc from drop cast.

Peak (m/z)	Molecular formula	Fragment
1745.72	$Fe_4(C_{11}H_{19}O_2)_5(C_{15}H_{27}O_4S)_2$	$[M\text{-}dpm]^+$
1036.38	$Fe_3(C_{11}H_{19}O_2)_4(C_{15}H_{27}O_4S)O$	$[M\text{-}Fe\text{-}2dpm\text{-}L+O]^+$
733.14	$Fe_3(C_{11}H_{19}O_2)_3O$	$[M\text{-}Fe\text{-}3dpm\text{-}2L+O]^+$

Table 3.8: Selected diagnostic peaks in the positive ions mode mass spectrum of Fe4C9SAc from drop cast.

Fe4C9SAc-exDCM

The mass spectra acquired for the **exDCM** monolayer of the cluster are shown in Figure 3.14. A strong signal can be observed at 1933.85 m/z: this peak could be assigned to $Fe4(dpm)_6LL^*$, where L* is the tripodal ligand where the sulphur atom has lost the acetyl group and has been oxidized to sulphonate, $R\text{-}SO_3^-$); this fragment, referred to as M* and sketched in Figure 3.15, has a molecular weight of 1933.86 Da.

Figure 3.15: Schematic representation of the oxidized species M* observed in ToF–SIMS spectra of Fe4C9SAc monolayers on Au(111).

Although this modification is rather unexpected, this peak seems to correspond to the molecular peak with a small peripheral modification. If one considers valid this interpretation, it is worth making some further considerations on the possible origin of such modification. The first fact to be kept in mind is that no sign of oxidized sulphur can be found in the XPS spectrum of **exDCM** systems (see Figure 3.9 and relative discussion); considering that XPS S_{2p} peak is a sensitive probe of electron density on sulphur, we can conclude that no such species as $Fe_4(dpm)_6LL^*$ is present on the surface of samples analyzed by means of XPS. One might postulate that this oxidation might take place in the case of Fe4 units bound with only one ligand, the second one being exposed to the atmosphere but, since ToF–SIMS samples were prepared in the same conditions as XPS ones, this is quite unlikely.

We must then suppose that the change around the sulphur atom is completely

related to some step of the mass spectrometry analysis, for example a recombination upon desorption from the surface; in this case one would expect to see the same peak also in spectrum of the bulk (DC) reference, unless the effect was directly related to an interaction of sulphur with the gold substrate, most probably a deacetylation of the bound sulphur atom and subsequent increased reactivity upon desorption. Supposing this, one could not only justify the differences between bulk and monolayer peaks, but would also have an indirect proof of the chemisorption of Fe4C9SAc on gold.

Other diagnostic peaks are reported in Tables 3.9 and 3.10. As can be seen, the mass spectra show molecular fragments that contain both unaltered ligands L and oxidized ones L*: in particular it is nice to observe the simultaneous presence of the $[M-2dpm]^+$ and $[M^*-2dpm]^+$ in the 1500 m/z area.

In line with STM and XPS measurements, ToF–SIMS data confirm that in **Fe4C9SAc-exDCM** systems molecules are grafted to the surface and keep their chemical integrity.

Peak (m/z)	Molecular formula	Fragment
1933.85	$Fe_4(C_{11}H_{19}O_2)_6(C_{15}H_{27}O_4S)(C_{13}H_{24}O_6S)$	$[M^*]^-$

Table 3.9: Selected diagnostic peaks in the negative ions mode mass spectrum of a **Fe4C9SAc-exDCM** monolayer.

Peak (m/z)	Molecular formula	Fragment
1746.42	$Fe_4(C_{11}H_{19}O_2)_5(C_{15}H_{27}O_4S)_2$	$[M-dpm]^+$
1036.45	$Fe_3(C_{11}H_{19}O_2)_3(C_{15}H_{27}O_4S)O$	$[M-Fe-3dpm-L+O]^+$
749.25	$Fe_3(C_{11}H_{19}O_2)_3O_2$	$[M-Fe-3dpm-2L+2O]^+$
733.24	$Fe_3(C_{11}H_{19}O_2)_3O$	$[M-Fe-3dpm-2L+O]^+$

Table 3.10: Selected diagnostic peaks in the positive ions mode mass spectrum of a **Fe4C9SAc-exDCM** monolayer.

Fe4C9SAc-exHex

ToF–SIMS analysis on this system gave very strong signals and a peak structure rather similar to the one found for **Fe4C9SAc-exDCM**. The oxidized molecular peak M* at 1933.86 m/z is among the most intense peaks of the spectrum and it exhibits the same isotopic distribution as the former system; such distribution could be successfully reproduced by calculations. Negative and positive ions mode spectra for this sample are reported in Figure 3.14. While the main spectral features are closely related to the **exDCM** adsorbate, there are a number of differences in some fragmentation patterns; the most significative peaks are reported in Tables 3.11 and 3.12.

Also in the case of **Fe4C9SAc-exHex**, collected data seem to confirm the presence of unaltered clusters on the surface. Two mass peaks between 1770

Peak (m/z)	Molecular formula	Fragment
1933.85	$Fe_4(C_{11}H_{19}O_2)_6(C_{15}H_{27}O_4S)(C_{13}H_{24}O_6S)$	$[M^*]^-$
1917.52	$Fe_4(C_{11}H_{19}O_2)_6(C_{15}H_{27}O_4S)(C_{13}H_{24}O_5S)$	$[M^*-O]^-$
1750.75	$Fe_4(C_{11}H_{19}O_2)_5(C_{15}H_{27}O_4S)(C_{13}H_{24}O_6S)$	$[M^*dpm]^-$
1550.8	$Fe_4(C_{11}H_{19}O_2)_4(C_{15}H_{27}O_4S)$-$(C_{13}H_{24}O_6S)$-OH	$[M^*-2dpm\text{-}OH]^-$
1534.8	$Fe_4(C_{11}H_{19}O_2)_4(C_{15}H_{27}O_4S)$-$(C_{13}H_{24}O_6S)$-$O_2H$	$[M^*-2dpm\text{-}O_2H]^-$
183.14	$C_{11}H_{19}O_2$	$[dpm]^-$

Table 3.11: Selected diagnostic peaks in the negative ions mode mass spectrum of a **Fe4C9SAc-exHex** monolayer.

Peak (m/z)	Molecular formula	Fragment
1899.92	$Fe_4(C_{11}H_{19}O_2)_6(C_{15}H_{27}O_4S)$-$(C_{13}H_{24}O_6S)$-$O_2H_2$	$[M^*-O_2H_2]^+$
1789.72	$Fe_4(C_{11}H_{19}O_2)_5(C_{13}H_{24}O_6S)_2H_2O_2$	$[M^{**}-dpm+H_2O_2]^+$
1773.74	$Fe_4(C_{11}H_{19}O_2)_5(C_{13}H_{24}O_6S)_2H_2O$	$[M^{**}-dpm+H_2O]^+$
1745.84	$Fe_4(C_{11}H_{19}O_2)_5(C_{15}H_{27}O_4S)_2$	$[M-dpm]^+$
1567.62	$Fe_4(C_{11}H_{19}O_2)_4(C_{15}H_{27}O_4S)$-$(C_{13}H_{24}O_6S)$	$[M^*-2dpm]^+$
1036.39	$Fe_3(C_{11}H_{19}O_2)_3(C_{15}H_{27}O_4S)O$	$[M\text{-}Fe\text{-}3dpm\text{-}L+O]^+$
749.25	$Fe_3(C_{11}H_{19}O_2)_3O_2$	$[M\text{-}Fe\text{-}3dpm\text{-}2L+2O]^+$
733.24	$Fe_3(C_{11}H_{19}O_2)_3O$	$[M\text{-}Fe\text{-}3dpm\text{-}2L+O]^+$

Table 3.12: Selected diagnostic peaks in the positive ions mode mass spectrum of a **Fe4C9SAc-exHex** monolayer.

and 1800 m/z are tentatively attributed to a fragment of a doubly oxidized
species (i.e. both ligands have oxidized sulphur atoms); such peaks are also
found, in the **exDCM**, yet they are very weak (thus not reported in Table
3.10); the molecular fragment with both tripods L in the oxidized form has been
termed M**. If we consider valid our hypothesis that oxidative desorption is
directly assisted by the sulphur-gold interaction, we may then infer that these
fragments are originated by clusters that were bound to the surface using both
ligands. If we now go back to the XPS study that has been described in
the previous section, we will recall that S_{2p} peak of **Fe4C9SAc-exHex** was
anomalously shifted and broadened, probably due to a bimodal distribution of
S-Au interaction: this would nicely fit with the hypothesis of the coexistence
of standing up and lying down units in **exHex** adsorbates, at variance with
exDCM ones.

Fe4C9SAc-exTol

Signals in the mass spectra were very weak for this system, nevertheless the
oxidized molecular fragment M* could be found as a negative ion also in this
case, along with fragments from both M and M*. Mass spectra are given in
Figure 3.14. while the most important peaks are reported in Tables 3.13 and
3.14.

Peak (m/z)	Molecular formula	Fragment
1933.85	$Fe_4(C_{11}H_{19}O_2)_6(C_{15}H_{27}O_4S)(C_{13}H_{24}O_6S)$	$[M^*]^-$
1917.52	$Fe_4(C_{11}H_{19}O_2)_6(C_{15}H_{27}O_4S)(C_{13}H_{24}O_5S)$	$[M^*\text{-O}]^-$
183.14	$C_{11}H_{19}O_2$	$[dpm]^-$

Table 3.13: Selected diagnostic peaks in the negative ions mode mass spectrum of a **Fe4C9SAc-exTol** monolayer.

Peak (m/z)	Molecular formula	Fragment
1745	$Fe_4(C_{11}H_{19}O_2)_5(C_{15}H_{27}O_4S)_2$	$[M\text{-}dpm]^+$
1704	$Fe4(C_{11}H_{19}O_2)_5(C_{15}H_{27}O_4S)_2+4O2H$	$[M^*\text{-dpm}+4O2H]^+$
1036.45	$Fe_3(C_{11}H_{19}O_2)_3(C_{15}H_{27}O_4S)O$	$[M\text{-Fe-}3dpm\text{-L}+O]^+$
749.25	$Fe_3(C_{11}H_{19}O_2)_3O_2$	$[M\text{-Fe-}3dpm\text{-2L}+2O]^+$
733.24	$Fe_3(C_{11}H_{19}O_2)_3O$	$[M\text{-Fe-}3dpm\text{-2L}+O]^+$

Table 3.14: Selected diagnostic peaks in the positive ions mode mass spectrum of a **Fe4C9SAc-exTol** monolayer.

Summary of ToF-SIMS measurements

In summary, we have performed ToF–SIMS measurements on the Fe4C9SAc
cluster in bulk phase and in monolayers. The excellently performing setup,

featuring a primary source using gold ions and an extremely sensitive time of flight analyzer allowed us to observe the molecular peak in both cases. Monolayers always gave an oxidized molecular peak, with one sulphur atom that has lost the acetyl group and has become a sulphonate. Fragmentation in bulk and monolayer samples was found to be quite different, mainly due to the simultaneous presence of oxidized and regular peaks in the latter systems. Considerable differences were found also in the fragmentation patterns of the monolayers prepared from the various solvents; in particular, the **exHex** monolayers gave two peaks that could be modeled by considering both sulphur containing ligands as oxidized.

Ligand oxidation has been ascribed to a desorption-related process, since no sign of oxidized sulphur could be found in XPS spectra: we can then conclude that the observed molecular peak is a good indication of the presence of intact clusters to the surface.

By taking this hypothesis one step forward and supposing that desorption-induced oxidation of sulphur is directly assisted by the bound gold atoms, and by cross linking the data from XPS, we could obtain putative information on the tendency of each type of adsorbate to bind with one or two active ligands to the surface.

3.3.4 Conclusions of Fe4C9SAc monolayer characterization

Apart from the case of dioxane, that seems to be incompatible with the deposition process of this Fe4 derivative, all solvents gave fairly similar adsorbates, toluene giving the weakest signals in XPS and in ToF–SIMS and hexane the strongest ones. The use of the standard solvent DCM seems to be a good choice for the following studies.

3.4 Fe4PhPhSMe

Following the successful preparation and grafting of the cluster Fe4C9SAc, another sulphur-functionalized derivative, namely Fe4PhPhSMe has been designed and prepared by Lapo Gorini, a former student of our group. The structure of this complex is sketched shown in Figure 3.16, as determined from single crystal x-ray analysis. The structure of the ligand PhPhSMe differs from that of C9SAc in both the spacer and the binding group: the former is an aromatic, consisting of a biphenyl unit whose length is similar to that of the nine carbon aliphatic chain of C9SAc, but that is more rigid and cannot bend. The binding group instead differs from the one used in C9SAc in the fact that the sulphur atom is protected as a thioether and not as a thioacetyl; thioethers as protecting groups have already been used in Mn12 derivatives (see for example Mn12PhSMe and Mn12BnSMe that have been described in the previous chapter) and are more stable than thioacetyls, for example they are not prone

to deprotection in the presence of basic nitrogen atoms. The synthesis of the ligand (whose structure is shown in Figure 3.2) is explained in detail in Lapo Gorini's PhD thesis, together with the variations to the standard ligand exchange procedure that are needed in order to insert PhPhSMe around the Fe4 core to yield Fe4PhPhSMe.

This Fe4 derivative then is a complex with a relatively rigid structure and at variance with Fe4C9SAc, it is unlikely that this complex can bind using the two sulphur atoms simultaneously, thus orienting the easy axis parallel to the surface. In this case in fact, a distortion greater than $90°$ would completely rest on just one carbon atom, namely the quaternary carbon of the tripod, while the flexible aliphatic chain of C9SAc allows in principle a distribution of the distortion among all the carbon atoms. Another important difference between the aliphatic and the aromatic ligands is the degree of electron delocalization: in fact, the extended π electron system of PhPhSMe makes the ligand far more conducting than the aliphatic counterpart, so the grounding of the two complexes with respect to the conducting surface to which they are grafted is expected to be different. This can be an interesting modulation in the case of electron transport experiments on single molecules,[94,95] since switching from weak to strong coupling of the nanomagnet with the electrodes may give rise to completely different conduction regimes.

Also in the case of this complex a complete set of measurements was carried out on adsorbates obtained from the four solvents used to graft Fe4C9SAc to gold (namely dichloromethane, hexane, toluene and dioxane). At variance with the preparation protocol that was adopted for Fe4C9SAc monolayers, Fe4PhPhSMe layers were prepared by incubating the gold surface in the solution of the complex for shorter time, i.e. 3 hours (instead of 20), on the basis of the experience gained with Mn12 methylthioether derivatives; all other steps were maintained unvaried.

In addition to the morphological and chemical characterization that is presented in this section, XAS and XMCD experiments have been carried out on Fe4PhPhSMe monolayers on gold; these will be discussed in Chapter 5.

3.4.1   STM Studies

Like for Fe4C9SAc, STM imaging on Fe4PhPhSMe monolayers proved to be a challenging task, the monolayer being tightly packed yet disordered, with the long chains of the second tripodal ligand and the six *dpm* ligands free to move, thus strongly lowering the scan quality. Nevertheless, also in this case careful optimization of the scanning conditions allowed us to obtain images of sufficient quality to resolve at least part of the round objects, the size being in reasonable agreement with the crystallographic dimensions of the complex.
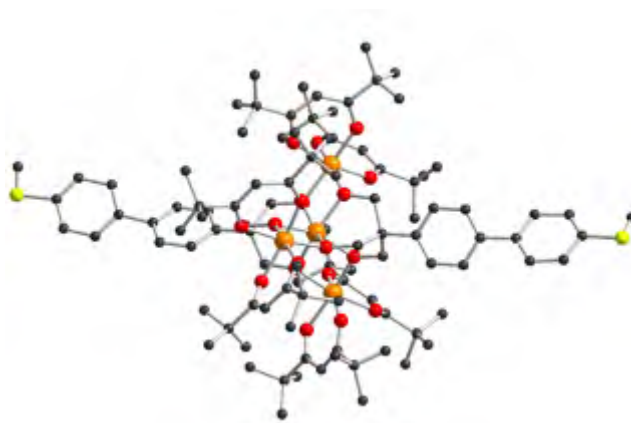
Figure 3.16: Complex Fe4PhPhSMe, as obtained from diffraction data.
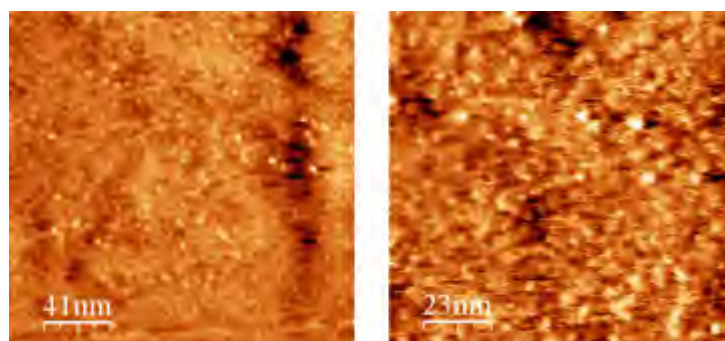
Figure 3.17: STM topography images (tunneling conditions: $U = 0.35$ V, $I = 9$ pA) of a typical **exDCM** adsorbate.

Fe4PhPhSMe-exDCM

Fe4PhPhSMe-exHex

A very tight layer of objects was observed, and round features in the texture could be partially resolved; these are sized around 2 nm and are reasonably considered to be Fe4 units. A set of representative STM images is shown in Figure 3.18. Some protruding round objects can be observed in some areas of the surface, which are probably to be attributed to Fe4 units absorbed with a different geometry, i.e. in a fully vertical fashion, due to layer packing.
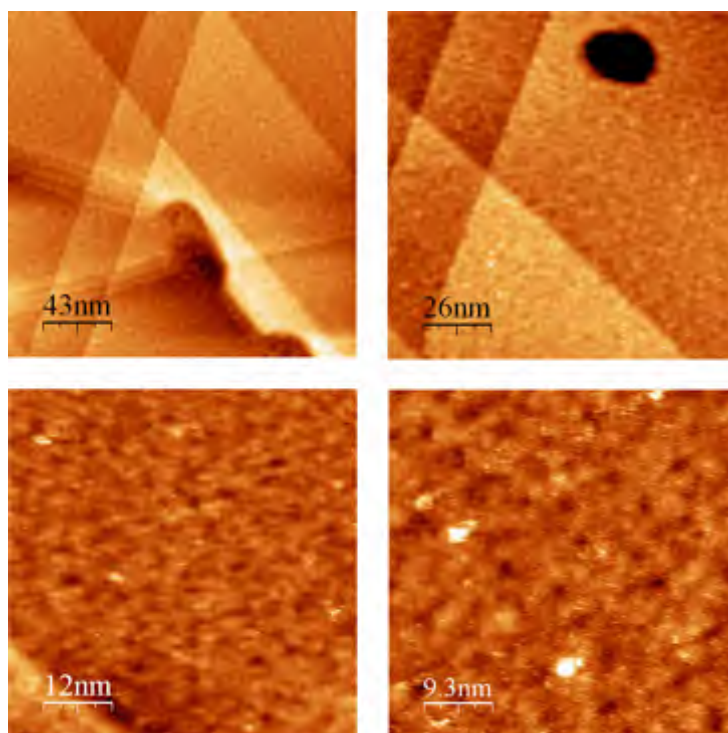
Figure 3.18: STM topography images (tunneling conditions: $U = 0.35$ V, $I = 9$ pA) of a typical **exDCM** adsorbate.

Fe4PhPhSMe-exTol

Monolayers obtained from toluene solutions gave the same tightly packed monolayer observed for **exDCM** and **exHex** monolayers, with no particular morphological difference.

Fe4PhPhSMe-exDiox

Samples prepared from dioxane solutions showed an anomalous, interesting morphology. At variance with **exDiox** monolayers of Fe4C9SAc, no decomposition of the cluster seems to take place, but the gold surface is only partially covered by what appears to be a very diluted sub–monolayer of objects sizing around 2 nm. Some representative scans are shown in Figure 3.19; as can be seen, the behavior is somewhat similar to what has been observed in some Mn12 samples. In this case, however, the coverage seems much less homogeneous and no kind of lateral ordering can be seen. This is nevertheless a nice example of control of surface coverage obtained simply by changing the solvent used.
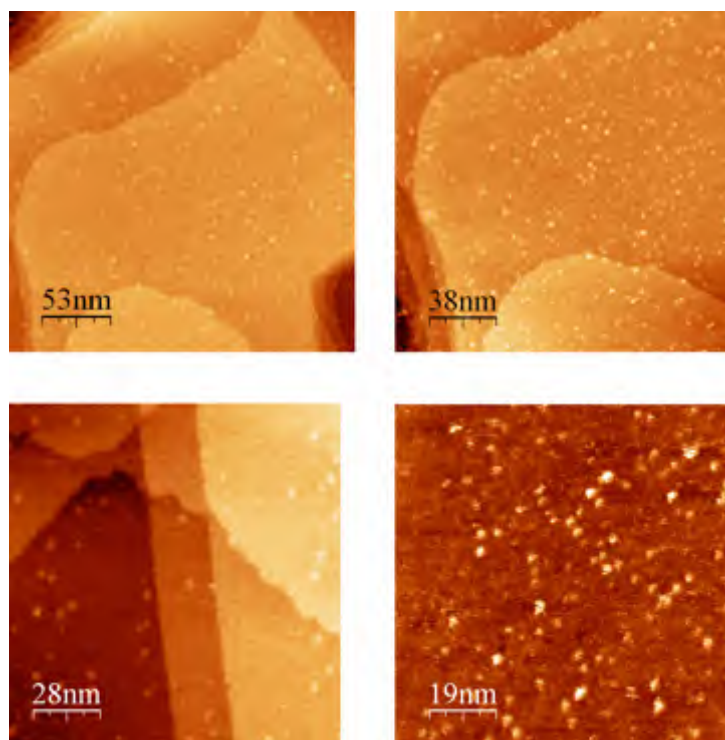
Figure 3.19: STM topography images (tunneling conditions: $U = 0.35$ V, $I = 9$ pA) of a typical **exDCM** adsorbate.

Summary of STM measurements

STM topography scan of Fe4PhPhSMe monolayers on gold gave very similar results to what has been observed for Fe4C9SAc, i.e. the clusters seems to organize on the surface to yield its complete coverage. No particular differences in the morphology of the adsorbates were observed when changing the incuba-

tion solvent, except in the case of dioxane, that gave very diluted, non–ordered sub–monolayers.

3.4.2   XPS Studies

The characterization of Fe4PhPhSMe monolayers by means of photoelectron spectroscopy gave similar results to what was found for Fe4C9SAc layers. Once again, sample preparation was carried out inside a glove bag, that was directly linked to the fast entry chamber of the XPS apparatus. All samples were incubated for 3 hours; in addition, in the case of the **exDCM** system a brief screening of the dependence on incubation time was carried out, by studying also a sample incubated for 45 minutes and one for 20 hours.

Bulk phase Fe4PhPhSMe

The XPS study started from the characterization of a bulk phase of the complex: a drop cast sample on gold was chosen since such systems were found to be more convenient than crystalline samples (see section 3.3.2 for considerations on this topic). Survey and multiplex spectra are shown in Figures 3.20 and 3.21, respectively. In similar way to what has been observed for Fe4C9SAc drop cast systems, no signals of the gold substrate were found, and some charging effects were detected, which were estimated to be around 1 eV, based on the C_{1s} aliphatic carbon signal shift; the spectra shown in Figures 3.20 and 3.21 are not corrected for this effect. No contamination from silicon was found in for Fe4PhPhSMe.
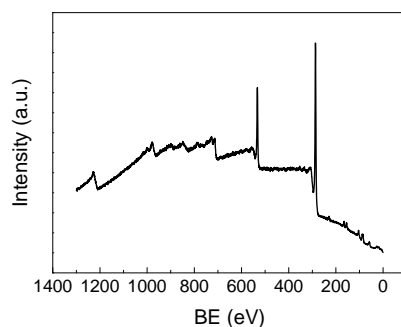
Figure 3.20: XPS survey spectrum of drop cast Fe4PhPhSMe on a Au(111) surface.

Expected atomic percentages for Fe4PhPhSMe were calculated by considering the brute formula $Fe_4C_{96}O_{20}S_2$ and using the values $n_{tot} = 124$, $n_{Fe} = 4$ $n_S = 2$ $n_C = 100$ and $n_O = 18$ in eq. (2.2). Calculated values are reported in
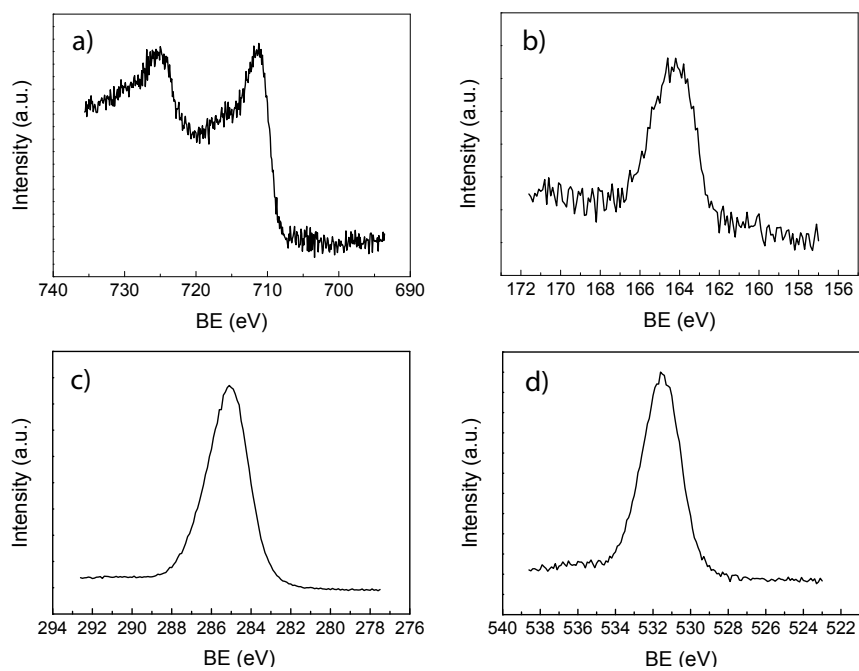
Figure 3.21: Detailed XPS spectra of a) Fe_{2p}, b) S_{2p}, c) C_{1s} and d) O_{1s} peaks carried out on Fe4PhPhSMe drop cast sample.

Table 3.15, along with found values for the drop cast Fe4 system; agreement between theoretical and experimental values is good, notwithstanding a not perfect agreement of the Fe/S ratio, that with a value of 2.5 slightly exceeds the expected ratio of 2:1.

	Fe	S	C	O
%Calculated	3.2	1.6	80.6	14.5
%Drop cast	3.3	1.3	78.8	16.5
BE (eV)	71	16	28	53

Table 3.15: Comparison of expected and found relative elemental abundance in the Fe4PhPhSMe drop cast sample.

Peak deconvolution was carried out on C_{1s} using just components, as sketched in Figure 3.22. Quantitative data extracted from single peak integration gave a ratio between the two carbon types that is inn fair agreement with the expected values (Table 3.16).
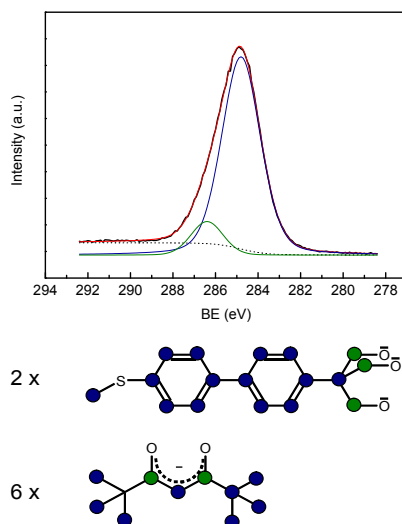
Figure 3.22: Peak deconvolution for C_{1s} of drop cast Fe4PhPhSMe and color-coded scheme of the types of carbon atoms.

Fe4PhPhSMe-exDCM

Survey scan of a **Fe4PhPhSMe-exDCM** monolayer is reported in Figure 3.23; gold photopeaks are the most distinct features, while carbon, oxygen,

BE (eV)	FWHM (eV)	%Calculated	%Found
284.8	2.1	82.0	88.4
286.4	1.8	18.0	11.6

Table 3.16: Component details and relative abundance for the deconvolution of the C_{1s} peak in a Fe4PhPhSMe drop cast sample.

iron and sulphur can be spotted in their distinctive peaks. Detailed scans of the areas containing Fe_{2p}, S_{2p}, C_{1s} and O_{1s} photopeaks are reported in Figure 3.24, where the same spectral areas of the other monolayers are shown as well. No shifts are observed in the binding energies of the peaks studied, in good agreement that no charging effects are to be expected on a monolayer on a conductive surface; all elements gave good signals, and even if sulphur S_{2p} peak is quite weak and broad, reasonable integration could be carried out. Found values are reported in Table 3.17.

If we consider in more detail the BEs of the peaks we studied, we can can notice some differences from the behavior of the Fe4C9SAc monolayers. Let us look at the S_{2p} in the first place: no significant shift can be observed between the BE found for the **Fe4PhPhSMe-exDCM** system and the (corrected) value found for the bulk reference (around 164 eV), while in Fe4C9SAc monolayers a shift of about 1.5 eV could be easily spotted. The fact that no shift is observed in this system indicates that electronic density on the sulphur atom is substantially unvaried upon interaction of the cluster with the gold surface. On the other hand, a significant shift in the BE of the $Au_{4f7/2}$ peak was found to 84.6 eV, indicating a depletion of electron density on the surface of gold, probably related to the Au-S interaction; the same BE or very similar values were found for all Fe4PhPhSMe adsorbates.

As mentioned above, we prepared two variations of this system by changing the incubation times to 20 minutes and 20 hours: no significant spectral differences were found in Fe_{2p} and C_{1s} peaks, while a slight peak shift was seen for the the O_{1s} peak of the short incubation time sample toward high BE. Critical differences are instead present between the S_{2p} peaks: while the short incubation time sample gives a rather weak yet definite signal, the long incubation time sample shows a very broad, that can be seen in Figure 3.25, where S_{2p} spectral areas of the three samples are compared. If we examine the quantitative data found for the 20 hours incubated sample, we find that Fe/S ratio is largely inferior to the expected value of 2, being quite close to one instead (see Table 3.17); this observation, coupled to the irregular shape of the S_{2p} peak itself, suggested us to study the latter more in detail by performing its deconvolution into two components (shown in Figure 3.25), the first at higher BE that is found in all other systems (around 163.5 eV) and the second at lower BE (162 eV) relative to a sulphur atom more negatively charged, such as a sulphide ion.[96] The relative abundance of the two species can be roughly estimated to be 1:1: we can then subtract the contribution of the sulphide from the total

integration value of the S_{2p} peak and re-normalize all atomic percentages with respect to the new value of the sulphur integral: such values are reported in Table 3.17 as corrected values for the 20 hours incubated sample. It can be seen that such values agree nicely with the theoretical percentages, a hint that the deconvolution we carried out was a logical step; nevertheless, this suggests that some decomposition takes place at the solution-gold interface on a time scale of about 20 hours, and some over-reduced sulphur, not bound to the cluster, grafts to the surface in addition to the intact complex. This finding, in addition to the observation that the sample incubated for 20 minutes gave very weak - yet coherent - XPS signals, convinced us that a 3 hour incubation time is the most suitable one for this kind of derivative.
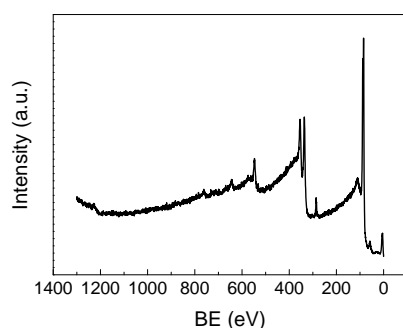
Figure 3.23: XPS survey spectrum of a **Fe4PhPhSMe-exDCM** adsorbate on Au(111).

	Fe	S	C	O
%Calculated	3.2	1.6	80.6	14.5
%**exDCM** 20'	2.5	1.1	78.7	17.7
BE (eV)	71	16	28	53
%**exDCM** 3 h	4.7	2.4	78.5	14.4
BE (eV)	71	16	28	53
%**exDCM** 20 h	5.0	4.3	75.7	15.0
%**exDCM** 20 h (corr.)	5.1	2.2	77.3	15.3
BE (eV)	71	16	28	53

Table 3.17: Comparison of expected and found relative elemental abundance in **Fe4PhPhSMe-exDCM** monolayers on Au(111).

Peak deconvolution was carried out on the 20 hour and 3 hour incubated samples (Figure 3.26), using the same procedure described for drop cast sam-
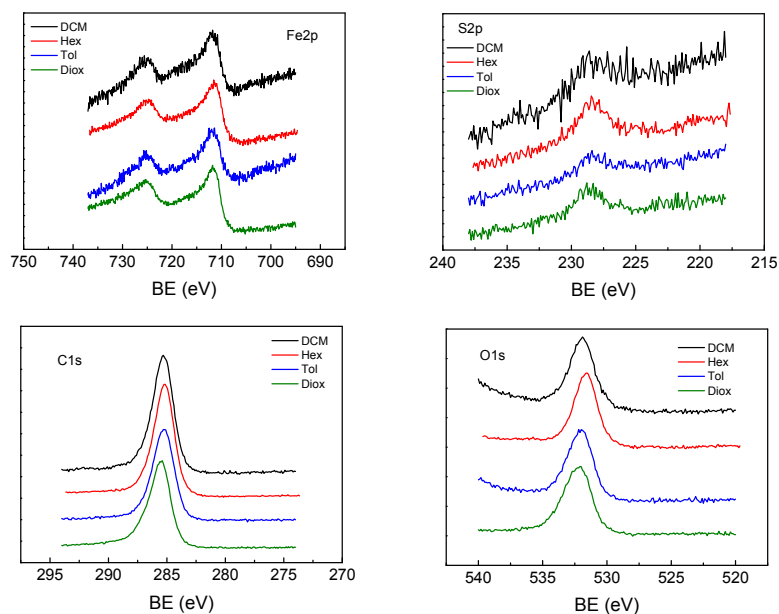
Figure 3.24: Detailed spectra of **exDCM**, **exHex**, **exTol** and **exDiox** mono-
layers of Fe4PhPhSMe on Au(111).
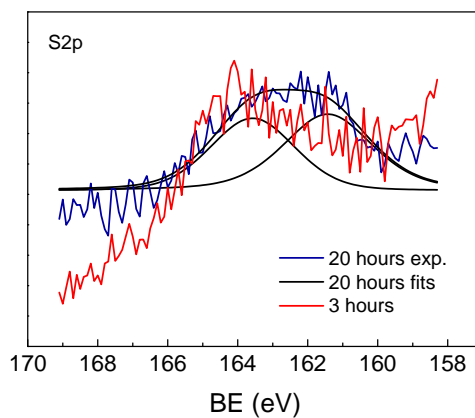
Figure 3.25: Comparison of the S_{2p} photopeaks of **Fe4PhPhSMe-exDCM**
monolayers incubated for 20 minutes, 3 hours and 20 hours respectively. De-
convolution of the latter peak into the complex bound and sulphide components
is shown as well.

ples. Relative abundance of the species is given in Tables 3.19 and 3.18, respectively.
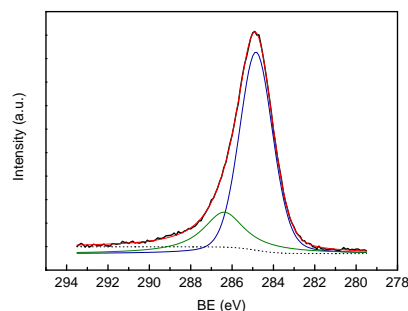
Figure 3.26: Peak deconvolution for C_{1s} of a **Fe4PhPhSMe-exDCM** monolayer (3 h incubation).The color–coding scheme is given in Figure 3.22.

BE (eV)	FWHM (eV)	%Calculated	%Found
284.8	1.9	82.0	73.4
286.4	2.3	18.0	26.6

Table 3.18: Component details and relative abundance for the deconvolution of the C_{1s} peak in a **Fe4PhPhSMe-exDCM** monolayer.

BE (eV)	FWHM (eV)	%Calculated	%Found
284.8	2.0	82.0	82.8
286.5	2.0	18.0	17.2

Table 3.19: Component details and relative abundance for the deconvolution of the C_{1s} peak in a **Fe4PhPhSMe-exDCM** monolayer.

Fe4PhPhSMe-exHex

This type of monolayer gave strong and definite peaks; the survey scan for this system is shown in Figure 3.27. Found BEs are very similar to those of the **exDCM** samples: a slight shift of less than half eV toward high BE was found for the S_{2p} photopeak, that is not significant as that observed for the corresponding Fe4C9SAc adsorbate. Detailed scans of the elements of interest are show in Figure 3.24. The BE of the gold peak is the same as that found for the **exDCM** systems.

Relative atomic abundance is reported in Table 3.20: while Fe/S ratio, which is the most important indicator of the integrity of the cluster is good
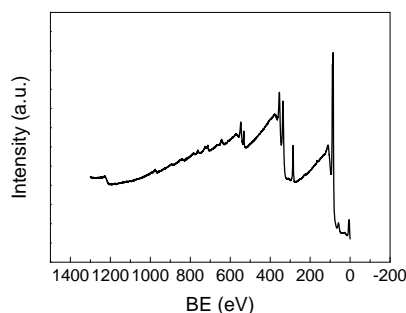
Figure 3.27: XPS survey spectrum of a **Fe4PhPhSMe-exHex** adsorbate on Au(111).

(2.4), carbon is once again in slight defect, as it has been observed for **Fe4PhPhSMe-exDCM** samples and all Fe4C9SAc monolayers.

	Fe	S	C	O
%Calculated	3.2	1.6	80.6	14.5
%exHex	5.2	2.2	77.6	14.7
BE (eV)	71	16	28	53

Table 3.20: Comparison of expected and found relative elemental abundance in **Fe4PhPhSMe-exHex** monolayers on Au(111).

Fe4PhPhSMe-exTol

The relatively weak signals detected for the **exTol** adsorbate are shown in Figures 3.28 (survey scan) and 3.24 (multiplex). Quantitative information is given in Table 3.21: as can be seen found values are in very good agreement with the expected ones.

	Fe	S	C	O
%Calculated	3.2	1.6	80.6	14.5
%exTol	3.7	2.0	79.5	14.8
BE (eV)	71	16	28	53

Table 3.21: Comparison of expected and found relative elemental abundance in **Fe4PhPhSMe-exTol** monolayers on Au(111).
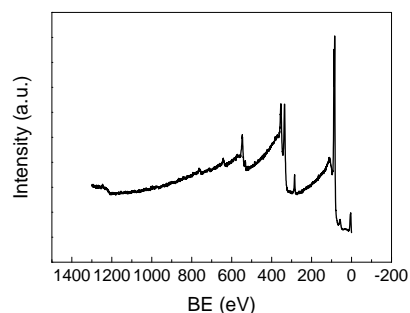
Figure 3.28: XPS survey spectrum of a **Fe4PhPhSMe-exTol** adsorbate on Au(111).

Fe4PhPhSMe-exDiox

In the previous section, we showed that dioxane solutions of the complex have the remarkable property of yielding low coverage of the gold surface upon incubation. XPS confirmed the presence of the complex on the surface; survey scan is shown in Figure 3.29 and detailed spectra are given in Figure 3.24, along with those of all other systems. Relative atomic abundance (Table 3.22) is in rather good agreement with the expected values for Fe4PhPhSMe, Fe/S ratio being 2.5 and oxygen being in slight excess.
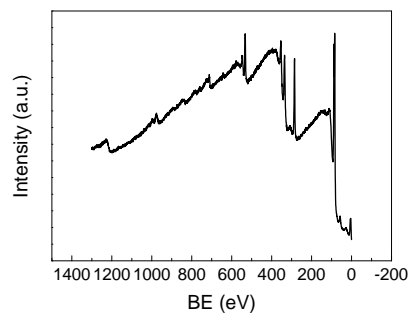
Figure 3.29: XPS survey spectrum of a **Fe4PhPhSMe-exDiox** adsorbate on Au(111).

Summary of XPS measurements

All samples gave well resolved peaks, and quantitative analysis gave results that were generally in good agreement with the expected values. In particular, a sys-

	Fe	S	C	O
%Calculated	3.2	1.6	80.6	14.5
%**exDiox**	3.6	2.3	73.4	20.7
BE (eV)	71	16	28	53

Table 3.22: Comparison of expected and found relative elemental abundance in **Fe4PhPhSMe-exDiox** monolayers on Au(111).

tematic slight excess of oxygen was found in all samples, the most pronounced case being the **exDiox** system for which, on the other hand, integration is expected to be least trustworthy since STM suggests a low coverage of the surface by Fe4 units. Time evolution during incubation was briefly studied for the **exDCM** system, which resulted in very weak peaks for the short incubation (20 minutes) sample, while the long incubation one (20 hours) strong gave peak broadening in the S_{2p} photopeak, which was deconvoluted and interpreted to contain a strongly negative species not contained in the cluster in addition to the cluster-related sulphur. We then decided to use an intermediate incubation time of 3 hours for all depositions.

An interesting shift toward high BEs was observed for the $Au_{4f7/2}$ peak of the substrate, probably due to sulphur-gold interaction that decreases electronic density on the superficial gold atoms. Such an effect was not found for Fe4C9SAc adsorbates.

On the other hand, the shift of the S_{2p} maximum toward low BE in all adsorbates with respect to the normalized bulk sample that was observed for Fe4C9SAc was not found in the case of Fe4PhPhSMe. This could either indicate a different Au-S interaction in the two cases (also considering the different BEs of the gold peaks) or could simply be due to a better conductivity of the highly conjugated Fe4PhPhSMe complex with respect to the aliphatic Fe4C9SAc, that could help the non-bound second sulphur atom of each molecule to establish more efficient grounding to the gold substrate.

3.4.3   ToF-SIMS Studies

All spectra were acquired in the same conditions as described in the previous section for FeC9SAc. Coherently with STM and XPS experiments, data acquisition for monolayer samples as carried out on the 3 hour–incubated series. Signals were very weak and badly resolved, so we limited the discussion to the molecular peak, without attempting further assignments. For this reason, a single paragraph groups all four experiments on monolayers.

Bulk phase Fe4PhPhSMe

Drop cast gave a rather strong molecular peak centered at 1925.9 m/z in the negative ions (Figure 3.30).

Fe4PhPhSMe Monolayers

Despite the weakness of the signals, some peaks related or closely related to the molecular peak could be spotted for each sample. As can be seen in Figure 3.30 the molecular peak with no modifications can only be seen in the **exTol** monolayer, while for all other systems a modified peak at around 1958 m/z is visible, that can be ascribed to a species of the type $[M+SH_2]^-$ or $[M+O_2H_2]^-$. In the **exDiox** system such peak is extremely weak, but a reasonable signal can be seen in the the positive ions (Figure 3.30) that corresponds to the [M-$2dpm]^+$. such peak is present in all spectra. The extreme weakness of the signal for the **exDiox** sample is coherent with the qualitative information given by STM measurements.

From this set of ToF–SIMS experiments we can conclude in agreement with the other techniques used that Fe4PhPhSMe can be successfully grafted to Au(111) surfaces.
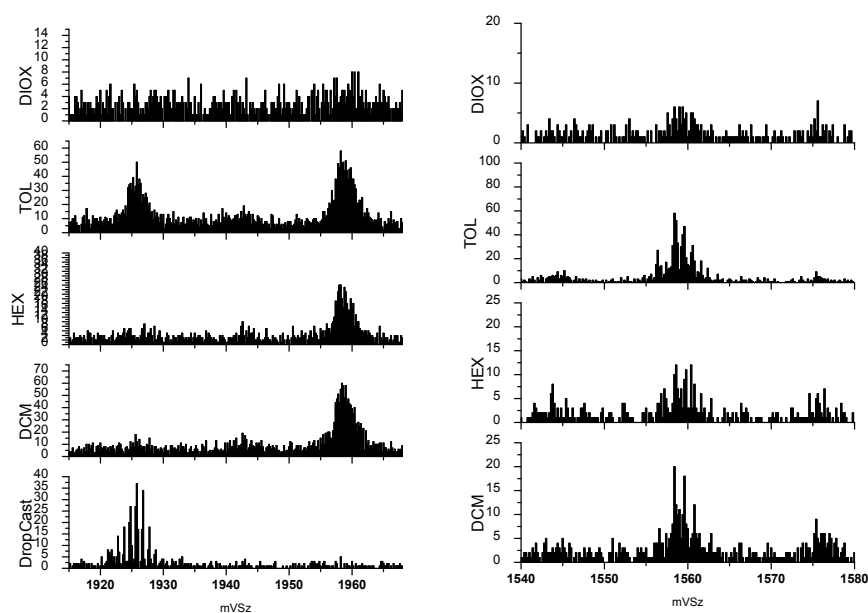
Figure 3.30: Negative (left) and positive (right) ions ToF–SIMS spectra of Fe4PhPhSMe.

Chapter 4

Magnetic circular dichroism on SMMs

4.1   The quest for ultra-sensitive magnetic probes

Monolayers of Mn12 derivatives have been known for a few years and, as the first part of this thesis shows, their characterization from the point of view of standard surface science has been carried out rather thoroughly. Nevertheless, a significant gap in the elucidation of the properties of a magnetic molecule has always been the impossibility of obtaining any kind of hint on the magnetic properties of its adsorbates. In fact, notwithstanding the great advances in sensitivity of SQUID detection, standard magnetometry is incapable of picking up the signal of such a small ensemble of molecules; the picture is worsened by the fact that, at such degree of dilution, the diamagnetic contribution of the gold substrate, as well as paramagnetic signals from impurities become preponderant.

A good candidate for this kind of studies would be EPR: if not able to give direct information on magnetization dynamics in fact, EPR spectroscopy is in principle both an excellent technique to gain information on the spin structure of magnetic complexes[23] and an extremely sensitive spin probe. For instance, it is possible to detect EPR signals from a monolayer of thiol-functionalized nitronyl nitroxide radicals grafted to gold, as recently shown.[97] Unfortunately, one of the key features of single molecule magnets is the large spin ground state (for instance the Mn12 family has $S = 10$, and Fe4 complexes $S = 5$), which is associated with a large magnetic anisotropy that spreads the resonances over a wide field range. This reduces the sensitivity of the technique, which is expressed in number of spins per unit of field. Moreover the large anisotropy requires, for a full characterization, the use of unconventional high-field/high-frequency EPR, spectrometer that often do not work with a resonant cavity, so this type of measurement is very challenging and very sensitive to param-

agnetic impurities, which are likely to give huge sharp signals with respect to the signal from Fe4.

We now consider a completely different approach, that is to say scanning probe microscopy. Mainly four scanning probe techniques are able to give information on the magnetic properties of the scanned surface, namely MFM, SP-STM, SHPM and ESN-STM: without going into details, we will just mention that the two most promising techniques among these are, in our opinion, SHPM and SP-STM. Unluckily a series of technical difficulties make these kind of studies very difficult on SMMs; nonetheless these techniques, SP-STM in particular, are definitely the top candidates for the study of SMMs grafted to surface, since they allow to probe a very limited ensemble of molecules (even a single molecule in the case of SP-STM).

Of all magnetism–related techniques, the spectroscopic ones based on dichroism (Magnetic Circular Dichroism, MCD and X-ray Magnetic Circular Dichroism, XMCD) seemed to us the most appealing, due to their extreme sensitivity and, in the case of XMCD, element selectivity. As we will show in detail in Chapter 5, we finally succeeded in addressing the magnetic properties of a single layer of magnetic molecules by means of a synchrotron radiation technique taken to its extreme capabilities, namely XMCD at very low temperature.

On the other hand, MCD experiments were the first ones to give some information on the magnetic properties on the monolayers of SMMs, information that was later confirmed by XMCD. While MCD studies might seem a little debased by the latter large–scale facility experiments, such laboratory scale measurements were fundamental in the understanding of the behavior of Mn12 and Fe4 magnets in non-crystalline environments.

4.2   The principles of magnetic circular dichroism

The interaction between light and matter is traditionally described with the aid of a phenomenological model, namely the refractive index. In general, this index is dependent on the frequency and the polarization of the electromagnetic (EM) wave. In the case of frequency dependence, refractive index varies in such a way that near resonant frequencies it must be described as a complex dimensionless quantity:[98,99]

$$n(\omega) = 1 - \delta(\omega) + \mathrm{i}\beta(\omega), \tag{4.1}$$

in which the real part $\delta(\omega)$ is related to the refraction of the EM wave, while the imaginary part $\beta(\omega)$ is associated with absorption by the medium.

Let us now consider the polarization dependence of the refractive index: this is called *birefringence*, that falls into the two categories of linear and circular birefringence, depending on the polarization of the incident light. The term

refringence, later replaced with *refraction*, shares with the latter its Latin origin from the verb *frangere*, meaning to break. The polarization dependence of the absorptive part $\beta(\omega)$ is termed *dichroism*.

This effect owes its name to the property of certain crystals that may appear in two different colors, or dichroic, when white light is incident along two different directions. This is due to differences in absorption of polarization components and frequencies along different directions.

Optical effects may be included into four main areas:

- **Birefringence** The phenomenon of the simultaneous presence of two indices of refraction for polarized incident light. Linear and circular birefringence may exist.

- **Dichroism** The dependence of photon absorption on polarization. Dichroism can originate from interaction of the polarized photons with charge distribution only (natural linear dichroism and natural circular dichroism) or of spin distribution as well (Magnetic linear dichroism and magnetic circular dichroism).

- **Optical activity** The rotation of the polarization plane by a non-magnetic material. Optical activity is typically associated with chirality, or handedness of the charge distribution in space.

- **Magneto-optical rotation** The rotation of the linear polarization direction by a magnetic sample. It arises from the presence of aligned magnetic moments, which give the sample a handedness in time through breaking of time-reversal symmetry.

Modern theory approaches the interaction of polarized light with matter using an approach based on time-dependent perturbation theory and the quantum mechanical operator and matrix element method; in this framework, the interaction of polarized photons with matter listed above can be cast in terms of a scattering problem. The final formalism has a close resemblance with the classical approach based on the refractive index since scattering is expressed in terms of a complex atomic scattering factor:

$$F(\boldsymbol{Q},\omega) = F^0(\boldsymbol{Q}) + F'(\omega) - \mathrm{i}F''(\omega), \tag{4.2}$$

where $\boldsymbol{Q}$ is the momentum transfer of the scattering process ad $F^0(\boldsymbol{Q})$ the atomic form factor. All factors, $F^0(\boldsymbol{Q})$, $F^0(\omega)$ and $F''(\omega)$ are real numbers in units of electrons per atom. Equation (4.2) can then be developed in different ways, according to the wavelength range involved in the experiment (i.e visible, infra-red, x-ray).

The aim of this section is to give a brief introduction to the theoretical background underlying the Faraday effect (Faraday geometry is sketched in

Figure 4.1) and the related Magnetic Circular Dichroism (MCD). We shall not
cover the details of the classical, or phenomenological approach to this effect, if
not to mention that in the classical framework it is related to a decrease in the
symmetry of the dielectric tensor $\vec{\varepsilon}$ of the medium in which the EM travels when
a magnetization $\boldsymbol{M}$ is present. In this case the tensor elements $\varepsilon_{i,j}$ become
dependent on $\boldsymbol{M}$, so also the complex refractive index n does. This can be
decomposed into the refractive indexes n_+ and n_-, related to the propagation
speeds of the two circularly polarized components of light. The interaction of
polarized light with a magnetized medium finally is related to changes in these
two refractive indexes both in their real and imaginary parts:[100]

$$\theta_F = \frac{\omega l}{2c} \mathrm{Re}(n_+ - n_-) \tag{4.3}$$

$$\eta_F = -\frac{\omega l}{2c} \mathrm{Im}(n_+ - n_-), \tag{4.4}$$

l being the path length of the EM wave in the magnetic medium. The phys-
ical content of (4.3) is related to the polarization dependence on magnetization
of the the EM wave: for instance, if the incoming wave had linear polariza-
tion, the outgoing wave still has linear polarization, but its plane is rotated of
an angle θ_F (the so-called *Faraday rotation*) with respect to the plane of the
incoming wave. The second term, described in (4.4), is instead linked to the
absorptive part of the complex refraction index; it indicates that the two com-
ponents of opposite circular polarization, that are attenuated differently, thus
having different amplitudes in the outbound EM wave, give rise to an elliptic-
ity η_F. The ellipticity corresponds to the ratio of the minor to the major axes
of the polarization ellipsoid, and is related to the magnetic circular dichroism
which is defined by the difference of the absorption coefficient μ between the
right and left circularly polarized light:

$$\Delta\mu(\omega) = \mu_+(\omega) - \mu_-(\omega) = -\frac{4\eta_F(\omega)}{l}. \tag{4.5}$$

Magnetic circular dichroism in the UV-visible range is capable of achiev-
ing better resolution than the simple absorption spectrum; in fact, being a
signed quantity, it can partially resolve overlapping absorption bands. In ad-
dition it is able to simultaneously provide information on both the ground
and excited states of the system, thus bridging EPR, which primarily probes
the electronic ground state, and absorption or resonance Raman spectroscopy,
which primarily probe electronically excited states. Moreover, MCD is able to
show orientational selectivity even for frozen solution or disordered ensembles
of molecules. Due to the sensitivity of the MCD intensity to the transition
polarizations, only a subset of randomly oriented molecules will contribute to
a given MCD signal.
The theory of MCD spectroscopy, pioneered by Stephens,[101,102] is treated to
various degrees of completeness also by Piepho and Schatz,[103] Mason[104] and
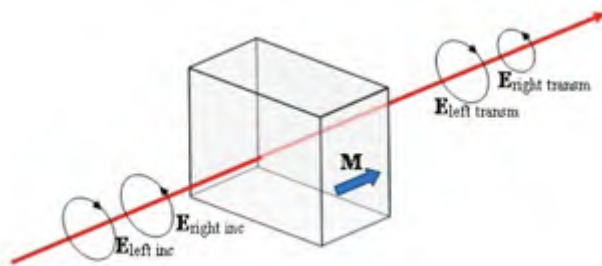
Figure 4.1: Scheme of the Faraday geometry, with the wave propagation vector parallel to the magnetization.

Solomon and Neese;[105] here, we shall only give a basic introduction to the concepts of MCD using a quantum mechanical approach.

A MCD spectrum is the difference in absorption between left- and right-circularly polarized light induced in a sample by a net magnetic moment oriented parallel to the direction of light propagation. The difference in absorption is given by $\Delta\alpha = \alpha_- - \alpha_+$ and is the result of the combined effect of the lower symmetry induced in the material by a non-zero magnetization and the spin-orbit coupling.

Being based on optical absorption, the effect obeys Beer-Lambert law $I(l) = I_0 e^{-kd}$, where k is the absorption coefficient (that depends on the molar concentration of the absorbing species) and l is the length of the optical path through the absorbing medium. In addition, the intensity of the MCD effect, in terms of $\Delta\alpha$, is proportional to the applied magnetic field:

$$\Delta\alpha \propto \Delta\varepsilon_M cd\boldsymbol{B}, \tag{4.6}$$

where c indicates the molar concentration of absorbers and $\Delta\varepsilon_M$ is the differential molar absorptivity per unit of applied field. In the domain where the MCD is a linear function of the applied magnetic field, the signal for an ensemble of randomly oriented molecules is given by:

$$\frac{\Delta\varepsilon}{E} = \frac{\varepsilon_- - \varepsilon_+}{E} = \frac{1}{lc}\frac{\alpha_- - \alpha_+}{E} == \gamma\mu_B B\left[\left(-\frac{\partial f(E)}{\partial E}\right)\overline{A}_1 + \left(\overline{B}_0 + \frac{\overline{C}_0}{kT}\right)f(E)\right],$$
$$\tag{4.7}$$

where γ is a collection of constants,[105] μ_B is the Bohr magneton, k is the Boltzmann constant, T is the temperature, B is the magnetic flux density, $f(E)$ is a line shape function, l is the path length through the medium, c is the concentration of absorbers and $E = \hbar\omega$ is the energy of the incident radiation. $\overline{A}_1$, $\overline{B}_0$ and $\overline{C}_0$ are called *MCD-terms* and are characteristic numbers that depend on the electronic and geometric structure of the molecule under investigation. In particular, while $\overline{A}_1$ and $\overline{B}_0$ also exist in molecules with a

spin-singlet ground state ($\overline{A}_1$ is present only in case the molecule has orbital degeneracy), $\overline{C}_0$ is present only in paramagnetic molecules. For paramagnetic transition metal complexes at very low temperatures (which is the case of our investigation) the temperature-dependent $\overline{C}_0$ term (C-term in the following) dominates the spectrum. In this regime the relation between MCD intensity and applied field is not linear if not for very small values of B, since saturation is reached for high B/T ratios.

Each of the three of the three MCD terms can be associated directly to a physical meaning:[104]

- **The A-term** $\overline{A}_1$ describes a derivative-shaped band and is present only if the energy levels of the system have degeneracies that can be lifted by the Zeeman effect.

- **The B-term** $\overline{B}_0$ arises as a result of field-induced mixing of the zero-field wavefunctions.

- **The C-term** $\overline{C}_0$ is the result of electronic transitions within a degenerate ground state whose levels are differently populated upon the application of a magnetic field.

We will now derive an expression of the MCD intensity as a function of temperature and applied field, starting from the *Fermi's Golden Rule* applied to the valence band electronic transitions[a], assuming a pure electric dipole mechanism for the transitions from an initial quantum state $|a\rangle$ with Boltzmann population N_a to a final quantum state $|j\rangle$ with Boltzmann population N_j. The Franck-Condon and the Born-Oppenheimer principles are used, and $\Delta\epsilon/E$ is given by:

$$\frac{\Delta\varepsilon}{E} = K\sum_{aj}(N_a - N_j)[|\langle a|m_-|j\rangle|^2 - |\langle a|m_+|j\rangle|^2]f(E) \qquad (4.8)$$

where m_- and m_+ are the transition dipole moment operators for left- and right- circularly polarized in a laboratory fixed reference coordinate system, and $f(E)$ is the density of states function, which is taken to be invariant with the applied field assumed. The initial N_j population, corresponding to the excited electronic states of the system, is assumed to be zero. The wavefunctions used to describe the system are taken with a molecule's fixed coordinate system (the calculation is then averaged over all possible orientations of the molecule) and they treat all quantum numbers together in the element α, while the spin quantum number S_α is treated separately; the form of the wavefunction is thus: $|\alpha S_\alpha M\rangle_0$, M being projection of the spin state S_α on the z-axis. Spin-orbit coupling is treated as a first-order perturbation, and in the one-electron approximation its operator is described by:

---

[a]See Section 5.1 for a similar approach on core to valence band transitions applied to x-ray absorption spectroscopy and for a more precise definition of the *Fermi's Golden Rule*.

$$H_{SO} = \sum_{Nj} \xi(r_{iN}) \vec{l}_N(i) \vec{s}(i) = \sum_{m=0,\pm 1} (-1)^m \sum_i h_{-m}(i) s_m(i) \qquad (4.9)$$

where $\vec{l}_N(i)$ is the orbital momentum of the i-th electron of the nucleus N, $\vec{s}(i)$ is the spin angular momentum operator for electron i and $h_{-m}(i)$ is a standard component of the reduced spin-orbit vector operator; the transition moments between the perturbed states are evaluated though the electric dipole operator:

$$\vec{m} = \sum_N Z_N \vec{R}_N - \sum_i \vec{r}_i, \qquad (4.10)$$

expressed in atomic units, with Z_N indicating the charge and position of the N-th nucleus respectively, and $\vec{r}_i$ indicating the position of the i-th electron. The applied magnetic field modifies the wavefunctions $|\alpha S_\alpha M\rangle_0$ of the system; such modifications can be summarized as follows:

1. The M components of the wavefunctions relative to the initial and final states, $|ASM\rangle$ and $|JSM\rangle$ respectively, are mixed.

2. The relative energies of the ground state sublevels change.

3. As a consequence of 2, Boltzmann populations N_a of the states change as well.

From here, we can make some approximations that let us neglect A-term and B-term from the dipole transition between $|a\rangle$ and $|j\rangle$ electronic states: we shall not consider transitions between Zeeman split sublevels, thus eliminating the A-term contribution, and we will consider only mixing between initial state components, so out of state B-terms are neglected. In addition, we shall not contemplate zero field splitting in the excited state $|JSM_i\rangle$.

We can now use these approximations, consider the spin-orbit coupling and switch from the molecule to the laboratory reference frame in eq. (4.8); after the perturbative expansions for the matrix elements $\langle ASM|\vec{m}|JSM''\rangle$ and some rearranging we obtain three terms that contribute to the MCD, each one depending on the spin-orbit coupling between different sets of levels:

$$\frac{\Delta\varepsilon^{(1)}}{E} = \frac{\gamma}{S} \vec{l}(\vec{D}^{AJ} \times \Delta\vec{D}^{JA}) \Delta_{JA}^{-1} \sum_i \frac{e^{-E_i^{(A)}/kT}}{Z} (\overline{L}_{AJ}^x \langle S_x \rangle_i + \overline{L}_{AJ}^y \langle S_y \rangle_i + \overline{L}_{AJ}^z \langle S_z \rangle_i)$$

$$\frac{\Delta\varepsilon^{(2)}}{E} = \frac{\gamma}{S} \sum_{K \neq A,J} \vec{l}(\vec{D}^{KA} \times \vec{D}^{AJ}) \Delta_{KJ}^{-1} \sum_i \frac{e^{-E_i^{(A)}/kT}}{Z} (\overline{L}_{KJ}^x \langle S_x \rangle_i + \overline{L}_{KJ}^y \langle S_y \rangle_i + \overline{L}_{KJ}^z \langle S_z \rangle_i)$$

$$\frac{\Delta\varepsilon^{(3)}}{E} = \frac{\gamma}{S} \sum_{K \neq A,J} \vec{l}(\vec{D}^{AJ} \times \vec{D}^{JK}) \Delta_{KA}^{-1} \sum_i \frac{e^{-E_i^{(A)}/kT}}{Z} (\overline{L}_{KA}^x \langle S_x \rangle_i + \overline{L}_{KA}^y \langle S_y \rangle_i + \overline{L}_{KA}^z \langle S_z \rangle_i).$$

$$(4.11)$$

Apart from the morass of symbols, these three equations express sign and
magnitude of the MCD transition between the initial (A) and final (J) states
as a function of temperature, applied field and orientation, as we demanded;
temperature dependence is explicit in the Boltzmann population distribution,
the orientation dependence arises from $\vec{l}$ and the dependence on the applied
field is described by spin expectation values $\langle\vec{S}\rangle_i$. As can be seen, equations
(4.11) also indicate that no MCD effect is to be expected in the absence of
spin-orbit coupling.

Finally, to model an orientation averaged measurement of the MCD spectrum,
or of a MCD *vs H* curve, it is necessary to integrate over all orientations of the
field, according to:

$$MCD_{av}(E) = \frac{1}{4\pi} \int_0^\pi \int_0^{2\pi} \frac{\Delta\varepsilon^{(1)} + \Delta\varepsilon^{(2)} + \Delta\varepsilon^{(3)}}{E} \sin\theta d\theta d\phi. \qquad (4.12)$$

We now have the theoretical instruments to profitably use the MCD signal
as a sensitive probe of the magnetic properties of our systems.

4.3   The experimental setup

The MCD setup used during this thesis work is a home-made setup developed
by Dr. Lucia Cavigli and Dr. Lapo Bogani.[106–108] During the time the experi-
ments described in this chapter were carried out, the instrument was operated
by two members of our group, Dr. César De Julian Fernandez and Rafael
Leonardo Novak.

The instrument can work in MCD and MOKE (Magneto-optical Kerr Effect)
modes, is equipped with a superconducting magnet that can sweep the field
between ± 100 kOe, is capable of cooling the sample down to 1.5 K and works
with discrete wavelengths obtained from laser sources. In the following sections
we shall describe briefly the parts of the setup.

4.3.1   Light sources

For the sake of simplicity, the instrument was developed using discrete sources
(i.e. lasers); this approach has the advantages of not needing any wavelength
dispersive unit and yielding intense, quasi-monochromatic light. On the other
hand, it is not possible to acquire a full MCD spectrum, and only variations of
the MCD signal at a fixed wavelength can be monitored as a function of another
parameter (temperature or applied field, for instance). Different lasers are
employed, covering a wide range of wavelengths. We use a stabilized Helium-
Neon (He:Ne) laser for measurements at 632.8 nm. This is also our first choice
light source, as it is the most stable available and yields the best signal-to-
noise ratios. For wavelengths in the blue-green region of the spectrum we
use an Argon ion (Ar:ion) laser rated at 5W. The lines are separated by an

external prism, thus yielding light with 476.5 nm, 488 nm, 496.5 nm and 514 nm wavelength and with powers at the order of 100mW with a rather high background noise. Finally, several laser diodes were employed, working at the following wavelengths: 405 nm, 534 nm, 658 nm, 690 nm, 785 nm and 904 nm. Diodes have a good signal to noise ratio and were used extensively.

4.3.2   Superconducting magnet cryostat

The cryostat of the setup is a Oxford Spectromag® SM4000-11.5; it is equipped with windows that allow optical access to the sample. The superconducting magnet is a split coil type, that produces horizontal magnetic fields up to 100 kOe (115 kOe if the lambda refrigerator is used) with field sweep rates up to 1Tesla/minute. Figure 4.2 shows a photograph of the cryostat. The windows are made of synthetic vitreous silica (SPECTROSIL B) that is not birefringent. This fact, together with the strain-relieved low temperature mounts on which they are glued, assures that they will not affect polarized light. The geometry allows for light propagating both parallel and perpendicularly to the magnetic field direction.

The temperature in the sample zone is controlled by a variable temperature insert (VTI) between 1.5 and 300 K. Cooling is obtained with a helium flux between the VTI and the helium bath, controlled by a needle valve and a pump, while gas temperature is regulated by an electric heater.

The arrangement of the windows allows measurements to be made in both Faraday/MCD (transmitted beam) and MOKE (reflected beam) configurations.

The sample holder rod is a long thin-walled tube made of non-magnetic stainless steel ending with a copper cylinder containing a heater, a temperature sensor, and a calibrated Hall probe. Samples are mounted on thin teflon slab at the end of the rod. These slabs are perforated and can hold up to 7 samples.

The Hall probe is used in order to precisely determine the magnetic field intensity in the sample space during MOKE/MCD versus applied field measurements (sensitivity > 10mV/T with a bias current of 100 mA). The estimated error of these magnetic field measurements is lower than 0.5%.

4.3.3   Light polarization and acquisition setup

In order to obtain a MCD spectrum one should acquire two spectra with opposite polarizations and their subtraction. In practice however, to maximize the signal to noise ratio and increase the sensitivity, the system uses a polarization modulation technique obtained by means of a photoelastic modulator (PEM) linked to lock-in detection[109]

The PEM is a device that behaves like a variable retardation waveplate that modulates the beam's polarization periodically at a frequency of 50 kHz, with an adjustable degree of polarization. The device is a rectangular bar of fused silica that oscillates in resonance with a quartz piezoelectric element that is
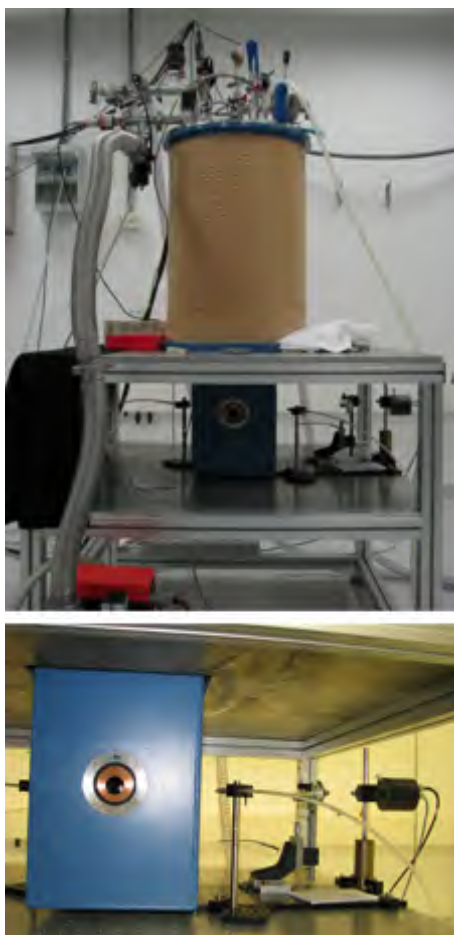
Figure 4.2: The superconducting magnet cryostat (upper picture) and a detail of the optical windows and the photodiode detector (lower picture).

attached to one side of the bar. The deformation leads to birefringence to give what is called *photoelastic effect*. This birefringence induces a time-dependent phase shift $\delta = A_0 sin(2\pi ft)$ between the polarization components of the incoming light beam that are parallel and perpendicular to the PEM optical axis. Adjusting the peak retardation magnitude A_0, the operator can then choose different peak polarization states for the resulting beam. For example, in order to obtain an output beam whose polarization state oscillates between right and left-circularly polarized, we must set the PEM for quarter-wave retardation (for a particular wavelength) and the incoming beam must be linearly polarized in a plane forming an angle of $45°$ with the optical axis of the PEM.

The detector is a silicon photodiode (Hinds Instruments Model DET-100-001) with 5 mm^2 active area, 1 ns rise time, DC - 500kHz frequency response and a spectral range between 350 and 950 nm. The detector is connected to a signal conditioning unit, that amplifies the signal, and separates it into a DC component proportional to the average intensity of the transmitted light beam, and into an AC component at the same frequency of the polarization modulation. The DC component is measured by a digital multimeter and the AC by a lock-in amplifier (with reference signal provided by the PEM control electronics). The MCD setup as it has been described above is shown in Figure 4.3.
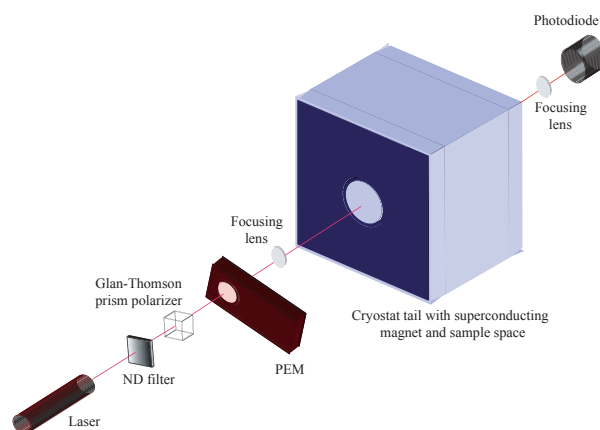
Figure 4.3: Scheme of the MCD setup.

4.4   Bulk measurements

Our study of SMMs with MCD has two main aims: the first one is to get a deep insight of the correlations between the magnetic and the magneto-optical properties of our systems, while the second is to use the high sensitivity of the system to retrieve information on the magnetic properties of samples where only

few molecules are present, such as the monolayers we have been describing in the previous chapters. In this thesis work, I have focused on the second point, in line with the scope of the whole work I have been carrying out. A more detailed dissertation on the first point (as well as on the second) can be found in R.L. Novak's PhD thesis,[110] with whom I have been collaborating in Florence and who has dedicated his thesis work to the study of MCD and to the development of the machine.

In this section we shall cover studies on what can be considered as *bulk* samples: measurements in the Faraday mode of course require that the inspected sample is transparent to the probing light. In order to comply with this requirement, Mn12 and Fe4 clusters need to be removed from the crystalline environment of a typical powder sample and be dispersed in a non-absorbing matrix, such as a siloxanic resin or a dissolvable polymer. The properties of such matrices are very important since they must interact with the molecules.

We shall now introduce the basic features and preparation methods of the samples, both for siloxanic resins and dissolvable polymers.

4.4.1 Preparation of the samples

All matrix-dispersed cluster samples were prepared by adding a solution of the SMM to the matrix before solidification; after solvent evaporation and/or solidification, the sample can be regarded as a solid solution of the cluster in the matrix.

When preparing such solid solutions, one must bear in mind a few points, namely i) that the matrix should be chemically inert with respect to the dissolved molecule, but ii) it should be able to easily dissolve it at least at the concentrations used, in order to prevent agglomeration that would be detrimental of the optical properties of the sample and iii) that the surface of the sample is as regular as possible, in order to minimize superficial scattering of the probe light.

PDMS The siloxanic elastomer used in this work was purchased from Dow Corning (Sylgard 184 Silicone Elastomer) is a two-component resin consisting of a base and a curing agent acting as a cross linker to be mixed in a 10:1 proportion. The base is poly(dimethylsiloxane), a polymer made basically of linear -O-Si-O- chains in which the two remaining positions on the silicon atom are occupied by methyl groups; it is a highly viscous liquid; thickening to a rubber-like solid is achieved by partial cross-linking induced by the curing agent. The resulting composite can be casted into a proper container and reaches its final texture after 24 hours at room temperature (yet the microscopic structure evolves for about 7 days; shorter curing times are necessary if heat is applied) to give a rubber-like object that has good mechanical properties and can easily be cut into the correct size to be mounted on the sample holder. The curing process has no effect on the volume of the material, that is not varied to any extent.

PMDS samples obtained just by mixing the base and the curing agents were casted into a small Petri dish (ø ≃ 5 cm) and were allowed to solidify; samples prepared in this way are air bubble-free, since air included in the highly viscous mixture is free to migrate to the surface within the first hour after casting; typical thickness of the sample is around 5 mm. For what concerns the optical quality of the two surfaces, the one in contact with the glass of the Petri dish is perfectly smooth, and the one in contact with air is of very good quality as well. The size of the Petri dish is quite important, since for smaller diameters the meniscus of the composite is too close to the center of the sample, thus causing the upper surface to be curved: this is detrimental to the optical quality of the samples, that would show an undesired 'lens effect' on propagating light.

These were then used as blank reference samples for all measurements: in particular they were characterized by means of UV-visible spectroscopy and VSM magnetometry.

The optical absorption spectrum, shown in Figure 4.4, shown practically no transition up to 350 nm, coherently with the observation that the sample is completely transparent. Magnetometric measurements, instead showed that traces of paramagnetic species are present, as can be seen in the magnetization curve shown in Figure 4.5 where a positive value of M is recorded for fields up to ~ 1 T. In addition to this, blank samples were used also in MCD experiments to measure the background signal.
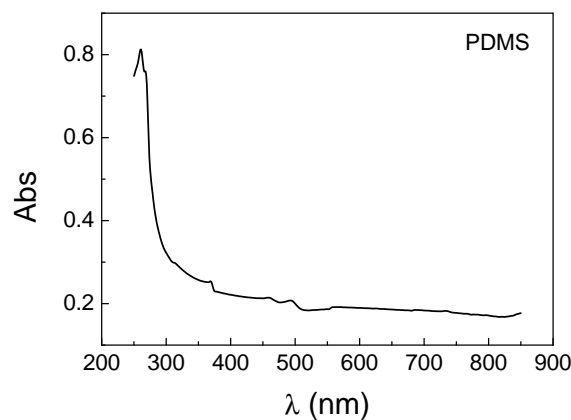
Figure 4.4: UV-Visible absorption spectrum of a blank PDMS sample.

In order to prepare Mn12 and Fe4 samples in PDMS, we dissolved the desired cluster in a small amount of dichloromethane and added this concentrated solution to the elastomer a few minutes after the curing agent was added to the base. The presence of the solvent is kept as low as possible in the mixture so as
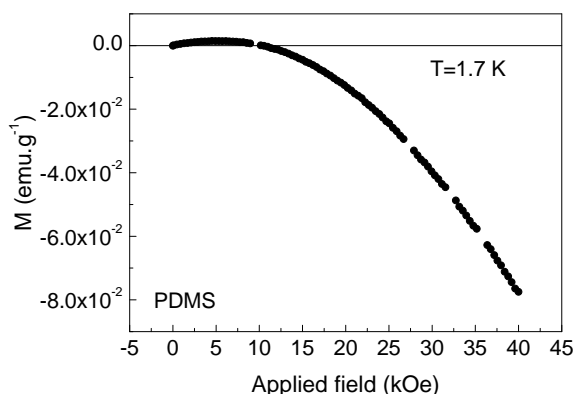
Figure 4.5: Magnetization curve of a blank PDMS sample.

to have quicker completion of its evaporation and to minimize its interference with the curing process. The final concentration of the cluster in PDMS in then calculated as a molarity, in which the elastomer is considered to be the solvent. In the amorphous 3D host matrix the clusters are randomly oriented and far from each other so that intercluster interaction effects may be ignored.

PMMA and PS   Two polymers, poly(methyl methacrylate) (Sigma-Aldrich, MW=900 KDa) and poly(styrene) (Sigma-Aldrich, MW=285 KDa), were used to obtain thin films containing the SMMs under study. Both polymers can be dissolved in organic solvents, mixed to a solution of the complex to be included, cast as a drop on a smooth surface and allowed to solidify upon solvent evaporation. From the chemical point of view, the main difference of PMMA and PS with respect to PDMS (apart from the fact that this is silicon-based) is that in the formers polymerization is already complete, and thickening is not obtained by some reaction between chains, but just as the result of solvent loss; this is an advantage from the point of view of chemical inertness of the matrix. For the same reason, from a mechanical point of view, these polymers undergo severe volume reduction upon solidification; this observation, coupled to their good strength makes them good candidates for thin film casting, with a typical thickness of about 20 μm. Thin films were usually prepared on a tensed poly(ethylene) membrane that allows very easy removal of the cast film upon solidification, while the process can be more difficult if the sample is casted o glass surfaces. Since evaporation of the solvent cools the surface, atmospheric moisture tends to adsorb and be included in the film, thus causing its whitening with subsequent loss of optical quality. To overcome this issue evaporation can be slowed down by covering the surface with a reversed beaker or, preferably,

carrying out the whole procedure under the inert atmosphere of a glove box.
In order to have a certain extent of reproducibility in film thickness it is very
important to work with polymer-cluster solutions with a fixed viscosity, i.e.
to use a fixed amount of solvent per unit mass of polymer (typically 5 ml of
solvent to dissolve 100 mg of polymer). PMMA was dissolved in DCM, while
PS was dissolved in toluene; both polymers were characterized by means of
UV-Visible spectroscopy and were found not to absorb above 400 nm and both
SQUID magnetometry and EPR spectroscopy revealed the complete absence
of paramagnetic species.
Also in this case the samples containing only the polymer were regarded as
the 'neat solvent' or blank, and SMM-containing samples were considered solid
solutions the molarity of which was evaluated considering the polymer as the
solvent.

4.4.2   Mn12

The study on bulk[111] focussed on the Mn12 derivative $Mn_{12}O_{12}(^tBuCOO)_{16}(H_2O)_4$,
Mn12Piv), that features a high solubility both in solvents and in the polymers
due to its pivalate groups and on Mn12PhSMe, that has been already described
and that has been used for MCD studies of Mn12 monolayers (see section 4.5).
In the case of Mn12 samples, PMDS and PMMA were used as matrices. PDMS
solid solutions had typical concentrations of 10^{-5} M and thicknesses in the or-
der of $10^{-3}m$, while for PMMA concentrations of $\sim 10^{-2}$ M and thicknesses of
around $10^{-5}m$ were used.
We performed optical absorption measurements on the samples to identify
Mn12Piv in the polymer, by comparison with the spectrum of the same com-
pound in solution; both are shown in Figure 4.6.

In addition to optical absorption measurements, we probed the integrity of
the included Mn12 complexes in the matrix by means of the observable that
is directly linked with the properties that we are going to study with MCD,
i.e. the magnetization. Measurements were performed on PDMS in a VSM
magnetometer, with a field sweep rate of 10 kOe/min. This was the same rate
used by the magnet of the MCD setup to measure the same samples. The results
are shown in Figure 4.7; the diamagnetic contribution of the matrix becomes
dominant at high field, where the paramagnetic contribution increases slowly
since the system is close to saturation, while diamagnetic contribution scales
linearly and with opposite sign. Such component was subtracted as a linear
background correction. From the magnetization curves of Figure 4.7 it can be
seen that both derivatives, Mn12Piv and Mn12PhSMe, retain their magnetic
hysteresis as low temperature (1.6 K), despite the smaller coercive fields with
respect to the crystalline phase.
Samples in which Mn12 is included in PMMA showed a similar behavior.

MCD measurements were carried out by mounting the sample on the teflon
sample holder and fixing them with copper adhesive tape. After sample was
inserted, it was cooled in He flow down to around 1.5 K with no applied field.
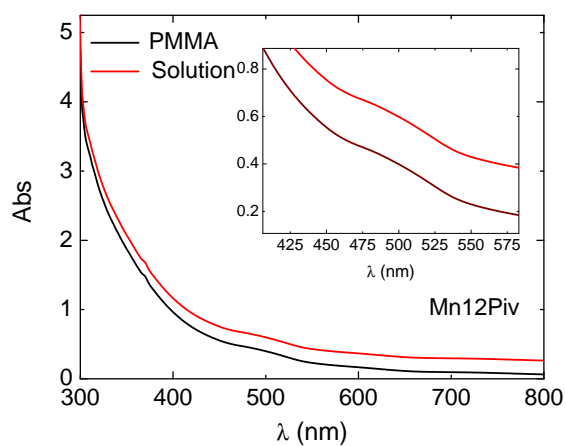
Figure 4.6: UV-Visible absorption spectrum of a Mn12Piv in PMMA sample (solid line) compared to the spectrum of the same compound in DCM solution (dashed line).
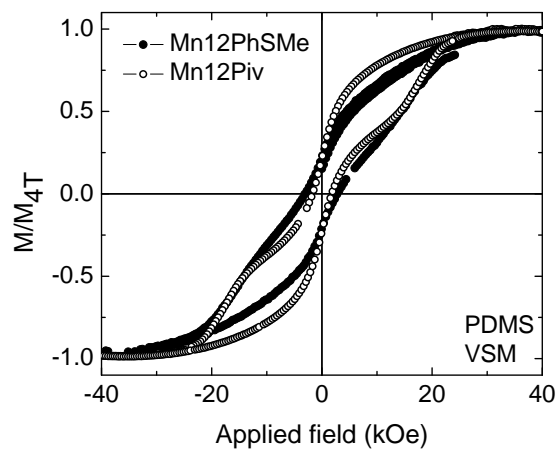
Figure 4.7: VSM hysteresis loops of Mn12Piv and Mn12PhSMe included into a PDMS matrix at $T = 1.6$ K and sweep rate of 10 kOe/min.

The most appropriate light source to probe Mn12 was, among those we could use, the 632.8 nm He:Ne laser source. This is coherent with what is reported by McInnes *et al.*[112] in a seminal work of MCD on Mn12 clusters.

We studied a sample of Mn12Piv in PDMS with a concentration of 1.0×10^{-5} M measured at 1.65 K. The sample displays the same behavior as in the magnetic measurements, with 'butterfly'–shaped hysteresis loop and small coercivity compared to the bulk (in this case a crystal powder, with $H_c = 8.5$ kOe at 1.85 K). The coercivities was found to be 3.2 kOe for the less concentrated sample and 6.2 kOe for the more concentrated one. The MCD hysteresis loops for the two samples are shown in Figure 4.8.
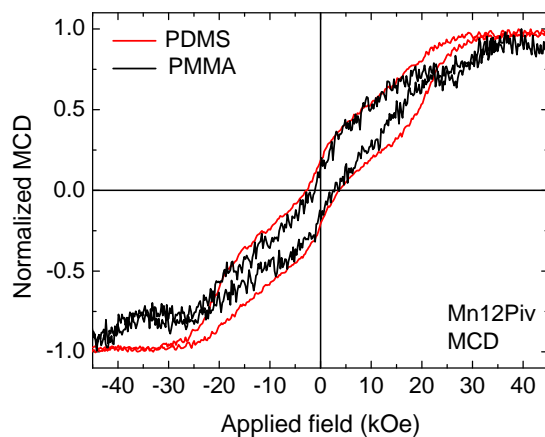
Figure 4.8: MCD hysteresis loops of Mn12Piv in a PDMS matrix ($C = 1.0 \times 10^{-5}$ M) and in a PMMA matrix ($C = 2.0 \times 10^{-2}$ M) probed with 632.8 nm light and sweep rate of 10 kOe/min.

The same Mn12 derivative, included in PMMA thin films was measured with the 476.5 nm line of the Ar:ion laser source and yielded an open hysteresis loop with a coercivity of 2.5 kOe (Figure 4.8). Small differences with respect to the curves measured with magnetometric techniques can be due to optical effects that are typical of the MCD measurement process.[112] The electronic dipole transition moments associated to magnetic circular dichroism are highly polarized with respect to the molecular reference frame and the energy of the transition. As a consequence, there is an orientation selection that probes only a subset of the molecules impinged by light: such selectivity can explain the differences between M vs H and MCD vs H curves acquired on the same sample.

In order to obtain some quantitative information on the sample, we must con-

sider the optical path of the light beam through the sample ($l \simeq 0.5$ mm), and the beam spot area (0.03 mm^2). Considering the concentration of the diluted sample (1×10^{-5} M), the number of clusters probed by the beam is estimated to be around 3.61×10^{11}. The saturation values of the MCD signal, taken at 40 kOe, is equal to 420 ± 20 μrad which is about 70 times greater than the instrumental sensitivity, and yields a MCD per Mn12 cluster value of 1.16×10^{-15} rad/cluster.

4.4.3   Fe4

The Fe4 clusters were included in PDMS, PMMA and PS.[113] Studies with the latter polymer were started due to the observation of a long term instability of Fe4 in PMMA dissolved in DCM: after several months, such solutions shift from pale yellow to dark orange, indicating that the tetrairon complex has dissociated into dimers. Solid solutions in PMMA (i.e. after solvent evaporation) however, proved to be stable for months. The PS matrix, dissolved in toluene, did not give rise to any visible decomposition of the dissolved Fe4 units even after months of shelf life.
Since the blocking temperature of Fe4 derivatives lies well under 1 K, no opening of the hysteresis loop, either recorded with a magnetometer or with MCD, is expected to show any reversibility.
The Fe4 derivative used in this study was the sulphur-functionalized Fe4C9SAc, that has already been described, and that has been used for MCD measurements at the monolayers level. Hysteresis loops from magnetometric and MCD measurements of Fe4C9SAc in PDMS and PMMA are shown in figures 4.9 and 4.10. Correction for the diamagnetic contribution for the PDMS sample was carried out in the same way as described for Mn12.

The magneto-optical measurements were carried out with 476.5 nm light provided by an Ar:ion laser, which produces a fairly high saturation magnetic dichroism in this sample. Values as high as 4.5 mrad at 40 kOe were obtained with a high concentration (10^{-2} M) PDMS sample. A comparison between the MCD and the magnetic curves shows that the paramagnetic character of the Fe4 cluster at this temperature is well reproduced, indicating a dominant C-term contribution to the dichroism. However, the response to the field is quite different when directly comparing magnetization and MCD signals: the latter in fact reach saturation for lower values of applied field, and this can be attributed, like for Mn12, to the partial orientational selectivity of MCD with respect to magnetometric techniques. Let us now directly compare the magnetization curves of the PDMS and the PMMA samples both for induction based measurements (Figure 4.11) and for MCD experiments (Figure 4.12): we can see that in the PMMA matrix, Fe4C9SAc reaches saturation values for lower fields.

A possible explanation of this behavior, that is technique-independent, is that clusters in PMMA are not distributed with completely random orientations and that Fe4 units are partially aligned in the matrix, in particular with
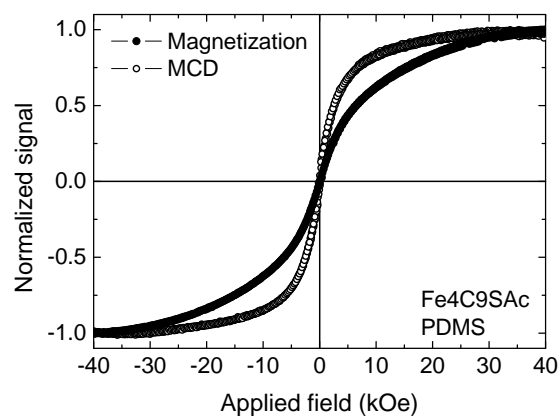
Figure 4.9: VSM and MCD hysteresis loop of Fe4C9SAc in a PDMS matrix probed with 632.8 nm light and sweep rate of 10 kOe/min. Concentration: $C = 1.3 \times 10^{-4}$ M.
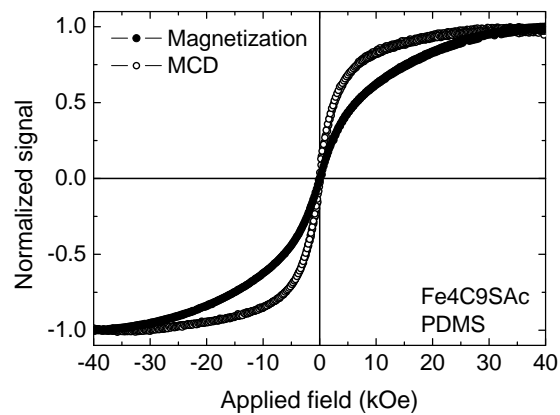
Figure 4.10: SQUID hysteresis loop and MCD hysteresis loop of Fe4C9SAc in a PMMA matrix probed with 632.8 nm light and sweep rate of 10 kOe/min. Concentration: $C = 2.0 \times 10^{-4}$ M.
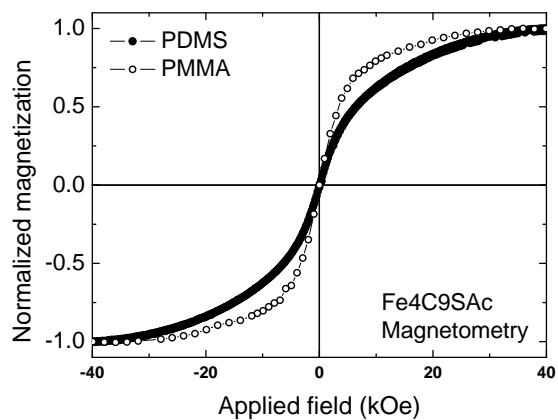
Figure 4.11: Induction based hysteresis loops of Fe4C9SAc in PDMS and PMMA matrices.
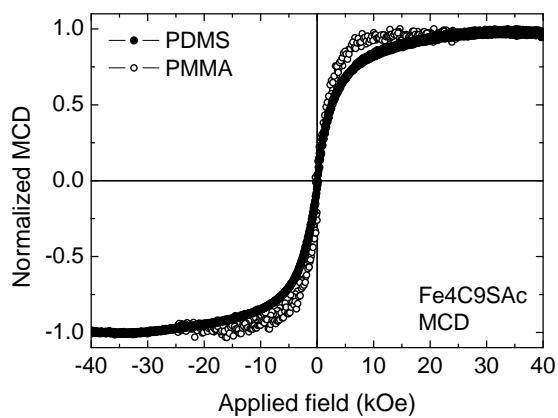
Figure 4.12: MCD hysteresis loops of Fe4C9SAc in a PDMS and PMMA matrices probed with 476.5 nm light and sweep rate of 10 kOe/min.

their easy axis, that corresponds to the idealized trigonal axis, normal to the film surface and thus parallel to the applied field.

This effect may be the result of the PMMA casting process. In fact, during the evaporation of the solvent from the [PMMA + Fe4C9SAc + solvent] drop a strain is induced in the film by higher rates of solvent evaporation from the face of the film compared with that at the edges during evaporation of the solvent. In order to gain some insight about the possible preferential orientation of Fe4C9SAc in thin films, we performed an angle-resolved X-band EPR experiment. Since the same process takes place in the formation of PS thin films, and this polymer is more inert toward Fe4, we carried out the experiment on Fe4 embedded in PS.

EPR experiments were carried out in our laboratories with Dr. Lorenzo Sorace, who also carried out all simulations presented here. Spectra were acquired at several angles between the magnetic field and the film plane (which we will call α), between 0 and 180 degrees. The initial position (0°) corresponds to the magnetic field parallel to the sample plane. The spectra, recorded at 5K, are shown in Figure 4.13.
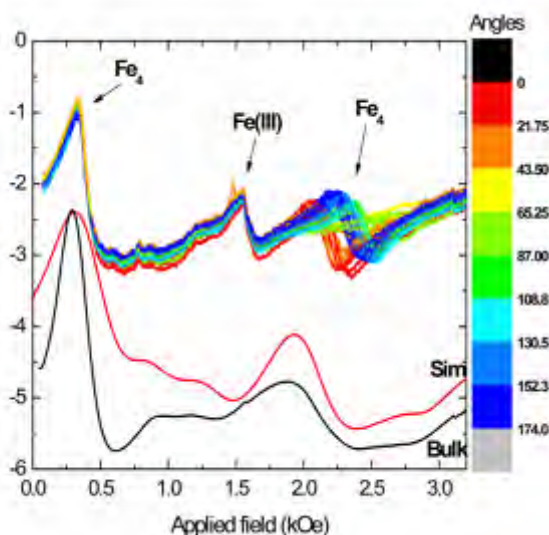
Figure 4.13: Angular dependence of the X-band EPR spectrum of Fe4C9SAc in PMMA at 5K. A simulated spectrum (red trace) and a spectrum of a bulk sample (black trace) are shown for comparison.

The spectra consist of three transitions, two at approximately 330 Oe and 1580 Oe that show no angular dependence and one between 2120 and 2450 Oe showing angular dependence. A spectrum taken from a bulk (powder) sample

of Fe4Ph is reported for comparison, as well as a simulated spectrum[b]. A good qualitative agreement between all these spectra is observed, indicating that the lines at the extremes of the spectra taken from the Fe4 in PS sample (the low field and the high field transitions) arise from transitions in the Fe4 $S = 5$ ground state multiplet. This confirms the presence of the intact cluster in these polymeric solutions. Further information regarding the levels involved in these transitions may not be obtained working with X-band EPR, as they correspond to an overlap of many transitions that may not be correctly assigned at this magnetic field range.[115] As the zero-field splitting in this cluster at this magnetic field range ($\sim$ 5000 Oe) is much larger than the Zeeman splitting (in this case, the ZFS is about 10 times larger than the Zeeman splitting) these transitions may only be assigned at high frequencies (high field EPR),[40,115] but the angular dependence strongly supports the partial orientation of clusters in the thin polymer samples. The transition at 1580 Oe is neither present in the simulated nor in the bulk spectrum, and is associated to the presence of impurities of uncoupled Fe(III) ions in the polymer.

In Figure 4.14 the transition field of the angle dependent transition is plotted as a function of the measurement angle α. A periodicity of the transition field with the angle is observed, and a sum of cosine functions fits the data (red trace). Besides, a transition at slightly higher fields appears at angles approximately between 30° and 90°. The presence of this second transition is also evidenced by the simulation results shown in Figure 4.15.
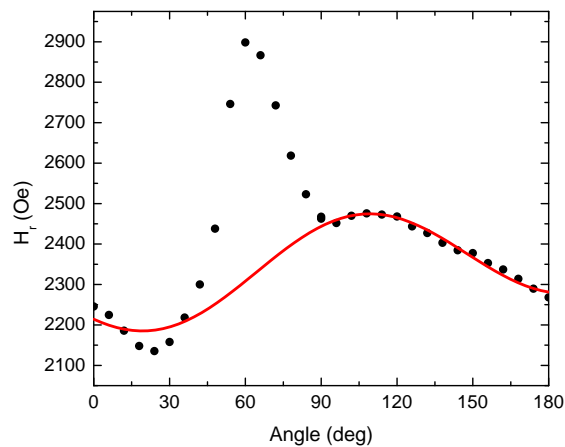
Figure 4.14: Angular dependence of the transition fields observed in the EPR spectra of Fe4C9SAc in PS.

---

[b]Simulation done with the software package SIM by H. Weihe.[114]
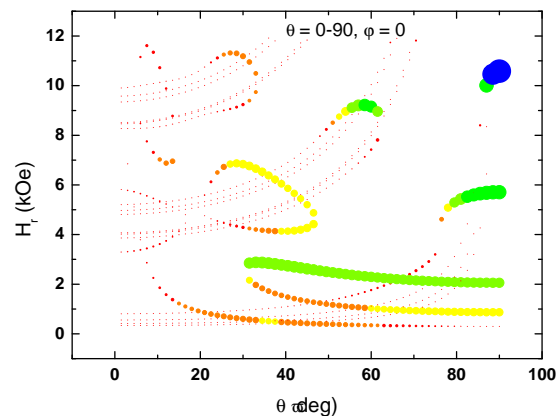
Figure 4.15: Simulated dependence of the EPR transition fields and the transition intensities with the orientation of the Fe4 units with respect to the magnetic field, given by the angle θ.

In these graphs the transition fields are plotted as a function of the angles θ defining the relative orientation between the molecule easy axis and the applied magnetic field. The color and the dimensions of the symbols denote the intensity of the transition. A transition (in green) appears for θ between 30° and 90° and resonant fields between 2900 and 2100 Oe. This could explain the peak in 4.14, considering the arbitrary initial point for the rotations (θ_0) in the simulations. If the sample was made of randomly oriented Fe4Ph molecules, no angular dependence of the spectrum would be expected. Even if the assignment of these transitions is not possible, the presence of a small angular dependence shows that a partial orientation results from the polymer film casting process. A similar explanation was invoked (yet not proved) before for Mn12 in PMMA films studied by MCD.[112] These facts suggest that this simple polymer casting process could be used to produce thin transparent films containing oriented molecules.

4.5   Monolayer measurements

We discuss here the results obtained in the study of the monolayers of Mn12[111] and Fe4 with MCD. The preparation and full characterization of such monolayers can be found in Chapters 2.4 and 3. The only difference between samples described in those chapters and the ones studied with MCD is the fact that the latter need to be transparent to the probing light, and that the support of the gold layer needs to be magnetically inert. As a consequence, instead of

the 200 nm thick, mica supported gold substrates, we used a transparent 5 nm thick gold layer grown on a Ti adlayer on silica slides. These substrates were especially prepared by SSENS (Hengelo, the Netherlands).

4.5.1   Mn12

The experiment of detecting monolayers of Mn12 by means of MCD is a very fascinating challenge, that makes use of the high sensitivity of the setup. We have been working on monolayers of the well known Mn12PhSMe from THF solution, that have been fully characterized from morphological and chemical points of view (see Chapter 2.4). From the diameter of the Mn12PhSMe cluster, that is around 2.7 nm (determined by x-ray single crystal diffraction) and the surface density, estimated to be 3×10^{-13} units/mm^2 (from STM topography measurements) we can calculate and expected saturation signal of 5.9 μrad, according to the parameters discussed in the previous section. This lies at our instrument's sensitivity limit, so in order to enhance the signal we stacked 5 samples on each other prior to a measurement, to yield an expected saturation MCD of $5 \times 5.9 = 29.5$ μrad for full monolayer coverage.

The measured curve is shown in Figure 4.16, that was acquired using the same instrumental parameters used for bulk Mn12 measurements ($T = 1.5$ K, 632.8 nm light and sweep rate of 10 kOe/min). The observed saturation value is 20 μrad, lower than what expected for full monolayer coverage, in agreement with STM data. No opening of the hysteresis was observed for this sample, despite the fact that the temperature at which the measurement was carried out is well below the blocking temperature of Mn12. This behavior can be due either to chemical modifications that take place upon surface grafting, or to changes in the magnetization dynamics that result in faster relaxation in these non-crystalline conditions. Unfortunately, the MCD technique cannot give an answer on the causes of such loss of magnetic properties of Mn12 on surface, yet it gave a very important answer, even if negative, to the possibility of using this class of SMM on surfaces.

4.5.2   Fe4

Monolayers of FeC9SAc were thoroughly characterized by means of STM, XPS and ToF-SIMS (Chapter 3). Also in this case the cluster were grafted to the transparent substrates described above. A first set of MCD measurements was carried out at 1.5 K using the 405 nm light of a laser diode. This wavelength was used instead of the 476.5 nm line of the Ar:ion laser that gave the strongest MCD effect on the bulk sample since the latter is more noisy than the laser diode source. The fluctuations of the order of ± 250 μrad observed at saturation on the bulk sample PMMA would mask the expected signal from the monolayer sample, of the order of tens of μrad. Such value was calculated in a similar way to what has been done for Mn12PhSMe monolayers, considering a areal density (derived from STM images) of 6×10^{-14} units/mm^2 and a laser
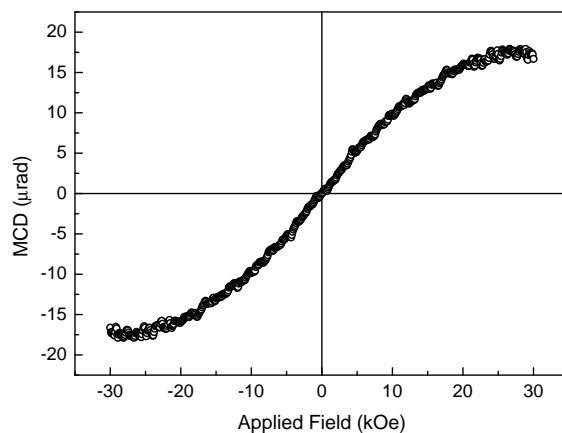
Figure 4.16: MCD hysteresis loop of a Mn12PhSMe monolayer on gold prepared from THF solution, probed with 632.8 nm light and sweep rate of 10 kOe/min at 1.5 K.

beam spot area of 0.44 mm^2 (the 405 nm laser has a larger spot size). Such calculated value for the saturation MCD is 0.99 μrad for 1 monolayer. This value is well below the sensitivity limit of 6-8 μrad. In this conditions, even stacking 5 samples, as we did for the Mn12 SAMs is not expected to yield a strong enough signal. In effect, measurements carried out on such samples did not give any distinguishable signal from that coming from clean substrates.
Surface plasmon resonance is well known to significantly amplify Raman scattered signal[116,117] and is now routinely used in SERS (Surface Enhanced Raman Spectroscopy) experiments. A few reports exist also on the effect of local intense fields on the amplification and/or sign change of MCD signal of magnetic nanoparticles absorbed to gold surfaces.[118,119] A 5-fold increase of the saturation MCD has been observed for measurements in transmission, of magnetic nanoparticles bound to noble metal nanoparticles,[120] as well as Yttrium-Iron Garnet films with Au nanoparticles embedded in them.

The substrates were prepared in our laboratories by thermal evaporation of Au on a clean quartz slab with no adlayer. The evaporation was performed in high vacuum conditions (base pressure inside the chamber of the order of $1x10^{-7}$ mbar); the thickness of the deposited gold layer was controlled by a calibrated Quartz Crystal Microbalance (QCM) and was estimated to be around 13 nm. The degree of roughness of the surface depends on the gold evaporation rate; the morphology of such substrate was evaluated by means of STM microscopy. In Figure 4.17 two representative scans are presented, showing the rugosity that is distributed on two length scales, the first around 50 nm and

the second around 10 nm, thus confirming that the substrate has the correct roughness to exhibit localized plasmon resonances.
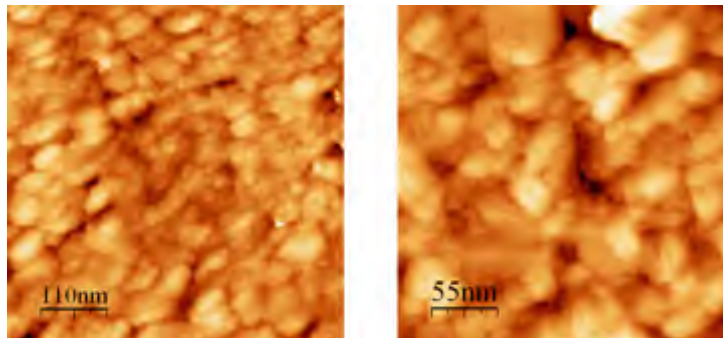
Figure 4.17: STM constant current topography images of rough gold surfaces at different scales.

After recording the MCD curve of this substrate (the 'blank'), we prepared a monolayer of Fe4C9SAc on its surface and measured it at 1.5 K with 405 nm light. The resulting curve, after the substrate contribution was subtracted and averaged over 4 measurements, is shown in Figure 4.18. Quite interestingly, we can see that it is was possible to detect a signal that resembles a paramagnetic behavior, with saturation at fields beyond 20 kOe. The extremities of the curves are noisier because of small displacements of the sample holder rod at high fields during the field sweep (sweep rate 10 kOe/min). The saturation values are roughly $+16\mu$rad and -18μrad, meaning that the MCD values are not symmetric with respect to the applied field. The enhancement, if real, is nevertheless quite impressive, considering that we have calculated a saturation MCD value of about 1 μrad for one monolayer of Fe4C9SAc. It must be pointed out though that part of the enhancement is certainly to be ascribed merely to an increase of the superficial area of the rough substrate, since the calculation is carried out based on the very flat Au(111) surfaces used for STM imaging (see for example Figure 3.3).

The results obtained with the Magnetic Circular Dichroism measurements presented in this chapter can be thus summarized: we first developed and verified a series of techniques to include Mn12 and Fe4 derivatives into transparent polymeric matrices, then performed a detailed study of the magneto-optical properties of such systems. These experiments gave us two types of valuable information: on one side we could study the MCD response of these SMMs in the bulk phase, while on the other side we provided us with a set of reference data for monolayer measurements, that are the main aim of this thesis work. We highlight the finding of a partial spontaneous ordering of Fe4C9SAc clusters in the PS matrix, as suggested by MCD measurements and supported by *ad hoc* EPR studies.

We then moved to the study of monolayers of both families of clusters. The
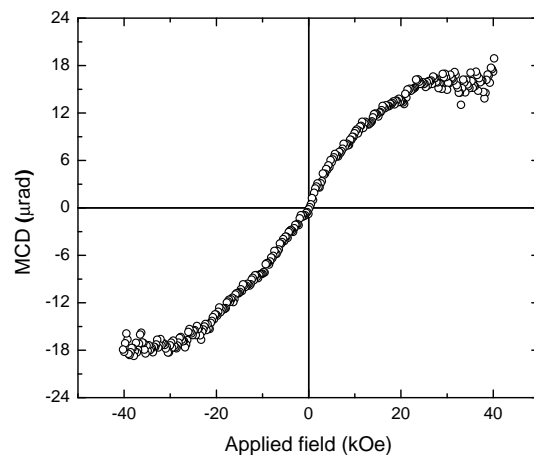
Figure 4.18: MCD hysteresis loop of a Fe4C9SAc monolayer on rough gold prepared from DCM solution, probed with 405 nm light and sweep rate of 10 kOe/min at 1.5 K. The loop was symmetrized by adding a constant value.

archetypal Mn12 could be measured with relative ease, but gave the disappointing result of not showing any opening of the hysteresis, suggesting that some modification of the cluster was taking place on the surface and thus opening a 'case' on the compatibility of the archetypal, extensively studied Mn12 SMM with the surface environment. Monolayers of the second family of clusters, Fe4, proved to be more difficult to address with MCD, given their lower MCD signal, at least at the wavelengths that were at our disposal and were sufficiently stable. We could not detect any signal from Fe4C9SAc adsorbed on standard Au substrates, but we were able to measure a reasonable MCD curve on home made rough Au substrates, exploiting signal amplification resulting from surface plasmon resonance induced in gold by the roughness. No opening of the hysteresis could be observed due the very low (< 1 K) blocking temperature of Fe4.

MCD experiments on monolayers of SMMs gave us information that, though unprecedented and valuable, did not allow us to draw final conclusions on the magnetic properties of SMMs grafted to surface. In the next chapter, we shall describe how these pieces of information were confirmed and extended by XMCD experiments at very low temperature.

Chapter 5

X-ray magnetic circular dichroism on SMMs

5.1 Why XMCD?

We have already mentioned that X-ray Absorption Spectroscopy (XAS) and the related techniques that measure the dichroism induced by a magnetic field are, among all magnetometry-related techniques, the only ones that were able to give us satisfactory and reliable information on the fate of SMMs grafted to surfaces. In this section we shall explain in some detail which are the features of polarized x-ray absorption spectroscopy that are critical for our type of study, and more in general for the study of magnetic ultrathin layers. This section precedes those related to proper introduction to the working principles and the experimental setup in order to allow the reader to get an immediate picture of the advantages of the technique for the investigation of the systems studied in this thesis.

The key points that XAS and XMCD analysis feature can be summarized as follows:

- **Extreme surface sensitivity** - High photon flux and beam stability coupled to the particular surface selective detection mode (Total Electron Yield, TEY) allow for reliable acquisition of polarized x-ray absorption spectra of monolayers of SMMs grafted to metallic surfaces.

- **Atomic species selectivity** - Unlike most of other techniques devoted to the study of magnetic properties of materials, x-ray absorption yields magnetic information from transitions related to the very localized core levels of the inspected species, thus revealing element and even oxidation state specific magnetic properties.

- **Electronic and spin structure information** - XAS spectra can be used to ascertain the electronic structure of the metal centers, while

XMCD spectra can give precious information on the coupling between spins in the system.

These are just a few of the powerful instruments that synchrotron radiation provides us with for the study of SMMs. As one can easily realize, the type of information is very valuable also for the study of bulk phase materials: the fact that all features are also applicable to monolayer study is indeed very welcome. There is also a set of properties, such as the surface sensitivity of TEY detection for instance, that are in principle interesting for monolayer studies, but which turned out to be crucial for the understanding of the magnetic behavior of bulk systems, as we will show in detail in section 5.6.
On the other hand, all these very appealing features would turn out to be sadly unexploitable for the study of SMMs due to the very low temperatures at which these show slow relaxation of the magnetization: on this regard synchrotron radiation techniques show a weak side, due to the relatively limited offer of suited endstations. In our case, we availed us of one of the most advanced ones, the TBT (Très Bas Temperature) endstation developed in France by Philippe Sainctavit and Jean-Paul Kappler, equipped with a dilution setup capable of reaching temperatures lower than 300 mK under photon flux; details on the TBT setup can be found in section 5.3.4.

5.2   Synchrotron radiation

When a high energy electron or positron beam is deviated from its trajectory to a curved path, the subsequent energy loss is released as electromagnetic waves. Synchrotrons generate radiation using this principle: electrons with the energy of several tens of MeV are produced by an electron gun and are then accelerated by a linear accelerator up to several hundreds of MeV. The electrons are then injected into the booster ring where their energy is increased to several GeV. Finally, the electrons are further injected into a storage ring where, due to centripetal acceleration of the bending magnet, the electrons emit electromagnetic radiation. The storage ring consists of straight portions where electrons travel in a collimated beam of $\sim 10\mu$m diameter. The electron beam is deviated from its linear trajectory by magnets (bending magnets and insertion devices) which accelerate the electrons producing electromagnetic radiation. The energy lost by the electrons during this process is restored to them as they travel through the radio frequency cavities.

Synchrotron radiation has a number of unique properties:

- **High brightness**: synchrotron radiation is extremely intense (hundreds of thousands of times higher than conventional X-ray tubes) and highly collimated.

- **Wide energy spectrum**: synchrotron radiation is emitted with a wide range of energies, allowing a beam of any energy to be produced.

- **Polarization**: Synchrotron radiation is highly polarized.

Today's synchrotrons are dynamic, high performance, open to users large scale facilities that attract scientists from the most diverse backgrounds. However, synchrotrons have a rather long history, that has been marked up to now by three jumps in features and users base: the oldest structures, known as first generation synchrotron sources were high energy physics accelerators, where the synchrotron radiation was an unwanted by-product. In the 1960s, physicists and chemists began to use the radiation from several of these accelerators in a 'parasitic mode'. The second generation of synchrotron radiation facilities, such as the Photon Factory in Japan, were constructed expressly to provide synchrotron X-rays for research. In more recent years, third generation facilities were and are still being completed, for example, the 7 GeV Advanced Photon Source in the USA, and are providing even higher brightness X-ray beams, about 10,000 times higher than those of the second generation.
We will now briefly describe the two parts of the synchrotron that are responsible for the production of photons: bending magnets and insertion devices.

5.2.1   Bending magnets

The purpose of bending magnets (BM) is to give the electrons a transverse acceleration that modifies their linear uniform motion inside the vacuum of the ring's tubing (see Figure 5.1). Such an acceleration is defined as centripetal when considering the electrons' motion around a circular trajectory, and is responsible for a loss in kinetic energy that results in an emission of photons. The electromagnetic radiation is emitted in a cone that is often described as a searchlight propagating in a direction that is tangent to the trajectory of the electrons; its spreading in energy goes from the infrared to the hard x-ray region, highest intensity being reached in the x-ray region.
A parameter that is often used to characterize radiation sources is brightness, which is defined as:

$$\text{Brigthness} = \frac{\text{Photons}}{\text{Second} \cdot \text{Beam collimation} \cdot \text{Source area} \cdot \text{Spectral distribution}}$$
(5.1)

where beam collimation is expressed in mrad^2 and relates to the degree of divergence of the photon beam as it propagates, while the source area corresponds to the electron beam size in units of mm^2. Spectral distribution refers to the photon energy range accepted for the measurements. By convention a bandwidth of 0.1% is used; i.e. for a measurement at a given energy ω, photons with energy $\omega \pm \Delta\omega$ so that $\Delta\omega/\omega = \pm 0.1\%$, are recorded.
The electric component of electromagnetic radiation is parallel to the acceleration vector and therefore the light emitted by a bending magnet is linearly polarized in the plane of the storage ring. This is not true for the radiation

emitted above or below the plane of the storage ring, which are elliptically polarized. These polarization properties will be discussed below.
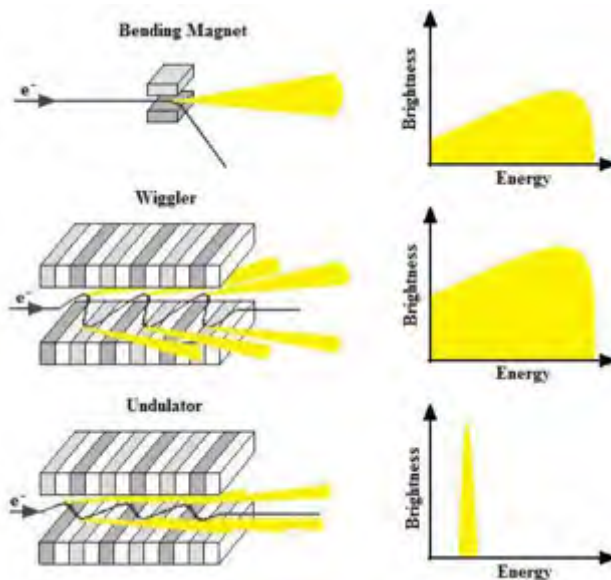
Figure 5.1: Schematic representation of bending magnet, wiggler and undulator (left). Diagram of typical brightness profile produced by these radiation sources (right).

5.2.2   Insertion devices

Insertion devices (ID) were designed in the first place to increase the brightness of the radiation. Using bending magnets, if fact, brightness can be increased either by using higher magnetic fields or increasing the kinetic energy of the electron beam: both these solutions would face serious complications both from the technical and economical points of view. Insertion devices on the other hand are able to generate brighter light with greater coherence over a wider energy range. IDs are made up of periodic arrays of magnets placed above and below the electron pathway in straight section of the storage ring (Figure 5.1). We define the length of one magnet section as N_m; each contiguous section is magnetized with opposite direction to the previous one, so electrons traveling through the ID are continuously deviated into a wiggling motion. At each change of trajectory, that takes place every $2N_m$ lengths, photons are emitted. IDs are divided into two categories: wigglers and undulators, that are able to produce linearly or elliptically polarized light.

Wigglers in this type of ID, magnetic fields are rather large and cause a large amplitude oscillation of the electrons. Radiation is thus of high energy (10-20 KeV) and poorly collimated, comparably to that emitted from BMs, but with a greater total brightness than these, owing to the larger number of deviations to which the electrons undergo.

Undulators The structure of this kind of ID is quite similar to that of wigglers, but the opposing fields of the aligned magnets are smaller, thus electron experience smaller deviations and oscillate with reduced amplitude. This results in narrower radiation cone and a smaller spectral width. The tunability of the narrow radiation energy band is achieved by changing the gap between the two rows of magnets, i.e. changing the magnetic field experienced by the electrons.

As described above, undulators produce radiation that is linearly polarized in the plane of the ring (horizontally polarized light), much the same as wigglers do; however, by using four sets of magnet arrays, two above and two below the electron pathway, it is possible to control polarization of the photons in any desired way by changing the relative positions of the four sets. Such type of undulator is called elliptically polarized undulator[121,122] and is depicted in Figure 5.2, along with the different geometries that yield linear (horizontal and vertical) and circular polarization of the outgoing photons. In particular, in each row one quadrant is fixed and one is movable longitudinally along the electrons axis (z). Translation of the four quadrants changes the phase between the vertical and horizontal components of the magnetic field (Bx and By). When Bx and By are 90° out of phase circularly polarized x-rays are generated and for 180° phase shift, vertical polarized x-ray.
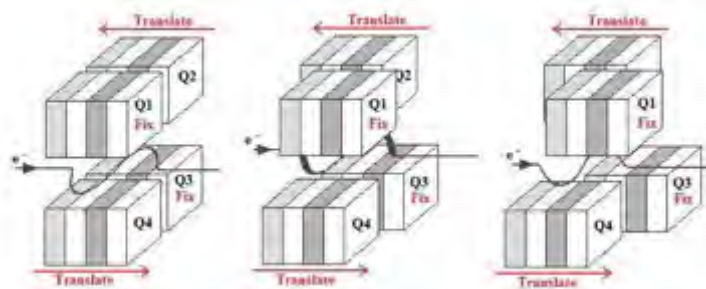
Figure 5.2: Scheme of elliptically polarized undulator with (from left to right) 0°, 90° and 180° phase shifts yielding horizontal linear, circular and vertical linear photon polarizations, respectively.

5.3 The principles of x-ray magnetic circular dichroism

5.3.1 Historical perspective

On November 8th, 1895, Röntgen discovered, more or less accidentally, what he called later X rays. His first report, was entitled: *On a new kind of rays*, and got published very fast in the Proceedings of the Physical Medical Society of Würzburg on December 28th, 1895.[123] Already on January 1st, 1896, he distributed copies of his manuscript to several renowned physicists. Within days, his discovery became a worldwide sensation, unprecedented in the history of physics.

Experiments on x-rays were run at almost every major laboratory in the world. A number of experiments were proposed to detect eventual polarization properties of x-rays. Already in the February issue of Nature in 1896, J.J. Thomson published a letter in which he reported on his attempts to polarize x-ray radiation and his negative conclusions. In the years to follow, a great number of experiments in this direction were tried, and the list of failed attempts is rather long.

Finally, in 1905 C.G. Barkla demonstrated that x-rays could be polarized by scattering at 90° in his famous paper on polarized x-rays.[124] He proved that the primary x-rays emitted by an x-ray tube were partially polarized with a rate of $\sim 20\%$. In a second paper on the polarization properties of x-rays,[125] he showed that it was possible to produce a linearly polarized x-ray beam with a polarization rate close to 100%.

Starting with the assumption that x-ray radiation was a kind of light of very short wavelength, investigation started in order to find a possible rotation of the plane of polarization of x-rays when interacting with matter,[126] in a similar way to what had previously been observed by Faraday and Kerr for visible light. The first half of XX century saw many attempts and no definite success, all experiments leading to dubious of utterly negative conclusions.

The first theoretical investigation on such light-matter interaction in the x-ray range was carried out by E.A. Stern et al.[127,128] who performed a band structure calculation and predicted a magnetic circular dichroism at the M2,3 absorption edges of ferromagnetic nickel. No serious attempt was made to check this theory experimentally though, and the first experimental results came only ten years later. In 1979, Hrdý *et al.* tried to establish the upper limits of the x-ray Faraday rotation in nickel, cobalt and magnesium ferrite[129] and concluded that these limits were even smaller than those predicted either by Froman[130] or by Kartschagin and Tschetwerikova[131]nearly 50 years earlier. Similar conclusions were drawn also by Hart and Rodriguez[132] who failed to measure a Faraday effect with x-rays as well. Their upper limits determined for cobalt, nickel and iron were, however, in quantitative agreement with the results of Hrdý *et al.* Interestingly, they concluded that the detection of a Faraday rotation with x-rays could be possible only with the use of synchrotron radiation

and only near absorption edges. In 1983, G. Sch*üu*tz and her colleagues used circularly polarized x-rays in order to elucidate the influence of the magnetic state of iron on x-ray absorption spectra[133] using circularly polarized L emission lines in oriented Ir isotopes after internal conversion decay resulting in the emission of photons with discrete energies ranging from 8 to 13 keV. Also in this case the sensitivity of the experimental setup was insufficient to detect any spin-dependent contribution to x-ray absorption.

The first attempt to measure x-ray magnetic circular dichroism using synchrotron radiation was done in 1984 by E.A. Stern and coworkers, who carried out experiments a the L_3 edge of Gd in a $Gd_{18}Fe_{82}$ alloy. Unfortunately, in this experiment, the circular polarization rate of the incident x-rays was only ca. 5% and the authors again failed to detect any reliable effect.

Independently, using an atomic multiplet approach, Thole *et al.*[134] reported in 1985 new calculations which led them to conclude the existence of a quite significant x-ray magnetic linear dichroism at the $M_{4,5}$ edges of rare-earths. They pointed out that linearly polarized synchrotron radiation could be used most efficiently to determine accurately the magnitude and orientation of the local rare earth magnetic moments. One year later, collaborating with other colleagues,[135] they produced the first experimental evidence of a strong x-ray magnetic linear dichroism at the Tb $M_{4,5}$ absorption edges in the ferrimagnetic garnet $Tb_3Fe_5O_{12}$ using the linearly polarized synchrotron radiation emitted by the storage ring ACO at LURE in Orsay.

A few years later, G. Schutz *et al.* reported the first experimental evidence of X-ray Magnetic Circular Dichroism[136] at the K edge of an iron foil. The weak but significant dichroism was carried out uning the elliptically polarized light produced by a bending magnet at DESY in Hamburg. It was rapidly anticipated that magnetic circular dichroism should not be restricted to only the X-ray Absorption Near Edge Structure (XANES) region but should also manifest itself in the Extended X-ray Absorption Fine Structures (EXAFS). The confirmation of this hypothesis came with the experiments also performed by Schütz *et al.* at the L edges of Gd in Gd metal and in the ferrimagnetic garnet $Gd_3Fe_5O_{12}$.[137] An important step forward was made by C.T. Chen *et al.* who extend XMCD experiments into the soft x-ray range,[138] finding huge dichroic signals at the $L_{2,3}$ edges of a ferromagnetic Ni film. The field of XMCD became a mature research area when B.T. Thole and P. Carra[139,140] developed a set of magneto-optical sum rules which made it possible to relate the integrated intensities of XMCD spectra to the orbital[139] and spin[140] moments carried by the absorbing atom. Sum rules allowed experimentalists to analyze XMCD spectra recorded at spin-orbit split absorption edges (e.g. $L_{2,3}$ edges) and to extract magnetic moments, both in magnitude and direction, with the full benefit of the element and orbital selectivity of x-ray absorption spectroscopy.

In 1990 also x-ray Faraday rotation was detected by Siddons *et al.*[141] who measured a very small rotation angles in a Co-Fe alloy and in a Co metallic glass at the Co K edge. In addition to magnetic circular and linear dichro-

isms and to Faraday rotation, other interesting magneto-optical spectroscopies like the transverse and the longitudinal magneto-optical Kerr effects,[142,143] and the Voigt effect[144] could be finally observed with x-rays. Also, after almost a century from the first experiments, optical activity of chiral systems in the x-ray range was unambiguously detected only in 1998 using X-ray Natural Circular Dichroism (XNCD) in a non-centrosymmetrical crystal of $LiIO_3$.[145] More recently, time-reversal odd optical activity effects, also referred to as non-reciprocal, magnetochiral dichroism and non-reciprocal magnetic linear dichroism, were observed in the x-ray range.[146,147] New edge-selective sum rules for optical activity were derived by Carra *et al.*[148,149] and revealed how closely related were optical activity and orbital magnetism.

5.3.2   Description of X-ray Absorption Spectroscopy

One-electron picture   The resonant x-ray absorption process in its simplest picture consists of electronic transitions from core levels to valence levels induced by photon absorption or, to describe it differently, the photon transfers its energy to a core electron and the electron is excited into an unoccupied electronic state. This description is termed *one-electron* picture and simply follows what happens to the photoelectron. It is also referred to as the *active electron approximation*[150] since it ignores the fate of all other electrons in the atom, that are considered *passive* during the excitation process. Such description has the advantage of being intuitive, on the other hand it lacks rigor and is insufficient to fully describe the XAS. In fact, electrons not directly involved in the excitation are not actually *passive*, but rather influence the fate of the active electron.

Let us illustrate the one-electron picture for the L-edge x-ray absorption spectrum of a *3d* transition metal atom, as shown in Figure 5.3a: in the *initial state* or $2p$ core state, the electron has an angular momentum $l = 1$ and spin $s = 1/2$, so spin-orbit coupling produces two energy states with $j = l \pm s$. The four substates of $2p_{3/2}$ with $j_+ = 3/2$ experience an energy shift $E_{j_+} = \zeta_l/2$ and the two substates of $2p_{1/2}$ with $j_- = 1/2$ are shifted by $E_{j_-} = \zeta_l$, with the separation given by the Landé interval rule $E_{j_+} - E_{j_-} = \zeta_l j_+$, ζ_l being the spin-orbit coupling constant related to the angular momentum l.

When it reaches the *final state* the electron is in the $3d$ shell with angular momentum $l = 2$ and spin $s = 1/2$. Also in this case, spinorbit coupling splits energy states into two components with $j = l \pm s$, that is states $3d_{5/2}$ ($j = 5/2$) and $3d_{3/2}$ /$j = 3/2$), as shown in Figure 5.3a. In practice, since core shells are more compact than the valence shell, the spinorbit coupling constant ζ_{2p} is considerably larger (of order 15 eV) than that of the valence shell ζ_{3d} (of order 50 meV); for this reason the $2p_{3/2} - 2p_{1/2}$ (L$_3$ - L$_2$) splitting is the dominant one.

Configuration picture   The one-electron depicts the spinorbit splitting of the p core shell as an *initial state* effect. In effect, the p shell is filled in the

ground state and there is therefore no observable effect of the spinorbit inter-action. The *configuration picture* gives a more proper description of the x-ray absorption process, in which an atom is excited from a ground or initial state configuration to an excited or final state configuration[a] Resonant L-edge absorption is thus described by an initial state configuration $2p^6 d^n$ and a final state configuration $2p^5 d^{n+1}$.

In the case of transition metals, that are the systems studied in our work, the case that is easiest to describe is that of configuration d^9. We can in fact reverse the description by using the hole formalism, obtaining a hole configuration d^1, that fully describes the initial state (p shell is closed, so it has no holes); the final state $p^5 d^{10}$ has a closed d-shell and a p^5 electron or p^1 hole configuration. L-edge spectra of such a system described in a configuration hole picture are then described by a transition from the configuration d^1 to p^1 (Figure 5.3b). Now the spinorbit splitting of the p shell is properly described as a final state effect. The two pictures in Figure 5.3are e completely equivalent in describing the electronic transitions (the energy order of the j states is inverted because electrons and holes have opposite spin).

In general though, the one electron and configuration pictures are not equivalent. Open shells with two or more holes or electrons give different transition landscapes and exchange and correlation effects between the particles may be large. Such effects lead to multiplet structure between the d electrons in the ground, as well as between the core p and valence d electrons in the excited state.
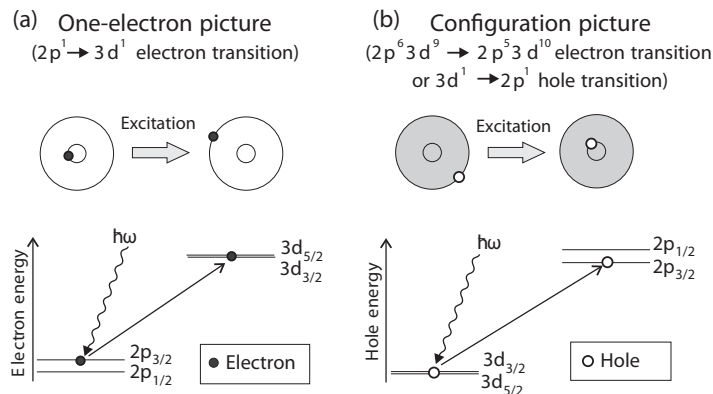
Figure 5.3: Resonant L-edge x-ray absorption. a) One electron picture and b) configuration picture for a d^9 ground state, described with holes formalism.

---

[a]Transitions between these configurations are treated omitting all closed subshells since they are spherically symmetrical and their net angular momentum is zero.[151]

Fermi's Golden Rule   The cross-section of x-ray absorption is calculated by considering a time-dependent perturbation of the sample by the electromagnetic (EM) field. The time-dependent EM field induces transitions between an initial state $|i\rangle$ and final state $|f\rangle$, where both states contain an electronic and a photon part; such process is a first-order process.

We can now describe the time-dependent transition probability with a formalism derived by Kramers and Heisenberg[152] and by Dirac,[153] that is valid for processes up to the second-order[b]:

$$T_{if} = \frac{2\pi}{\hbar} \left| \langle f | \mathcal{H}_{int} | i \rangle + \sum_n \frac{\langle f | \mathcal{H}_{int} | n \rangle \langle n | \mathcal{H}_{int} | i \rangle}{\varepsilon_i - \varepsilon_n} \right|^2 \delta(\varepsilon_i - \varepsilon_f)\rho(\varepsilon_f). \quad (5.2)$$

The sum runs over all possible energy states ε_n. The transition probability T_{if} expressed in units of [time$^{-}1$]. The interaction Hamiltonian $\mathcal{H}_e^{int}$ for x-ray absorption and resonant scattering is the product of the momentum operator **p** and the vector potential **A**:[154–157]

$$\mathcal{H}_e^{int} = \frac{e}{m_e} \mathbf{p} \cdot \mathbf{A}. \quad (5.3)$$

In free space $E = -\partial A/\partial t$, so eq. (5.3) indicates that the electronic transition is driven by the electric field **E** of the EM wave. The states and energies in eq. (5.2) are relative to the combined photon plus atom system, wave functions $|i\rangle$ and $|f\rangle$ being products of electronic and photon states and energies being sums of electronic and photon energies. The quantity $\rho(\varepsilon_f)$ is the density of final states per unit energy.

As can be seen, eq. (5.2), contains a first order-term and a second-order term: the second-order term, derived by Kramers and Heisenberg,[152] was called by Fermi the 'Golden Rule No. 1'[158] and is known also as the *Kramers-Heisenberg relation* and will not be further discussed in this thesis, since it relates, as we have already mentioned, to resonant scattering phenomena. The first-order term, derived by Dirac[153] and was called by Fermi the 'Golden Rule No. 2',[158] but it usually known as *Fermi's golden rule*.

We can relate the transition probability T_{if} to the total cross-section σ by normalizing with respect to the incident photon flux Φ_0:

$$\sigma = \frac{T_{if}}{\Phi_0}. \quad (5.4)$$

The transition matrix and the dipole approximation   The next step is to calculate the intensities of strong resonances like those associated with $2p_{3/2}, 2p_{1/2} \rightarrow 3d$ transitions: in order to do this it is convenient to simplify expression (5.2) by separating its matrix elements into electronic and photon

---

[b]a second-order process is, for example, the x-ray resonant scattering, in which the system evolves from $|i\rangle$ to $|f\rangle$ through and intermediate state $|n\rangle$.

parts. This can be achieved by quantizing the electromagnetic field;[159] one thus obtains the matrix elements in terms of transitions between two electronic states $|a\rangle$ and $|b\rangle$. Such matrix elements have the general form:

$$\mathcal{M} = \langle b| \, \mathbf{p} \cdot \epsilon e^{i\mathbf{k}\cdot\mathbf{r}} \, |a\rangle \,, \tag{5.5}$$

with $\mathbf{p}$ indicating the electron momentum vector, ϵ the unit photon polarization vector, and $\mathbf{k}$ the photon wave vector. We are now going to describe the matrix using the so called *dipole approximation*, which consists in eliminating the $\mathbf{k}$-dependence of the matrix element so the electron momentum operator $\mathbf{p}$ can be expressed in terms of the length operator $\mathbf{r}$:

$$\mathcal{M} = \langle b| \, \mathbf{p} \cdot \epsilon (1 + i\mathbf{k}\cdot\mathbf{r} + \dots |a\rangle \simeq \langle b| \, \mathbf{p} \cdot \epsilon \, |a\rangle = im_e\omega \, \langle b| \, \mathbf{r} \cdot \epsilon \, |a\rangle \,, \tag{5.6}$$

where m_e is the electron rest mass and $\omega = \omega_b - \omega_a$ the photon frequency associated with the transition from state $|a\rangle$ to state $|b\rangle$. Dipole approximation is valid if the size of the absorbing atomic shell is small relative to the x-ray wavelength ($|\mathbf{r}| \ll 1/|\mathbf{k}| = \lambda/2\pi$), so that the electric field which drives the electronic transition is constant over the atomic volume. Since photon energies involved in the process we studied are in the range of $\hbar\omega \leqslant 1000$ eV, corresponding to a wavelength $\lambda = 1.2$ nm and transitions involve the $2p$ core shells which have radius $|r| \simeq 0.01$ nm, we have $|r| \simeq 0.01\text{nm} \ll \lambda/2p \simeq 0.2\text{nm}$, the dipole approximation is reasonable.
We can now express the x-ray absorption cross-section σ^{abs} in the framework of the dipole approximation:

$$\sigma^{abs} = 4\pi^2 \frac{e^2}{4\pi\epsilon_0\hbar c} \hbar\omega \, |\langle b| \, \epsilon \cdot \mathbf{r} \, |a\rangle|^2 \, \delta[\hbar\omega - (E_b - E_a)]\rho(E_b). \tag{5.7}$$

Finally, we can express the x-ray absorption resonance intensity, I_{res} as the energy integral over the cross-section[c]:

$$I_{res} = \mathcal{A} \, |\langle b| \, \epsilon \cdot \mathbf{r} \, |a\rangle|^2 \,, \tag{5.8}$$

where $\mathcal{A}$ is a proportionality factor and is expressed as follows:

$$\mathcal{A} = 4\pi^2 \frac{e^2}{4\pi\epsilon_0\hbar c} \hbar\omega. \tag{5.9}$$

5.3.3   Polarization dependent spectroscopies

The phenomenon of polarization dependent absorption of light is referred to as *dichroism*. The origin of dichroic behavior from a microscopic point of view originates from the spatial anisotropy of the charge or the spin. In cases

---

[c]In this expression the functions $|a\rangle$ and $|b\rangle$ are assumed to be volume normalized to unity.[160]

where the effect only depends on charge, dichroism is termed *natural*, or *charge* dichroism, in contrast with the cases in which the origin of dichroism is due to preferential spin alignment or magnetic order. In these cases one speaks of *magnetic* dichroism.

The four most prominent dichroism-based spectroscopic experiments are listed below: the first two fall under the category of natural dichroism methods, while the remaining ones belong to the area of magnetic dichroism.

- **XNLD** X-ray Natural Linear Dichroism is due to an anisotropic charge distribution. The effect is parity even and time even.

- **XNCD** X-ray Natural Circular Dichroism may be present for anisotropic charge distributions that lack a center of inversion. The effect is parity odd and time even.

- **XMLD** X-ray Magnetic Linear Dichroism arises from a charge anisotropy induced by axial spin alignment. The effect is parity even and time even.

- **XMCD** X-ray Magnetic Circular Dichroism arises from directional spin alignment. The effect is parity even and time odd.

Of these types dichroism, three are connected and in contrast to XNCD they all arise within the dipole approximation. Figure 5.4 depicts one typical example for each of the four spectroscopies.

In other more complex types of dichroism, charge and spin effects are both present[164,165] such as in x-ray magnetochiral dichroism, that arises from axial spin alignment and a chiral charge distribution and is parity odd and time odd.[147] X-ray nonreciprocal linear dichroism arises from charge chirality that is induced by an axial spin alignment and the effect is parity odd and time odd.[146]

In this context, only XMCD will be discussed in more detail, since it is the type of experiment that has been used extensively in this thesis work. X-ray magnetic circular dichroism is used to obtain information on the size and direction of magnetic moments in the inspected material. Both the magnetic moments and the XMCD effect are time odd and parity even. Figure 5.4d represents the Fe L-edge in Fe metal; as can be seen, the XMCD effect is maximum when the X-ray angular momentum is parallel and antiparallel to the magnetic moment of the sample. The effect is large at the resonance positions and is opposite at the L_3 and L_2 edges; this is due to the opposite sign of the spin component at the two edges, namely $j = l + s$ at the L_3 edge and $j = l - s$ at the L_2 edge. Since the presence of a magnetic alignment is necessary to see any XMCD effect, this is zero for antiferromagnets.

We must also remember that if we suppose that the moment of the transition is reasonably treated only as dipolar in nature, in order to observe XMCD it is necessary to have spinorbit coupling, because the photon angular momentum
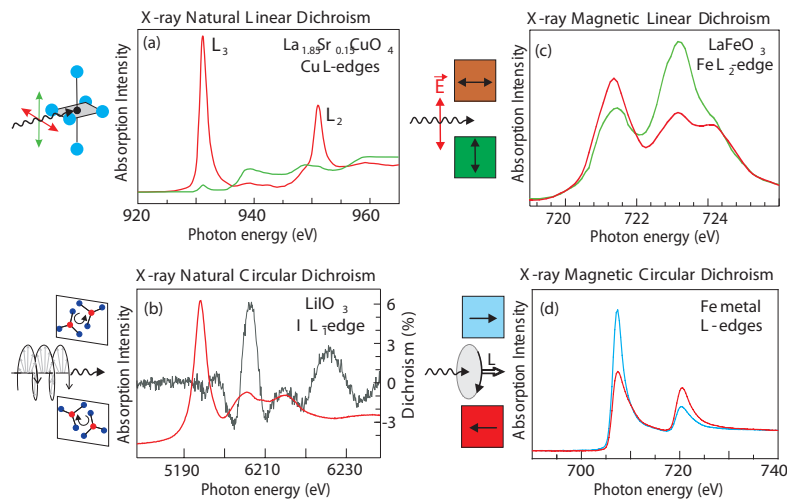
Figure 5.4: Four important types of dichroism. a) X-ray natural linear dichroism spectra of $La_{1.85}Sr_{0.15}CuO_4$ near the Cu L-edge.[161] b) X-ray absorption spectrum (red) of single crystal LiIO3 and the difference spectrum (gray), the X-ray natural circular dichroism spectrum, obtained from absorption spectra with left and right circularly polarized X-rays, incident along a special crystalline axis.[145] c) Magnetic linear dichroism spectrum of an epitaxial thin film of antiferromagnetic LaFeO3 with the E vector aligned parallel and perpendicular to the antiferromagnetic axis.[162] d) X-ray magnetic circular dichroism spectrum around the L_3 and L_2 edges of Fe metal.[163]

does not directly couple to the electron spin but only indirectly via the orbital angular momentum.

XAS spectroscopy probes the electron and hole structure of the d levels; since in XMCD the absorption process is spin dependent it is possible to measure an intensity difference that corresponds to the difference between the number of spin-up and spin-down holes, that is to say, the magnetic moment. The essence of the XMCD effect is better understood assuming a one-electron picture where the valence states exhibit a Stoner splitting; the case of Fe metal is shown in Figure 5.5, in which the density of states corresponds to that calculated for Fe metal by band theory. XMCD is maximum when the magnetization direction M of the sample and the photon's angular momentum L_{ph} are collinear. As illustrated on the left side of Figure 5.5, the dichroism effect is then given by the difference of the $p \rightarrow d$ transition intensities, measured for photons with *positive* angular momentum (assumed to be positive when L_{ph} points in direction of the wavevector $\mathbf{k}$) and *negative* angular momentum (L_{ph} points in direction of $-\mathbf{k}$) aligned along the fixed magnetization direction M of the sample. It was demonstrated that fixing the x-ray photon spin direction and switching the magnetization directions is completely equivalent.[166]
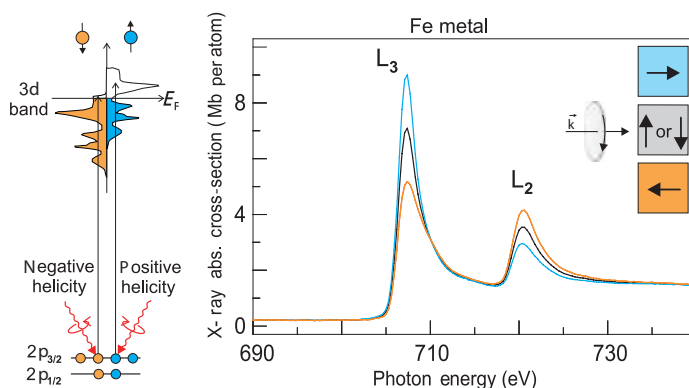
Figure 5.5: Scheme of the origin of dichroism in L-edge transitions (left) and example of Fe $L_{2,3}$ edges polarization-dependent spectrum (right).

Denoting the magnetization M and photon angular momentum L_{ph} directions with arrows, the dichroism depends on the relative alignment of the two arrows. The sign of the XMCD spectrum is arbitrary and by convention the dichroism intensity of the $3d$ transition metals Fe, Co and Ni is taken to be negative at the L_3-edge. From Figure 5.5, this is verified subtracting the two spectra according to the following rule:

$$\Delta I = I^{\uparrow\downarrow} - I^{\uparrow\uparrow} \tag{5.10}$$

The XMCD difference intensity, defined as the absorption edge intensity difference between antiparallel and parallel orientations of the sample magnetization and the incident photon spin, is directly proportional to the atomic magnetic moment.

The spin selectivity of the XMCD process can be described by a simple two-step model: the *first* step is the photon absorption, in which conservation of angular momentum requires a transfer of the angular momentum of the incident circularly polarized x-rays to a core electron. If the electron is excited from a spinorbit split level, such as the $2p_{3/2}$ level (L_3-edge), part of the photon's angular momentum is transferred to the spin through the spinorbit coupling and the excited photoelectrons are spin polarized. The spin polarization is opposite for incident x-rays with positive $(+\hbar)$ and negative $(-\hbar)$ photon spin. In addition, spin polarization is opposite in photoelectrons originating from L_2 and L_3-edges, since $2p_{3/2}$ and $2p_{1/2}$ levels have opposite spinorbit coupling. The photoelectron spin quantization axis is identical to that of the photon spin, so it can be parallel or antiparallel to the x-ray propagation direction.

In the *second* step the exchange split valence shell with unequal spin-up and spin-down populations acts as the detector for the spin of the excited photoelectrons. Such detection has maximum sensitivity when valence shell spin quantization axis is collinear to the photon spin or photoelectron spin quantization axis. In Figure 5.5 we can see that a transition from the $2p$ orbitals can only promote the electron into a partially unfilled spin-up$3d$ valence shell since the dipole operator does not act on spin and therefore does not allow spin-flips during excitation.

It is possible to evaluate the relative intensity of the XMCD signal at the L_3 and L_2-edges: at the L_3-edge, x-rays with positive spin excite 62.5% spin-up electrons and negative spin x-rays excite 37.5% spin-up electrons. At the L_2-edge instead, 25% spin-up electrons for positive spin and 75% spin-up electrons for negative spin x-rays. The $2p3/2$ state has double population with respect to $2p1/2$: considering this, one finds the dichroic intensity differences at the L_3 and L_2 edges are identical in magnitude but of opposite sign.

It must be pointed out that the pure photon spin configurations with angular momenta $\pm\hbar$ are not converted into pure (100%) electron spin configurations. Part of the angular momentum of the photon is converted into electron orbital momentum which is also carried by the photoelectron. The excited electron thus carries the angular momentum absorbed from the photon as spin and orbital momentum degrees of freedom. In a simple picture, in the absorption process a handed photon transfers its angular momentum to a core electron. The x-ray energy is tuned so that the created photoelectron is excited into the valence shell. If the valence shell has a preferential angular momentum direction the transition probability will depend on whether the photon and valence shell angular momenta are parallel or antiparallel. The dependence of XMCD on the spinorbit coupling has the benefit that it allows the separate determination of spin and orbital angular momenta (and therefore moments) from linear combinations of the measured L_3 and L_2 dichroism intensities.

A set of three very useful relations has been developed in order to decouple spin and orbital contributions of the signal; these are known as *sum rules*.[167–171] In particular, sum rules link the polarization dependent absorption intensities with valence band properties, in particular the number of empty states or 'holes' N_h per atom, the spin magnetic moment m_s per atom and the orbital magnetic moment m_o per atom. The first step consists in correlating the number of empty valence states per atom to the transition intensity of core electrons into the empty valence states; this is shown in Figure 5.6a for the L-edge in the magnetic 3d transition metals.

The **first sum rule**, or *charge sum rule* relates the peak intensity to the number of empty states N_h:

$$\langle I \rangle = CN_h, \tag{5.11}$$

where the constant C is defined by:

$$C = \frac{4\pi\hbar\omega\mathcal{R}^2}{137} \frac{L}{3(2L+1)}, \tag{5.12}$$

$\mathcal{R}$ being the radial $nc \rightarrow n'L$ matrix element that shall not be further discussed in this context. For a more detailed description see, for instance the excellent text by Stör.[172]

In the case of transition metal L-edges, (5.11) for the two spinorbit split components becomes:[169]

$$\langle I_{L_3} + I_{L_2} \rangle = CN_h. \tag{5.13}$$

C is typically given in units of [Mb eV] (cross-section area × energy) and it typical value for the $3d$ transition metals is ~ 10 MbeV.[173]

In a typical experiment, one magnetically saturates the sample along the direction of $\boldsymbol{k}$ and obtains the dichroic intensities A and B at the L_3 and L_2 edges (Figure 5.6b; notice that A and B components have opposite sign).

The **second sum rule**, or *spin sum rule* (5.6b), developed by Carra *et al.*[140] uses the integrals A and B and links the dichroism intensities to the size of the spin moment per atom:

$$\langle -A + 2B \rangle = \frac{C}{\mu_B} m_s. \tag{5.14}$$

In the case if Fe, Co and Ni, m_s and m_o are parallel because the d shell is more than half full. The spin moment becomes anisotropic only in higher order through the spinorbit coupling which is significantly smaller than the dominant isotropic exchange interaction; on the other hand, the orbital moment may be strongly anisotropic, due to ligand field splitting. It is then essential that the experiment is carried out in orientation-averaged conditions, either by working on a polycrystalline sample or by performing measurements along the different axes.

The **third sum rule**, or *orbital moment sum rule* (5.6c), developed by Thole

et al.[167] links the orbital moments m_o to the same integrals A and B taken in a different linear combination with respect to the *spin sum rule*:

$$-\langle A + B \rangle = \frac{3C}{2\mu_B} m_o. \tag{5.15}$$

In practice, the determination of mo requires high quality data and careful data analysis since A+B is typically a small number, obtained by subtraction of two large numbers since $A < 0$ and $B > 0$. If the two intensities have the same size but opposite signs the orbital moment is zero.
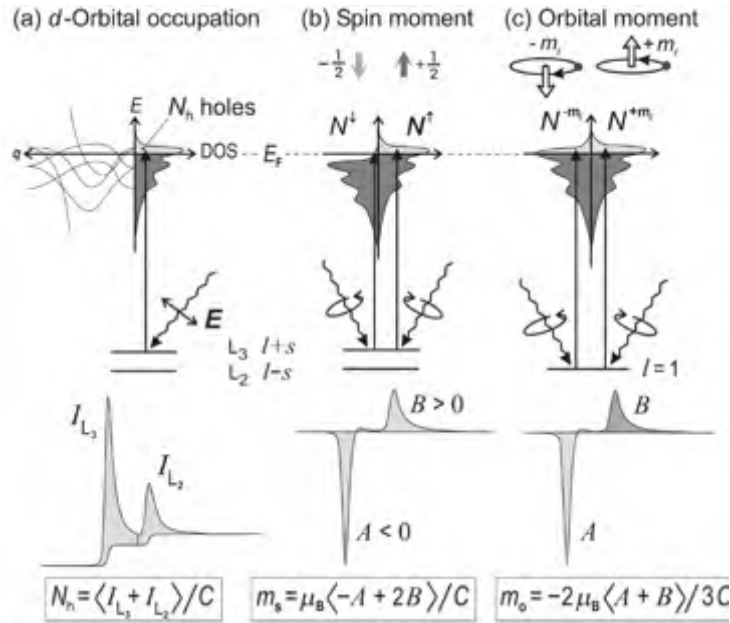
Figure 5.6: Schematic of processes, spectra, and intensities underlying the quantitative determination of valence band properties with sum rules.

5.3.4   The TBT endstation

The experiments described in this chapter could be carried out thanks to the experience acquired in casting and handling single layers on molecules on surface and to very performing light sources (especially X11MA beamline at SLS), but the best results would have been impossible to achieve without the unique properties of the Très Bas Temperature (TBT) endstation. This setup, shown in Figure 5.7 was developed by the joint efforts of Dr. Philippe Sainctavit of Institut de Minèralogie et de Physique des Milieux Condensès (IMPMC), Universitè Pierre et Marie Curie, Paris and Dr. Jean-Paul Kappler of Institut de Physique et de Chimie des Matèriaux de Strasbourg (IPCMS). In addition to

the standard features of a cryogenic endstation suited for studies in magnetism, TBT can be equipped with a ^{3}He-^{4}He dilution setup that can cool the sample to temperatures as low as 200 mK in ultra high vacuum and under the x-ray flux of a synchrotron beamline.[174,175]

We will now describe the basic features of this endstation. The advantages of a dilution based refrigeration is twofold: the extremely low temperature it can reach and the long time for which such temperatures can be kept stable. A liquid ^{4}He bath in fact can be pumped to 0.1 mbar and will reach a temperature around 1 K. On the other hand, a pumped ^{3}He bath can reach temperatures as low as 0.3 K, but the limited supply and high cost of this cryogenic liquid make so that typical helium tank will be able to keep the temperature stable for no longer than a few hours. The ^{3}He-^{4}He dilution refrigerator overcomes both these issues; we will not cover here the theoretical principles of dilutions systems, details of which can be found in several specialized publications.[176,177]

Figure 5.7: Photograph of the TBT dilution cryostat as mounted at the UE46-PGM beamline in BESSY II (Berlin).

The system is made of two parts. An antecryostat consisting of an outer liquid N_2 tank and an inner liquid ^{4}He tank. The whole dilution refrigerator is mounted on an independent vertical insert at the end of which the sample is attached.

As briefly mentioned above, one of the peculiarities of this systems is that the sample area is adapted to UHV experiments; the system is not bakeable, nevertheless working pressures as low as 10^{-10} mbar are routinely reached in the sample chamber thanks to the efficient cryogenic pumping of the N_{2liq} and $^4He_{liq}$ antecryostats.

In a fully shielded chamber the cryostat can reach 30 mK on the sample; for XAS experiments however, the system must include windows that are transparent to the x-ray beam, thus reducing thermal insulation.

In addition, experiments in magnetism require an applied field, so the dilution insert is surrounded by a 70 kOe superconducting split coil mounted on a six-flange cross in the ^{4}He antecryostat. Applying of a magnetic induction though, induces eddy currents in the copper sample holder that also limit the minimum temperature. In normal conditions with x-ray photon flux on the sample and switching the magnetic induction, temperatures as low as 200 mK can be achieved, although thermal stabilization is hard to reach. At around 300 mK, the temperature can be constantly controlled over periods exceeding 20 h. Nitrogen and helium refills of the antecryostats must be carried out every 36 h and have no effect on the sample temperature.

Since the dilution refrigerator works in UHV, the device cannot contain exchange gas for the pre-cooling of the system. A dedicated circuit for the pre-cooling of the inserted device down to around 10 K is thus present. Another constraint of this system is that the sample change has to be made with the mixing chamber at room temperature. This requires heating up the whole dilution refrigerator (mixing chamber and still), so that the process of warming up the sample, changing for a new one and cooling it down to 300 mK takes around 12 hours. This is quite incompatible with the strict scheduling of beamtime in synchrotron radiation facilities: for this reason a special sample holder able to mount four samples was designed and built for our experiments.

We shall now describe more in detail the main parts of the dilution refrigerator:

The ^{3}He-^{4}He circuit   This part contains an injection section, a mixing chamber, and an evaporating/pumping section. In the injection section the ^{3}He-^{4}He mix, at 300 K and between 1 and 3 bars, is cleaned by means of a N_{2liq} trap where all contaminants, mostly water and pumping oil are removed. This cleaning process prevents the obstruction of the dilution capillaries. The ^{3}He-^{4}He gas is injected in fine tubes and is cooled by a heat exchanger connected to the ^{4}He antecryostat. Several impedances allowing JoulesThomson decompressions cool the fluid down to less than 1 K. Under 50 K, the isoenthalpic decompression of ^{3}He-^{4}He is endothermic.[174] This step is essential to obtain the phase dissociation. The use of an isoenthalpic decompression step makes it possible to avoid the 1 K pot that is mounted on most dilution setups. The phase separation, or dilution, between a ^{3}He rich phase and a ^{3}He poor phase takes place in the mixing chamber. This section is shown in Figure 5.8. The mixing chamber is the coldest part of the device and is responsible for the final cooling of the sample. The evaporation of ^{3}He takes place in the still,

which is situated over the mixing chamber. The extraction of ^{3}He from the ^{3}He-poor phase is most efficient at 800 mK: in order to maintain the still at this temperature, it is heated by resistance.

The sample holder is make of copper block and is fixed to the mixing chamber through a drilled sapphire. The sapphire allows thermal conduction and electrical insulation (> 500 GΩ); in addition a hole through the sapphire permits thermal contact between the ^{3}He-poor phase and the sample holder. Excellent electrical insulation is needed to have low noise in the total electron yield detection mode, which shall be described further in the text.

The volume and shape of the copper sample holder are optimized to minimize the power dissipated by the eddy currents created by magnetic field sweeping. Finally, ^{3}He evaporated from the still is removed by a pumping unit with a flux of 33 m^{3}h^{-1} at a pressure around 0.2 to 0.4 mbar. The pumped ^{3}He gas is then compressed between 1 and 3 bars and is re-injected in the setup.
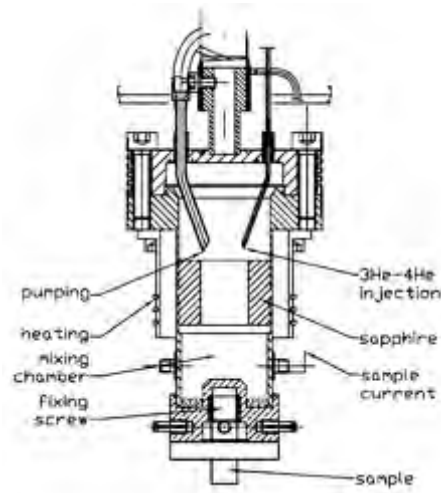
Figure 5.8: Schematics of the inner part of the dilution refrigerator.

The pre-cooling circuit As mentioned above, this component circuit is essential for UHV environment cooling. For normal operation, the heat exchanger of the antecryostat, the still, the mixing chamber, and the pipes connecting them have to be thermally isolated from each other. Since phase separation can occur only when the still and the mixing chamber are cooled below 4 K, pre-cooling is needed before the endothermic dilution can take place. For this purpose, a special ^{4}He circuit is used to inject gaseous helium at high pressure (310 bars). This circuit is made of a capillary winded around the heat exchanger of the ^{4}He antecryostat, the mixing chamber, and the still. The high-pressure ^{4}He gas is first cooled to 4 K by the thermal exchanger, then it

cools down the still and the mixing chamber. When the temperatures of the mixing chamber and the still are lower than 10 K, the helium gas is pumped out of the pre-cooling pipes so as to avoid thermal bridging between the heat exchanger of the ^{4}He antecryostat and the mixing chamber and still.

The temperature measurement systems   There are two types of temperature sensors mounted on the cryostat: for the temperature range between 300 K and 4 K silicon diodes are used, ruthenium oxide resistances are needed below 4 K. Si diodes are used on the sample holder to monitor the temperature from 4 to 300 K and on the heat exchanger of the antecryostat to monitor the cooling of the cryostat. RuO_2 resistances are used on the sample holder to monitor the temperature during the experiment and on the still to regulate the heating resistance. RuO_2 resistances can be probed with currents as low as nanoamperes, corresponding to a power dissipation of less than 10^{-10} W, a value that does not influence the temperature of the setup. Moreover, the sensitivity of RuO_2 resistances increases when the temperature decreases, resulting in very high sensitivity below 1 K.
Eddy currents caused by field ramping can cause he temperature to rise significantly in the millikelvin range: fir instance, at 300 mK, changing the magnetic induction from 0 to 50 kOe and back to 0 at a rate of 10 kOe/min make temperature reach 700 mK. The eddy currents responsible for this increase appear in the copper sample holder; in order to minimize this effect, great care was applied to design the sample holder so that eddy currents would be kept as low as possible. With this modification, and by decreasing magnetic induction sweeping rate down to 10 kOe/3 min t is possible to have a transient increase of the temperature of only 150 mK.

The detection systems   The TBT setup is equipped both with a Ge fluorescence detector able to pick up the signal originating from 7 elements

and a TEY detector systems that records the drain current with Keithley 617 electrometers. We will give a brief description of the principles underlying the latter system, since it is the one we have been using in all our experiments.

Photon absorption and subsequent photo-excitation of a core electron leads to the formation of a core-hole and short lived core excited states that can evolve though different relaxation processes. The two prominent relaxation processes are the emission of fluorescence photons and Auger electrons, as shown in Figure 5.9a. Photoionization occurring by loss of one electron from the core shells also relaxes through the same channels (Figure 5.9b). Since both fluorescence and Auger electron emission can reasonably be considered to be proportional to the photon absorption cross-section, a XAS spectrum can be generated by measuring the quantity of emitted photons or electrons as a function of incident photon energy.
The relative probability of each process is related to the atomic number (Z) of the elements present in the sample. For absorption edges below ~ 2000 eV,

which is the case of the edges we have been studying, Mn_{2p} and Fe_{2p}, Auger electron emission dominates the relaxation processes. The Auger relaxation process, schematized in Figure 5.9 consists in the emission of valence electrons that dissipates the energy lost by another valence electron that decays to the core levels in order to fill the core-hole: during the decay process the excess of energy released by the valence electron is transferred to another valance electron, the Auger electron, which is then emitted. TEY detection measures the drain current on the sample that is involved to restore electroneutrality. An additional detection technique, not found on the TBT setup, is Partial Electron Yield (PEY) that detects emitted electron by means of an electron detector in situated near the surface of the sample: such detection technique is not sensitive to greatly scattered electrons with low kinetic energy (hence the term 'partial). If the electron detector also performs energy analysis it is possible to discriminate the kinetic energy of the emitted electrons; by setting the energy window of the energy analyzer to a narrow range centered on the energy of the Auger peak, one can measure the Auger Electron Yield (AEY) as a function of excitation energy. All these detection methods are sensitive to the first layers of the inspected material, most of the signal coming from the topmost 2 nm, i.e. a much less than the penetration depth of the x-ray. This is due to the fact that Auger electrons are formed in the whole sample area that is reached by the photons, and give rise to an electron cascade, but only electrons emitted from the superficial layers can escape the sample.

TEY detection needs a normalization against a non-absorbing material to monitor the incident photon flux (I_0). How this is done depends on the features of the beamline, the most common method being measuring the drain current from a mesh located upstream from the sample. Normalization is then calculated as: $TEY = \frac{I}{I_0}$.
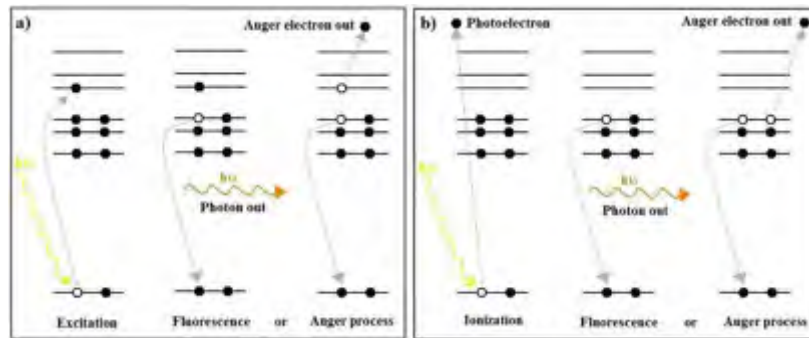
Figure 5.9: Diagram of the possible core-hole filling routes in the case of a) a quantized transition and b) photoionization.

5.4   Methods

5.4.1   XMCD measurement protocol

A XMCD spectrum is defined as the difference between two spectra acquired with opposite photon polarizations on a sample whose spins are mainly oriented in one direction, or spectra recorded with the same photon helicity and opposite spin polarization of the sample. A standard set of spectra that are necessary to properly calculate one XMCD spectrum is made up of 8 acquisitions: four are carried out while applying a positive external field (i.e. polarizing the spins in one direction) and four in a negative field (spins polarized in the opposite direction.). For each of the two field directions, photon helicity is varied twice. When field and photon helicity have the same sign (photon helicity is taken to be positive according to the right hand rule), the spectrum is called *positive* (σ^+); if field and photon polarization are of opposite sign, the spectrum is referred to as *negative* (σ^-). A typical acquisition cycle is carried out in the following order:

Photon helicity	Applied field	Resulting spectrum
+	+	σ^+
−	+	σ^-
−	+	σ^-
+	+	σ^+
+	−	σ^-
−	−	σ^+
−	−	σ^+
+	−	σ^-

Table 5.1: The complete XCMD acquisition pattern

The order of such sequence is important, since it is able to partially cancel the influence of parameters that vary regularly and in the same direction with time (i.e. drifting), since each type of spectrum is acquired twice and in such a way that drifting is canceled by averaging around a mean value; this principle is explained in Figure 5.10.

This series of 8 spectra is the minimum repetitive unit to acquire a XMCD spectrum; however, when the signal is very weak, as in the case of monolayers, several acquisitions need to be carried out in order to increase signal to noise ratio to an acceptable level.
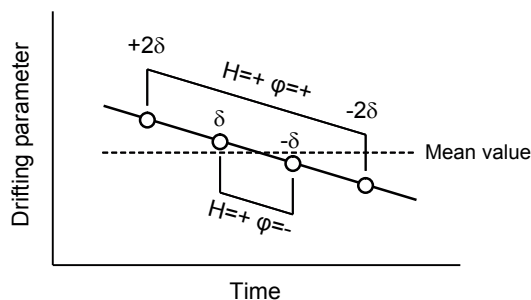
Figure 5.10: Schematic picture of error canceling through the acquisition sequence shown in Table 5.1.

5.4.2 Hysteresis and time decay measurement protocol

The XMCD signal is proportional to the number of orbitals that are populated by one electron with a certain spin value thus, provided that the XMCD peak under analysis does not overlap with other signals, it can be considered proportional to the magnetization relative to a single atomic species. It is then possible to follow the variation of the XMCD signal while changing a different parameter (such as applied field, temperature, or simply time), thus performing experiments that are analog to the standard magnetometric ones.
In order to pick the correct signal, the raw drain current (I) on the sample at the XMCD peak must be normalized against I_0, as already mentioned; in addition to this though, a further normalization must be carried out to measure a signal that has physical meaning. XMCD intensity must be acquired as the magnitude of the edge jump, so the peak signal needs to be divided by the signal of the pre-peak (usually ~ 10 eV before the peak, but the exact position must be evaluated from each spectrum), thus obtaining:

$$I_{XMCD} = \frac{{}^{norm}I_{peak}}{{}^{norm}I_{prepeak}} = \frac{I_{peak}/I_{0peak}}{I_{prepeak}/I_{0prepeak}}. \tag{5.16}$$

Indeed, for such experiments the method used by the beamline for polarization switching is a key factor in the quality of the measurement. In standard beamlines, the two polarizations are switched by changing the relative horizontal position of the permanent magnets of the undulators: the typical time scale of this process is around one-two minutes, which is a relatively long time if one thinks it multiplied by the number of points of a normal magnetization measurement. For this reason, a magnetization curve based on XMCD signal is typically recorded first with one polarization by sweeping the field, then with the other polarization at the energy of the XMCD maximum, then the process is repeated for the pre-peak energy; this is the acquisition method we used for our measurements at UE46-PGM in BESSY II.
It is quite clear that such method is prone to every type of instability that can

easily have dire consequences on the quality of the measurements, especially when working with the very weak signal of a monolayer of magnetic material; nevertheless, using great care and abundant averaging it was possible to make good static magnetic measurements with this setup.

However when it comes to dynamic experiments, in highly diluted and fast relaxing magnetic systems like monolayers of SMMs, standard polarization switching becomes a limiting factor in the performance of the whole setup. While some beamlines are developing fast polarization switching IDs based on electromagnets (like DEIMOS beamline at SOLEIL synchrotron, Paris F) that can reach switching rates of a few Hz, an already established method that has been adopted in beamline SIM X11-MA at SLS, Villigen CH is that of using two similar undulators, set to deliver opposite polarizations, that are alternatively tuned and detuned (by moving the gap of about 2 mm).

This process, that is shown in Figure 5.11 compared to standard operation mode, takes merely few seconds to change photon helicity on the sample and allowed us to design a different acquisition pattern for magnetization curves. For each applied field value, both polarizations were acquired in sequence; at the end of the field scan the same procedure was applied to the pre-peak signal. This allowed us to have particularly good quality data, since each value of the XMCD signal came from the system that was in one single state, at variance with the previously described method, in which every XMCD signal came from two different field scans.

In the case of time decay measurements, the signal relative to the two opposite polarizations was recorded alternatively at regular time intervals. For this type of measurement, even more than for hysteresis loops, tune/detune fast polarization switching, coupled to the extreme beam stability at SLS, proved to be a necessary condition for the success of the experiment.
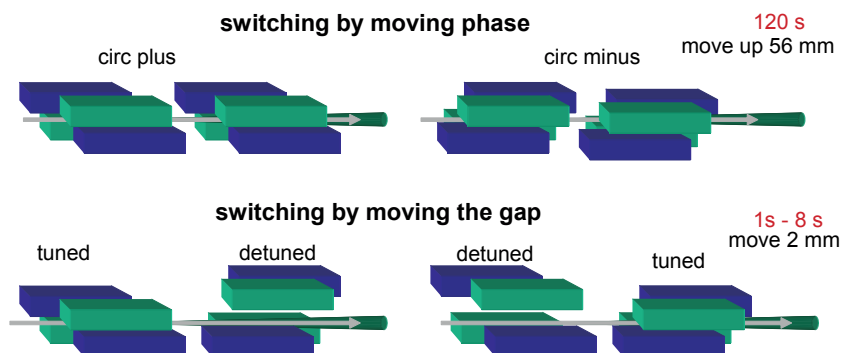
Figure 5.11: Diagram of the two polarization switching modes a) by moving phase and b) by moving the gap.

5.5   Measurements on Mn12 monolayers

The archetypal single molecule magnet Mn12 was the first complex of this class of molecules that was functionalized to be grafted to surfaces, as we have widely described in Chapter 2.4. The experience of our group in this field dates back to 2003[64] and the possibility to bind these molecules to gold surfaces without altering its size and shape, and maintaining the chemical composition (in terms of relative elemental abundance) is quite well known and established. If we add that Mn12 features one of the highest blocking temperatures[d], it is no wonder that we, and other few groups more or less in parallel, chose this particular SMM as a first candidate as a starting ground for the study of monolayers with synchrotron radiation.

When our XAS-XMCD study on the archetypal Mn12Ac derivatives began, XAS studies had already been carried out by Moroni *et al.*[178] and Ghigna et al.[179] on bulk samples of the archetypal Mn12Ac, that were a useful starting point for our investigation. We started our work from the study of monolayers of Mn12 on gold. The two derivatives that were chosen for grafting were those that appear in most of our work in the field, Mn12C15SAc[64] and Mn12PhSMe.[54,85]

### 5.5.1   Preliminary study on bulk standards

Preliminary experiments were carried out at beamline UE46-PGM situated in BESSY II synchrotron radiation facility in Berlin. Measurements were carried out using the TBT endstation described in section 5.3.4, allowing us to operate at temperatures lower than 1 K. We first performed experiments measuring spectra of the Mn $L_{2,3}$ edges on a series of bulk microcrystalline samples in order to obtain a standard set of data to get a reliable comparison base. In particular, we studied in depth Mn12PhSMe as it is one of the two complexes that we used to prepare the monolayers studied.[180] Since it is known both from DFT calculations[181] and experimental observations that Mn12 complexes are rather unstable toward reduction to Mn^{2+}, we also studied a one-electron reduced Mn12 derivative, $(PPh_4)[Mn_{12}O_{12}(O_2CPh)_{16}(H_2O)_4]$ (hereafter Mn12Red); in this way we were able to inspect the properties of a Mn^{2+} species in one of the Mn^{3+} sites of the complex:[178,179] by measuring a controlled one-electron reduced Mn12 derivative is a good way to probe the sensitivity of XAS and XMCD measurements in spotting possible reduction, due to photon flux or other causes.

UE46-PGM is a soft x-ray insertion device-based beamline, which can deliver linearly and circularly polarized photons by means of an Apple II undulator. In the energy range of Mn $L_{2,3}$ edges, the undulator's third harmonic is monochromated by meas of a plane grating mirror. When making measurements on these

---

[d]The second better performing SMM in terms of blocking temperature at the time this thesis was written was a Mn-based complex reported by Christou's group.[5]

samples we tried to avoid the effect of photoreduction by carefully setting the beamline parameters in such a way to shine on the sample a flux that would not cause any time evolution of the acquired spectra over at least 10 hours of measurement. In particular, we acted on the cooled apertures downstream the undulator by setting them to 0.2×0.2 mm^2, while the monochromator's exit slit has been set to 20 μm; parallel beam on the sample was obtained by means of a defocusing mirror. Cooled aperture and exit slits cut the photon flux by factor of 500, while the parallel beam toroidal mirror lowered the photon density on the sample by an extra factor 400.

Spectra were acquired both in the liquid helium range of temperatures (4.2 K) and in the sub-Kelvin range, by means of the dilution insert of the TBT setup. XMCD spectra were obtained as the difference of two sets XAS spectra with photon helicity parallel and antiparallel to the external field respectively; data for Mn12PhSme is shown in Figure 5.12. The spectra indicated as XAS are in effect the isotropic spectra (i.e. the average of the two dichroic spectra); this formalism shall be adopted throughout the text.
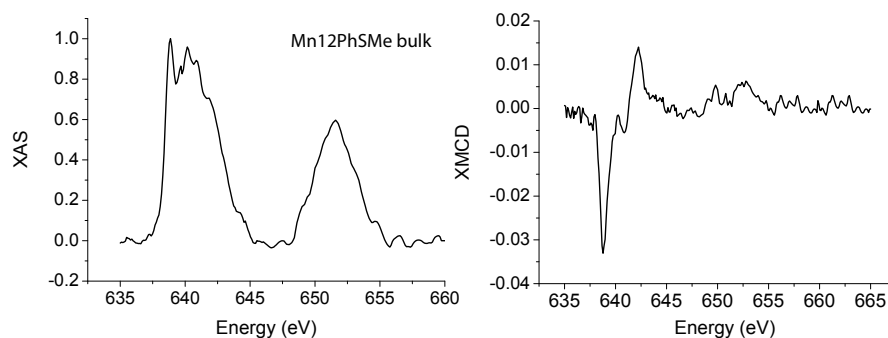
Figure 5.12: XAS (left) and XMCD (right) spectra of a microcrystalline sample of Mn12PhSMe.

The XAS spectra of the two compounds are very similar, and XMCD spectra have some naked eye-observable differences in the area of 640 eV. In order to extract more precise information on the spin structure though, some type of fitting must be carried out, to correlate the different relative intensities of the Mn transitions to the oxidation number distribution and spin polarization of the inspected system.

A widely used method for the analysis of XAS and XMCD spectra is the use of the so called sum rules:[167] these allow to enucleate the spin and orbital contributions to the total magnetic moments of the atoms. In the case of Mn12 though, the simultaneous presence of different oxidation states of the adsorber and the overlap of the bands related to $2p^6 3d^n \rightarrow 2p^5 3d^{n-1}$ make this approach poorly suited for the purpose.

To analyze the spectra instead we chose a semi-empirical approach: we fit-

ted experimental data with of linear combinations of experimental spectra of reference compounds: XAS and XMCD data of Mn^{2+} ions were taken from a previous work by Arrio *et al.*,[182] while Mn^{3+} and Mn^{4+} from Moroni's work,[178] with all polarizations of the spins parallel to the applied field. Reference spectra are reported in Figure (α = II, III, IV). In order to apply this type of analysis, all reference signals need to normalized in terms of intensity: the data were thus normalized to the experimental conditions of used for the acquisition of our data, that is a degree of polarization of 80%, temperatures of 4.2 and 0.5 K and magnetic inductions of 4 and 20 kOe. In particular, the dichroic signal is assumed to scale linearly with the degree of polarization and to variate according to a simple Brillouin function with temperature and applied field. By normalizing in such a way, we were able to maintain the original relative intensities of XAS and XMCD signals.

The experimental spectra of reference compounds were combined according to the following relation:

$$I(E) = \Sigma_\alpha c^\alpha I^\alpha(E) \tag{5.17}$$

where I is the intensity of the absorption, α runs over the three oxidation states (α = II, III, IV) and c^α is the minimized parameter. The values of c^α give information on the relative abundance of the different valence states and percent values P_α can be thus extracted:

$$P_\alpha = 100 \frac{c^\alpha}{\sum_i c^i}. \tag{5.18}$$

This approach was used to elaborate the XAS spectra of Mn12Red; The fitted spectrum, along with the experimental data, is reported in Figure 5.13, while P_α values for the different valence states extracted from the fitting are shown in Figure 5.19, page 158, and are in good agreement with the expected ones.

XMCD spectra were analyzed using a similar approach in order to gain semi-quantitative information on the orientation of magnetic moments in the single oxidation states. The energy dependence of the dichroic signal, $S(E)$, is expressed as a linear combination of of model spectra for each oxidation state S_α normalized, as done for the isotropic parts, according to the formula:

$$S(E) = \Sigma_\alpha c^\alpha \delta^\alpha S^\alpha(E) \tag{5.19}$$

where α runs over the oxidation states, c^α are the coefficients resulting from the deconvolution of XAS spectra, and δ^α accounts for the average polarization of the local magnetic moment in the applied field (positive if parallel to the field).

We first compared the experimental XMCD spectrum of Mn12PhSMe to a simulation in which the four Mn^{4+} ions are combined antiparallel to the eight Mn^{3+} centers, thus resembling the actual spin distribution of Mn12, driven by
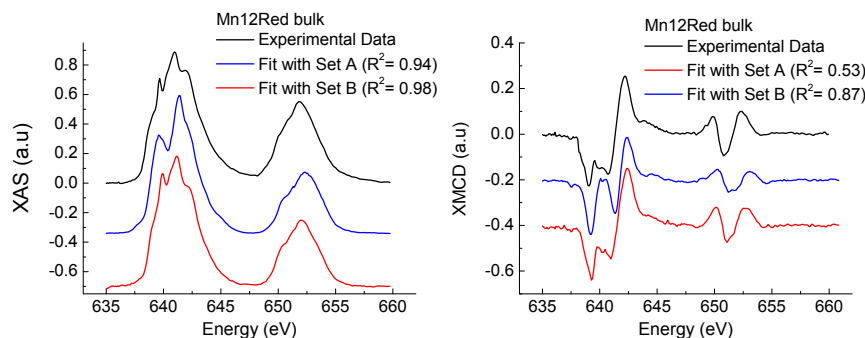
Figure 5.13: Experimental XAS (left) and XMCD (right) spectra of Bulk Mn12Red compared to the fittings obtained using Set A and Set B.

antiferromagnetic coupling between Mn^{4+} and Mn^{3+} ions; the simulation is in quite good agreement with the experimental data.

We can then conclude that discrimination between types of coupling between Mn ions in different oxidation states is achievable with this method. With these simulations we can also obtain information on the XMCD spectral regions that are mainly involved in the coupling type: the most prominent sign for AF coupling is the shape of the positive XMCD signal in the energy range between 642 and 645 eV. The signature of the ferrimagnetic spin structure is the sharp positive XMCD signal in the energy region between 641.5 eV and 645 eV.

The analysis of the XMCD data for Mn12Red provided the following values for the polarization: $\delta^{II} = +3$, $\delta^{III} = +1$ and $\delta^{IV} = -1$. These values are very rough estimates (δ^{II} in particular, since the value of c^{α} is very small), but their sign is in agreement with the spin structure of Mn12Red suggested by the large spin of the ground state.[63,183]

A simulation of a fully uncoupled situation ($\delta^{II} = \delta^{III} = \delta^{IV} = +1$) has been carried out as well, in order to check the sensitivity to coupling patterns in XMCD. As can be seen in Figure 5.14, there is no agreement between the fully polarized spectrum and the experimental data.

Taking a step backward, we analyzed more in depth the agreement of the fine features between the experimental XAS spectra of the two compounds and the fittings, and found that it was not fully satisfactory. We then used a different source for the Mn^{3+} reference spectrum, that we obtained by subtracting the Mn^{4+} contribution from the spectrum of Mn12PhSMe shown in Figure 5.12; this was done by using the sum rules,[184] in agreement with the observation that the electronic structure on Mn12 can be accessed by means of XAS and XMCD. In particular, extrapolated XAS and XMCD contributions were calculated using the relation:
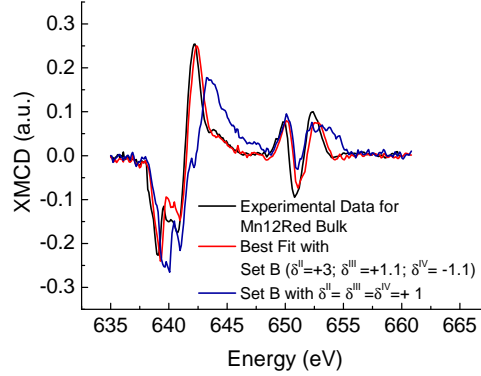
Figure 5.14: Experimental XMCD spectrum of Mn12Red compared to calculated spectra obtained with best fit parameters and simulating full decoupling between Mn^{2+} Mn^{3+} and Mn^{4+} species. Employed data are Set A.

$$I^{III}(E) = (12I^{12}(E) - 4I^{IV}(E))/8 \qquad (5.20)$$
$$S^{III}(E) = (12S^{12}(E) + 4S^{IV}(E))/8,$$

where I^{12} and S^{12} indicate respectively XAS and XMCD spectra of Mn12PhSMe. A further step in the normalization of the spectra must be carried out to take into account the number of holes h in the systems by using the following formula:

$$h = Sc^{\alpha} \times h^{\alpha}/Sc^{\alpha}, \qquad (5.21)$$

in which h^{α} indicates the number of holes of the oxidation state α. For the case of Mn12, equation 5.21 becomes:

$$h = Sc^{12} \times h^{3}/12 = 6.33. \qquad (5.22)$$

The standard spectra we have just described are shown in Figure 5.15. Further in the text, we shall refer to the combination of independently measured Mn^{3+} and Mn^{4+} as Set A, while the combination of spectra that uses the Mn^{3+} signal extrapolated from the experimental spectrum of Mn12 is tagged as Set B. When necessary, Mn^{2+} was added in the calculations, and it shall be specified in those cases.

In this section we have described measurements carried out in reference bulk samples of Mn12 and its one-electron reduced derivative; we also have discussed the development of a solid analysis method that allows us to extrapolate both
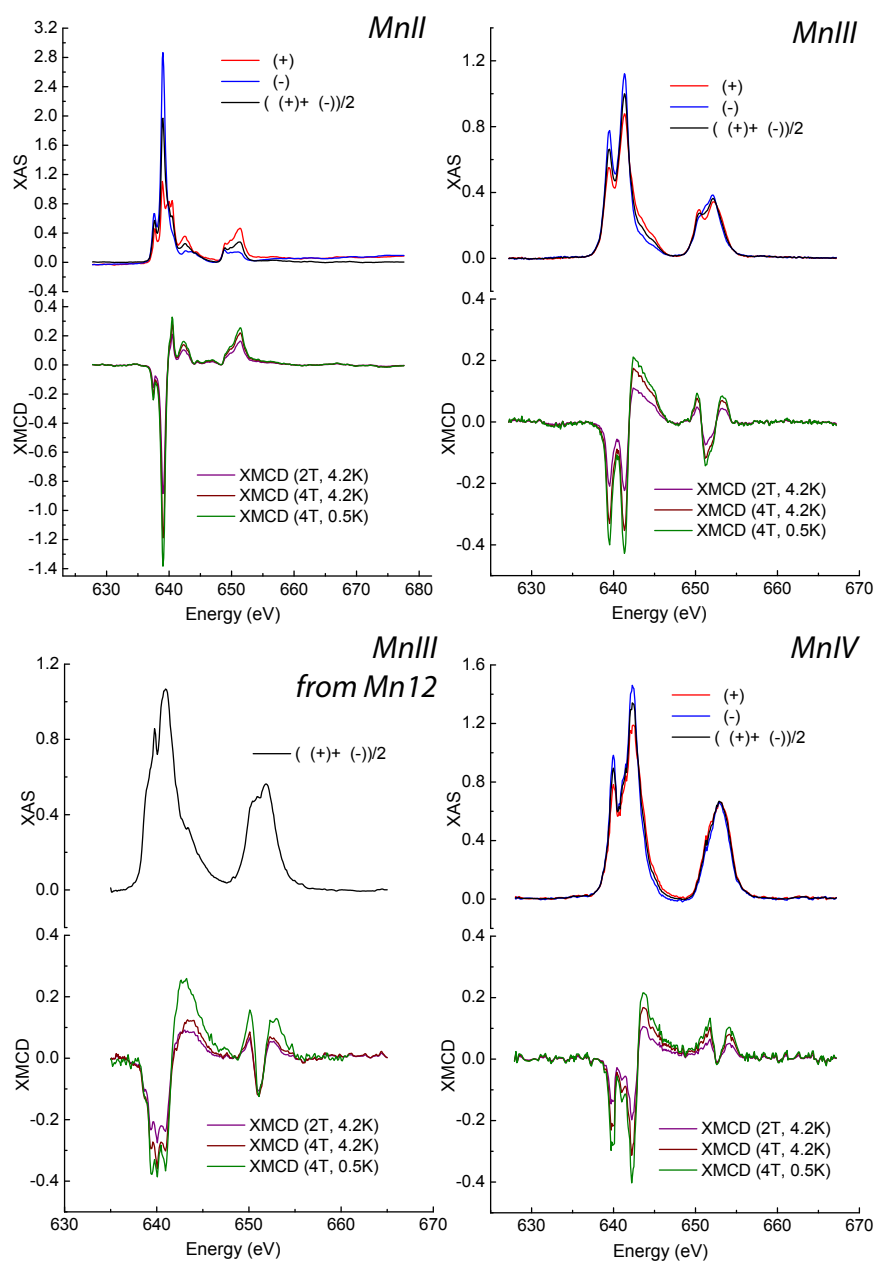
Figure 5.15: XAS (top) and XMCD (bottom) standard spectra used in the fitting calculations; all data are normalized for three sets of conditions: 20 kOe and 4.2K, 40 kOe and 4.2K, 40 kOe and 0.5K. Mn^{3+} is reported both from independent data and as extrapolated from the Mn12PhSMe spectrum.

relative oxidation state abundance (from XAS) and degree and direction of polarization for each oxidation state (from XMCD). We can now move to the more tricky task of making measurements on monolayers of these SMMs.

## 5.5.2 Mn12PhSMe and Mn12C15SAc monolayers

The extreme sensitivity of x-ray adsorption spectroscopy, in particular when coupled to the surface specificity of total electron yield mode detection, allowed us to study Mn12 adsorbates even if manganese ions are present in very low amounts on the gold surface (significantly less than 1 ML, considering that a good portion of the surface is occupied by organic ligands).
The choice of Mn12 derivatives used in this study[180] is motivated by the fact that Mn12C15SAc[64] and Mn12PhSMe[54] are the most deeply studied derivatives for surface grafting in our laboratories, and are differentiated by the nature of the ligands that separate the core of the cluster form the gold surface: in the former they are made of a long, insulating and flexible alkyl chain, while in the latter a short aromatic moiety acts as a conducting rigid spacer. This difference was thought to possibly have a role in the interaction of the magnet with the metallic surface of the substrate.
Monolayers of the first derivative, Mn12C15SAc, were prepared from THF solutions according to the standard preparation method under nitrogen atmosphere inside a portable glove bag; the samples were then loaded into the fast entry system of the TBT setup directly from the glove bag, in order to minimize atmospheric contamination.
XAS and XMCD spectra of the system are reported in Figure 5.16, along with their fittings using Set A and Set B reference data (experimental conditions: $T = 4.2$ K, $H = 20$ kOe): even if these spectra have some similarities to those of bulk Mn12 derivatives, a significant fraction of Mn^{2+} is observed. By fitting the observed intensities using the method described in last section, we obtain a ratio between Mn^{2+}, Mn^{3+} and Mn^{4+} contributions of $25 : 55 : 20$ using Set A and $20 : 65 : 15$ with Set B. This suggests a significant modification of the electronic structure, with an alteration of the average oxidation state from $+3.33$ in neutral Mn12 to $+2.95$. Comparison with the data obtained on Mn12Red (Figure 5.13) clearly indicates that the process cannot be described as a one electron reduction. Also, if we compare the found oxidation state ratios with those of bulk Mn12PhSMe (our standard), $0 : 67 : 33$, we can infer that the reduction to Mn^{2+} takes place mainly at the expense of Mn^{4+} sites, in contrast with the established redox behavior of bulk Mn12 complexes described for Mn12 Red.[185]

We then carried out measurements on monolayers of Mn12PhSMe: as we have pointed out in Chapter 2.4, the solvent used to dissolve this derivative has a dramatic effect on the quality of the adsorbate. In particular, THF solutions of Mn12PhSMe yield isolated molecules (**exTHF**), while DCM (**exDCM**) gives a tightly packed full layer of Mn12 units. XAS and XMCD spectra of the (**exTHF**) monolayer are shown in Figure 5.17, along with their fittings with
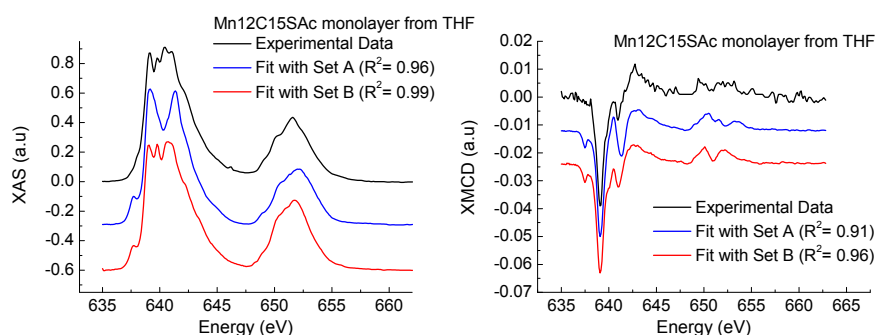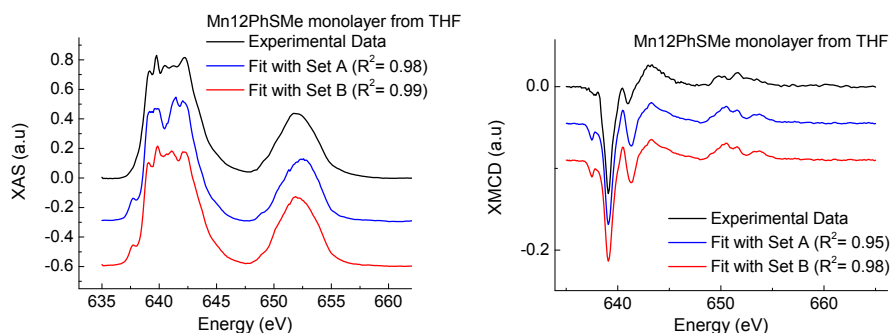
Figure 5.16: Experimental XAS (left) and XMCD (right) spectra of a Mn12C15SAc monolayer compared to the fittings obtained using Set A and Set B.

Set A and Set B reference data. The spectra were acquired at $T = 4.2$ K and $H = 40$ kOe.

Fitting with Set B gave a 20 : 40 : 40 ratio of oxidation states for an average oxidation number of $+3.20$ for Mn. The percentage of Mn^{2+} is substantially the same as in the Mn12C15SAc monolayer, but in this case the reduction seems to occur at Mn^{3+} sites instead of Mn^{4+} sites. The higher Mn^{4+}/Mn^{3+} ratio in **Mn12PhSMe-exDCM** as compared with Mn12C15SAc is clearly reflected in the greater extension of the L_3 edge on the high energy side. We can then conclude that, even if the reduction process seems to proceed through different pathways in the two systems, different ligands do not provide any particular shielding to the Mn12 core, since the percentage of Mn^{2+} is basically the same in the two systems.

High coverage monolayers obtained from DCM solutions **Mn12PhSMe-exDCM** were analyzed under the same conditions of the previous systems; XAS and XMCD spectra are shown in Figure 5.18 ($T = 0.5$ K, $H = 40$ kOe), where fittings made using both Set A and Set B reference data are shown. The analysis of the XAS spectrum provided and $Mn^{2+}:Mn^{3+}:Mn^{4+}$ ratio of 30:50:20, corresponding to an average oxidation state of $+2.90$. The significant reduction of the Mn^{4+} contribution bears strong resemblance with the results obtained for monolayers of Mn12C15SAc deposited from THF. In effect, STM analysis of that sample[64] revealed very similar morphological features to the **Mn12PhSMe-exDCM** monolayers described in Chapter 2.4: both systems feature a high degree of surface coverage and a relatively weak interaction of the adsorbed molecule to the substrate. This analogy, coupled to the similar reduction pathway (at the expense of Mn^{4+} in both cases), suggests that the strength of the interaction of the cluster with the surface might have a role in

Figure 5.17: Experimental XAS (left) and XMCD (right) spectra of a **Mn12PhSMe-exTHF** monolayer compared to the fittings obtained using Set A and Set B.

the type of transformation the molecules undergo upon grafting.
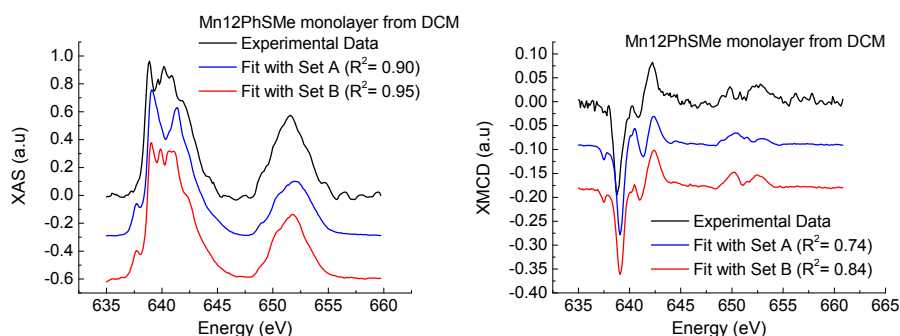
Figure 5.18: Experimental XAS (left) and XMCD (right) spectra of a **Mn12PhSMe-exDCM** monolayer compared to the fittings obtained using Set A and Set B.

As a last observation on the XAS of monolayers of Mn12 on gold, we report that a similar XAS spectrum to those reported herein (in particular to that of **Mn12PhSMe-exTHF**) and quite distinct from that of bulk Mn12 was obtained by Voss *et al.* for another Mn12 derivative (R=Ph-Ph) deposited on Au(111) using a completely different procedure, namely ligand exchange on a preformed monolayer of 4-mercapto-2,3,5,6-tetrafluorobenzoic acid;[186] a quantitative data analysis was not attempted by those authors, but this similarity suggests that core reduction cannot be considered a specific consequence of our

deposition procedure.

The analysis of dichroic spectra for the three monolayers was carried out using the same procedure described in the previous section. For all samples we were able to extract information on the degree and direction of polarization of each type of Mn ion, even is values are quite approximate. Data reported in Figure 5.19 and summarize all found degrees of polarization along with relative oxidation states percentages, both with Set A and Set B of reference data.

First of all, an apparent reduction of the degree of magnetic polarization is observed in monolayers of Mn12C15SAc and Mn12PhSMe are deposited from THF. We can rule out total fragmentation of the clusters to isolated paramagnetic ions in the temperature and field conditions of the experiment; in this case in fact the XMCD spectrum would give full polarization $\delta^{II} = \delta^{III} = \delta^{IV} = +1$.

In our case instead, Mn^{2+} ions feature a small magnetic polarization and are presumably exchange-coupled species (at least part of them) even if the degree of polarization is different from that observed in Mn12Red, the one-electron reduced derivative. It must also be pointed out that in both monolayers obtained from THF the negative polarization of Mn^{4+} disappears (i.e. Mn^{4+} ions are polarized parallel to the applied field), thus loosing what is considered to be the fingerprint of the Mn12 spin structure.

In the case of **Mn12PhSMe-exDCM** instead, larger polarizations are detected and the magnetic moment residing on Mn^{4+} ions is antiparallel to the applied field. The observed behavior is reminiscent of the spin structure of Mn12 clusters, although the fraction of Mn^{2+} ions can be quantified from the fitting of the XAS spectrum to be around 30%, which is a higher value than that found for adsorbates obtained from THF solutions.

The XMCD signal was recorded as a function of the applied field at 641 eV, the energy at which XMCD amplitude is maximum for Mn12 clusters. By sweeping the field between ± 50 kOe, no hysteresis was observed down to the lowest temperature reached in our experiment (T$\simeq 500$ mK).

In conclusion, the present investigation confirms that grafting large molecular clusters on conducting surfaces is not a straightforward process and is accompanied by significant modification in electronic and spin structures, which are not detected by standard surface characterization. In particular, although XPS and STM investigations suggest that intact Mn12 clusters are present as monolayers on the gold surface, the XAS reveals a systematic, partial reduction to Mn^{2+}. The XMCD analysis suggests that these Mn^{2+} ions are not present as isolated paramagnetic species and that the magnetic polarization at metal sites is decreased as compared with bulk complexes. Our results are therefore still compatible with the hypothesis that reduction of deposited clusters does not dramatically alter their chemical composition and size. The observed XAS and XMCD spectra indicate that the involved process is not a simple one-electron transfer from the substrate. Furthermore, the details of the reduction (average

Figure 5.19: Synoptic table of the relative oxidation state abundance and degree of polarization of Mn12 samples, calculated using Sets A and B.

oxidation state and ratio of oxidation states) are very sensitive to the adopted deposition protocol.

The analysis reported herein demonstrates the potential of a combined use of XAS and XMCD to characterize magnetic molecular materials at surfaces. Studies can be carried out without significant sample damage, while retaining sufficient sensitivity to probe monolayers and even submonolayers of molecules.

5.6 Bulk phase XMCD studies on Mn12 and Fe4

5.6.1 Motivation

The finding that Mn12 monolayers fail to maintain their chemical integrity is an issue that can certainly be regarded as a major obstacle to the exploitation of this complex on surfaces. Nevertheless this could also be considered to be an extreme justification for the absence of magnetic memory effect of such monolayers: in fact even if the measurements we carried out suggested that at least part of the molecules in the **Mn12PhSMe-exDCM** systems had maintained their integrity, the presence of great quantities of Mn species resulting from degradation is far from being a safe landscape to asses the absolute incompatibility of the molecule with surface grafting.

The method that we developed to adsorb Mn12 clusters to gold is in fact one that we considered to be valid and reproducible, at least before XMCD experiments were carried out on the resulting adsorbates. At any rate, it is still a method that is based on grafting from solution and, even if the portable glove bag setup is able to preserve the prepared sample from the atmosphere until it is mounted in UHV, these conditions are far from being fully protective toward the adsorbed molecules; in addition it must be considered that the grafting method itself could bear some incompatibility with the Mn12 core that is directly related to the adsorption process.

Other groups found similar alterations in monolayers of different Mn12 derivatives[186] grafted by using rather different techniques; as a consequence, some effort was taken by them in optimizing the deposition method in order to avoid disruption of the cluster.

We decided to tackle the question from a different point of view,[187] by making a step backward: considering that our knowledge on the XAS and XMCD properties of Mn12 in its bulk phase are quite well established, both on the basis of previous work[178,179] and from our studies carried out at BESSY II (described in the previous section), we decided to devote some beamtime at the SLS synchrotron radiation facility (Villigen, CH) to the study of the dynamic magnetic properties of Mn12 in drop cast deposits, i.e. in its bulk phase.

On the other hand, we thought that some seminal studies on the bulk phase of the Fe4C9SAc complex were needed in order to explore its potential as new SMM for XMCD investigation in the monolayer regime. Therefore, we studied

in parallel the behavior of this Fe4 derivative in drop cast deposit with the same set of experiments as Mn12PhSMe.[187]

5.6.2   Drop cast Mn12PhSMe

Samples were prepared as described before for XPS and ToF-SIMS investigations, by depositing a drop ($\sim 50 \mu l$) of millimolar solutions on a mica-supported gold substrate and allowing it to evaporate under nitrogen atmosphere in a portable glove bag. The samples were then directly transferred from the glove bag to the fast entry system of the cryostat.

We started our experiment by optimizing the beamline's settings in order to shine a relatively small number of photons on the sample, so as to avoid photodegradation. No time evolution of the XAS and XMCD spectra was observed throughout the experiment time.

The first efforts were taken to obtain XAS and XMCD spectra that were in line with what had been previously observed for this type of sample in BESSY II and with the studies on the un-functionalized Mn12 cluster (Figure 5.20. The series of spectra were acquired at $H = \pm 30$ kOe and at $T = 0.75$ K; we settled at a rather low temperature in order to be working widely within the temperature range in which the Mn12 clusters behave as SMMs. From the XAS and XMCD data one can assess that no degradation to Mn^{2+} has occurred, and the spin structure of the Mn core is intact.

After finding the exact energy at which the XMCD signal is maximum (643.0 eV, indicated with an arrow in Figure 5.20), we recorded hysteresis loops between ± 50 kOe at the same temperature as that at which XAS and XMCD spectra were acquired. The magnetization curve shown in Figure 5.21, averaged over all the measured ones, clearly denotes the absence of hysteretic behavior in the sample. It is important to stress the fact that in the present case no dirsuption of the cluster is detected in the XAS spectrum.

In order to get some insight in the anomalous behavior of the sample we compared field-dependent XMCD data to the predicted bulk magnetization at the same temperature as a function of applied the field. The magnetization was evaluated using the energy levels calculated from the simple Spin Hamiltonian

$$\mathcal{H} = DS_Z^2 + g\mu_B \mathbf{H} \cdot S \tag{5.23}$$

where $\mathbf{H}$ is the magnetic field, g the Landé factor, μ_B the Bohr magneton, and $D < 0$ describes the easy-axis magnetic anisotropy. The magnetization was averaged over all possible field orientations, as appropriate for randomly-oriented clusters. The values of these parameters were taken from the fitting of measurements carried out on a bulk sample of Mn12PhSMe and are: $S = 10$, $D/k_B = -0.66$ K and $g = 2.00$.[17] The curve calculated in this manner, shown as a continuous line in Figure 5.21, is clearly very different from the experimental data: in particular, the latter increases less abruptly at low field, suggesting
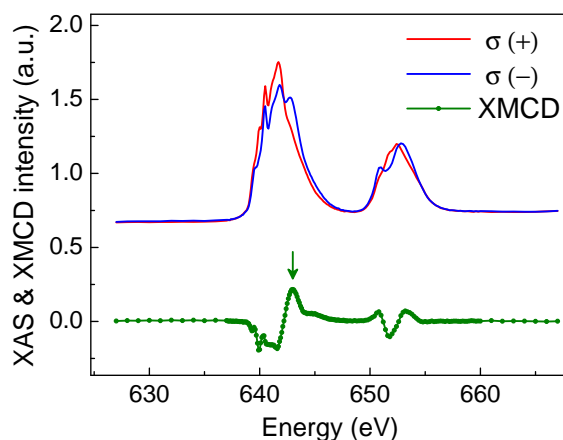
Figure 5.20: XAS and XMCD spectra of Mn-$L_{2,3}$ edges of a drop cast sample of Mn12PhSMe measured at 0.75 K and ± 30 kOe.

that the molecules in the first layers experience a reduced anisotropy[e], even if no changes in the oxidation states are detected by the XAS investigation.

In order to ascertain that no modification accompanies the drop cast deposition process, the same sample was later tested by means of standard magnetometry. The hysteresis loop recorded on a VSM magnetometer (Oxford Instruments MAGLAB2000) is shown in Figure 5.22 and regular opening of the hysteresis can be observed already at temperatures around 2 K, as expected for Mn12 derivatives.

Comparing the two sets of data coming from XMCD and VSM might cause some distress in the the first place, since both techniques seem to agree on the point that the complex is not damaged; nevertheless, they definitely diverge on the ground of dynamic magnetic properties. What emerges from this comparison is instead probably one of the most fascinating effects described in this thesis. We must consider first of all that there is a topological difference in the probing method of the two techniques: while standard magnetometry detects an induced current that is due to the whole object moving through the pick-up coils, TEY detection is specific for probing the first few layers of materials, since all physical phenomenons involved in this kind of detection are in a way or another related to electron escape depth (see section 5.3 for details). We must then conclude that failure of Mn12PhSMe to behave as a slow relaxing magnet only concerns the first few layers of material of the drop cast deposit, the ones

---

[e]The magnetic response of a sample in function of the applied field is related to the spacing between spin energy levels, which in turn depends in SMMs on the degree of axial anisotropy.
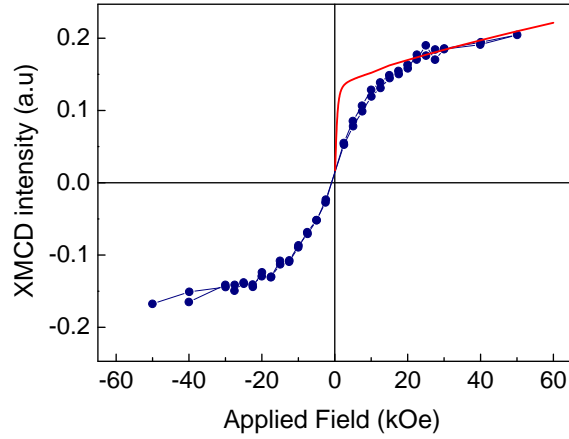
Figure 5.21: Hysteresis curves of a drop cast sample of Mn12PhSMe measured with XMCD in TEY detection mode at 0.75 K (straight line represents the simulation obtained as described in the text).
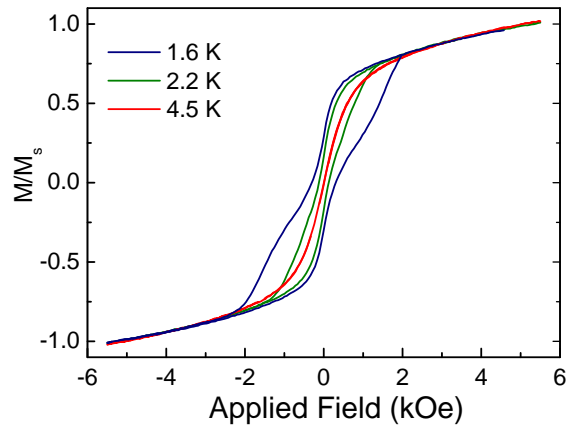
Figure 5.22: Hysteresis curves of a drop cast sample of Mn12PhSMe measured with VSM magnetometry at various temperatures.

facing UHV, and that these layers are by no means chemically damaged by the fact of being superficial, as testified by full XAS and XMCD spectra. A very nice confirmation of this conclusion would have been the possibility to observe XMCD hysteresis in x-ray fluorescence detection mode, since this technique probes a greater depth of the sample, thus giving access to the XMCD properties of the underlying layers of material; unfortunately, while TBT endstation is equipped with fluorescence detectors, these work at a temperature of 77 K, so the thermal shielding of the sample space would be highly impaired by the opening of the detector window, thus making very low temperature fluorescence measurements impossible.

The loss of slow relaxation of the magnetization in the topmost layers of deposit without any actual degradation of the inorganic core of Mn12 can be explained considering that the energy barrier that originates makes spin re-equilibration slow is the result of a delicate interplay between electronic and structural parameters of the single metallic centers and their mutual interaction: the surface, even that of the material itself, is a strongly asymmetric and strained environment, and it is very reasonable to suppose that these strains are more than enough to cause distortions in the clusters that are fatal, if not to the spin coupling pattern, to the degree of axial anisotropy of the complex. For instance, it is enough that one single Mn^{3+} ion has its Jahn–Teller elongation axis flipped onto the plane perpendicular to the easy axis of Mn12 that the axial anisotropy is lowered and the energy barrier decreased, thus leading to a faster relaxation of the magnetization.[57] Figure 5.23 shows the flipped elongated axis; such J-T isomer is usually found to be present along with the standard isomer with higher anisotropy in crystalline samples of some Mn12 derivatives, and can clearly be spotted in χ_1 and χ_2 plots of an AC measurement as distinct, faster relaxing peaks.
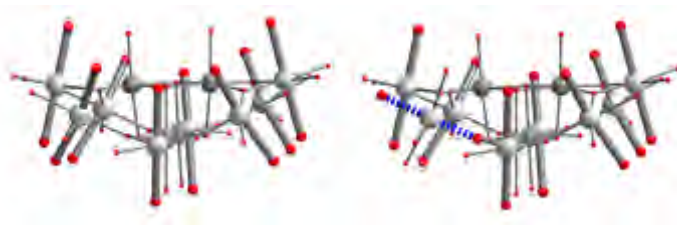
Figure 5.23: An example of Jahn–Teller isomerism in Mn12. On the right is shown a regular structure of the oxide core, with J-T elongation axes indicated as thicker solid lines. The dashed line in the structure on the right shows the isomer with a flipped J-T axis that lowers the axial anisotropy of the core.

With these experiments, we believe to have given a rather conclusive answer to a question that has been the interest of many research groups in the past few years, namely if it is possible to exploit the magnetic properties of Mn12 while it is sitting on a surface. If the previous set of experiments carried out

on monolayers of Mn12 on gold still left some doubts due to the presence of damaged clusters on the surface, in this case we have information on the lack of robustness of SMM behavior in this family of clusters.
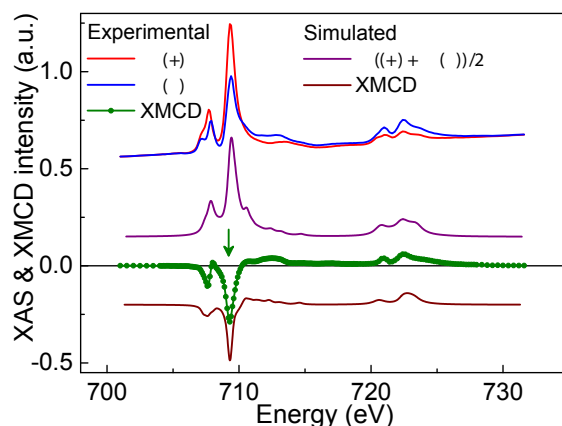
5.6.3 Drop cast Fe4C9SAc

Drop cast deposits of Fe4C9SAc were prepared following the same procedure used for Mn12PhSMe and introduced in the cryostat directly from the portable glove bag. Using the same beamline settings that yield a low photon flux on the sample, sets of XAS spectra with variable polarization were acquired at the Fe-$L_{2,3}$ edges. The XAS spectra, acquired at 0.75 K and at ± 30 kOe are shown in Figure 5.20 along with the corresponding XMCD spectra. Since no in-depth analysis of the spectral features of Fe4 had been carried out yet at the time this thesis was written, this series of spectra underwent an extensive analysis based on the Ligands Field Multiplets model.

This approach is based on a code developed by Thole[139] in the framework established by Cowan[151] and Butler[188] and takes into account all of the electronic Coulombic repulsions, the $3d$ and $2p$ spin-orbit coupling, and treats the geometrical environment of the absorbing atom by a crystal field potential.[189] The spectrum is calculated as the sum of all possible transitions for an electron jumping from the $2p$ to the $3d$ level in the electric dipole approximation, electric dipole allowed $2p$ to $4s$ transitions being negligible. The interelectronic repulsions are introduced through Slater integrals calculated by an atomic Hartree-Fock model. For the simulation of the Fe^{3+} $L_{2,3}$ edges in Fe4, the Slater integrals were scaled by a reduction factor $\kappa = 60\%$ to account for the electronic delocalization. The surrounding of the Fe^{3+} ions was described by an octahedral crystal field with $10Dq = 1.5$ eV.

Modeling of the XAS spectra gave indication that no photoreduction is occurring during the experiments; on the other hand, simulated XMCD spectra confirmed that the ferrimagnetic structure of the four Fe4 centers is still present, antiferromagnetic coupling between the central ion and the three peripheral ones being evidenced by calculations. We can therefore conclude that the topmost layers of the deposit are made of intact Fe4 clusters.

We then proceeded to investigate the field dependence of the XMCD signal of the sample; in order to do this we selected as a measuring channel the photon energy at which the L_3 negative peak is strongest (this peak is indicated with an arrow in Figure 5.24). Three hysteresis loops between ± 20 kOe were acquired at different temperatures (Figure 5.25): the highest temperature hysteresis, acquired at 1.4 K shows a completely closed loop, as expected from the dynamic parameters of Fe4C9SAc. At an intermediate temperature of 0.75 K a slight opening of the loop is observed, and at the lowest temperature we investigated, 0.55 K a fully open hysteresis can be seen. The peculiar butterfly shape of the loop is due to very efficient tunneling of the magnetization at zero field, that leads to a fast non thermal spin relaxation. A set of variable

Figure 5.24: Experimental and simulated XAS and XMCD spectra of Fe-$L_{2,3}$ edges of a drop cast sample of Fe4C9SAc measured at 0.75 K and ± 30 kOe.

temperature hysteresis loops measured on a single crystal of Fe4C9SAc measured by a classical magnetometry technique (μ-SQUID, measurement by W. Wernsdorfer) is reported in Figure5.26 for comparison.

The magnetization curves obtained by XMCD at the three temperatures were compared with the predicted bulk magnetization curves calculated in the same way as for Mn12PhSMe: these are reported in Figure 5.25 as solid lines superimposed to the experimental data. The Spin-Hamiltonian (eq. (5.23)) parameters determined from bulk samples used in the calculation were $S = 5$, $D/k_B = -0.629$ K and $g = 2.00$;[7] as can be seen, agreement between calculated and experimental data is excellent at all three temperatures, thus confirming that the magnetic properties are unaltered, in particular the splitting of the sublevels of $S = 5$ in zero field, thus the axial anisotropy of the molecule.

Although hysteresis loops are the most immediate and jazzy probes to directly access the magnetic dynamic properties of SMMs, dynamic parameter cannot be extrapolated from them. We then though of another method to do this, that is in effect inspired to one of the basic experiments in magnetometry: we measured realtime time decay of the XMCD signal in magnetized samples. To the best of our knowledge, this technique has never been applied in synchrotron radiation measurements. The technique consists in magnetizing the sample with a rather strong field (20 kOe in the case of Fe4), then quickly sweeping the field to zero or to a very small value of opposite sign (-2.5 kOe in our case) and measuring the XMCD signal as a function of time. This type of measurement can be carried out only in synchrotron radiation facilities where the beam is very stable (such as SLS) and the polarization can be switched
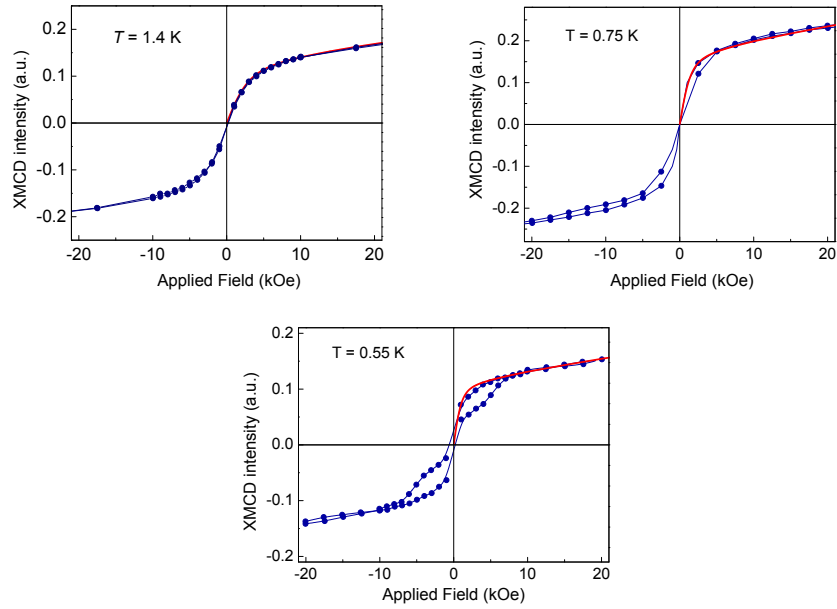
Figure 5.25: Hysteresis curves of a drop cast sample of Fe4C9SAc measured with XMCD in TEY detection mode at different temperatures (straight line represents the simulation obtained as described in the text).
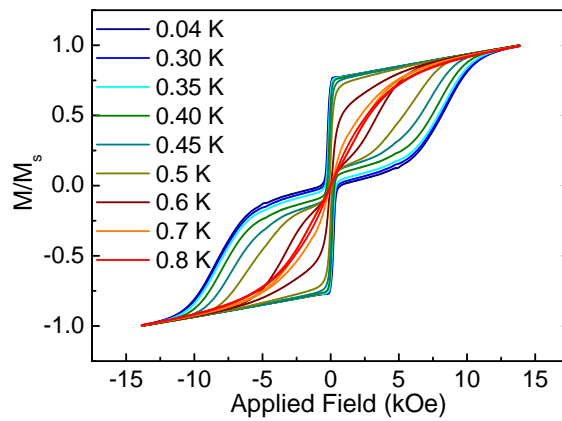
Figure 5.26: Hysteresis curves of a single crystal of Fe4C9SAc measured with μ-SQUID magnetometry at various temperatures.

very quickly, since it is necessary to acquire left and right polarized photon
absorption data at very close time intervals.

Choosing a non-zero field to record the decay can have two advantages: the
first one is directly connected to the detection method of the technique, since
TEY is more noisy in zero field. The second advantage is that Fe4, like all
SMMs, exhibits a non-thermal relaxation pathway through quantum tunneling
of magnetization, which is instead suppressed at $|H| = 2.5$ kOe.

Time decay of the XMCD signal was recorded at two temperatures, and they
are shown in Figure 5.27; the evolution of the signal is present, and a tem-
perature dependence can be observed as well. The inset of the figure shows
the same type of measurements carried out under the same conditions on the
Mn12PhSMe drop cast sample: it can be seen that no time evolution of the
XMCD signal is present, coherently with the absence of hysteretic behavior.
The magnetization decay process of dynamic origin can be modeled as a mono-
exponential process like the following:

$$I(t) = I_\infty + (I_0 - I_\infty)e^{-\frac{t}{\tau}} \tag{5.24}$$

where I, I_0 and I_∞ represent the XMCD intensity at the time t, at the
beginning of the experiments ($t = 0$) and at the equilibrium ($t = \infty$) respec-
tively and τ is the characteristic time of the process. This equation was used
to fit the two time decays measured at 0.70(5) K and 0.55(5) K on the sam-
ple. The fittings, represented in Figure5.27 as straight lines superimposed to
the experimental data, gave the values of the characteristic time of the process
tau, which does increase - as expected - at lower temperature. Such values,
$\tau = 87(5)$ s at $T = 0.70(5)$ K and $\tau = 285(10)$ s at $T = 0.55(5)$ K, have been
compared in Figure 5.28 to those found over a greater temperature range from
μSQUID measurements on a single crystal of Fe4C9SAc and were found to be
in reasonable agreement.

The opening of the hysteresis, the time decay experiments and the field depen-
dence of the magnetization measured in XMCD experiments confirmed us that
the topmost layers of Fe4C9SAc do not suffer from superficial strain issues that
caused Mn12PhSMe to modify its properties for the worse. These were very
good news for us since, while loosing the one long standing class of SMM as a
candidate for surface studies, we found a very promising candidate to replace
it.

The following step, covered by next section, was the study of such promising
family of Fe4 clusters as monolayers on gold.

5.7   Measurements on Fe4 monolayers

Self-organized monolayers of the cluster Fe4C9SAc have been described in detail
in Chapter 3, both for what concerns their preparation and their characteriza-
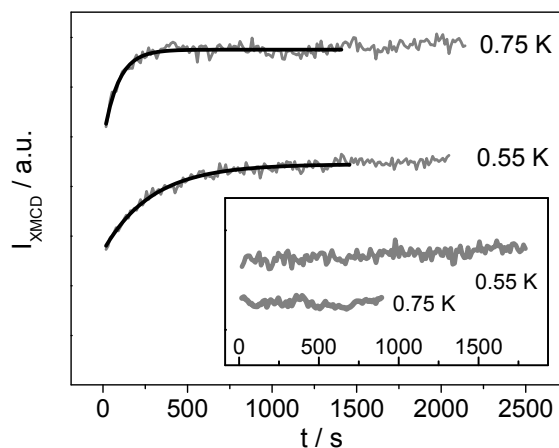
Figure 5.27: Time decay measurements of the XMCD signal of a drop cast sample of Fe4C9SAc measured with XMCD in TEY detection mode at 709.2 eV and at different temperatures (straight line represents the mono-exponential fitting). Sample was magnetized in a 20 kOe field and signal was measured at $H = -2.5$ kOe. Inset shows the same measurement carried out on the Mn12PhSMe drop cast sample.
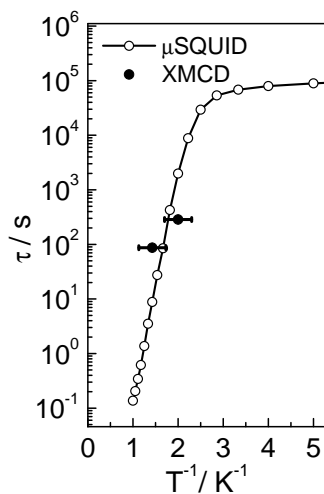
Figure 5.28: Arrhenius plot of the Fe4C9SAc cluster measured on a single crystal sample in the μ-SQUID setup and the two points obtained from XMCD decay measurements.

tion, by means of the complementary techniques of STM, XPS and ToF-SIMS. On the other hand, the encouraging answers given by XMCD measurements on bulk samples of this complex suggested that the observation of SMM behavior down to the monolayer of material grafted to a conductive surface was indeed a reachable goal.

XAS and XMCD measurements were carried out in BESSY II and in SLS (mostly) synchrotron radiation facilities.[190] All samples were prepared following the standard procedure of a 20 hour incubation and a wash in fresh solvent (we always used dichlorometane) under nitrogen atmosphere in a portable glove bag.

Exploratory measurements were carried out on the monolayers in order to gain information on the oxidation states and the spin structure of the grafted complex. The spectra, shown in Figure 5.29, were recorded at $T = 0.50 \pm 0.05$ K and under a field of 30 kOe; the two sets of right and left circularly polarized XAS spectra, while sitting on a rather strong background signal due to the underlying gold substrate, are well resolved and present all the spectral features that we observed in the drop cast samples of the same molecule (see Figure 5.24), that shall be regarded as our well understood standard.

The ratio between edge jump and the XAS intensity at the L_3 peak, $EJ = \frac{I_{peak} - I_{pre}}{I_{peak}} \times 100$, was found to be around 10%, with excellent reproducibility; EJ can be roughly correlated to the quantity of the probed element that is on the surface. If we compare the found value of EJ for these monolayers with the value for drop cast samples, i.e. the signal coming from about 5 nm of Fe4C9SAc, we find that the former is some five times smaller (EJ in drop cast is around 50%) The difference of the σ_+ and σ_- spectra gives a XMCD signal that is superimposable to that of the bulk sample, thus confirming that the ferrimagnetic spin structure is preserved in the monolayer; in addition to this, also the intensity ratio between XMCD and XAS, which was found to be around 0.25-0.30, perfectly matches that found in the bulk sample. In fact, as we have discussed more in detail about the drop cast sample measurements, due to the very similar coordination environment of the central and peripheral iron centers, an antiferromagnetic interaction is expected to afford an approximately halved XMCD/XAS ratio as compared with full polarization induced by the magnetic field. Fragmentation into simple paramagnetic units or dramatic alterations of the core structure would then be accompanied by significant changes in the XMCD/XAS ratio as compared with the bulk, that are not not observed here. This was a very satisfactory finding since, as we have been extensively exposing in section 5.5, the analogous monolayers of Mn12PhSMe were found to be modified upon interaction with the gold surface.

As we have been able to learn from experience though, integrity of the spin structure is not enough for the complex to behave as a SMM, since axial anisotropy can be lost simply by means of structural distortions. We then used part of a beamtime at BESSY II for which no dilution setup was mounted to make field-dependent XMCD measurements at temperatures higher than the
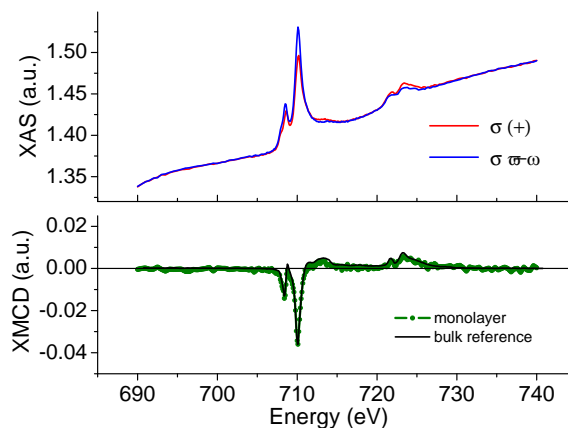
Figure 5.29: XAS and XMCD spectra of Fe-$L_{2,3}$ edges of a Fe4C9SAc monolayer measured at $T = 0.50 \pm 0.05$ K and $H = 30$ kOe.

blocking temperature of Fe4: by doing this, we were able to collect valuable information on the energy separation of sublevel splitting of $S = 5$ in the surface grafted clusters. The field-dependent XMCD curves, shown in Figure 5.30 were acquired at 709.2 eV and at two different temperatures (1.5 K and 4.5 K). These curves are plotted in the figure against H/T: the magnetization isotherms so obtained do not rescale on a unique curve, in agreement with what expected for a paramagnet exhibiting ZFS. The field dependence of the XMCD signal well compares with the magnetization curve calculated using the spin Hamiltonian which describes the magnetic behavior of bulk samples, also shown in Figure 5.30.

After these encouraging results, we employed our next low temperature beamtime in SLS in condensing all our acquired knowledge on the sample and the fine-tuning of all instrumental features, from beamline parameters to cryostat dilution setup in the attempt to achieve the long-awaited goal of recording an open magnetic hysteresis of a monolayer of SMMs on a surface. And failed. In order to communicate how delicate is the equilibrium between all parameters in this type of measurement, I will report the reason of our first failure to observe the opening of the hysteresis on this system.

As it has been described in section 5.3.4, thermal shielding of the sample space is a very delicate issue, since the sample itself cannot be completely insulated from the external environment. The most delicate point is the opening that lets the beam into the chamber. In the TBT setup, this opening was shielded by a Be foil that, at the price of some attenuation of the beam, gave a good thermal shielding. Unfortunately, the foil contained Fe impurities that are completely negligible while working in strong edge absorption regime, but that
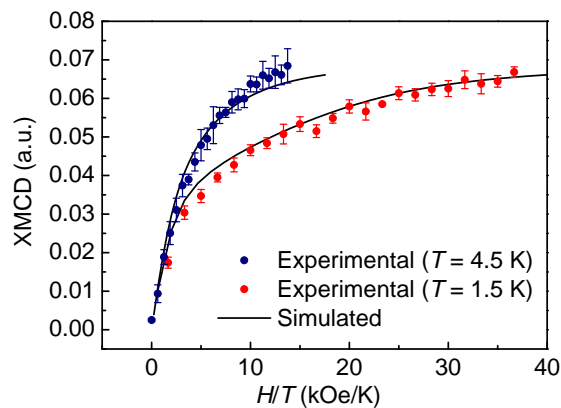
Figure 5.30: Field-dependent curves of the XMCD signal versus H/T of a Fe4C9SAc monolayer measured at 709.2 eV and at 1.5 K and 4.5 K.

became dominant in such a diluted sample regime as a monolayer, thus giving a negative peak. If such shield was removed, the temperature failed to remain under the 0.7 K necessary to observe unambiguous traces of irreversibility in the magnetic behavior.

In order to overcome this problem, we had to partially modify the TBT setup: the beryllium window was replaced with a thin ultrapure aluminium foil (0.7 μm, Lebow Company, Goleta, CA, USA. Iron content $< 0.01\%$); with this upgrade it was possible to reach very low temperature and observe nice signals at the Fe-$L_{2,3}$ edges. The hysteresis loops shown in Figure 5.31 were measured at 709.2 eV and at three different temperatures. A sweeping rate of 20 Oe/s has been employed and the error bars were obtained by averaging three runs. The butterfly shape is very similar to that found in the bulk sample (Figure 5.25) with the same method, and to what is expected for Fe4.

A further evidence of the presence of slow relaxation of magnetization was gathered by measuring the time decay of the XMCD signal, in a similar way to what has been done for the bulk sample (Figure 5.27). The decay curve of the monolayer is shown in Figure 5.32; at $T = 0.50 \pm 0.05$ K the sample was magnetized in a a strong positive magnetic field (+20.0 kOe), then the field was rapidly ramped to a moderate negative value (-2.5 kOe), and the time dependence of the dichroic signal was measured. The measurement was repeated four times and averaged, grey vertical bars representing the standard deviation. Though significantly noisier than the ones measured on the bulk, it clearly shows the presence of a time evolution of the signal in the expected direction; the fitting made with the mono-exponential decay function (5.24) is shown as the solid line in the figure; found characteristic time was $\tau = 218(14)$ s, which is good

agreement with what was found for the drop cast sample ($\tau = 285(10)$ s at the same temperature).
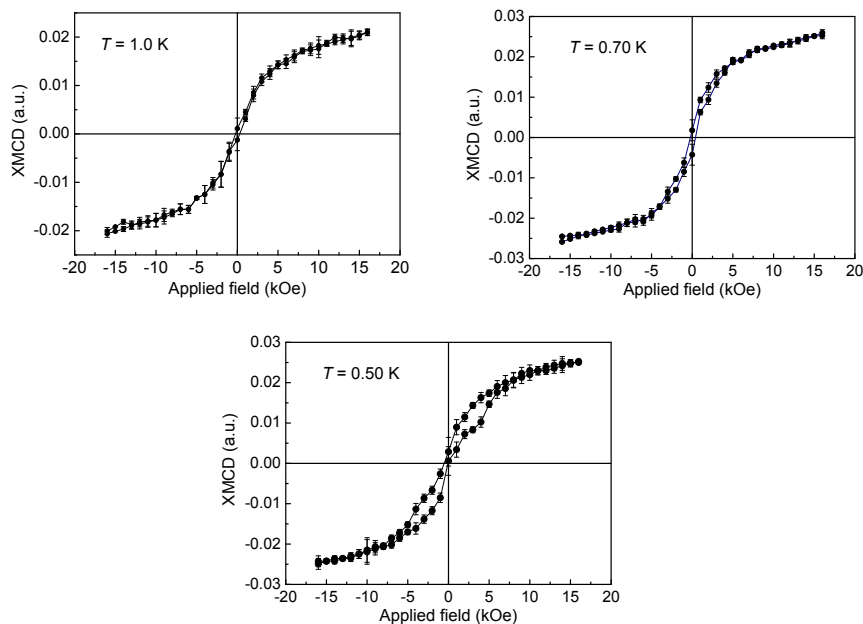
Figure 5.31: Hysteresis curves of a monolayer of Fe4C9SAc on gold measured with XMCD ($E = 709.2$ eV) in TEY detection mode at different temperatures.

In conclusion these results gave a positive answer to a key question, i.e. there are no fundamental reasons which preclude the observation of magnetic hysteresis when SMM are wired to a conducting substrate. This conclusion is not at all trivial given the peculiar origin of magnetic bistability in SMM: geometrical distortions as well as changes in the environment and in the effectiveness of spin-phonon coupling are indeed known to have a profound influence on the spin dynamics of SMM.

It is also worth pointing out the potential of XMCD for the characterization of monolayers of magnetic molecules; in these very demanding systems a series of factors, from chemical decomposition to the weakness of the signals to surface contamination can concur to failure in a satisfactory characterization.
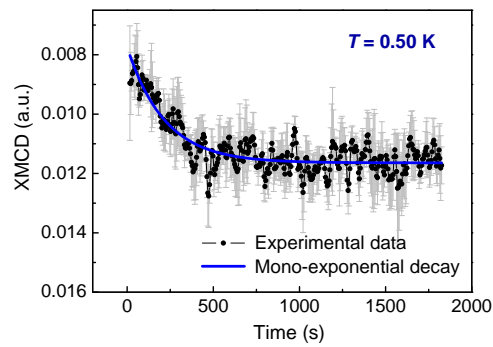
Figure 5.32: Time decay measurements of the XMCD signal of a monolayer of Fe4C9SAc on gold measured with XMCD in TEY detection mode at 709.2 eV and at $T = 0.50 \pm 0.05$ K (straight line represents the mono-exponential fitting). Sample was magnetized in a 20 kOe field and signal was measured at $H = -2.5$ kOe.

Summary and Conclusion

What I have learned   The work carried out during the three years of this thesis involved the acquisition and strengthening of skills in preparation of monolayers and their handling in protective environments, and in the surface science techniques necessary to inspect them. In addition to this, the precursor materials (bulk SMMs) were partly prepared by chemical synthesis and characterized with standard spectroscopic and magnetometric techniques. Skills for the inclusion of SMMs in polymeric matrices has been acquired as well, along with a basic knowledge of the theory and experimental techniques of MCD. Finally, experience in various synchrotron radiation facilities gave me the knowledge base on conduct and working principles of electron storage rings. Extensive use of beamtime for XMCD experiments enabled me to understand the basic level of theory underlying the measurement and to acquire data processing skills, as well as beamline endstation control.

What we have found   The studies on Mn12 monolayers on Au(111), which already were at an advanced degree of development in our group, were continued in depth, to find a strong dependence of the adsorbate's morphology on the solvent used to dissolve the SMM. In particular, tetrahydrofuran was found to yield sub–monolayers of fully isolated Mn12 units, that occasionally spontaneously organize into parallel rows; dichloromethane instead yields adsorbates of tightly packed molecules, that interact weakly with the gold surface. We also studied the possibility of inserting a Mn12 derivative into a preformed layer of simple aromatic thiols, and found the insertion process to be correlated to the structural features of the preformed SAM.

Magneto–optical studies were carried out on Mn12, in transparent polymers first, in order to have a good knowledge of the MCD response of the clusters, then on monolayers. This challenging type of measurement, carried out at the limit of the sensitivity of the setup, did not yield the long–awaited open hysteresis loop on the monolayer.

We could better understand the situation of Mn12 on the gold surface with the aid of XAS and XMCD, which revealed that Mn12 undergoes severe reduction on gold, almost completely loosing its spin structure; further XMCD studies on the first few molecular layers of bulk deposits of Mn12 showed no opening of the hysteresis, thus finally ruling out this complex for surface–grafting studies.

The second SMM, able to graft to gold due to a recent chemical functionalization, Fe4, was deposited on surface and accurately studied by means of STM, XPS and ToF–SIMS, and with MCD. Due to the very low blocking temperature of Fe4, the MCD setup is not able to detect any opening of the hysteresis, however we performed some interesting experiments both on Fe4 embedded in polymers and on monolayers. For polymers found that Fe4 is partially oriented in thin films of polystyrene, and for monolayers we recorded an enhancement of the MCD signal due to the plasmon resonances of an especially prepared rough gold substrate.

XMCD experiments on the surface of bulk deposits of Fe4 carried out at very low temperature gave the opening of the hysteresis loop, confirming the idea that a more rigid structure like Fe4 compared to Mn12 is less prone to superficial strains that alter the magnetic properties. In a subsequent set of measurements, after careful optimization of every part of the experiment, we were able to record the opening of the hysteresis also for a monolayer sample of Fe4, and to carry out other magnetic measurements, such as real–time decay of the XMCD signal, that confirmed the dynamic nature of the hysteresis.

We can then conclude that synchrotron radiation, and in particular the XMCD experiment coupled to a unique cryostat, able to reach sub–Kelvin temperature under photon flux, proved to be an invaluable tool, not only for its sensitivity, but for its high specificity.

We can also say that the choice of SMM is definitely a crucial step, since the unique magnetic properties of this class of compounds stems from a delicate interplay of structural and electronic parameters that, like in the case of Mn12, can be discomposed by much milder factors then chemical disruption.

Finally, we must reckon that this appears to be a quite special moment for the field of molecular magnetism: for the first time in fact we can state that SMMs can be covalently attached to metallic surfaces without loss of their properties, thus opening the way to the refinement of the deposition techniques and to a whole new series of experiments in the field of molecular spintronics. The magnetic addressing of individual SMMs, that is to be regarded as the final goal, is now open to scanning probe techniques and nano-gap fabrication and can be considered to be hindered only by technical issues.

References

1. Sessoli, R.; Gatteschi, D.; Caneschi, A.; Novak, M. A. *Nature* **1993**, *365*, 141–143.

2. Thomas, L.; Lionti, F.; Ballou, R.; Gatteschi, D.; Sessoli, R.; Barbara, B. *Nature* **1996**, *383*, 145–147.

3. Fort, A.; Rettori, A.; Villain, J.; Gatteschi, D.; Sessoli, R. *Phys. Rev. Lett.* **1998**, *80*, 612–615.

4. Pederson, M. R.; Porezag, D. V.; Kortus, J.; Khanna, S. N. *J. Appl. Phys.* **2000**, *87*, 5487–5489.

5. Milios, C. J.; Vinslava, A.; Wernsdorfer, W.; Moggach, S.; Parsons, S.; Perlepes, S. P.; Christou, G.; Brechin, E. K. *J. Am. Chem. Soc.* **2007**, *129*, 2754.

6. Cornia, A.; Costantino, A. F.; Zobbi, L.; Caneschi, A.; Gatteschi, D.; Mannini, M.; Sessoli, R. *Single-Molecule Magnets And Related Phenomena* **2006**, *122*, 133–161.

7. Barra, A. L.; Bianchi, F.; Caneschi, A.; Cornia, A.; Gatteschi, D.; Gorini, L.; Gregoli, L.; Maffini, M.; Parenti, F.; Sessoli, R.; Sorace, L.; Talarico, A. M. *Eur. J. Inorg. Chem.* **2007**, 4145–4152.

8. Carlin, R. *Magnetochemistry*; Springer-Verlag, Berlin, 1986.

9. Carlin, R. L.; van Duyneveldt, A. J. *Magnetic Properties of Transition Metal Compounds*; Springer-Verlag, New York, 1977.

10. Willet, R. D.; Gatteschi, D.; Kahn, O. *Magneto-Structural Correlations in Exchange Coupled Systems*; Reidel Publishing, Dordrecht, 1983.

11. Manriquez, J. M.; Yee, G. T.; Mclean, R. S.; Epstein, A. J.; Miller, J. S. *Science* **1991**, *252*, 1415–1417.

12. Ferlay, S.; Mallah, T.; Ouahes, R.; Veillet, P.; Verdaguer, M. *Nature* **1995**, *378*, 701–703.

13. Holmes, S. M.; Girolami, G. S. *J. Am. Chem. Soc.* **1999**, *121*, 5593–5594.

14. Train, C.; Gheorghe, R.; Krstic, V.; Chamoreau, L. M.; Ovanesyan, N. S.; Rikken, G. L. J. A.; Gruselle, M.; Verdaguer, M. *Nat. Mater.* **2008**, *7*, 729–734.

15. Caneschi, A.; Gatteschi, D.; Sessoli, R.; Barra, A. L.; Brunel, L. C.; Guillot, M. *J. Am. Chem. Soc.* **1991**, *113*, 5873–5874.

16. Sessoli, R.; Tsai, H. L.; Schake, A. R.; Wang, S. Y.; Vincent, J. B.; Folting, K.; Gatteschi, D.; Christou, G.; Hendrickson, D. N. *J. Am. Chem. Soc.* **1993**, *115*, 1804–1816.

17. Gatteschi, D.; Sessoli, R. *Molecular Nanomagnets*; Oxford University Press, Oxford, 2006.

18. Gatteschi, D.; Sessoli, R. *Angew. Chem. Int. Ed.* **2003**, *42*, 268–297.

19. Sanvito, S. *Nat. Mater.* **2007**, *6*, 803–804.

20. Ishikawa, N.; Sugita, M.; Ishikawa, T.; Koshihara, S.; Kaizu, Y. *J. Am. Chem. Soc.* **2003**, *125*, 8694–8695.

21. AlDamen, M. A.; Clemente-Juan, J. M.; Coronado, E.; Marti-Gastaldo, C.; Gaita-Arino, A. *J. Am. Chem. Soc.* **2008**, *130*, 8874.

22. Kahn, O. *Molecular Magnetism*; VCH, Weinheim, 1993.

23. Bencini, A.; Gatteschi, D. *Electron Paramagnetic Resonance of Exchange Coupled Systems*; Springer-Verlag, 1990.

24. Kambe, K. *J. Phys. Soc. Jpn* **1950**, *5*, 48.

25. van Slageren, J.; Rosa, P.; Caneschi, A.; Sessoli, R.; Casellas, H.; Rakitin, Y. V.; Cianchi, L.; Giallo, F. D.; Spina, G.; Bino, A.; Barra, A. L.; Guidi, T.; Carretta, S.; Caciuffo, R. *Phys. Rev. B* **2006**, *73*, 14422.

26. Barra, A.; Caneschi, A.; Cornia, A.; Fabrizi de Biani, F.; Gatteschi, D.; Sangregorio, C.; Sessoli, R.; Sorace, L. *J. Am. Chem. Soc.* **1999**, *121*, 5302–5310.

27. Cornia, A.; Fabretti, A. C.; Garrisi, P.; Mortalo, C.; Bonacchi, D.; Gatteschi, D.; Sessoli, R.; Sorace, L.; Wernsdorfer, W.; Barra, A. L. *Angew. Chem. Int. Ed.* **2004**, *43*, 1136–1139.

28. Saalfrank, R. W.; Scheurer, A.; Bernt, I.; Heinemann, F. W.; Postnikov, A. V.; Schunemann, V.; Trautwein, A. X.; Alam, M. S.; Rupp, H.; Muller, P. *Dalton Trans.* **2006**, 2865–2874.

29. Raghu, C.; Rudra, I.; Sen, D.; Ramasesha, S. *Phys. Rev. B* **2001**, *64*, 64419.

30. Regnault, N.; Jolicoeur, T.; Sessoli, R.; Gatteschi, D.; Verdaguer, M. *Phys. Rev. B* **2002**, *66*, 54409.

31. Gatteschi, D.; Pardi, L. *Mol. Cryst. Liq. Cryst.* **1993**, *232*, 577–590.

32. Goodenough, J. B. *J. Phys. Chem. Solids* **1958**, *6*, 287.

33. Goodenough, J. B. *Magnetism and the Chemical Bond*; Interscience, New York, 1963.

34. Kanamori, J. *J. Phys. Chem. Solids* **1959**, *10*, 87.

35. Kanamori, J. *Magnetism*; Acad. Press, New York, 1963; Vol. 1.

36. Lis, T. *Acta Cryst. B* **1980**, *36*, 2042.

37. Ako, A. M.; Hewitt, I. J.; Mereacre, V.; Clerac, R.; Wernsdorfer, W.; Anson, C. E.; Powell, A. K. *Angew. Chem. Int. Ed.* **2006**, *45*, 4926–4929.

38. Abragam, A.; Bleaney, B. *Electron Paramagnetic Resonance of Transition Ions*; Dover, New York, 1986.

39. Bencini, A.; Gatteschi, D. *Transit. Metal Chem.* **1982**, *8*, 1.

40. Gatteschi, D.; Barra, A. L.; Canschi, A.; Cornia, A.; Sessoli, R.; Sorace, L. *Coord. Chem. Rev.* **2006**, *250*, 1514.

41. Barra, A. L.; Caneschi, A.; Gatteschi, D.; Sessoli, R. *J. Magn. Magn. Mater.* **1998**, *177*, 709–710.

42. Hill, S.; Perenboom, J. A. A. J.; Dalal, N. S.; Hathaway, T.; Stalcup, T.; Brooks, J. S. *Phys. Rev. Lett.* **1998**, *80*, 2453–2456.

43. Caciuffo, R.; Amoretti, G.; Murani, A.; Sessoli, R.; Caneschi, A.; Gatteschi, D. *Phys. Rev. Lett.* **1998**, *81*, 4744–4747.

44. Barra, A. L.; Gatteschi, D.; Sessoli, R.; Abbati, G. L.; Cornia, A.; Fabretti, A. C.; Uytterhoeven, M. G. *Angew. Chem. Int. Ed.* **1997**, *36*, 2329–2331.

45. Goldberg, D. P.; Telser, J.; Krzystek, J.; Montalban, A. G.; Brunel, L. C.; Barrett, A. G. M.; Hoffman, B. M. *J. Am. Chem. Soc.* **1997**, *119*, 8722–8723.

46. Bencini, A.; Ciofini, I.; Uytterhoeven, M. G. *Inorg. Chim. Acta* **1998**, *274*, 90–101.

47. Chibotaru, L. F.; Ungur, L.; Soncini, A. *Angew. Chem. Int. Ed.* **2008**, *47*, 4126–4129.

48. Villain, J.; Hartmanboutron, F.; Sessoli, R.; Rettori, A. *Europhys. Lett.* **1994**, *27*, 159–164.

49. Caneschi, A.; Ohm, T.; Paulsen, C.; Rovai, D.; Sangregorio, C.; Sessoli, R. *J. Magn. Magn. Mater.* **1998**, *177*, 1330–1336.

50. Accorsi, S.; Barra, A. L.; Caneschi, A.; Chastanet, G.; Cornia, A.; Fabretti, A. C.; Gatteschi, D.; Mortalo, C.; Olivieri, E.; Parenti, F.; Rosa, P.; Sessoli, R.; Sorace, L.; Wernsdorfer, W.; Zobbi, L. *J. Am. Chem. Soc.* **2006**, *128*, 4742–4755.

51. Novak, M. A.; Sessoli, R. *Quantum Tunneling of Magnetization - QTM'94*; Kluwer, Dordrecht, 1995; pp 171–188.

52. Friedman, J. R.; Sarachik, M. P.; Tejada, J.; Ziolo, R. *Phys. Rev. Lett.* **1996**, *76*, 3830–3833.

53. Caneschi, A.; Gatteschi, D.; Sessoli, R. *J. Chem. Soc. Dalton* **1997**, 3963–3970.

54. Zobbi, L.; Mannini, M.; Pacchioni, M.; Chastanet, G.; Bonacchi, D.; Zanardi, C.; Biagi, R.; Del Pennino, U.; Gatteschi, D.; Cornia, A.; Sessoli, R. *Chem. Commun.* **2005**, 1640–1642.

55. Holland, H. L.; Brown, F. M.; Larsen, B. G.; Zabic, M. *Tetrahedron-Asymmetr.* **1995**, *6*, 1569–1574.

56. Altomare, A.; Burla, M. C.; Camalli, M.; Cascarano, G. L.; Giacovazzo, C.; Guagliardi, A.; Moliterni, A. G. G.; Polidori, G.; Spagna, R. *J. Appl. Crystallogr.* **1999**, *32*, 115–119.

57. Aubin, S. M. J.; Sun, Z. M.; Eppley, H. J.; Rumberger, E. M.; Guzei, I. A.; Folting, K.; Gantzel, P. K.; Rheingold, A. L.; Christou, G.; Hendrickson, D. N. *Inorg. Chem.* **2001**, *40*, 2127–2146.

58. Bouwen, A.; Caneschi, A.; Gatteschi, D.; Goovaerts, E.; Schoemaker, D.; Sorace, L.; Stefan, M. *J. Phys. Chem. B* **2001**, *105*, 2658–2663.

59. Saalfrank, R. W.; Bernt, I.; Chowdhry, M. M.; Hampel, F.; Vaughan, G. B. M. *Chem. Eur. J.* **2001**, *7*, 2765–2769.

60. Bigelow, W. C.; Pickett, D. L.; Zisman, W. A. *J. Colloid Interface Sci.* **1946**, *1*, 513.

61. Nuzzo, R. G.; Allara, D. L. *J. Am. Chem. Soc.* **1983**, *105*, 4481.

62. Ulman, A. *Chemical Reviews* **1996**, *96*, 1533–1554.

63. Eppley, H. J.; Tsai, H. L.; Devries, N.; Folting, K.; Christou, G.; Hendrickson, D. N. *J. Am. Chem. Soc.* **1995**, *117*, 301–317.

64. Cornia, A.; Fabretti, A. C.; Pacchioni, M.; Zobbi, L.; Bonacchi, D.; Caneschi, A.; Gatteschi, D.; Biagi, R.; Del Pennino, U.; De Renzi, V.; Gurevich, L.; Van der Zant, H. S. J. *Angew. Chem. Int. Ed.* **2003**, *42*, 1645–1648.

65. Pineider, F.; Mannini, M.; Sessoli, R.; Caneschi, A.; Barreca, D.; Armelao, L.; Cornia, A.; Tondello, E.; Gatteschi, D. *Langmuir* **2007**, *23*, 11836–11843.

66. Naitabdi, A.; Bucher, J. P.; Gerbier, P.; Rabu, P.; Drillon, M. *Advanced Materials* **2005**, *17*, 1612–+.

67. Voss, S.; Fonin, M.; Rudiger, U.; Burgert, M.; Groth, U. *Applied Physics Letters* **2007**, *90*, 133104.

68. Voss, S.; Zander, O.; Fonin, M.; Rudiger, U.; Burgert, M.; Groth, U. *Physical Review B* **2008**, *78*, 155403.

69. Bain, D.; Troughton, E.; Tao, Y.-T.; Evall, J.; Whitesides, G. M.; Nuzzo, R. G. *J. Am. Chem. Soc.* **1989**, *111*, 321.

70. Poirer, M. J., G. E.; Tarlov *Langmuir* **1994**, *10*, 2853.

71. Kaefer, D.; Witte, G.; Cyganik, P.; Terfort, A.; Wöll, C. *J. Am. Chem. Soc.* **2006**, *128*, 1723.

72. Moulder, J. M.; Stickle, W. F.; Sobol, P. E.; Bomben, K. D. *Handbook of X-ray Photoelectron Spectroscopy*; Perkin-Elmer Corporation: Eden Prairie, MN, 1992.

73. Kang, J. S.; Kim, J. H.; Kim, Y. J.; Jeon, W. S.; Jung, D. Y.; Han, S. W.; Kim, K. H.; Kim, K. J.; Kim, B. S. *J. Korean Phys. Soc.* **2002**, *40*, L402–L405.

74. Chambliss, D. D.; Wilson, R. J.; Chiang, S. *Phys. Rev. Lett.* **1991**, *66*, 1721–1724.

75. Wöll, C.; Chiang, S.; Wilson, R. J.; Lippel, P. H. *Phys. Rev .B* **1989**, *39*, 7988.

76. Dishner, M. H.; Ivey, M. M.; Gorer, S.; Hemminger, J. C.; Feher, F. J. *J. Vac. Sci. Technol. A* **1998**, *16*, 3295–3300.

77. Mina, B.; Alemozafara, A.; Bienera, M.; Bienera, J.; C.M., F. *Top. Catal.* **2005**, *236*, 77.

78. Rousset, S.; Croset, B.; Girard, Y.; Prevot, G.; Repain, V.; Rohart, S. *C. R. Phys.* **2005**, *6*, 33–46.

79. Xie, Z. X.; Huang, Z. F.; Xu, X. *Phys. Chem. Chem. Phys.* **2002**, *4*, 1486–1489.

80. Hara, M.; Sasabe, H.; Knoll, W. *Thin Solid Films* **1996**, *273*, 66–69.

81. Mannini, M.; Bonacchi, D.; Zobbi, L.; Piras, F. M.; Speets, E. A.; Caneschi, A.; Cornia, A.; Magnani, A.; Ravoo, B. J.; Reinhoudt, D. N.; Sessoli, R.; Gatteschi, D. *Nano Lett.* **2005**, *5*, 1435–1438.

82. Liu, G. Y.; Xu, S.; Qian, Y. L. *Acc. Chem. Res.* **2000**, *33*, 457–466.

83. Martin, Y.; Wickramsinghe, H. *Appl. Phys. Lett* **1987**, *50*, 1455.

84. Oral, A.; Bending, S. J.; Henini, M. *Appl. Phys. Lett.* **1996**, *69*, 1324–1326.

85. Pineider, F.; Mannini, M.; Sangregorio, C.; Gorini, L.; Sessoli, R. *Inorg. Chim. Acta* **2008**, *361*, 3944–3950.

86. Kelly, K. F.; Shon, Y. S.; Lee, T. R.; Halas, N. J. *J. Phys. Chem. B* **1999**, *103*, 8639–8642.

87. Tao, Y. T.; Wu, C. C.; Eu, J. Y.; Lin, W. L.; Wu, K. C.; Chen, C. H. *Langmuir* **1997**, *13*, 4018–4023.

88. Ulman, A. *An Introduction to Ultrathin Organic Films*; Academic Press, Boston, 1991.

89. Love, J. C.; Estroff, L. A.; Kriebel, J. K.; Nuzzo, R. G.; Whitesides, G. M. *Chem. Rev.* **2005**, *105*, 1103–1169.

90. Biebuyck, H. A.; Bian, C. D.; Whitesides, G. M. *Langmuir* **1994**, *10*, 1825–1831.

91. Troughton, E.; Bain, C.; Whitesides, G. *Langmuir* **1988**, *4*, 365.

92. Wiesendanger, R.; Guntherodt, H. J.; Guntherodt, G.; Gambino, R. J.; Ruf, R. *Phys. Rev. Lett.* **1990**, *65*, 247–250.

93. Condorelli, G. G.; Motta, A.; Pellegrino, G.; Cornia, A.; Gorini, L.; Fragala, L. L.; Sangregorio, C.; Sorace, L. *Chemistry Of Materials* **2008**, *20*, 2405–2411.

94. Heersche, H. B.; de Groot, Z.; Folk, J. A.; van der Zant, H. S. J.; Romeike, C.; Wegewijs, M. R.; Zobbi, L.; Barreca, D.; Tondello, E.; Cornia, A. *Physical Review Letters* **2006**, *96*, 206801.

95. Bogani, L.; Wernsdorfer, W. *Nat. Mater.* **2008**, *7*, 179.

96. Galtayries, A.; Grimblot, J. *Journal of Electron Spectroscopy and Related Phenomena* **1998**, 98–99.

97. Mannini, M.; Sorace, L.; Gorini, L.; Piras, F. M.; Caneschi, A.; Magnani, A.; Menichetti, S.; Gatteschi, D. *Langmuir* **2007**, *23*, 2389–2397.

98. Attwood, D. *Soft X-Rays and Extreme Ultraviolet Radiation: Principles and Applications*; Cambridge University Press, Cambridge, 2000.

99. Jackson, J. *Classical Electrodynamics*; Wiley, New York, 1999.

100. Siegmann, H. C. *J. Electron Spectrosc. Relat. Phenom.* **1994**, *68*, 505–514.

101. Stephens, P. J. *J. Chem. Phys.* **1970**, *52*, 3489.

102. Stephens, P. J. *Adv. Chem. Phys.* **1976**, *35*, 197.

103. Piepho, S. B.; Schatz, P. N. *Group Theory in Spectroscopy*; John Wiley and Sons, 1983.

104. Mason, W. R. *A Practical Guide to Magnetic Circular Dichroism Spectroscopy*; Wiley-Interscience, 2007.

105. Neese, F.; Solomon, E. I. *Inorg. Chem.* **1999**, *38*, 1847.

106. Cavigli, L. *Dottorato di Ricerca in Scienza e Tecnologia dei Materiali*, Dipartimento di Fisica – Università degli Studi di Firenze, 2006.

107. Bogani, L. *Dottorato di Ricerca in Scienze Chimiche*, Dipartimento di Chimica – Università degli Studi di Firenze, 2006.

108. Cavigli, L.; de Julian Fernandez, C.; Gatteschi, D.; Gurioli, M.; Sangregorio, C.; Mattei, G.; Mazzoldi, P.; Bogani, L. *J. Magn. Magn. Mater.* **2007**, *316*, e798–e801.

109. Badoz, J.; Silverman, M. P.; Canit, J. C. *J. Opt. Soc. Am. A* **1990**, *7*, 672.

110. Novak, R. Ph.D. thesis, Dottorato in Scienze Chimiche,University of Florence, 2008.

111. Bogani, L.; Cavigli, L.; Gurioli, M.; Novak, R. L.; Mannini, M.; Caneschi, A.; Pineider, F.; Sessoli, R.; Clemente-Leon, M.; Coronado, E.; Cornia, A.; Gatteschi, D. *Adv. Mater.* **2007**, *19*, 3906–+.

112. McInnes, E. J. L.; Pidcock, E.; Oganesyan, V.; Cheesman, M. R.; Powell, A. K.; Thomson, A. *J. Am. Chem. Soc.* **2002**, *124*, 9219.

113. Novak, R. L.; Pineider, F.; Fernandez, C. D.; Gorini, L.; Bogani, L.; Danieli, C.; Cavigli, L.; Cornia, A.; Sessoli, R. *Inorg. Chim. Acta* **2008**, *361*, 3970–3974.

114. Jacobsen, C. J. H.; Pedersen, E.; Villadsen, J.; Weihe, H. *Inorg. Chem.* **1993**, *32*, 1216–1221.

115. Sorace, L. *Dottorato di Ricerca in Scienze Chimiche*, Dipartimento di Chimica – Università degli Studi di Firenze, 2001.

116. Nie, S.; Emory, S. R. *Science* **1997**, *275*, 1102.

117. Kneipp, K.; Moskovits, M.; Kneipp, H. *Surface-Enhanced Raman Scattering Physics and Applications*; Springer Berlin / Heidelberg, 2006; Vol. 103.

118. Shemer, G.; Markovich, G. *J. Phys. Chem. B* **2002**, *106*, 9195 – 9197.

119. Lieberman, I.; Shemer, G.; Fried, T.; Kosower, E. M.; Markovich, G. *Angew. Chem. Int. Ed.* **2008**, *47*, 4855 – 4857.

120. Li, Y.; Zhang, Q.; Nurmikko, A. V.; Sun, S. *Nano Lett.* **2005**, *5*, 1689.

121. Young, A. T.; Arenholz, E.; Marks, S.; Schlueter, R.; Steier, C.; Padmore, H. A.; Hitchcock, A. P.; Castner, D. G. *J. Synchrotron Radiat.* **2002**, *9*, 270–274.

122. Marks, S.; Cortopassi C, J., .and DeVries; Hoyer, E.; Leinbach, R.; Minamihara, Y.; Padmore, A., H.and Young The Advanced Light Source elliptically polarizing undulator. *Proceeding of the Particle Accelerator Conference*, 1997.

123. Röntgen, W. *Sitzber. Physik. Med. Ges.* **1895**, *137*, 132.

124. Barkla, C. *Phil. Trans.* **1905**, *A204*, 467.

125. Barkla, C. *Proc. Roy. Soc. London* **1906**, *A 77*, 247.

126. Chapman, J. *Phil. Mag.* **1913**, *25*, 792.

127. Bennet, H.; Stern, E. *Phys. Rev.* **1965**, *137*, A448.

128. Erskine, J.; Stern, E. *Phys. Rev. B* **1975**, *12*, 5016.

129. Hrdý, J.; Krouský,; Renner, O. *Phy. Stat. Sol. (a)* **1979**, *53*, 143.

130. Froman, D. *Phys. Rev.* **1932**, *41*, 693.

131. Kartschagin, W.; Tschetwerikova, E. *Zeitsch. für Physik* **1926**, *39*, 886.

132. Hart, M.; Rodriguez, A. *Phil. Mag. B* **1981**, *43*, 321.

133. Schütz, G.; Zech, E.; Hagn, E.; Kienle, P. *Hyperfine Interact.* **1983**, *16*, 1039.

134. Thole, B.; van der Laan, G.; Sawatzky, G. *Phys. Rev. Lett.* **1985**, *55*, 2086.

135. Van der Laan, G.; Thole, B.; Sawatzky, G.; Goekoop, J.; Fuggle, J.; Esteva, J.; Karnatak, R.; Remeika, J.; Dabkowska, H. *Phys. Rev. B* **1986**, *34*, 6529.

136. Schütz, G.; Wagner, W.; Wilhelm, W.; Kienle, P.; Zeller, R.; Frahm, R.; Materlik, G. *Phys. Rev. Lett.* **1987**, *58*, 737.

137. Schütz, G.; Frahm, P., R. Mautner; Wienke, R.; Wagner, W.; Wilhelm, W.; Kienle, P. *Phys. Rev. Lett.* **1989**, *62*, 2620.

138. Chen, C. T.; Sette, F.; Ma, Y.; Modesti, S. *Phys. Rev. B* **1990**, *42*, 7262–7265.

139. Thole, B.-T.; van der Laan, G.; Fuggle, J.; Sawatzky, G.; Karnatak, R.; Esteva, J.-M. *Phys. Rev. B* **1985**, *32*, 5107.

140. Carra, P.; König, B.; Thole, B.; Altarelli, M. *Physica B* **1993**, *192*, 182.

141. Siddons, D.; Hart, M.; Amemiya, Y.; Hastings, J. *Phys. Rev. Lett.* **1990**, *64*, 1967.

142. Sacchi, M.; Mirone, A. *Phys. Rev. B* **1998**, *57*, 8408.

143. Hellwig, O.; Kortright, J. B.; Takano, K.; Fullerton, E. E. *Phys. Rev. B* **2000**, *62*, 11694–11698.

144. Mertins, H. C.; Oppeneer, P. M.; Kunes, J.; Gaupp, A.; Abramsohn, D.; Schafers, F. *Phys. Rev. Lett.* **2001**, *87*, 47401.

145. Goulon, J.; Goulon-Ginet, C.; Rogalev, A.; Gotte, V.; Malgrange, C.; Brouder, C.; Natoli, C. R. *J. Chem. Phys.* **1998**, *108*, 6394–6403.

146. Goulon, J.; Rogalev, A.; Goulon-Ginet, C.; Benayoun, G.; Paolasini, L.; Brouder, C.; Malgrange, C.; Metcalf, P. A. *Phys. Rev. Lett.* **2000**, *85*, 4385–4388.

147. Goulon, J.; Rogalev, A.; Wilhelm, F.; Goulon-Ginet, C.; Carra, P.; Cabaret, D.; Brouder, C. *Phys. Rev. Lett.* **2002**, *88*, 237401.

148. Carra, P.; Jerez, A.; Marri, I. *Phys. Rev. B* **2003**, *67*, 45111.

149. Goulon, J.; Rogalev, A.; Wilhelm, F.; Goulon-Ginet, C.; Carra, P.; Marri, I.; Brouder, C. *J. Exp. Theor. Phys.* **2003**, *97*, 402–431.

150. Stöhr, *NEXAFS Spectroscopy*; Springer, 1992.

151. Cowan, R. *The Theory of Atomic Structure and Spectra*; University of California Press, 1981.

152. Kramers, H.; Heisenberg, W. *Z. Phys.* **1925**, *31*, 681.

153. Dirac, P. *Proc. R. Soc. A* **1927**, *114*, 243.

154. Messiah, A. *Quantum Mechanics*; Wiley, 1958.

155. Als-Nielsen, J.; McMorrow, D. *Elements of Modern X-Ray Physics*; Wiley, 2001.

156. Schiff, L. *Quantum Mechanics*; McGraw-Hill, 1968.

157. Mandl, F.; Shaw, G. *Quantum Field Theory*; Wiley, 1993.

158. Fermi, E. *Nuclear Physics*; University Chicago Press, 1950.

159. Loudon, R. *The Quantum Theory of Light*; Clarendon, Oxford, 1973.

160. Brouder, C. *J. Phys.: Condens. Matter* **1990**, *2*, 701.

161. Chen, C. T.; Tjeng, L. H.; Kwo, J.; Kao, H. L.; Rudolf, P.; Sette, F.; Fleming, R. M. *Phys. Rev. Lett.* **1992**, *68*, 2543–2546.

162. Luning, J.; Nolting, F.; Scholl, A.; Ohldag, H.; Seo, J. W.; Fompeyrine, J.; Locquet, J. P.; Stohr, J. *Phys. Rev. B* **2003**, *67*, 214433.

163. Chen, C. T.; Idzerda, Y. U.; Lin, H. J.; Smith, N. V.; Meigs, G.; Chaban, E.; Ho, G. H.; Pellegrin, E.; Sette, F. *Phys. Rev. Lett.* **1995**, *75*, 152–155.

164. Rogalev, A.; Wilhelm, F.; Jaouen, N.; Goulon, J.; Kapler, J. *Magnetism: A Synchrotron Radiation Approach*; Springer, 2006.

165. Goulon, J.; Rogalev, A.; Wilhelm, F.; Jaouen, N.; Goulon-Ginet, C.; Brouder, C. *J. Phys.: Condens. Matter* **2003**, *15*, S633–S645.

166. Stöhr, J.; Wu, Y. *New Directions in Research with Third-Generation Soft XRay Synchrotron Radiation Sources*; Kluwer, Netherlands, 1994; p 221.

167. Thole, B. T.; Carra, P.; Sette, F.; Vanderlaan, G. *Phys. Rev. Lett.* **1992**, *68*, 1943–1946.

168. Carra, P.; Thole, B. T.; Altarelli, M.; Wang, X. D. *Phys. Rev. Lett.* **1993**, *70*, 694–697.

169. Stöhr, J.; Konig, H. *Phys. Rev. Lett.* **1995**, *75*, 3748–3751.

170. Wu, R. Q.; Wang, D. S.; Freeman, A. J. *Phys. Rev. Lett.* **1993**, *71*, 3581–3584.

171. Wu, R. Q.; Freeman, A. J. *Phys. Rev. Lett.* **1994**, *73*, 1994–1997.

172. Stöhr, J.; Siegmann, H. *Magnetism - From Fundamentals to Nanoscale Dynamics*; Springer Series in solid-state sciences; Springer-Verlag Berlin Heidelberg, 2006.

173. Stohr, J.; Nakajima, R. *IBM J. Res. Dev.* **1998**, *42*, 73–88.

174. Sainctavit, P.; Kappler, J.-P. *Magnetism and Synchrotron Radiation*; Editions de Physique, Paris, 2000; pp 235–253.

175. Letard, I.; Sainctavit, P.; Cartier dit Moulin, C.; Kappler, J. P.; Ghigna, P.; Gatteschi, D.; Doddi, B. *J. Appl. Phys.* **2007**, *101*, 113920.

176. Pobell, F. *Matter and methods at low temperatures*; Springer, New York, 1996.

177. Lounasmaa, O. *Experimental Principles and Methods Below 1K*; Academic Press, London, 1974.

178. Moroni, R.; Moulin, C. C. D.; Champion, G.; Arrio, M. A.; Sainctavit, P.; Verdaguer, M.; Gatteschi, D. *Phys. Rev. B* **2003**, *68*, 64407.

179. Ghigna, P.; Campana, A.; Lascialfari, A.; Caneschi, A.; Gatteschi, D.; Tagliaferri, A.; Borgatti, F. *Phys. Rev. B* **2001**, *64*, 132413.

180. Mannini, M.; Sainctavit, P.; Sessoli, R.; Moulin, C. C. D.; Pineider, F.; Arrio, M. A.; Cornia, A.; Gatteschi, D. *Chem. Eur. J.* **2008**, *14*, 7530–7535.

181. Barraza-Lopez, S.; Avery, M. C.; Park, K. *Phys. Rev. B* **2007**, *76*, 224413.

182. Arrio, M. A.; Scuiller, A.; Sainctavit, P.; Moulin, C. C. D.; Mallah, T.; Verdaguer, M. *J. Am. Chem. Soc.* **1999**, *121*, 6414–6420.

183. Aubin, S. M. J.; Sun, Z. M.; Pardi, L.; Krzystek, J.; Folting, K.; Brunel, L. C.; Rheingold, A. L.; Christou, G.; Hendrickson, D. N. *Inorg. Chem.* **1999**, *38*, 5329–5340.

184. Thole, B. T.; Vanderlaan, G.; Fabrizio, M. *Phys. Rev. B* **1994**, *50*, 11466–11473.

185. Soler, M.; Chandra, S. K.; Ruiz, D.; Davidson, E. R.; Hendrickson, D. N.; Christou, G. *Chem. Commun.* **2000**, 2417–2418.

186. Voss, S.; Fonin, M.; Rudiger, U.; Burgert, M.; Groth, U.; Dedkov, Y. S. *Phys. Rev. B* **2007**, *75*, 45102.

187. Mannini, M.; Pineider, F.; Sainctavit, P.; Arrio, M.-A.; Wernsdorfer, W.; Cornia, A.; Gatteschi, D.; Sessoli, R. *Adv. Mater.* **2009**, *21*, 167–171.

188. Butler, P. *Point Group Symmetry, Applications, Methods and Tables*; Plenum, New York, 1991.

189. De Groot, F.; Fuggle, J.; Thole, B.; Sawatzky, G. *Phys. Rev. B* **1990**, *42*, 5459.

190. Mannini, M.; Pineider, F.; Sainctavit, P.; Danieli, C.; Otero, E.; Sciancalepore, C.; Talarico, A.; Arrio, M.-A.; Cornia, A.; Gatteschi, D.; Sessoli, R. *Nat. Mater.* **2009**, Accepted for Publication.

Acknowledgement

I thank my parents Maria and Carlo for their continuous care and for the support to my formative path.

I wish to extend my gratitude to all the members of the Laboratory of Molecular Magnetism, who have made my stay during this thesis a very stimulating and pleasant one. I am especially indebted to Prof. Roberta Sessoli, who constantly provided me with unequalled scientific guidance and encouraged me with her friendly presence. I sincerely thank Prof. Dante Gatteschi for the open–mindedness he has always been demonstrating toward his scholars and for the time he has been dedicating to dispense me with precious bits of knowledge. Prof. Andrea Dei and Prof. Andrea Caneschi constantly pervaded me with their wisdom, that I hope to have absorbed at least in part. Dr. Matteo Mannini has been trying very hard from the to make a tidy chemist out of me, and did not succeed much, I am afraid. He succeed instead in sharing with me much of his quickly developing knowledge and I hope he could stand without too great discomfort my utter verbosity. He is the colleague and friend with which I have shared the most of my research activity and of the sleepless nights in synchrotrons throughout Europe. Dr. Claudio Sangregorio followed my first, trembling steps in the world of scientific research even before these three years, and I am much indebted to him. I thank Drs. Lorenzo Sorace, César De Julian Fernandez, Claudia Innocenti Maria Fittipaldi, Federico Totti and Donella Rovai for their help and for the nice atmosphere they create in the group. A very fond acknowledgment goes to Ilaria Benvenuti, who can always give a helping hand when organization is required.

I wish to dedicate a thought of true affection to the late Prof. Alessandro Bencini, whose sudden demise left me, like many others who knew him, devoid of a person did not want any walls between the teacher's desk and the student's bench and that was at the same time our professor and our friend.

Not many of the fine results presented in this thesis could have probably been achieved without the tight and long standing collaboration with Prof. Andrea Cornia's Group in Modena. Prof. Cornia's ability and creativity in fact produced excellent ideas and even better molecules, also thanks to the skillful work of Dr. Chiara Danieli and Corrado Sciancalepore. A significant contribution